

Retzlaff, Rebecca

Vom Fachbereich VI
(Raum- und Umweltwissenschaften)
der Universität Trier
zur Erlangung des akademischen Grades
Doktor der Naturwissenschaften
(Dr. rer. nat.)
genehmigte Dissertation

**On the Potential of Small UAS for Multispectral Remote Sensing in
Large-Scale Agricultural and Archaeological Applications**

Betreuender und Berichterstatter:

Univ.-Prof. Dr. Thomas Udelhoven

Berichterstatter:

Univ.-Prof. Dr. Johannes Ries

Univ.-Prof. Dr. Patrick Hostert

Datum der wissenschaftlichen Aussprache:

20. November 2015

Trier, 2016

Acknowledgements

This work would not have been carried out had not Prof. Dr. Thomas Udelhoven, Dep. of Environmental Remote Sensing and Geoinformatics, given me the opportunity and encouraged me to this study to resume scientific life. Equally, Prof. Dr. Patrick Hostert, Geography Dep., Humboldt-Universität Berlin, supported the work right from the beginning, and Prof. Dr. Johannes Ries, Department of Physical Geography, Universität Trier has always welcomed discussion on unmanned aerial systems (UAS) and their applications in the field of archaeology. UAS was new to me and I have learned a lot about the technology from Gilles Rock. In the same way, I am indebted to Christian Bossung for taking part in numerous flight campaigns.

Within the study cases, I am much obliged to the following people:

- Dr. Daniel Molitor and Dr. Danièle Evers, Luxembourg Institute of Science and Technology (LIST) introduced us to the VITISOL project in Grevenmacher, carried out the plant-related work, provided in-situ data and viticulturist input for the grapevine study; Tom Wantzenrieder, Monica Perez and Christian Bossung supported the UAS flight campaigns with many hours and special thanks go to Gilles Rock for flying the drone safely in windy conditions.
- The Geobotany Department, always welcomed short-term use of their laboratory and stood aside with technological advice;
- Prof. Dr. Uwe Rascher and his team for supporting the fluorescence experiment during the Flex campaign, and we were particularly grateful for irradiation data provided by Dr. Micol Rossini from the Remote Sensing of Environmental Dynamics Lab, University of Milan-Bicocca, Italy;
- The opportunity to fly the UAS in Spain and look into archaeological drone applications was given by Prof. Dr. Trunk, Klassische Archäologie, Universität Trier and together with the departments of Geobotany and Physical Geography, have culminated in an intensive field trip at an interesting location. Likewise, Prof. Dr. Seifert and her team shared their geomagnetic finds.

I would like to thank Sebastian Lamprecht, Eric Hass and Gilles Rock for helping with Python-Scripting, R scripts and figures, Eric Hass for providing and discussion of texture measure scripts and Barbara Paschmionka for support vector machines. My deep gratitude goes to Dr. Achim Röder, Anja Brassel, Christian Bossung and Gilles Rock for their willingness to discuss the work structure and for critical comments when re-

viewing the chapters during the potentially hottest weather period in Germany that year. Equally, the whole department of Environmental Remote Sensing and Geoinformatics has again proven a lively academic society always up to scientific discussions, and Anne Menkhaus and Tana Watts have helped with administrative issues.

Above all, my special thanks go to my family who set me free to follow the field work even abroad, at holidays and weekends and their constant encouragement. Stefan, Saturdays are free to your disposals again!

Trier, July 2015

Table of Contents

Acknowledgements	I
Contents	III
List of Figures	IX
List of Tables	XVI
Abbreviations	XIX

Contents

1 Introduction	1
Part I	4
2 Unmanned Aerial Systems for Environmental Remote Sensing	5
2.1 Terms and Definitions	5
2.1.1 UAS versus UAV	5
2.1.2 UAS Benefits and Drawbacks	6
2.2 Categorization of Civil Unmanned Aircraft Systems	8
2.2.1 UAS Classification Based on Platform Propulsion	9
2.2.2 UAS Classification Based on Total Weight	9
2.2.3 UAS Classification Based on Altitude and Endurance.....	10
2.3 Outline of the Historic Evolution of Civil-Use UAS.....	10
2.3.1 First UAS and Developments until 2000.....	10
2.3.2 Recent Developments of Civil UAS (2000-2015).....	12
2.4 UAS Platforms Used for Environmental Remote Sensing and Archaeology.....	15
2.4.1 Lighter-than air platforms.....	15
2.4.2 Heavier-than air platforms	17
2.4.2.1 Fixed Wing Kites.....	17
2.4.2.2 Fixed Wing Paraglider.....	17
2.4.2.3 Fixed Wing Aircraft.....	17
2.4.2.4 Rotary Wing Small UAS	19
2.5 Ground Control Station.....	19
2.6 Autopilots: Navigation and Attitude Control	20
2.7 Navigation and Attitude Control	21
2.8 Communication – Telecontrol & Telemetry.....	21
2.9 Payload: Imaging Sensors for UAS	22
2.9.1 Digital Cameras	23
2.9.2 Digital SLR- and SLM-Cameras	23
2.9.3 Multispectral Cameras	24
2.9.4 Hyperspectral sensors	24

2.9.5	Thermal sensors	25
2.9.6	LIDAR	25
2.10	Airspace Regulation.....	32
2.10.1	European Airspace Regulation	32
2.10.2	Airspace Regulation in Germany.....	36
2.10.3	Airspace Regulation in Luxembourg.....	37
2.10.4	Airspace Regulation in Spain	38
3	Remote Sensing of Vegetation in Vis/nIR Spectral Range.....	39
3.1	Multispectral Properties of Plant Foliage	39
3.1.1	Leaf Structure	39
3.1.2	Biochemical Radiative Interactions with Leaves	40
3.1.3	Light interactions within the Photosystem II: Fluorescence and Non-Photochemical Quenching.....	43
3.1.4	Factors Influencing Leaf Reflectance	44
3.1.4.1	Leaf Architecture	44
3.1.4.2	Leaf Age	44
3.1.4.3	Leaf Water Content.....	45
3.1.4.3	Leaf Nutritions and Diseases	46
3.2	Multispectral Properties of Canopies.....	46
3.2.1	Sensor- and Illumination Geometry.....	46
3.2.1.1	Bidirectional Reflectance Effects of Canopies.....	46
3.2.1.2	The Bidirectional Reflectance Distribution Functions	48
3.2.2	Canopy parameters	50
3.2.2.1	Leaf's Pigments, Leaf Water and Structure.....	50
3.2.2.2	Leaf Area Index	51
3.2.2.3	Plant Geometry Effects.....	51
3.2.2.4	Soil Background Effects	54
3.2.2.5	Row Orientation and Density	54
3.3	Thermal Remote Sensing of Vegetation.....	57
3.3.1	Thermal Properties of Vegetation.....	57
3.3.2	Canopy Emissivity.....	57
3.3.3	Influence of Background	60
4	UAS, Sensors and Data.....	62
4.1	UAS: The md4-1000 Quadcopter.....	62
4.2	UAS Cameras	66
4.2.1	Digital Single Lens Reflex Camera: D3100	66
4.2.2	Multispectral Camera: Mini-MCA-6.....	67
4.2.3	Thermal Camera: Un-Cooled Module (UCM)	69
4.3	Reflectance Measurements: Spectroradiometer	70
4.4	Field Measurements of Plant Parameters	71
4.4.1	Leaf Area Index	71
4.5	Chlorophyll Measurements.....	72
4.5.1	Wet-chemical Analysis	72

4.5.2	Chlorophyll Meter SPAD-502	72
4.6	GPS Measurements	73
5	Radiometric and Photogrammetric Preprocessing of Aerial Image Data....	75
5.1	Systematic Camera Errors	75
5.1.1	Camera Interior Orientation	75
5.1.2	Lens Distortion	76
5.1.3	Vignetting Correction	83
5.1.4	Correction of Systematic Camera Errors for MiniMCA-6Data	83
5.1.4.1	Band Alignment	83
5.1.4.2	Data Conversion of 10-bit Data and Exposure Corrections	85
5.1.4.3	Lens Distortion Estimation from Structure from Motion Software	86
5.1.4.4	Noise	86
5.1.4.5	Vignetting Correction	87
5.2	Radiometric Correction of Atmospheric Effects	90
5.2.1	The radiation paths betw. solar irradiance, atmosphere and at-sensor radiance..	90
5.2.2	Topographic effects	92
5.2.3	Bidirectional Reflectance	93
5.2.4	Atmospheric Correction Using ATCOR-4	93
5.2.5	Empirical Line Method for Atmospheric Correction and Calibration	95
5.3	Geometric Processing	98
5.3.1	Exterior Orientation of Camera during Image Acquisition	98
5.3.2	Absolute Orientation of Camera during Image Acquisition	100
5.3.3	Bundle Block Adjustment	101
5.3.4	Structure from Motion Software for 3D Model Generation, Mosaicing of Orthophotos and Generating DEM	102
5.4	Discussion of Pre-processing Steps	106
6	Filter Wavelength Selection, Sensitivity Analysis and Scale Issues of the Multispectral Camera.....	107
6.1	The PROSAIL Canopy Reflectance Model	107
6.2	Filter Wavelength Selection	111
6.2.1	Introduction	111
6.2.2	Spectra Simulations	113
6.2.3	Wavelength Selection Algorithms	115
6.2.4	Results	116
6.2.4.1	Comparison of Wavelength Selection Algorithms	116
6.2.4.2	Crop-Type Dependent Wavelength Selection	119
6.2.5	Discussion	125
6.2.6	Conclusion	126
6.3	Bidirectional Reflectance Simulations and Measurements of a Maize Canopy Using a UAS Goniometer-Flight	127
6.3.1	Introduction	127
6.3.2	Data and Methods	128
6.3.3	Results	131

6.3.4	Discussion.....	141
6.3.5	Conclusion.....	142
6.4	Sensitivity of Signal to Flight Altitude and Air Mass.....	144
6.4.1	Data & Methods.....	144
6.4.2	Results.....	144
6.4.3	Discussion and Conclusion.....	147
Part II	149
7	The Impact of Soil Management Effects on Grapevine Physiological Variables and Vigour Using Multispectral UAS-Data.....	150
7.1	Introduction.....	150
7.2	Material and Methods.....	153
7.2.1	Study Site.....	153
7.2.2	Soil Management Strategies.....	154
7.2.3	Field Sampling and Analysis.....	156
7.2.4	UAS Image Acquisition.....	158
7.2.5	Data Preparation.....	161
7.2.5.1	Multispectral Image Data.....	161
7.2.5.2	2012 Thermal Data.....	165
7.2.6	Statistical Data Analysis.....	166
7.3	Results.....	168
7.3.1	Field assessments.....	168
7.3.2	Spectral Separability of Soil Management Strategies Observed by Different Viewing Angles (2011 Data).....	170
7.3.3	Separability of Soil Management Strategies Observed by Thermal Radiation (2012 Data).....	172
7.3.4	Ability to Predict Physiological Parameters and Yield for Grapevine Using Different Viewing Geometries (2011 Data).....	174
7.3.5	Predicting Seasonal Grapevine Physiological Parameters and Yield (2012)....	176
7.3.5.1	Chlorophyll Estimation (2012).....	176
7.3.5.2	LAI (2011 versus 2012).....	181
7.3.5.2	Yield Estimation (2012).....	182
7.4	Discussion.....	183
7.5	Conclusion.....	187
8	UAS-based Retrieval of Sun-Induced Fluorescence.....	189
8.1	Introduction.....	189
8.1.1	Remote Sensing of Sun-Induced Chlorophyll-Fluorescence.....	190
8.1.1.1	Radiance-Based Method for Fluorescence Retrieval.....	191
8.1.1.2	Fluorescence Reflectance and Method for Fluorescence Retrieval.....	194
8.1.2	The Impact of N-Fertilization on UAS-based Sun-induced Chlorophyll Fluorescence Measurements.....	196
8.1.3	UAS-Based Diurnal Observations of Sun-induced Chlorophyll Fluorescence.....	196

8.2	Experiment Campus Klein-Altendorf 1 (CKA1): N-Fertilization Rate and Fluorescence	197
8.2.1	Material and Methods	197
8.2.1.1	Field Data Collection	198
8.2.1.2	Airborne Campaign and Data Processing	198
8.2.1.3	Statistical Analysis	204
8.2.2	Results	205
8.2.3	Discussion	211
8.3	Experiment Campus Klein-Altendorf 2 (CKA2): Diurnal Solar-Induced Fluorescence Measurements of Sugar Beet	212
8.3.1	Material and Methods	212
8.3.1.1	Site Description	212
8.3.1.2	Field Data Collection	212
8.3.1.3	Airborne Campaign and Data Processing	213
8.3.1.4	Diurnal Sun-Induced Fluorescence Retrieval	213
8.3.2	Results	213
8.3.3	Discussion	223
8.4	Conclusion	225
9	UAS-Based Archaeological Reconnaissance at the Roman Settlement of Los Bañales de Uncastillo, Spain.....	227
9.1	Introduction	227
9.1.1	Overview of Geomatic Prospection Sensors	227
9.1.2	Remote Sensing of Cultural Heritage Patterns	228
9.1.2.1	Crop and Soil Mark Analysis	229
9.1.2.2	Feature Enhancements Used in Archaeological Remote Sensing	230
9.1.2.3	Land Cover Classification of Archaeological Sites	231
9.1.3	Using Small UAS for Archaeology	231
9.1.4	The Roman Settlement of Los Bañales	232
9.1.5	Objectives	233
9.2	Study Site	233
9.2.1	Historical Outline	233
9.2.2	Vegetation Patterns on El Pueyo	236
9.3	Data Sources	237
9.3.1	UAS Image Acquisition and Pre-Processing	237
9.3.2	GPS Data	238
9.3.3	Ancillary Data	238
9.4	Methods	239
9.4.1	Pre-Processing: Point Cloud Modelling and Image Mosaicing	239
9.4.1.1	Derivation of Orthophoto Mosaic and DEM for the Roman City of Los Bañales as a Mapping Base (flight #106 and #107)	239
9.4.1.2	Derivation of Multispectral Orthophoto Mosaics for El Pueyo	241
9.4.1.3	Derivation of Multispectral Orthophoto Mosaics for Cultural Pattern Reconnaissance in Agricultural Fields (#108 and #111)	242

9.4.2	Feature Enhancement.....	244
9.4.3	Land Cover Classification Using Support Vector Machines.....	245
9.5	Results.....	247
9.5.1	Base Map for Analysis of Settlement Patterns at El Pueyo and Surroundings .	247
9.5.2	Vegetation Type Classification as an Indicator for Former Land Use	249
9.5.3	Detection of Cultural Heritage Patterns in the Eastern and Southern Vicinity of El Pueyo	257
9.6	Summary.....	260
9.7	Conclusions.....	261
10	Summary and Discussion	263
11	Conclusion and Recommendations	271
12	References.....	273
	Summary	302

List of Figures

Figure 1.1 Reference hits by Google Scholar.....	2
Figure 2.1 Whittlesey's tethered balloon for archaeological reconnaissance in Turkey (Whittlesey 1970, p. 182)	11
Figure 2.2 References of different UAS categories listed in the respective UVSI Yearbooks within the past years (van Blyenburgh (ed.) 2011-2015).....	13
Figure 2.3 Referenced UAS by intended purpose in the UVSI Yearbooks 2011-2015 ..	14
Figure 2.4 Data source RPAS Yearbook 2014 (van Blyenburgh 2014a, p. 156).....	14
Figure 2.5 UAS Airframes referenced in the RPAS 2010-2015 (RPAS Yearbooks (van Blyenburgh 2010-2015). Rotary wing UAS includes shrouded rotary wing systems.....	15
Figure 2.6 The Goethe blimb (Rock 2010, p.24)	16
Figure 2.7 The model UAS Sirius by MAVinci (Rock 2015).....	18
Figure 2.8 VTOL development 1960-2012 (mod. from Watts et al. 2012)	19
Figure 2.9 mdCockpit Waypoint Editor (microdrones GmbH).....	20
Figure 2.10 Nikon D3100 used with md4-1000 (Photo: J. Besold)	23
Figure 3.1 Water and gaseous pathway through a model leaf (Source: mod.from Taiz and Zeiger 2010 p. 97).....	40
Figure 3.2 Leaf pigment absorption (Blackburn 2007, p. 857).....	41
Figure 3.3 Grass absorption, reflectance and transmittance (Source: Jensen 2007a, p.362).....	42
Figure 3.4 Reflectance of a green sugar beet leaf (black); characteristic fluorescence curve in red (Source: Meroni et al. 2009, p.2038).....	43
Figure 3.5 Fluorescence of healthy green and senesced vegetation (Source: Camp-bell and Wynne 2011, p. 51).....	44
Figure 3.6 Reflectance spectral of healthy and dried vegetation and soil (Source: Jones and Vaughan 2010, p. 46).....	45
Figure 3.7 Sources of anisotropic reflectances in the environment (mod from Beisl and Woodhouse 2004, p. 1684).....	47
Figure 3.8 Bidirectional reflectance differences for a spring barley field along the solar principal plane (sun azimuth 114°, sun altitude)	48
Figure 3.9 Anisotropy factors (nadir-normalized BRDF) of ryegrass for different wavelengths and a sun zenith angle of 35°(mod. Sandmeier and Itten 1999).....	49
Figure 3.10 Effects of variation of Prosail biophysical input parameters on spectral signatures	53
Figure 3.11 Reflectance (RC) polar plots of a uniform canopy model (o), a row model (•) and the Verhoef-Bunnik rectangular prism model (x) of wheat (Suits 1983, p.123).....	55

Figure 3.12 Polar plots of directional reflectances in the red (left) and nIR (right) retrieved by the row model for four wheat growth stages (I: sparse, II: low, denser canopy, III: well-developed canopy with less inter-row soil cover, III: homogenous canopy) (modified by Haho e Zhao et al. 2010)	56
Figure 3.13 Effect of LAI (left) and leaf angle distribution (right) on apparent emissivity of a vegetation canopy (mod. from Guoqan and Zhengzhi 1992).....	58
Figure 3.14 Changes in apparent emissivity with viewing distance [m] in relation to wavelength (Ribeiro da Luz and Crowley 2007).....	59
Figure 3.15 Emissivity spectral of young and old pines (MODIS UCSB Emissivity Library, http://www.ices.ucsb.edu/modis/EMIS/images/pinenew.gif and pineold.gif , access date 28/04/2015)	60
Figure 3.16 Diurnal course of radiant and kinetic temperature for different surfaces (Source: Jensen 2007a, p.725)	61
Figure 4.1 The md4-1000 with base station (photos: J. Besold 2011)	62
Figure 4.2 Rotor movement with the md4-1000 (microdrones GmbH 2008-2010)	63
Figure 4.3 mdCockpit 3.2 Waypoint editor (microdrones GmbH 2007-2013).....	64
Figure 4.4 Ground station device	64
Figure 4.5 GNSS and IMU data text files and positional accuracy as given by flight recorder data	65
Figure 4.6 Spectral response of a CMOS sensor (mod. El Gamal and Eltoukhy 2005)..	66
Figure 4.7 Nikon D3100 with wide angle lens.....	66
Figure 4.8 The Mini-MCA6 with front-filter mounting (photo: © Tetracam Inc.).....	67
Figure 4.9 Spectral sensitivity of the Mini-MCA-6' CMOS sensor response modified from Tetracam Inc.) and filters (filter transmission as supplied from producer) 68	
Figure 4.10 Mini-MCA-6 with front-to-rear filter rebuilt (left) with filters put behind the lens plate to facilitate filter access and change (right) (Photographs: M. Perez Saíz)	68
Figure 4.11 The thermal camera UCM (photo: G. Rock 2011)	69
Figure 4.12 Thermal image (7-14 μm) of a vineyard taken with UCM	70
Figure 4.13 Spectralon reflectance (white reference) developed by Labsphere Inc., North Sutton, NH, USA.....	71
Figure 4.14 The SPAD-502 chlorophyll meter	73
Figure 5.1 Interior orientation parameters (modified from Mikhail et al. 2001, p.21)....	76
Figure 5.2 Radial $\Delta\rho$ and tangential lens distortion ΔP . Image projection point is orthogonal to main autocollimation beam (AB) (mod. from Kraus 2004, p. 49).	77
Figure 5.3 Lens distortion types: original pattern (left) pincushion distortion (middle), barrel distortion (right)	77
Figure 5.4 Calibration checkerboard pattern (left) and screenshot with DSLR for estimating lens distortion.....	79
Figure 5.5 Radial and tangential distortion for Nikon D3100 lens used with 10 mm focal length	81
Figure 5.6 Nikon D3100 vignetting correction masks for RGB (left to right).....	83

Figure 5.7 Multispectral image with misaligned bands after use of global alignment parameters showing colour halos (left) and corrected band alignment (right)....	84
Figure 5.8 Lens calibration parameters retrieved for the MiniMCA-6: camera focal length in x- and y-direction (fx, fy), principal point on image plane (cx, cy), followed by radial distortion as retrieved by Agisoft software	86
Figure 5.9 Vignetting with dust particles visible for the MiniMCA-6 lenses with respective filter	87
Figure 5.10 False colour composite (R: 900 nm, G: 570 nm, B: 550 nm) of a maize field with vignetting (left) and corrected image (right)	88
Figure 5.11 Pre-processing flowchart for Mini-MCA6 data: from raw single images to multiband images.....	89
Figure 5.12 Radiance paths from sun to sensor (E0: solar irradiance, Ed: diffuse sky irradiance, θ : sun zenith angle, $\tau_{\theta 0}$: atmospheric transmittance, θ_v : exit angle towards sensor, LP: path radiance, LT target radiance/reflectance, LS total at-sensor radiance, mod. from Jensen 2007, p. 59).....	90
Figure 5.13 Bidirectional illumination differences for a tree stand with nadir viewing (Source: Holopainen and Wang 1998, p. 682)	93
Figure 5.14 Reference targets (left) and respective reflectance measurement with spectroradiometer (right)	94
Figure 5.15 The empirical line calibration	96
Figure 5.16 Absolute reflectance differences for reference panels after ELC	97
Figure 5.17 Exterior orientation (mod. from Intergraph Corporation 2013, p. 552).....	99
Figure 5.18 Flight plan geometry and bundle rays.....	101
Figure 5.19 Example of a 3D point cloud model with stray points requiring further editing	103
Figure 5.20 Textured 3D model representation of a site and its image locations obtained with Agisoft PhotoScan Professional	103
Figure 5.21 Orthophoto-mosaic and DEM retrieved by SfM software.....	104
Figure 5.22 Pre-processing chain applied to multispectral data.....	105
Figure 6.1 PROSAIL coupled model: black arrows indicate forward modelling mode, grey arrows indicate inverse modelling mode (mod. from Jacquemoud et al. 2009).....	110
Figure 6.2 Coefficient of determination (R^2) for linear regression of canopy reflectances and plant parameters for the given wavelengths. Abbreviations: GBM: green biomass, Chlconc: Chla+b, N: leaf nitrogen conc: concentration (Source: Hansen and Schjoerring 2003, p.545).....	111
Figure 6.3 R^2 values of linear relationships between EWT and leaf reflectances values (Mobasheri and Fatemi 2013, p.198).....	113
Figure 6.4 Correlation spectra between simulated reflectance spectrum and plant variable (bold green line: simulated Chla+b spectrum for grassland).....	117
Figure 6.5 Scatter plots for wavelength selection algorithms to predict Chla+b	118
Figure 6.6 Selected optimal filter locations for the prediction of grassland Chla+b.....	118

Figure 6.7 Simulated grassland spectrum with selected filter wavelengths for Chla+b and LAI.....	119
Figure 6.8 Six-band wavelength selections in relation to Chla+b for all iterations used in the Genetic Algorithm (GA). Red squares represent final selection.	122
Figure 6.9 Six-band wavelength selection in relation to LAI for all iterations used in the Genetic Algorithm (GA). Red squares represent final selection.	123
Figure 6.10 Three- (top) and four-band (bottom) filter wavelength selections retrieved by Genetic Algorithm (GA) for grassland. Red squares represent final select.	124
Figure 6.11: Raw UAS image of maize canopy (Tetracam MiniMCA-6 b. 900 nm)...	128
Figure 6.12: Goniometer-flight plan for maize field on the Ehranger Flur, Germany, presented on Google Earth data, image is oriented to the N (28/04/2014).....	129
Figure 6.13A: Simulated (left) versus measured (right) reflectances for goniometer flight over maize field at Ehranger Flur, 20/08/2011. Radius values define VZA, AA are deviation from the solar principal plane (0°-180°, sun position 137°, elevation 46°).....	134
Figure 6.13B: Simulated (left) versus measured (right) reflectances for goniometer flight over maize field at Ehranger Flur, 20/08/2011. Radius values define VZA, AA are deviation from the solar principal plane (0°-180°, sun position 137°, elevation 46°).....	135
Figure 6.14: Simulated relative reflectance differences for VZA (0-25°) across all AA derived from PROSAIL model.....	137
Figure 6.15: Absolute reflectances for VZA (0-25°) across all AA derived from UAS flight.....	138
Figure 6.16: Simulated and UAS-derived reflectances at 670 nm for solar principal plane (PP) and N-S transect (Sun elevation 46°, sun azimuth 137°).....	139
Figure 6.17: Simulated and UAS-derived reflectances at 900 nm for solar principal plane (PP) and N-S transect (Sun elevation 46°, sun azimuth 137°).....	139
Figure 6.18: Polar plots of simulated key vegetation indices obtained from PROSAIL for maize (sun elevation 44°, sun azimuth 136°, i.e. 0° in plots)	140
Figure 6.19 Reference panels in relation to flight altitude at Vis/nIR wavelengths.....	145
Figure 6.20 DN of white reference panel extracted for images of different flight altitudes.....	146
Figure 6.21 DN of black reference panel extracted for images of different flight alt... ..	147
Figure 7.1 Location of studied vineyard in Grevenmacher, Luxembourg, with soil management strategy plots (1-4) and replicates (A-D). Data source: UAS image (R: 900 nm, G 670 nm, B 550 nm; ESRI Data & Maps for ArcGIS® 2012)....	155
Figure 7.2 Seasonal nitrogen uptake and content for grapevine in relation to growth stages (modified from Schultz and Löhnertz 2002, p.20)	157
Figure 7.3 Flight route along the vineyard at Grevenmacher for 17/08/2011	159
Figure 7.4 Multispectral images from study vineyard (17/08/2011) taken with different viewing angles: top left: nadir; top right: 45° VZA illuminated; bottom: 45° VZA shaded canopy (RGB: 900 nm, 550 nm, 530 nm).	161

Figure 7.5 Polygons for retrieving canopy spectral value means (top: nadir VZA, bottom: 45° VZA).....	164
Figure 7.6 Mosaic of thermal histogram-matched images from 28/06/2012	166
Figure 7.7 Plot of the principal component 1 and 2 for all rows and nadir and oblique viewing geometries (Retzlaff et al. 2015, in press)	170
Figure 7.8 Box-plots of different vegetation indices versus SMS 1- 4 (x-axis) for the viewing geometries nadir, illuminated and shaded grapevine sides (black line: median, boxes minimum and maximum values, tails: non-outlier range, circles: outliers).....	171
Figure 7.9 Box-plot of thermal radiation signal versus SMS for 28/06/2012.....	173
Figure 7.10 ANOVA results of thermal radiation signal versus SMS for 28/06/212 ...	173
Figure 7.11 Heatmap of in-situ measured physiological variables in 2011 (red: high correlation, blue: low correlation, N: nadir; Shad: 45° VZA shaded; Illum: 45° VZA illuminated, I-IV are measurement dates of in-situ sampling from beginning of berry development to harvest).....	174
Figure 7.12 Cross-validated regression models and model coefficients for Chl and N content, and NBI for 2012	177
Figure 7.13 Chlorophyll estimation for image acquisition dates based on global regression model of in-situ derived Chl and reflectances in 2012 (repl. A).....	179
Figure 7.14 Mean seasonal course and standard deviation of measured Chl (Dualex) across all replicates in 2012 (SMS: soil management strategy; bars: standard deviation)	180
Figure 7.15 Cross-validated regression for LAI.....	181
Figure 7.16 Cross-validated regression models and model coefficients for different within-season times in 2012 (top left: 71 Fruit set; top right 77-79 Berries touching; 85 Softening of berries, 89 Berries ripe for harvest)	182
Figure 7.17 Plot of Chl (Dualex) versus N (top) and NBI (Dualex) versus N content for the field measurements in 2012	185
Figure 7.18 Time shift between seasonal field Chl measurements (arithmetic mean: black dots) and UAS image acquisition dates (grey asterix) in 2012.....	186
Figure 8.1 Location of Fraunhofer Line absorption maximum in relation to sensor band spectral resolution (mod. from Damm et al. 2011, p. 1886).....	190
Figure 8.2 Top-of-atmosphere radiance and top-of-canopy Fs for green vegetation and location of O ₂ -absorption bands (from: Guanter et. al. 2010, D1903).....	192
Figure 8.3 Sun-induced chlorophyll fluorescence for a sugar beet leaf (top) and its contribution to the reflectance signal (bottom) (from: Meroni et al. 2009, p. 2038).....	194
Figure 8.4 Diurnal Fs radiation for a maize-wheat field in China, 13/05/2010 (from Zhao et al. 2014, p. 10186).....	196
Figure 8.5 Study Site Campus Klein-Altendorf 1 (multispectral data).....	197
Figure 8.6 Camera locations and error estimates for.....	199
Figure 8.7 Study Site Campus Klein-Altendorf 1 (thermal data).....	202

Figure 8.8 Camera locations and error estimates for thermal UAS flight (Z error is represented by ellipse color, X,Y errors by ellipse shape)	203
Figure 8.9 Box-plots of band means and VIs versus N treatment (x-axis) for the CKA1 (black line: median, boxes: minimum and maximum values, tails: non-outlier range, circles: outliers)	207
Figure 8.10 Box-plots of band means and VIs versus sugar beet variety (x-axis) for the CKA1 (black l: median, boxes: min. and max. values,	208
Figure 8.11 Field measurement setup at CKA2: field spectrometer and grey-level reference panels (Photo: M. Perez).....	212
Figure 8.12 Incoming radiance measured with field spectrometer at 747.5 nm [$Wm^{-2}sr^{-1}nm^{-1}$] [mod. from Rascher et al. 2013]	216
Figure 8.13 Diurnal sun-induced fluorescence for CKA2 derived from multispectral UAS data (right axis, red triangles) and Ocean Optics Spectrometer (left axis, blue diamonds) retrieved by Meroni (2015, personal communication), 23/08/2012.	217
Figure 8.14 Correlation between field- and UAS-derived sun-induced fluorescence at 760 nm at CKA2, 23/08/2012.....	218
Figure 8.15 Diurnal course of F_s ,UAS (3FLD) values retrieved using different reference non-fluorescent target	219
Figure 8.16 Diurnal course of NDVI and PRI at CKA2, 23/08/2012 for spectrometer data (top) and MiniMCA-6/UAS data (bottom). Red square: NDVI, blue diamonds: PRI	220
Figure 8.17 Diurnal sun-induced chlorophyll F_s ,UAS (3FLD) for a sugar beet field at CKA2 (23/08/2012). Centre image HyFlex F_s , HyFlex data derived at noon at 600 m a.s.g. (white square shows field).....	221
Figure 8.18 Illumination (left) and viewing zenith angle (VZA) deviation from nadir (right) for UAS image acquisitions.....	224
Figure 8.19 F_s for CKA2 sugar beet field derived from airborne data obtained at 600 m a.g.l. (top right image corner). Image source has been subsetted from final HyFlex report (Rascher et al. 2013, p. 78).	224
Figure 9.1 Geomatic methods and their application scales in archaeological prospection (mo-dified from Bitelli 2012)	227
Figure 9.2 Crop-marks based on sub-surface cultural heritage features and their effects on upper soil moisture and crop growth: darker greyshades illustrate higher soil moisture and vice versa (modified from Lasaponara and Masini 2012, p. 5) ...	230
Figure 9.3 The study site of Los Bañales in Arragon, Spain. Dots indicate camera positions for individual flights.....	234
Figure 9.4 Roman buildings excavated at Los Banales (1: centro de El Pueyo, 2: domestic/craft centre, 3: Forum, 4: domestic centre, 5: Roman Baths)	235
Figure 9.5 Assumed natural water reservoir (front) and dam of Los Bañales.....	236
Figure 9.6 Typical vegetation type pattern along wall remains with <i>Artemisia herba-alba</i> Asso (A) and <i>Brachypodium re-tusum</i>	237

Figure 9.7 Results from geomagnetic prospections made by Prof. Dr. Seifert and her team (2012-2015).....	238
Figure 9.8 Camera locations and image overlap for UAS-DLSR flight. Numbers and colours illustrate amount of image overlap for the given location (i.e. projections)	240
Figure 9.9 Camera locations and image overlap for orthophoto of flight #109	242
Figure 9.10: Camera locations and image overlap for orthophoto of flight #108 (left) and flight #111 (right).....	243
Figure 9.11 Support vector (Melgani and Bruzzone 2004, p. 1781).....	245
Figure 9.12 GPS measurements (red cross: Trimble GPS, yellow cross: Garmin GPS) and GCP for orthophoto-productions (RGB: bands 1,2,3)	247
Figure 9.13 Digital elevation model of the study site as retrieved from DSLR UAS imagery (background data: SITAR orthophoto mosaic)	248
Figure 9.14 Hillshade of El Pueyo highlighting former settlement structures	248
Figure 9.15 Multispectral orthophoto of flight 1b109 (RGB: 900, 700, 670 nm) top left, NDVI900, 670 nm top right, NDVI700,530 nm: lower left, and TCARI (lower right. Red circles known Artemisia distribution sites; blue circles: other grassy/herb species)	250
Figure 9.16 Differences in DN texture for Artemisia sites (homogeneous greyvalues in cluster correlation) and more grassy/stony environments in between.....	251
Figure 9.17 Principal components computed from correlation matrix of the multispectral input bands (1-6) and NDVI700,530nm (PC1-7 from top left to bottom): PC 6 shows noise.....	252
Figure 9.18: Land cover classification for vegetation types using multispectral image-derived PCs, VIs and texture	255
Figure 9.19 Orthophoto mosaic (left) and land cover classification result (right)	256
Figure 9.20 Reconnaissance for the agricultural field to the E of El Pueyo: Top left: results of geomagnetic survey (Prof. Dr. Seifert & team, Universität Hamburg) compared to spectral data (RGB 700, 670, 570 nm) on the right. Bottom row left shows the spectral data with (RGB 900, 700, 570 nm) and on the right the fifth principal component.	258
Figure 9.21 NDVI image of agricultural field E of El Pueyo.....	259
Figure 9.22 Crop marks found in agricultural field SE of El Pueyo. Left: PC2, right: geomagnetic data (Prof. Seifert and team) with overlaid transparent multispectral image (RGB 900,700,670 nm).....	260
Figure 10.1 Summary of processing flowchart for UAS campaigns.....	265

List of Tables

Table 2.1 UVSI categorization of civil UAS (van Blyenburgh 2012, p. 151)	8
Table 2.2 Classification of UAS based on power-mechanism and lifting force (mod. from Eisenbeiss 2009, p.34)	9
Table 2.3 Classification of light UAS based on maximum take-off weight (mod. from van Blyenburgh (2015), p.156; * depending on legislation)	9
Table 2.4 Selected single lens cameras used for small UAS environmental and archaeological remote sensing applications used within recent years (camera details taken from respective producer's data sheet last access date 24/04/2015, n.i.: no information available; PA: Precision Agriculture).....	27
Table 2.5 DLSR cameras used for small UAS environmental and archaeological remote sensing applications used within recent years (camera details taken from respective producer's data sheet last access date 24/04/2015, n.i.: no information available; PA: Precision Agriculture).....	28
Table 2.6 Common multispectral imaging sensors of less than 1.5 kg weight for small UAS (camera details taken from respective producer's data sheet last access date 24/04/2015, n.i.: no information available; PA: Precision Agriculture)	29
Table 2.7 Common thermal imaging sensors of less than 1.5 kg weight for small UAS (camera details taken from respective producer's data sheet last access date 24/04/2015, n.i.: no information available; FPA: focal plane array).....	30
Table 2.8 Hyperspectral imaging sensors of less than 1.5 kg weight for small UAS (camera details taken from respective producer's data sheet last access date 24/04/2015, n.i.: no information available)	31
Table 2.9 Current UAS regulations in Europe as published by the UVSI (Source: van Blyenburgh 2014b; Abbrev.: * UAS Use is facilitated and granted by National Aviation Administrations; VLOS: visual line of sight; BLOS: Beyond line of sight)....	35
Table 3.1 Absorption features of leaf constituents in VIS – mIR (modified from Jones and Vaughan 2010, p. 41). Bold numbers show strongest absorption.	42
Table 3.2 Main Impact Factors on Canopy Bidirectional Reflectance (modified from Jensen 2007a, p. 368)	46
Table 5.1 Lens Distortion Parameters for Nikon D3100 Lens	81
Table 5.2 Lens Distortion Parameters for Tetracam MiniMCA-6 with filters.....	82
Table 5.3 Example camera alignment values	84
Table 5.4 Sensor and Filter Correction.....	85
Table 5.5 Absolute $\Delta\rho$ in percent of reference panels after ELC compared to in-situ measurements for given wavelength ρ	97

Table 6.1 Required input parameters for coupled PROSAIL model.....	109
Table 6.2: Range limits, and fixed values of input plant variables for different crops used for the PROSAIL model.....	114
Table 6.3 Filter wavelength selection for Chla+b and LAI for each selection algorithm.....	120
Table 6.4 List of vegetation indices used for Prosail simulations.....	130
Table 6.5 Measured field parameters for maize leaves as input to Prosail simulations.	131
Table 6.6 Photo attitude parameters and derived observer and AA for PROSAIL input (as derived from the ATCOR-4 solar position calculation tool)	132
Table 6.7 Absolute and relative differences in reflectances ($\Delta\rho$) between VZA 0° to VZA 25° for all AA as derived from PROSAIL simulations.....	136
Table 6.8 Flight altitudes and camera position angles for scaling flight.....	144
Table 7.1 Flight dates, sensors weather conditions and grape phenological stages at UAS flights in 2011 and 2012 (mod. Retzlaff et al. 2015, in press).....	160
Table 7.2 Empirical line and coefficient of determination (R^2) for radiometric correction of 2011 UAS flight.....	162
Table 7.3 Empirical line and coefficient of determination (R^2) for radiometric correction of 2012 UAS flights	163
Table 7.4 Vegetation indices and their focus on physiological variables used in this study	165
Table 7.5 Field parameters assessed in the experimental vineyard 2011 (Sampling dates: LLN, PG, Chl contents, NBI Dualex® at 17/08/2011; N at 21/09/2011, yield at 20/11 and 10/10/2011, pruning weight 30/11/2011)	168
Table 7.6 Field parameters assessed in the experimental vineyard for 2012 (arithmetic mean and \pm standard deviation; DOY: day of year; BBCH after Lorenz et al. 1995, SMS: Soil management strategy).....	169
Table 7.7 Standardized discriminant coefficients of the first two discriminant functions, proportion of trace and cross-validated total accuracies for LDA models for different viewing directions (n=215, LD: linear discriminant)	172
Table 7.8 Derived regression models for the prediction of measured vine physiological variables of 2011 field samples for each VZA (X: Band; significance codes: 0 ‘***’, 0.001 ‘**’, 0.01 ‘*’, 0.05 ‘.’, 0.1 ‘ ’ 1) (Retzlaff et al. 2015, in press).....	175
Table 7.9 Model coefficients for cross-validated regressions models for Chl, N and NBI in 2012 of Figure 6	178
Table 8.1 Photo attitude parameters and error estimates of multispectral UAS flight CKA1 (22/08/2012, 12:30 UTC).....	199

Table 8.2 Empirical line and coefficient of determination (R^2) for radiometric correction of UAS flight	200
Table 8.3: Vegetation and fluorescence indices used in this study (R: reflectance, nIR: near infrared)	201
Table 8.4 Photo attitude parameters and error estimates of UAS flight CKA1 (22/08/2012, 13:27 UTC) with thermal camera	203
Table 8.5 Ground control marker position residuals for georeferencing multispectral data	204
Table 8.6 Mean values and standard deviation for bands and fluorescence index for N treatments at CKA1	205
Table 8.7 Results of two-factorial ANOVA between spectral band/VI means versus N treatment/sugar beet variety	209
Table 8.8 Standardized linear discriminant coefficients for LDA models separating N treatment and sugar beet varieties with thermal and Vis/nIR bands (n=40)	210
Table 8.9 Standardized linear discriminant coefficients for LDA models separating N treatment and sugar beet varieties with VIS/nIR bands (n=40)	210
Table 8.10 ELC parameters for diurnal Fs retrieval at CKA2, 23/08/2012 (Δ rad: difference of resulting radiance values [$Wm^{-2}sr^{-1}nm^{-1}$] to the input reference panels' radiances rp: reference panel).....	214
Table 9.1 UAS flights and camera payload used for the Los Bañales Site	237
Table 9.2: GCPs and their locational projection errors for flight #106 and #107	241
Table 9.3 GCPs and their locational projection errors for flight #109 (Projections: indicates number of images where GCP could be located)	241
Table 9.4 Point cloud modelling and resolution parameters for multispectral data for the agricultural fields in the E (#108) and S (#111)	243
Table 9.5 GCPs and their locational projection errors for flight #111	243
Table 9.6 Selected radial kernel parameters for cross-validations in SVM LCC.....	253
Table 9.7 Area-weighted confusion matrix for land cover classification by SVM of multispectral orthophoto mosaic including texture for CV5 (variant A)	253
Table 9.8 Area-weighted confusion matrix for land cover classification by SVM of multispectral orthophoto mosaic without texture for CV5 (variant B)	254

Abbreviations

AA	Azimuth angle
ADS	Automatic Dependent Surveillance-Broadcast
a.g.l.	Above ground level
AOT	Aerosol optical thickness
a.s.l.	Above sea level
AUMAV	Autonomous unmanned micro aerial vehicle
B	Blue part of the electromagnetic spectrum
BDR	Bidirectional reflectance
BDRE	Bidirectional reflectance effects
BDRF	Bidirectional reflectance factor
C	Heat capacity
Cost	Cost parameter in SVM
CAA	Civil Aviation Authorities
CLP	Cluster prominence
CLS	Cluster shade
COH	Cluster coherence, Haralick's correlation measure (1973)
Chl	Chlorophyll
CP	Cross-solar principal plane
CR	Close range
CWL	Central wavelength
Δ	Delta/difference
DAC	Directorate of Civil Aviation
DIY	Do it yourself
DSLRL	Digital single lens reflex
DN	Digital number, greyvalue
E	Thermal energy
EASA	European Aviation Safety Agency
EC	European Commission
EDA	European Defence Agency
EL	Empirical line
ELC	Empirical line calibration
ESA	European Space Agency
EO	Earth observation
EUROCAE	European Organization for Civil Aviation Equipment
EUROCONTROL	European Organization for the Safety of Air Navigation
EXO	Exo stratospheric flight altitudes
fAPAR	fraction of absorbed photosynthetically active radiation
FAO	Food and Agricultural Organization
FOV	Field of view

FWHM	Full width half maximum
G	Green part of the electromagnetic spectrum
GA	Genetic Algorithm
GCP	ground control point
GLCM	greylevel co-occurrence matrix
Γ	Kernel parameter in SVM
GPP	gross primary production
GPS	Global Positioning System
GNSS	Global Navigation Satellite System
HALE	High Altitude Long Endurance
I	Sun incident radiance
IFOV	Instantaneous field of view
IMU	Inertial Measurement Unit
JARUS	Joint Authorities for Rulemaking on Unmanned Systems
K	Thermal conductivity
λ	Wavelength
L	Thermal radiation
LAD	Leaf angle distribution
LADP	Low Altitude Deep Penetration
LAI	leaf area index
LALE	Low altitude long endurance
LC	Land cover
LCC	Land cover classification
LIDF	Leaf inclination distribution function
LIST	Luxembourg Institute of Science and Technology
LUC	Land use classification
LUE	Light use efficiency
LuftVG	Luftverkehrsgesetz
LuftVO	Luftverkehrsordnung
MALE	Medium altitude long endurance
MCA	Multi-camera array
mIR	Mid-infrared/shortwave infrared
MLR	multiple linear regression
MRE	Medium range endurance
MTOM	Maximal take-off mass
N	Nitrogen, also leaf structure parameter in PROSAIL
NASA	National Aeronautics and Space Administration
NDVI	Normalized difference vegetation index
nIR	Near-infrared (range of electromagnetic spectrum)
NPQ	Non-photochemical quenching
OSAVI	Optimized soil adjusted vegetation index
P	Thermal inertia
p	density
ρ	Reflectance

PC	Principal component
PCA	Principal component analysis
PLS	Partial least squares
PP	Solar principal plane
PRI	Photochemical reflectance index
R	Red part of the electromagnetic spectrum
RDVI	Renormalized difference vegetation index
RE	Red edge; red edge ratio index
RGB	Red, green, blue
RLI	Regression linear interpolation
ROA	Remotely piloted aircrafts
RPAS	Remotely Piloted Aircraft System
SA	Simulated Annealing
SAIL	Scattering Arbitrary Inclined Leaves
SfM	Structure from Motion
SIFT	Scale-invariant feature transform
SIG	Special interest group
SMS	Soil management strategy/strategies
SR	Simple ratio (vegetation index) or Short range (UAS category)
STRATO	Stratospheric flight altitudes
SRTM	Shuttle Radar Topography Mission
SVM	Support vector machine
T	Temperature
TCARI	Transformed chlorophyll absorption in reflectance index
TIR	Thermal infrared
UAS	Unmanned aircraft system
UAT	Universal access transceiver
UAV	Unmanned aerial vehicle
UAVS	Unmanned Aerial Vehicle System Association
US	United States of America
UVSI	Unmanned Vehicle System International
Vis	Visible (range of electromagnetic spectrum)
VLOS	Visual line of sight
VTOL	Vertical take-off and landing
VZA	Viewing zenith angle/observer angle

1 Introduction

The world population is expected to reach 9 billion of people by 2050 (Godfray et al. 2010). Although the growth of food production leaves less people hungry today, a 14% of the world's population is still facing malnutrition. According to the FAO, farming systems face serious pressure by competitive land use (biofuels versus food crops), intensification caused soil degradation by salinization, soil erosion and climate change, and urbanization competition for water and land in rural-urban boundaries (Godfray et al. 2010; FAO 2011). Sustainable food production and food use therefore present today's challenge and a "sustainable intensification" (Godfray et al. 2010, p. 813) is called for, encompassing increasing agricultural production limits by use of genetically modified crops and more efficient livestock management, reducing food waste, changing diets and expansion of aquaculture (Godfray et al. 2010). The term "precision agriculture" subsumes the technical improvements aiming at agricultural practices more efficient yet less harmful to the environment. In this context, one prerequisite for productive agriculture is access to fast and cheap geospatial data and this is where unmanned aerial systems (UAS) have knocked their way into the remote sensing communities. Small UAS provide data at low costs and high local detail without lengthy processing chains compared to costly manned airborne missions and satellite data (Zhang and Kovacs 2012).

Civil unmanned aerial systems (UAS) have shown an immense development within the private sector and scientific community since the millennium. According to the RPAS Yearbook 2015 (van Blyenburgh 2015), the total number of quoted UAS has been ever increasing (400% from 2005 to 2015) and the same holds for producing countries. Focusing on Europe, the civil applications have outranged the originally military applications, and Germany, France, the U.K. and Spain are the big producer countries. Mostly Mini UAS (smaller than 5 kg take-off weight) and in this category mostly rotary wing systems are being developed as they offer flexible platforms. Some key applications are listed below

- Precision agriculture: monitoring crop development and health status to quickly adapt crop treatment,
- Archaeology: surveys and reconnaissance of former settlements and land use have been among the first civil applications of UAS,

- Conservation: monitoring protected sites and species, detection of poaching and fires
- Security: remote sensing of areas where access is impossible due to risks to human health (e.g. contaminated site of Fukushima; fires in difficult areas),
- Health services: use of small UAS to deliver life-aiding systems to remote patients.

Accompanying, publications in that field mirror this development and have increased ten-fold since the turn of the millennium:

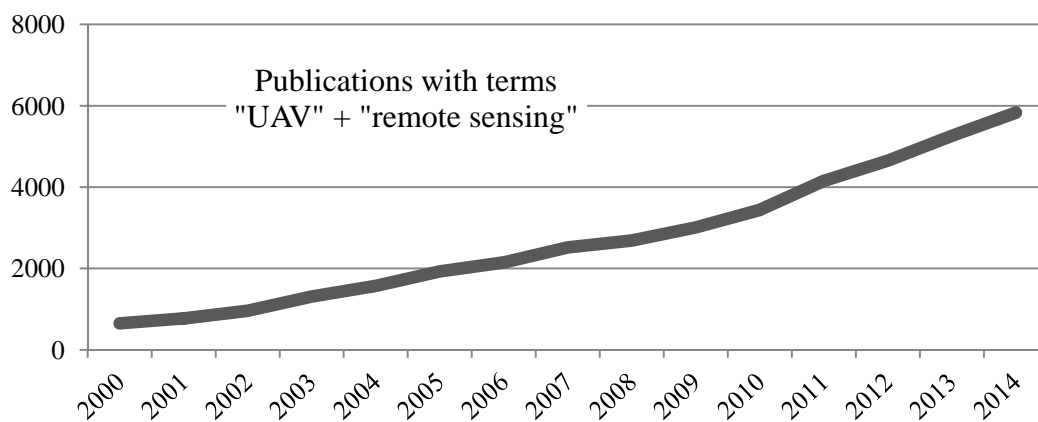


Figure 1.1 Reference hits by Google Scholar

Due to the relevancy of large-scale geospatial data for sustainable food production and also for cultural heritage, key research issues were defined: What is the potential of small UAS in multispectral and, to a lesser extent, broadband thermal infrared remote sensing within the field of agriculture and archaeology? And likewise, what are the limitations if not potential pitfalls? To study these topics, a md4-1000 quadrocopter UAS (microdrones GmbH), was purchased by the Department of Environmental Remote Sensing and Geoinformatics at the end of 2010.

The aim was to retrieve an operational sound processing chain for the use of multispectral or digital cameras, sensor calibration and radiometric correction, to be followed by point-cloud modelling leading to orthophoto mosaics which may then further be analyzed in relation to the respective scientific questions. The work is divided into two parts:

- Part I deals with introduction into the topic and sets the scientific background of data processing and requirements.
- Part II contains the application of the UAS in the context of agricultural and archaeological research questions.

In part I, chapter 2 gives an overview to UAS their historic evolution and recent platform development, especially rotary-based systems and sensors. Within this topic comes also the description of the regulatory framework for the operation of such systems. The latter often limp behind the technology's development and demand and may still impede the readiness for system use. Regulating bodies do work hard though on reaching international standards and safety regulations. Chapter 3 endows on multispectral and thermal broadband remote sensing of vegetation, setting a base for the consecutive case studies.

A detailed description of the used sensors, their calibration and radiometric correction of individual photos is given in chapter 4. Consecutively, the potential radiometric correction is presented followed by the description of topographic corrections, i.e. geometric correction, bundle-block adjustment, point-cloud modelling and final derivation of orthophoto mosaics (chapter 5). A sensitivity analysis then evaluates the selected wavelengths for the study of key vegetation parameters such as chlorophyll, leaf water content, brown pigments, leaf area index, a.o., pursued by bidirectional reflectance effects at multi-angular viewing geometries on the spectral signal and common vegetation indices (chapter 6).

Subsequently, the UAS system and processing chain is used in three common research questions, *i.e.*

- a) the potential of multispectral and multi-angular remote sensing of soil management effects on grapevine in a vineyard in Luxembourg (chapter 7),
- b) the impact of nitrogen-fertilization treatments on sugar beet on the multispectral (and thermal) signal in relation to stress-induced solar fluorescence, and the potential to use the system to map daily fluorescence as a stress indicator (chapter 8), and finally,
- c) the potential use of small UAS to archaeological surveys and reconnaissance at a former Roman settlement in Los Bañales, Spain (chapter 9).

The benefit and handicaps of small UAS in multispectral remote sensing applications are then summarized and discussed in chapter 10, followed by conclusions and recommendations for the use of small UAS in chapter 11. A summary concludes the work in chapter 12.

Part I

2 Unmanned Aerial Systems for Environmental Remote Sensing

Unmanned aerial systems (UAS) or remotely piloted aircraft systems (RPAS) for environmental remote sensing of agriculture and conservation, have emerged about a decade ago and find increasing and widening application experiencing a rapid technical development ever since (van Blyenburgh 2014a, p.153).

2.1 Terms and Definitions

2.1.1 UAS versus UAV

Only recently, the non-profit trade organization “Unmanned Aerial Vehicle System Association (UAVS), EUROCAE and ICAO suggested to harmonize terms from the term unmanned aircraft vehicle (UAV) to unmanned aircraft system (UAS) as a reusable, powered aircraft which is either steered remotely by a crew on the ground or flies autonomously following preprogrammed tracks (Unmanned Aerial Vehicle System Association 2011, ICAO 2011). The acronym UAV originated from a rather military perspective of drones as uncrewed radio-controlled aerial vehicle performing flight and payload operations for reconnaissance missions. Despite industry and regulating bodies adopting the term UAS, within scientific publications the acronym UAV persists.

Other terms used by ICAO and in European Aviation are remotely piloted aircraft systems (RPAS), remotely operated aircrafts (ROA), simply drones, or for the US Federal Aviation Administration unmanned aircrafts (UA) (Eisenbeiß 2009, p.1). Depending on the size, drones may also be termed autonomous unmanned micro aerial vehicle (AUMAV).

For civil and commercial applications, industry and regulating bodies now adopted the term unmanned aircraft systems (UAS), including all associated system elements like

- the aerial vehicle and its propulsion mechanism
- the payload
- the ground control station
- the communication means between ground station, the vehicle (i.e. remote control) and data downlinking, and

- the support equipment required to run, and transport the UAS (Austin 2010).
- UAS Components

A UAS comprises a platform and its propulsion system, the payload, a flight control system, a precision navigation system and, possibly, a sense & avoid system.

The sensors onboard may encompass one or more of the following:

- Digital or single lens reflex cameras (SLR), multispectral/hyperspectral sensors
- thermal infrared cameras (TIR), video cameras and scanners,
- LiDAR or radar systems, and/or
- environmental (gas) sondes.

The ground control station generally supports field missions during

- set-up, and through
- a monitoring display for camera live links,
- the system health diagnostics,
- navigation tasks,
- position mapping, and
- as a data downlinking and processing unit.

The telecommunication unit controls the transfer of the pilot's commands to the UAS (Jensen 2007; Austin 2010, Everaerts 2008).

2.1.2 UAS Benefits and Drawbacks

Clearly the biggest advantage is the immense flexibility in using drones. Whereas traditional aircrafts are cost-intensive and not always disposable, drones, especially smaller vehicles, may be obtained at much lower costs. Their main application lies in mapping at large scales and, in particular, in studying short-term variations of sites of interest whenever required: crop development during the growing period may be listed here, where traditional, manned aircraft would explode project costs. Presuming for adequate weather conditions, UAS may be flown when and as often as required and inform precision agricultural management. In some cases, flights may even be carried out when the weather is not ideal, *e.g.* during light rain, snow fall or underneath clouds.

UAS are further advantageous for overflights of areas of limited access where manned air missions might endanger crews, as, for instance, over volcanoes or areas of limited access after catastrophic events.

Also, other flight parameters may be selected to fit the research question: Depending on the object under study, variations of the flight height determine the scale of the obtained imagery. The choice of a beneficial flight time together with the flight direction determines object illumination. For thermal imagery morning or evening exposures may be beneficial whereas reflectance measurements generally are carried out during maximum solar illumination. Finally, the speed of the aerial vehicle and the chosen image acquisition rate steer image overlap, required for instance for photogrammetric measurements (Eisenbeiß 2009, p. 3-4).

Modern GPS-/inertia steered altitude and attitude reference systems stabilize the platform and, when using rotary-wing drones, the platform may hover over the site of interest as long as required. These systems also show the advantage of vertical take-off and landing (VTOL), requiring a minimum space for launching the UAS (Eisenbeiß 2009, p.4, microdrones GmbH 2009, Jones and Vaughan 2010). Finally, the mission may be programmed so that the vehicle follows pre-defined tracks and executes data acquisition autonomously.

The major drawback in using UASs is the relationship between platform weight and maximum payload. National air regulation legislation generally treat commercial and non-commercial UAS as model aircrafts and minimize their total weight to *e.g.* 5 kg in Germany, and thus, limiting the sensor size within general ascent permits. Furthermore, the flight altitude needs to conform to air traffic regulations and is, thus, limited to the space below manned air traffic. In most parts of Germany this amounts to 300 m above ground, which is generally still an adequate flight height, for general ascent permits, however, maximum altitude limits at 100 m above ground level (a.g.l.).

Although equipped with GPS/inertia systems, the comparatively rather miniaturised platforms still lack in flight stability when compared directly to traditional manned aircrafts, placing great demands on image processing. To enable post-processing for image orientation parameters, ground control points need to be installed in-situ. Other limiting factors are technical constrictions in battery capacity and weight. Longer flight times are achieved at the expense of payload. Model aircrafts have furthermore been restricted to visual line of sight flights and the range of radio communication.

2.2 Categorization of Civil Unmanned Aircraft Systems

Up until now, to the author's awareness, there is no European-wide official classification for UAS. EUROCONTROL together with other members from the UVSI have been working on this topic, more results are being soon expected (personal communication with Mike Lissone, UAS ATM Integration Manager, EUROCONTROL, 12.12.2011). UAS have also been grouped by lifting force (lighter than or heavier than air) or based on their propulsion system, i.e. powered versus passive systems, by their size and weight of their platform and payload and by flight altitude and endurance parameters. The UVSI within the recent years have categorized UAS by their altitude, range and weight and distinguish among tactical, strategic and special purpose UAS including military UAS and higher (exo-)atmospheric applications which will not be described further in this context.

Table 2.1 UVSI categorization of civil UAS (van Blyenburgh 2012, p. 151)

UAS Category (acronym)	Range [km]	Flight Altitude [m]	Endurance [h]	MTOW [kg]
Nano (η)	<1	100	< 1	< 0.025
Micro (μ)	<10	250	1	< 5
Mini	<10	150 - 300	< 2	Depending on national legislation MTOW < 30 or 150 kg
Close Range (CR)	10 – 30	3000	2 – 4	150
Short Range (SR)	30 – 70	3000	3 – 6	200
Medium Range (MR)	70 – 200	5000	6 – 10	1250
Medium Range Endurance (MRE)	>500	8000	10 – 18	1250
Low Altitude Deep Penetration (LADP)	>250	50 – 9000	0.5 – 1	350
Low Altitude Long Endurance (LALE)	>500	3000	>24	< 30
Medium Altitude Long Endurance MALE	>500	14000	24 – 48	1500
High Altitude Long Endurance (HALE)*	>2000	20000	24 – 48	4500 (Predator B)/ 12000

*Although developed for military applications, HALE UAS have been used for scientific studies.

Other categorizations are shortly mentioned in the following sections.

2.2.1 UAS Classification Based on Platform Propulsion

Eisenbeiß (2009, p.34) summarized UAS based on their propulsion and also lifting force mechanism:

Table 2.2 Classification of UAS based on power-mechanism and lifting force (mod. from Eisenbeiß 2009, p.34)

Lifting force\ Propulsion	Lighter-than-air	Heavier-than-air		
		Flexible wing	Fixed wing	Rotary wing (VTOL)
Unpowered	Balloon	Kite Hang glider Paraglider	Glider	Rotor-kite
Powered	Blimp	Paraglider	Propeller airplane Jet engine airplane	Single rotor Coaxial Quadrotor Multi-rotor

2.2.2 UAS Classification Based on Total Weight

Beside the desing, most national aviation authorities employ the total platform and payload take-off weight to group UAS for safety regulations. The RPAS Yearbook (van Blyenburgh 2015) differentiates light aircraft masses according to maximum take-off weight (Table 2.3).

Table 2.3 Classification of light UAS based on maximum take-off weight (mod. from van Blyenburgh (2015), p.156; * depending on legislation)

UAS Category	MTOW [kg]	Altitude [m]	Range [km]
Nano [η] UAS	< 0.025	100	< 1
Micro [μ] UAS	< 5	250	< 10
Mini UAS	<25 or 30 to 150*	300	< 10
ShortRange UAS	< 150	3000	10-30

Similar classes are used by the Australian Civil Aviation Safety Authority (Eisenbeiß 2009, p. 36).

2.2.3 UAS Classification Based on Altitude and Endurance

Another scheme uses as classification criterion the possible altitudes versus endurance:

HALE: high altitude (20000 – 35 0000 feet), long endurance, i.e. Global Hawk

MALE: medium altitude (10000 – 30000 feet), long endurance (24-48 hours), i.e. MQ-1 Predator

LALE: low altitude (~7000 feet), long endurance (>30 hours), i.e. Predator A

LASE close: low altitude (up to 6000 feet) and short endurance (several hours), overall weights of 2-5 kg.

STRATO: stratospheric flight altitudes

EXO: exo stratospheric flight altitudes

The LALE and LASE category were defined by the US Federal States Aviation Administration (quoted from Watts et al. 2012) and are not commonly used in European nomenclature, yet are mentioned in UAS Yearbook 2015.

2.3 Outline of the Historic Evolution of Civil-Use UAS

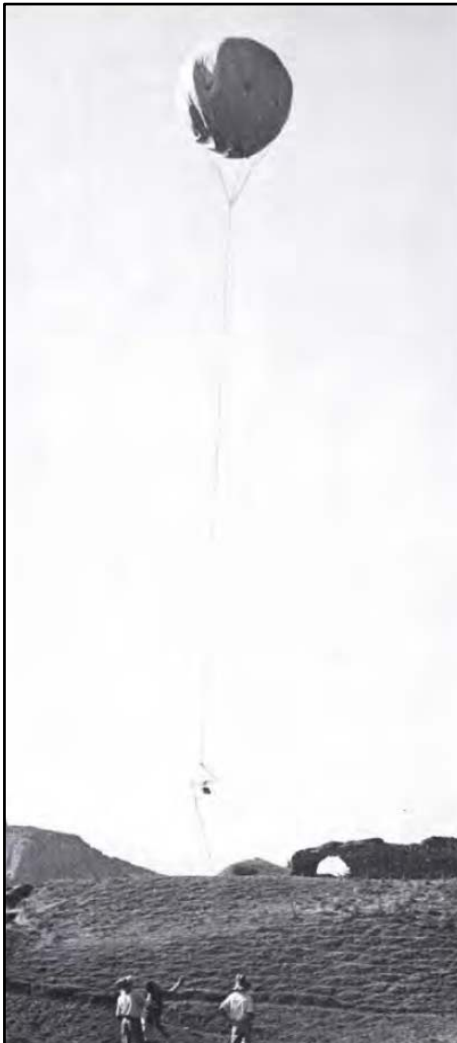
2.3.1 First UAS and Developments until 2000

One of the earliest applications of drones, were hydrogen-filled balloons for reconnaissance used in the American Civil War. The military even then tested offensive applications by timer-activated bomb-droppings (Krock 2002). However, their dependence on wind direction and speed made their use problematic, so that Charles Perley's patent for an "unmanned aerial bomber balloon" of 1863 was not being further employed (Clark 1997).

The first civil use was pioneered by Arthur Batut who took airphotos in France in 1890 using large kites. He could already foresee the implications for surveyors, archeologists, the military and agriculturists (Jensen 2007 p. 70).

Jensen (2007) also mentions rockets applications where cameras were shot into the sky by Amadee Denisse in 1888, or 1891 by Ludwig Rahrman in Germany. The latter also used large caliber guns to transport the camera into the air which then parachuted down.

It was at that time also that UAS started being used for photogrammetric purposes. Whittlesey (1970) employed a tethered balloon equipped with a Linhof 6x9 cm camera



to capture vertical airphotos from about 10 m height to map archaeological remains. He also experimented with stereographic cameras, i.e. a radio-controlled Hasselblad, taken up 2000 feet to photograph archaeological sites in Greece, and mentions “the U.S. Army Cold Regions Research and Engineering Laboratory [...] to measure plant growth and soil deformation” (Whittlesey 1970, p. 185).

Figure 2.1 Whittlesey's tethered balloon for archaeological reconnaissance in Turkey (Whittlesey 1970, p. 182)

During the Post-World War Period, during the Vietnam and later Cold War, UAS gained interest again. Especially the USA and Israel began to develop and deploy their own systems in the 1970ies/1980ies (Jensen 2007). During, the Cold War period, NASA's MiniSniffer program (1970-1980ies) according to Watts et al. (2012) made first attempts in atmospheric sampling at high altitudes.

In the nineties, during the Persian Gulf War, the U.S. Predator, developed by General Atomics Inc., used for reconnaissance missions, was becoming the ancestor for scientific UAS platforms. The NASA then acknowledged the need of the industry and science community for cost-effective, more flexible airborne remote sensing technology.

2.3.2 Recent Developments of Civil UAS (2000-2015)

Due to NASA's Environmental Research Aircrafts and Sensor Technology (ERAST) project (1993 to 2003), profound research and development in cost-effective UAS for environmental deployment resulted in the development of modern, slow-flying aircrafts such as Helios, Proteus, and Pathfinder (Nonami 2007, p.121, Curry 2009). In its second phase, the NASA's ERAST focus lay on solar-driven technology, consumable fuel UAS missions for earth science applications and UAS subsystem technologies (Curry 2009). A detailed description of HALE UAS application for scientific missions may be found in Curry (2009) and Watts et al. (2012).

To accommodate multiple civil research groups, a medium altitude – long endurance platform was developed based on the Predator-B, the NASA's Ikhana. It was developed in 2007 with a 20 m wingspan which may carry up to 1100 kg payload. It may reach 13000 m in altitude with up to 24 hours endurance (Dryden Flight Research Center 2007; Watts et al. 2012). According to the authors, the Ikhana was the first drone that received a US Certificate of Airworthiness (COA) and could be operated without accompanying aircraft and observers (Watts et al. 2012). It was tested on Western US States Fire Missions flights between 2006 to 2009 and provided stakeholders with georectified, near-real time imagery of wildfires (Watts et al. 2012).

Other MALE systems followed, like the Altus II for atmospheric research (Curry 2009, Watts et al. 2012), and later the Science Instrumentation Environmental Remote Research Aircraft – SIERRA for several recent scientific missions at regional scales, described by Watts and co-authors (2012 p. 1681f):

- CASIE – Characterization of Arctic Sea Ice Experiment (2009)
- greenhouse gas emission (2011),
- measurement of long-time earthquake hazards and groundwater measurement (2011-2013), and
- carbon dynamics of seagrass and shallow tropical coral ecosystems and atmospheric missions (2011-2013).

The SIERRA was designed by the Naval Research Laboratory (NRL) and may carry 45 kg payload and has a take-off weight of approximately 180 kg. It may fly at low altitudes of 3600 m with a speed of 100 km/h. It samples tropospheric chemistry and is used for remote sensing of arctic ice (Fladeland 2009; Watts et al. 2012). Its use in controlled airspace at altitudes typically used for manned aircraft does cause logistic problems (Watts et al. 2012).

Parallel to this HALE/MALE development, resulting from the logistic difficulties, costly missions, and the advancements in miniaturized systems and sensors, lighter UAS were being developed all over the world for civil and commercial applications and found a widening adoption for public authorities like law enforcement, public policy, agricultural and environmental monitoring and sampling, wildlife management as well as aerial imagery for every possible application thinkable (Krock 2002, Jensen 2007 p.85, Eisenbeiß 2009, p. 12ff, Watts et al. 2012, van Blyenburgh 2014a).

Within this year, according to the UVSI Yearbooks on RPAS and prior UAS, the Mini UAS have especially boomed and presented the largest category within the past years (Figure 2.2). Altogether, the year 2013 peaked and has become to be called the year of drones. Since then numbers of new developments have been declining slightly. Once legal regulations become more clear and harmonized across Europe and possibly world-

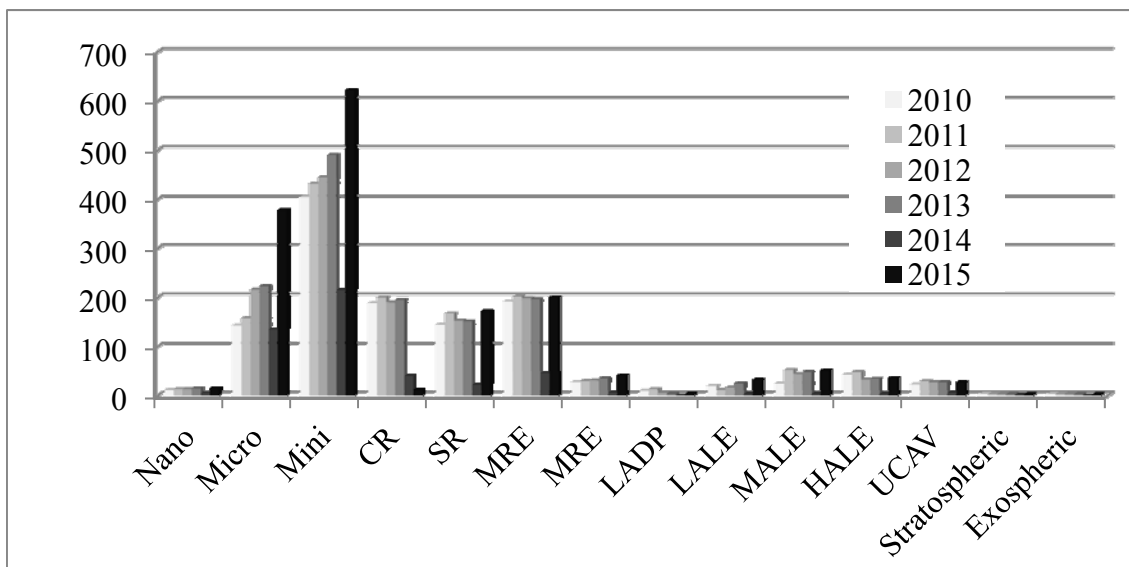


Figure 2.2 References of different UAS categories listed in the respective UVSI Yearbooks within the past years (van Blyenburgh (ed.) 2011-2015)

This trend is also repeated in the UAS intended purposes: military drone and dual use applications still exceed other usage, yet civil/commercial systems found increasing use until 2015 (van Blyenburgh 2011-2015).

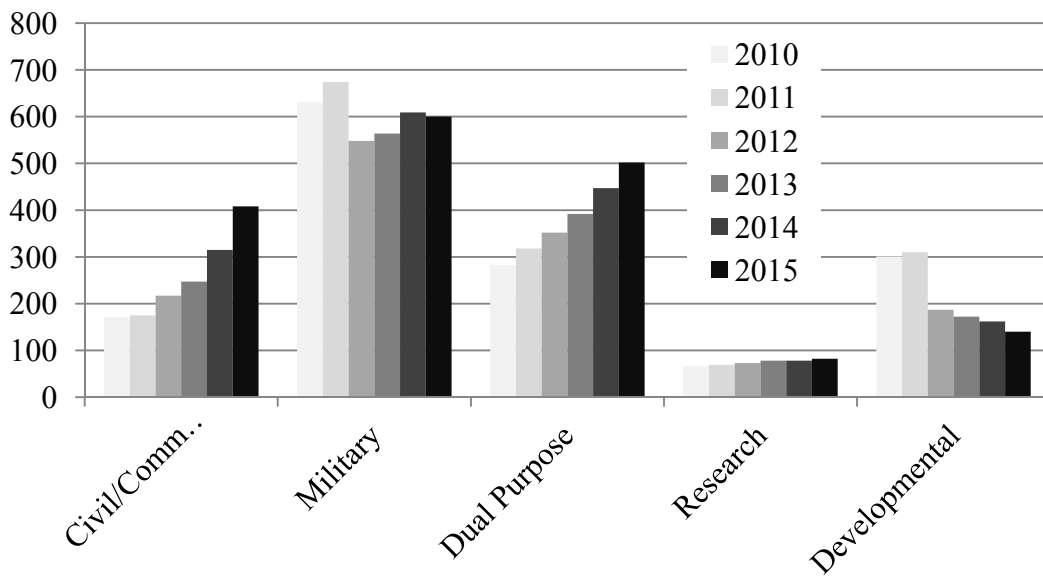


Figure 2.3 Referenced UAS by intended purpose in the UVSI Yearbooks 2011-2015

The world-wide drone development is still increasing and 2014 as in previous years, the world’s largest producer countries (also the strongest military developers) were the USA, followed by Russia and Israel (Figure 2.4). Recently China emerged, too. Within Europe France, Germany and UK haven been the largest producers recently followed by Italy and Spain.

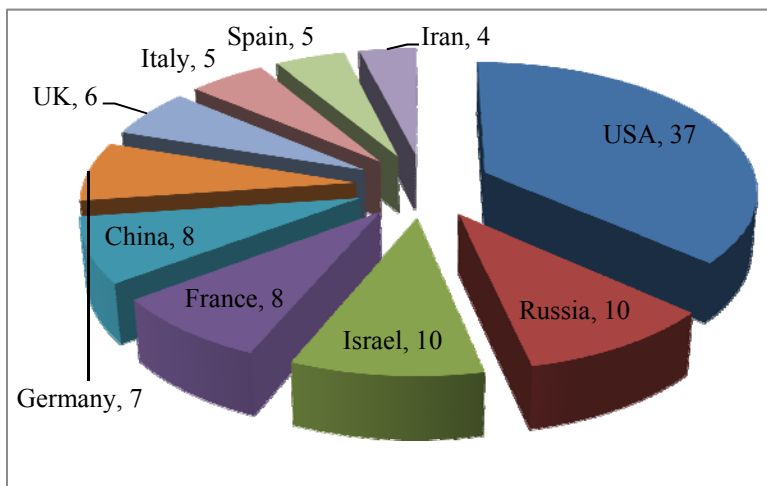


Figure 2.4 Data source RPAS Yearbook 2014 (van Blyenburgh 2014a, p. 156)

2.4 UAS Platforms Used for Environmental Remote Sensing and Archaeology

The following description will group current lightweight UAS according to their respective platform. As there are abundant UAS systems on the market all over the world (Figure 2.4), UAS types within this field will shortly be presented, pros and cons mentioned and focus laid on rotary wing vertical take-off and landing (VTOL) systems as this system has been used for this study and its production has been increasing within recent years (Figure 2.5). For a detailed list of producers and systems please refer to the RPAS Yearbooks (van Blyenburgh 2012, 2013, 2014a, 2015), Aber et al. (2012) and Watts et al. (2012), Eisenbeiß (2009) has compared and contrasted UAS airframe types.

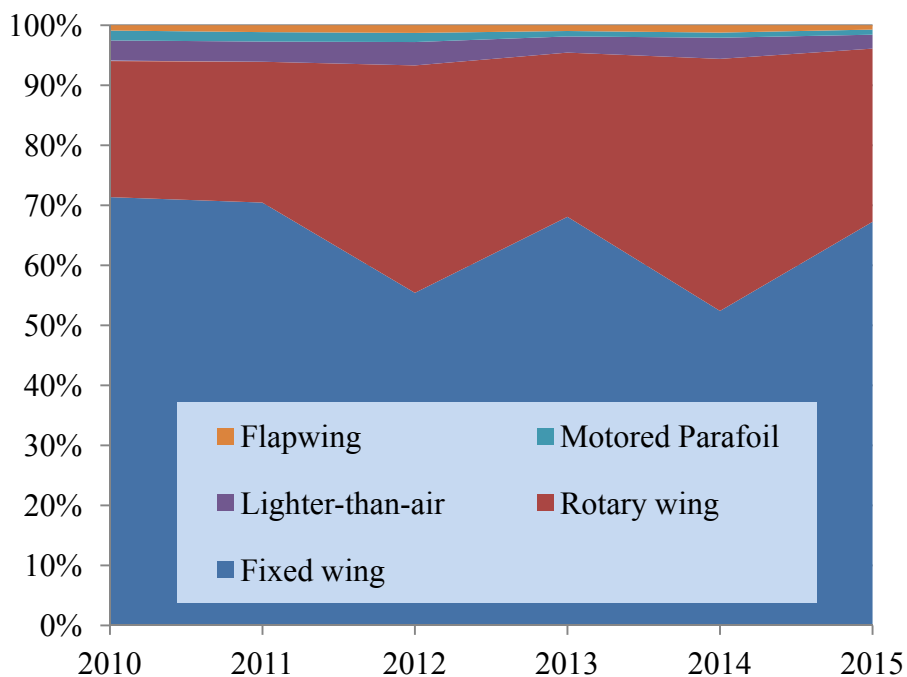


Figure 2.5 UAS airframes referenced in the RPAS 2010-2015 (RPAS Yearbooks (van Blyenburgh 2010-2015)).

2.4.1 Lighter-than air platforms

These platforms include balloons and blimps and, may be free-flying or tethered. Lifting gases include hydrogen, helium, methane or hot air (Federal Aviation Administration 2007 cited in Aber et al. 2010, p. 103). Nonami (2007, p.120) argues that unmanned aircrafts are driven by the dynamic lift and thrust given by their engines, so that strictly speaking, balloons which swim in the air or rockets following ballistic orbits do not count as UAS.

Vierling et al. (2006) summarize the advantages of tethered balloons compared to other UAS platforms: They are distinguished by longer endurance than active aircrafts, the flight altitude may be controlled more easily, they are reasonably easy to use and move in remote locations, and are cheaper to run.

The disadvantage of lighter-than-air-platforms lies in their reliance on wind still conditions. Free-flying balloons are seldomly used as they are more or less uncontrollable. The advantage of blimps compared to balloons is their higher stability in the air due to their streamline shape. According to Aber et al. (2010, p.99), they are also safer to rise as the danger of fabric being blown onto the burner flame is low. The helium-filling device makes it useable for several days. Its disadvantage however, lies in its susceptibility to wind, operative wind speeds amount to 10-15 km/h and availability of helium (Aber et al. 2010, Rock 2010).



Figure 2.6 The Goethe blimp (Rock 2010, p.24)

As an example, the “Goethe monitoring blimp” is illustrated in developed by the department of Physical Geography of the Frankfurt Johan Wolfgang von Goethe University. The system is described in detail in (Rock 2010 p.24-26). Due to its flying characteristics, blimp

systems are suited for small-format aerial photography at large scales. Aber et al.

(2010) use hot-air blimps for soil erosion and vegetation studies. Other applications have worked on coastal and periglacial sites, meteorological sounding, crop state and archaeological reconnaissance and mapping for now almost 50 years (Whittlesley 1970, Myers 1978, Ullmann 1971, Preu et al. 1987, Bitelli et al. 2004, Oberthür et al. 2007).

A multi-sensor platform is provided by the SWAMI apparatus which has been used with a tethered balloon (Vierling et al. 2006, p.257). See chapter 4.3.4 for more details.

2.4.2 Heavier-than air platforms

2.4.2.1 Fixed wing - kites

Kites are tethered aircrafts and have been known since the 5th century BC. They were invented in SE Asia (region of Indonesia) or by the Chinese, and have been used for signaling, testing wind direction, and measuring distances, amongst others. The advantage in using kites consists in the low costs, the high portability and flexibility in the field, the unlimited flight times assuming there is enough wind, and the easy to learn technology. There are soft kites inflated by wind pressure and rigid kites. Soft kites are very light-weight but collapse quite easily when the wind drops, rigid kites are supported by either graphite or fibre glass framework (Aber et al. 2010, p. 103). According to Aber et al. (2010) they perform better at low wind speeds and do not collapse as easily.

Kites are mounted by anchoring the line, hurling up the kite and pulling on the line. The payload generally consists of cameras being mounted either directly on the kite line or on a second line attached onto the kite line by means of a pulley. The latter allows for taking down the camera for film, card or battery changes without having to take down the whole system (Rock 2010 p. 27).

Kites have been used for small-format aerial photography for a.o. geomorphological studies, archeological mapping and vegetation studies and are a cheap means for large-scale photography (Anderson 2001; Aber et al. 2010).

2.4.2.2 Fixed wing – paraglider

Motored paraglider show the advantage of low flight speeds and have been used by Aber et al. (2010). The authors praise the inertia in flight, the low flight speeds and the robust landing, but do note the difficulty in steering the UAS, and in finding adequate runways in the field.

2.4.2.3 Fixed wing aircraft

Model airplanes or fixed wing aircrafts require considerable experience for their application in aerial photography (Aber et al. 2010). They may be either unpowered gliders or powered propeller or jet engine airplanes. Their biggest advantage is that they cover larger areas than kites, blimps, paragliders and rotary-wing UAS. Image acquisition planning needs to include forward motion which may cause difficulties in camera triggering and potentially cause motion blur in the photographs. Further difficulties arise from the type of engines used: either combustion engines or electrical motors. The first

allow for a longer flight time and higher payload. However, the engine vibration leads to suffering image quality. Electro motors on the other hand, are less affected by vibration and run much quieter. They are also much cheaper to obtain. Their disadvantage is the lower endurance (Rock 2010, p.30-31). A more detailed overview may again be found in the respective UAS and RPAS Yearbooks (<http://www.uvs-info.com>, access date 14.04.2015).

As an example, the MAVinci's SIRIUS (Figure 2.7) series is described in more detail. The German company uses an all-in-one software for flight planning, UAS control and picture matching. Their drone may map a maximum of 18 km² at 20 cm ground sampling distance (GSD) within one 40 minutes flight. The user creates the flight plan and determines at which interval rate the camera will take photos. The settings are then transferred to the on-board computer by radio communication. The aircraft is hand-launched, and once the pilot hands over to on-board navigation, the UAS follows its flight track and images will be acquired and stored on-board. The pilot may toggle back to remote control of the aircraft and may alter the flight-plan while flying. The plane



may carry various sensors with a take-off weight of 2.7 kg (MAVinci GmbH 2009-2011, MAVinci GmbH 2014).

Figure 2.7 The model UAS Siri-us by MAVinci (Photo: Rock 2015)

Within recent years, nano UAS have been developed for still rather military reconnaissance missions in hostile environments for short-time and low altitude: e.g. the Black Hornet Nano (Proxydynamics, Norway). The author is yet unaware of any scientific applications in environmental remote sensing.

2.4.2.4 Rotary wing small UAS

Rotary-wing UAS are vertical take-off and landing vehicles (VTOL) and may further be differentiated into single, double, quadro- or multi-rotor systems (Eisenbeiß 2009, p.34). Their biggest advantage is their ability to take-off and land without runway and to hover over sites of interests. Since the nineties, their development increased manifold (Figure 2.8) and there are numerous developers and vendors selling industry use or hobby use rotary-wing systems (van Blyenburgh (ed.) 2011; 2012, 2013, 2014a, 2015).

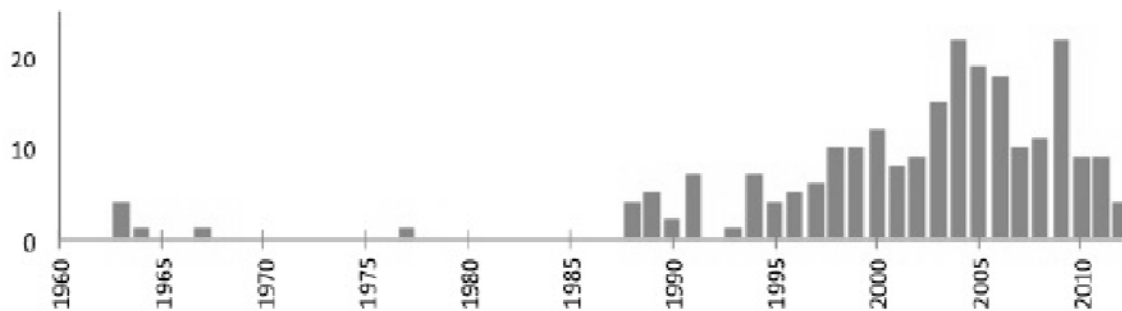


Figure 2.8 VTOL development 1960-2012 (mod. from Watts et al. 2012)

Single rotor systems or helicopters have one main rotor supplying lift and thrust and a tail rotor to balance yaw and torque. Double- or coaxial systems have more power than four or multi-rotor systems and thus may carry more payload and be taken to higher altitudes. (Eisenbeiß 2009, p. 35). A major advantage of quadro- or multicopters is their high maneuverability. All three axes may be steered alone by varying thrust and drift. Multi-rotary systems furthermore still function if some of the rotors breaks and may still be landed safely. Their disadvantage lies in the lower flight speeds compared to fixed wing UAS, restricting their use to smaller areal coverage.

For this study, a microdrones GmbH md4-1000 was employed which is described in more detail in chapter 4.

2.5 Ground Control Station

For the set-up, control, navigation and commanding the UAS in the field, ground control stations are used. They include hardware and software mostly provided by the drone producer. Hardware is generally a laptop but may also be a tablet PC or mobile phone, downlink antenna and a monitor to follow the UAS movement.

2.6 Autopilots: Navigation and Attitude Control

An autopilot generally measures the UAS attitude parameters position, velocity and attitude with the help of the GPS navigation and uses the information of the IMU to feed and correct the flight control for aircraft guidance and orientation systems estimate the position, velocity and attitude for post-processing of sensor orientation (Colomina and Molina 2014). An extensive list of worldwide autopilot system may be found in van Blyenburgh (2014, p. 236-238) and Colomina and Molina (2014) describe some in more detail. Autopilots often come as set systems with a UAS and sometimes as customized devices, where UAS users demand customization to one autopiloting system to facilitate piloting diverse UAS types (AP04 by UAV Navigation (see publications by Zarco-Tejada's QuantaLab in Spain: Calderón et al. 2014, Zarco-Tejada et al. 2013).

Flight planning or navigation is generally achieved by proprietary waypoint editing software. Microdrones GmbH, for instance, offers the Waypoint Editor that comes with the mdCockpit software (Figure 2.9, microdrones GmbH 2008-2010). The editor is linked with Google Maps, providing the base map used for defining waypoints and tasks for the drone (e.g. hover, climb, descend) and cameras attached.

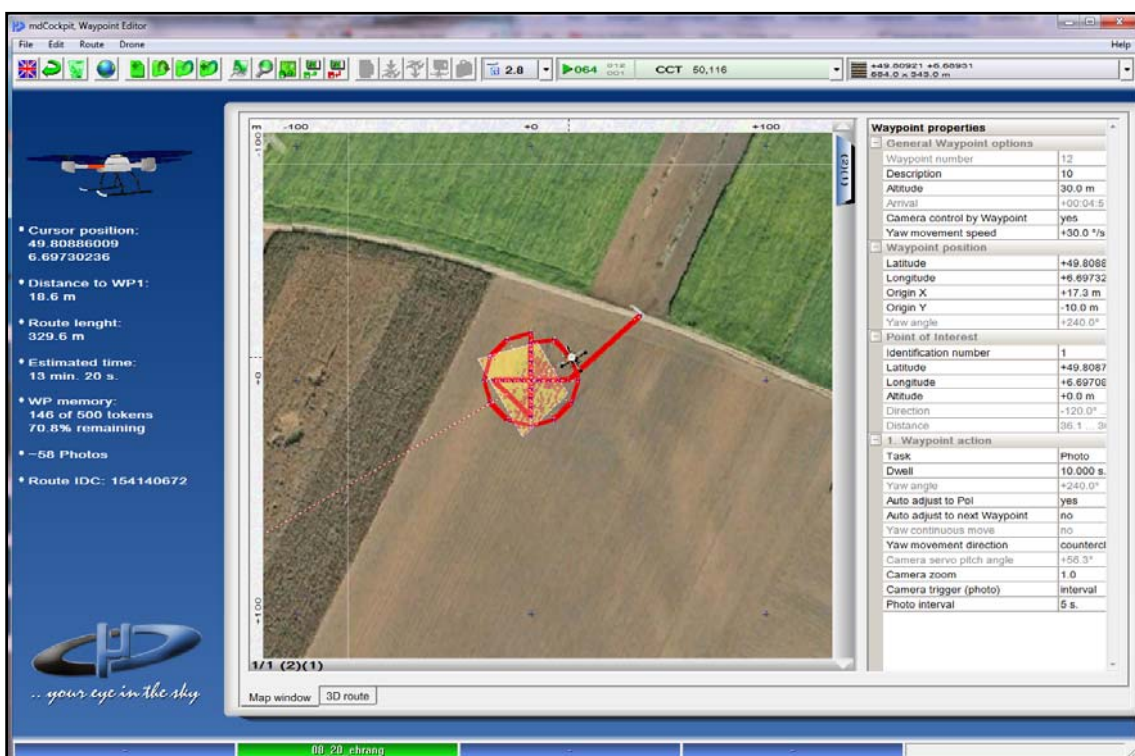


Figure 2.9 mdCockpit Waypoint Editor (microdrones GmbH)

Also, any other georeferenced map may be used as long as it is based on WGS84 geodetic reference system. The flight path is then directly transferred onto the microSD via USB connection and activated by telecontrol. The UAS now autonomously works off the flight route, navigating and positioning itself with the help of the GPS antenna and module.

MAVinci Desktop, the software for handling the Sirius UAS, may be connected to the internet in the field, using a 3G modem. As base maps any Web Mapping Service (WMS) server may be used (MAVinci GmbH 2011, p.27). The RPAS Yearbook 2015 lists available autopilots (van Blyenburgh 2015, p. 246-247)

2.7 Navigation and Attitude Control

Generally, small UAS use standard GPS modules to receive positions from the Global Navigation Satellite System (GNSS). For the md4-series from microdrones GmbH, the ublox LEA-5H chip is used. For attitude control and positioning, inertial measurement unit (IMU) maneuver aircrafts by gyroscopes, (measuring orientation and angular momentum), accelerometers for the three main axes (x,y,z), a magnetic sensor and a baro-altimeter. Furthermore, a barometer measures elevation by air pressure and temperature. Microdrones uses their own IMU system and do not hand out any more information. The sensor's measurements are generally fused using a Kalman filter (personal communication with Tobias Matschke, microdrones GmbH, 15.12.2011). Differential GPS (DGPS) are also being used, *e.g.* by MAVinci and senseFly Ebee (Roze et al. 2009-2015).

The RPAS Yearbook 2015 (van Blyenburgh 2015, p. 248-250) gives an extensive list of IMUs. Limitations lie within the derived accuracies. With hybrid measurement units which measure and process UAS positions in real-time using hybrid orientation systems (HOS), may thus deliver positions at cm-accuracies (Colomina and Molina 2014). The authors compare and contrast some of these and state accuracies of $0.015^\circ - 0.2^\circ$ for roll and pitch, and $0.03^\circ - 0.5^\circ$ for yaw angles (Colomina and Molina 2014, p. 85).

2.8 Communication – Telecontrol & Telemetry

Most small UASs are telecontrolled/steered by standard remote control (RC) devices as can be found in the leisure model aircraft community. As an example, the md4-1000 quadcopter comes with a MULTIPLEX Royal Pro 9, which uses a synthesizer HF

module to use any frequency within the 35 MHz band. microdrones GmbH developed a hardware module to emulate RC controller via a computer transmitted by a 10 kHz FM modulation. The commands to and from the module are sent by ASCII format (microdrones GmbH 2004-2007).

The UASs' telemetry data are transferred onto the ground station PC via serial interface/USB by a downlink decoder (plugged into the ground control station using an audio-chinch plug). It is using the WiFi at 2.3 to 2.5 GHz frequency and has a video bandwidth of 30 Hz – 30 MHz, and a audio bandwidth of 15 Hz to 6 KH. A standard telemetry kit for DIY drones in the UK and EU is the Xbee Telemetry Kit 2.4 GHz 63mw module.

The video signal is visualized with the help of a frame grabber which is integrated with-in the ground control station and transfers data by a USB connection. Additionally, video glasses may be used for UAS control (microdrones GmbH 2009, p.28).

All flight data, sensor measurements and commands received by the RC are, similar to an airplane's black box, tracked by the flight data recorder onto e.g. a microSD as for the md4-1000. For real-time monitoring of the individual flight parameters a real-time downlink transfers with a rate of 125 times per second onto the micro-SD which may be supervised using the ground control station's computer. Data is transmitted in ASCII format via the audio channel of the video transmitter (microdrones GmbH 2007, p.1).

The SIRUS ground station includes a wireless link connector for communication between the UAS, MAVinci Desktop and the Cockpit software. The range is up to 40 km in direct line-of-sight. The connector may also be used to connect to the internet using a 3G modem (<http://www.mavinci.eu/?command=components&sub=groundstation>, access date 20/12/2011).

2.9 Payload: Imaging Sensors for UAS

In the following, a selection of cameras and sensors for agricultural and environmental remote sensing will be described. An comprehensive list of available sensors worldwide may be found in (van Blyenburgh 2015). Table 2.4 to 2.7 subsequently summarize camera characteristics and their applications listed in this document.

2.9.1 Digital Cameras

Nearly any off-the-shelf camera residing within the payload capacity may be employed and the following mentions only a selection. A combination of two Kodak DC3200 was employed by for the assessment of fertilizer treatments on wheat crops (Jensen et al. 2007). In one camera a nIR-block filter was applied and the second camera was then equipped with filter blocking the red spectral ranges. Wundram and Löffler used a Nikon Coolpix camera to obtain aerial photos from kites (Wundram and Löffler 2008, p. 963). The camera was steered by a four-channel transmitter and video output was transmitted by a 300 m range video transmitter. Image downlink was visualized by video glasses, allowing accurate camera control. Recently, Mathews and Jensen (2013) applied a Canon PowerShot A480 RGB camera for analysing LAI in grapevine rows.

Suitable for vegetation canopy studies are the Agricultural Digital Camera series by Tetracam Inc, California, USA (Agüera et al. 2011). The single cameras' spectral sensitivity lies in the visible green, red part and near infrared part of the radiometric spectrum (520 nm to 920 nm). The lightweight version, the 3.2 megapixel ADC Lite (2048 x 1536 pixels), weighs only 200 g, and the ADC Air, the ruggedized weatherproof version of similar characteristics but 630 g of weight (Tetracam Inc. 2010, p.38).

2.9.2 Digital SLR- and SLM-Cameras

Principally any DSLR camera may be mounted on a UAS providing camera and lenses are within the payload capacity. The University of Trier uses a Nikon D3100 (Figure 2.10) with a wide angle lens of 18-55 mm to be mounted on a quadrocopter.



Figure 2.10 Nikon D3100 used with md4-1000 (Photo: J. Besold)

Hunt et al. employed a FinePix S3 (Fuji Photofilm Co., Ltd., Japan) UVIR 12 megapixel camera for evaluating fertilizer treatment on winter wheat (Hunt et al. 2010). Lelong et al. 2008 used two different digital SLR, a Canon EOS 350D and a SONY DSC-F828 on either a L'Avion Jaune or Pixy UAS to quantify LAI with the aid of NDVI and nitrogen uptake with GNDVI (Lelong et al. 2008, p.3561).

In future, Digital Single Lens Mirrorless (DSLM) cameras, e.g. the Panasonic LUMIX DMC-G-Series, may further be used as they are small, lighter and less complex than DSLR cameras.

2.9.3 Multispectral Cameras

A sensor that has been used for various multispectral agricultural applications is the miniMCA (MCA- multiple camera array; see chapter 4) developed by Tetracam Inc. (Berni et al. 2009; Suárez et al. 2010, Retzlaff et al. 2014, to be published). The light-weight camera array may be obtained as three models with either four, six or 12 lenses equipped with 25 mm standard filters in the spectral range of 400 to 1100 nm. As it has been used in this study, it will be described in more detail in chapter 5. Quest Innovations BV, Netherlands, also offers 3-5band UAS multispectral cameras, the Condor-Series with weights between 1-1-5 kg (Table 2.6, personal communication with Hendrik Jan van Es, 22/01/2014). Others have build their own cameras comparable to the Mini-MCA6 (Zarco-Tejada et al. 2013). For possible further providers please refer to the RPAS Yearbooks 2015 (van Blyenburgh 2015).

2.9.4 Hyperspectral sensors

Vierling et al. (2006) and Chen & Vierling (2006) have employed a non-imaging hyperspectral sensor for a small UAS system, the Short Wave Aerostat-Mounted Imager (SWAMI). It presents a remote sensing system for the acquisition of hyperspectral, photographic and other ancillary data and has been mounted on a tethered balloon. Here, a FieldSpec Dual UV/VNIR hyperspectral radiometer (Analytical Devices, Boulder, CO) is used with a color video camera and a thermal infrared sensor. The instantaneous field of view (IFOV) may be customized by 10° or 18° fore-optics and the spectral range lies within 350-1050 nm with a 3 nm spectral resolution.

Within recent years, several hyperspectral imaging sensors have been developed for light-weight UAS which were at the beginning of this study not yet light enough (< 1

kg) to being used with the md4-1000. Sensors applied within the UAS agricultural remote sensing community may be differentiated in snapshot and frame cameras. Snapshot cameras collect spectral data synchronously across the image area generally by using pixel groups with one wavelength filter which has the advantage of a simultaneous image yet less spatial resolution. Most sensors available are hyperspectral frame cameras based on Piezo-Actuated Fabry-Perot interferometers (Bareth et al. 2014). Their advantage lies in the selectability of wavelengths, however, the time lag of imaged wavelengths introduces spatial offsets which require postprocessing (band-to-band-alignment). A new introduction to the market is the Gamaya OXI series, where hyperspectral data is recorded simultaneously by filters onto the CMOS sensor using a global shutter, and therefore avoiding shift between spectral bands (Gamaya SA 2015).

Present small hyperspectral cameras are listed in Table 2.8, interested readers are again referred to the RPAS Yearbook 2015/2016 (van Blyenburgh 2015).

2.9.5 Thermal sensors

The SWAMI mentioned above also carries a thermal infrared sensor (EW-39669-00, Cole-Parmer, Vernon Hills, IL) sensitive within the spectral range of 7.6 -18 μm with adjustable emissivity between 0.02 and 1.00, measuring from 0°C to 180°C. The IFOV amounts to approximately 30° (Vierling et al. 2006, p.260). Other cameras widely applied (Berni et al. 2009, Israel 2011) are the thermal cameras developed by FLIR (<http://www.gs.flir.com/products/unmanned/>, access date 29.09.2011). The Zeiss UCM is described in more detail in chapter 4.

2.9.6 LIDAR

LiDAR has been employed for photogrammetric purposes for several years now. For crop and vegetation monitoring, however, LIDAR has only recently been introduced. Nagai et al. (2009) were among the first to integrate a SICK LMS-291 laser with a Tetracam ADC onto a RPH2 helicopter to retrieve 3D NDVI models for vegetation volume estimation (Nagai et al. 2009). Recently, the Ibeo LUX laser scanner had been applied in photogrammetric measurements (Lin et al. 2011, Wallace et al. 2012). It reaches a maximum range of 200 m scanning at maximum four parallel layers within a horizontal field of view (FOV) of 85° (35° to -50°) and a vertical FOV of 3.2°. The angular resolution is 0.125°, vertically 0.8°.

A nearly comprehensive list of imaging sensors and non-imaging sensors is published by the RPAS Yearbook 2015/2016 (van Blyenburgh 2015). A list of LiDAR and imaging sensors for photogrammetric applications may be found in Colomina and Molina (2014).

Table 2.4 Selected single lens cameras used for small UAS applications in environmental and archaeological remote sensing used within recent years (camera details taken from respective producer's data sheet last access date 24/04/2015, n.i.: no information available; PA: Precision Agriculture)

Camera / Producer	Detector Type	Spectral sensitivity	[Mega-pixel]	Sensor size [pixels]	Radiom. Resolution	Focal length [mm]	Camera size [mm]	Weight [g]	Comments Exemplatory Application
Single Sensor									
ADC Snap Tetracam Inc.	CMOS	3 bands: 520 – 920 nm	1.3	1280 x 1024	10 bit	8.43	75 x 59 x 33	90	fixed lens, global shutter (For applications see (http://www.tetracam.com/Products1.htm ; 24/08/2015)
ADC Lite Tetracam Inc.	CMOS	3 bands: 520 – 920 nm	3.2	2048 x 1536	10 bit	8.0	114 x 77 x 61	200	user-changeable lens, Rolling shutter; as above
Canon PowerShot G5/Canon, Japan	CCD	RGB	5	2592 x 1944	n.i.	n.i.	121 x 74 x 70	410	mapping riparian forest (Dunford et al. 2009); LAI and 3D mapping of vineyards (Mathews and Jensen 2013)
Kodak DC3200 adapted/ Eastman Kodak Company, New York, USA	CCD	400 - 500 nm 500 – 600 nm 600 – 700 nm 700 - ~1050 nm	1	1152 x 864	24 bit	39	113 x 81 x 53	2 x 300	grain yield, wheat protein content (Jensen et al. 2007)
Nikon Coolpix / Nikon	CCD	RGB	4	n.i.	n.i.	Adjusted to 4.95	n.i.	n.i.	vegetation classification (Wundram and Löffler 2008)

Table 2.5 DLSR cameras used for small UAS applications in environmental and archaeological remote sensing used within recent years (camera details taken from respective producer's data sheet last access date 24/04/2015, n.i.: no information available; PA: Precision Agriculture)

Camera / Producer	Detector Type	Spectral sensitivity	[Mega- pixel]	Sensor size [pixels]	Radiom. Resolution	Focal length [mm]	Camera size [mm]	Weight [g]	Comments Exemplatory Application
Digital SLR									
Canon EOS 350 D/ Canon, Japan	CMOS	RGB	8.2	22.2 x 14.8 mm		n.i.	127 x 94 x 64	485	PA: fertilization (Lelong et al. 2008); mapping riparian forest (Dunford et al. 2009)
FinePix S3 Pro / Fuji Photofilm, Ltd., Japan	Super CCD SR II	red light blocked with interference filter B, G, NIR	12.1	23 x 15.5 mm	12 bit	n/a	148 x 135 x 79	1240	PA: fertilization (Hunt et al. 2010)
SONY DSC-F828	4-colour Super HAD CCD™	RGB, Cyan	8	16.93 mm diagonally	48 (RAW), 24 bit	28-200	134 x 91 x 157	942 g	PA: fertilization (Lelong et al. 2008)

Table 2.6 Common multispectral imaging sensors of less than 1.5 kg weight for small UAS (camera details taken from respective producer's data sheet last access date 24/04/2015, n.i.: no information available; PA: Precision Agriculture)

Camera / Producer	Detector Type/ Pixel size [µm]	Spectral sensitivity	[Mega- pixel]	Image size [pixels]	Bit depth [bit]	Focal length [mm]	Speed [frames/ sec]	Camera size	Weight	Application/Comments
Micro-MCA-6/ Tetracam Inc.,	6	standard 25 mm diameter spectral filters 450–1050 nm	1.3	1280 x 1024	as above	9.6	as above	115x18x68	530	Tetracam Inc. 2015 both MCAs are available with 4, 6 or 12 detectors; global shutter
Mini-MCA-6 / Tetracam Inc.	6 CMOS/ 5.2 x 5.2	standard 25 mm diameter spectral filters 450–1050 nm	1.3	1280 x 1024	10 bit	9.6	1.3	115x18x80	700	rolling shutter ((http://www.tetracam.com/ , access date 24/04/2015); VI and chlorophyll concen- tration, water stress (Berni et al. 2009, Retzlaff et al. 2015)
SimCam/ QuantaLab	6	Filters similar to above		2592x1944	10 bit	8.4	n.i.			PA: VI (Zarco-Tejada et al. 2013)
The Condor UAV-sCMOS / Quest Innova- tions BV, The Netherlands	Fairchild CIS1910 F 6.45x6.4 5	B1: 400-500 nm B2: 500-590 nm B3: 590-670 nm B4: 670-830 nm B5: 830-1000 nm	1.4	1360 x 1024	12 bit	50 or 15	5-30	150x130x177 or 150x130x247	1450 or 1950	PA, environmental map- ping according to home page (http://www.quest- innova- tions.com/aerial.html , 24/04/2015)

Table 2.7 Common thermal imaging sensors of less than 1.5 kg weight for small UAS (camera details taken from respective producer's data sheet last access date 24/04/2015, n.i.: no information available; FPA: focal plane array)

Camera / Producer	Detector Type/ Pixel size [μm]	Spectral sensitivity	[Mega- pixel]	Image size [pixels]	Bit depth [bit]	Focal length [mm]	Speed [frames/ sec]	Camera size	Weight	Application/Comments
Tau640 / FLIR, USA	FPA UCM 17 μm	NEDT 50 mK at f/1.0 7.5-13.5 μm		640 x 512	n.i.	13 -100	3.5	38x38x30	79 - 475	FLIR ^R Systems Inc. 2011 game guard (Isreal 2011)
Thermovision A40/ FLIR, USA FLIR, USA	FPA UCM	7.5-14 μm		320 x 240	16 bit	18.7 - 150	0.5	207x 92x109	1400	VI, chlorophyll concentra- tion, water stress (Berni et al. 2009), fluorescence (Zarco-Tejada et al. 2009)
Zeiss UCM		NEDT 90 mK at 40°C f/1.0		640 x 480	8 bit	n.i.	50-60	95x48x48	170	Carl Zeiss Optronics GmbH 2008, 2011

Table 2.8 Hyperspectral imaging sensors of less than 1.5 kg weight for small UAS (camera details taken from respective producer's data sheet last access date 24/04/2015, n.i.: no information available)

Camera / Producer	Detector	Spatial resolution [pixel]	Spectral sensitivity [nm]	Spectral resolution [nm]	Spectral bands	Focal Length, F No.	Speed [frames/sec]	Camera size	Weight [g]	Bit depth	Comments/ Applications
Micro-Hyperspec Series/Headwall Photonics	Silicon CCD or CMOS, or InGaAs or MCT	320 -1600 dep. on sensor range	400-1000, 900-1700 550-1650 900-2500	1.6-1.9 VIS 5-6 nIR 10 SWIR	325-370 (VisnIR) 67-96 nIR 166 (SWIR)	2.5	n.i.	See data sheet	680 to 1300	12-16	Headwall Photonics Inc. 2014a
Micro-Nanospec/Headwall Photonics	CMOS	640 x 480	400-1000	5 (2.2 SSI)	270	2.5	200-480 (full)	76x76x120	680	12	Headwall Photonics Inc. 2014b
OXI-snapshot series / Gamaya	n.i.	2048-1088	Variating within 450-950	n.i.	16	n.i.	16	n.i.	160-250		Gamaya SA 2015
Pika II / Resonon	n.i.	640	400-900	2.1	240	3	145	97x168x64	1300	12	Resonon 2015
Pika NIR / Resonon	n.i.	1600	900-1700	5.4	148	2	120	102x229x76	1474	14	Resonon 2015
Rikola Hyperspectral Camera/ Rikola Ltd.	CMOS	1010 x1010	500-900	10	380	9 mm, 2.8	30	80x92x150	720	12	Rikola Ltd. 2015; Precision agriculture, DTM (Honkavaara et al. 2013) Bareth et al. 2014
UHD 185 / Cubert	Si CCD	n.i.	450-950	8 (SSI 4)	125	16mm, 2.8, 2/3	5	Minimum 60x55x40	470	12	Bareth et al. 2014

2.10 Airspace Regulation

Before a UAS mission may be planned, airspace regulations need to be considered as research applications do not fall under leisure use of UAS. The ICAO, the UN-agency for developing standards and common practice in international civil aviation, had been requested to initiate procedures to avoid dangers to aviation and to issue operating authorizations for the use of international civil UAS in 2005 (ICAO 2011). Their Circular 328 issued in 2011 called upon member states to integrate UAS into their non-segregated airspace and aerodromes (ICAO 2011). The next sections will therefore give a to-date summary (July 2015) of European, German, Luxembourgian and Spanish airspace regulations for small UAS.

2.10.1 European Airspace Regulation

With emerging UAS development in the last decade, the European Aviation Safety Agency (EASA) produced a policy statement on the “Airworthiness Certification of Unmanned Aircraft Systems (UAS)” in August 2009 (Colomina and Molina 2014, p.83). At about the same time, the EC and European Defence Agency (EDA) held a high-level conference on UAS on 1 July 2010 where the potential use and benefit of non-military use of UAS was presented and where it was generally acknowledged that missing regulatory frameworks hindered the development of civil UAS industry to move forward (Blyenburgh 2012). The UVS International was then commissioned to produce a document on the structural and strategic approach to integrate UAS. Following this, on 18 April 2011, the EC “announced a new UAS initiative... meant to provide the EC with the necessary expertise and input to develop a strategy for the future of UAS in the European Union, and to identify the most pressing issues.” (Blyenburgh 2012, p. 118). Workshops were held on the industrial sector and market, the insertion into airspace and radio frequencies, safety issues of UAS, societal dimensions of UAS and the R&D for UAS, which final reports may be found in the staff working document “Towards a European strategy for the development of civil applications of Remotely Piloted Aircraft Systems (RPAS)” (EC 2012).

Regarding regulations, the main conclusions were

- the priority of the secure integration of UAS into the European airspace,
- the subsequent development of technologies and aviation regulation framework at the EU and national levels, and

- the coordination between EASA, Civil Aviation Authorities (CAA), European Organization for Civil Aviation Equipment (EUROCAE), European Organization for the Safety of Air Navigation (EUROCONTROL), Joint Authorities for Rulemaking on Unmanned Systems (JARUS), and industry a.o..

An UAS Roadmap shall achieve these goals within the next 15 years with the help of a European RPAS Steering Group (ERSG) holding the following bodies: EC, EASA, Eurocontrol, ECAC, EUROCAE, JARUS, EDA, European Space Agency (ESA), UVS International a.o. (ERSG 2013), some of their contributions are described in the following.

The European Unmanned System Centre (EuroUSCTM) is the EC regulating Qualified Entity (EC Regulation 216/2008 Article 13) and was set up in 2009. It assesses all light UAS with a maximal take-off mass (MTOM) of under 150 kg. Herein, in approval by the Civil Aviation Authority (CAA) the accredited body of Light UAS Scheme (LUASSTM) was set up which has the following tasks:

- airworthiness assessment,
- pilot competency qualification and
- operational assessment (Clot 2012).

In Europe, EUROCONTROL is the intergovernmental “European Organisation for the Safety of Air Navigation [...] committed to building a Single European Sky” (<http://www.eurocontrol.int/content/about-us>, 10/02/2013, Tytgat 2012, p. 36). For the integration of light UAS to the European sky, UAS need to fit into the Air Traffic Management (ATM) system. UAS are to be incorporated into the manned aircraft regulations. Currently, several obstacles lie in the way of UAS being permitted in non-segregated airspace: the capability to see and to be seen, communication links between controllers/pilot/navigation and surveillance systems. Here, frequencies need to be made available (Tytgat 2012). EUROCONTROL therefore works with other European entities to develop airport and regulatory guidelines.

Just how recent the issue of granting flight approval is, shows the current work of EUROCAE in France. EUROCAE is the European Organisation for Civil Aviation Equipment and therefore the forum for setting aviation standards for airborne and ground systems and equipments (<http://www.eurocae.net/about.html>, 10/02/2013). In May 2012, it set off a working group on lightweight UAS (WG93). The goal is to harmonize European rules and regulations for visual line of sight operations (VLOS) and

beyond visual line of sight (BVLOS) to support European countries' aviation authorities with regulation guidance regarding command, control and communication, airworthiness, operator approval, UAS classification and safety assessment, amongst others (Leijgraaf 2012b). Furthermore, the working group 73 (WG 73) on Unmanned Aircraft Systems was set up in 2006 and aims at delivering standard protocols for the safety and regulations of UAS missions (Kallevig 2012). Parallel to this and also co-operating is the international JARUS group: The Joint Authorities for Rulemaking on Unmanned Systems (JARUS) group over 22 countries worldwide (including Germany) to participate in harmonizing and coordinating operational requirements and certification issues to support aviation authorities in rule-making which they may or may not integrate in national or regional law (Leijgraaf 2012a).

Table 2.9 gives an overview over prevailing UAS regulations in European countries (van Blyenburgh 2014b). After the first hype of using UAS for leisure and also environmental and remote sensing, regulating bodies have in some countries stopped UAS use for civil/commercial and leisure use due to civil protection issues. Spain, for example, has stopped civil commercial and professional UAS operations in 2014 until national regulations are specified (Agencia Estatal de Seguridad Aérea 2014).

In March 2015, the European Cockpit Association (ECA) addressed the dangers of light and also recreational (toy) UAS in low-level airspace where they may get into the way of air rescue, firefighting and police missions. They published a position paper to outline key regulatory standards demanded for a safe integration of light UAS into European lower airspace:

- compulsory registration of UAS
- introduction of automated detection and avoidance systems
- UAS pilots responsibility to see and avoid manned aircraft
- mandatory pilot training and licencing
- definition of weather standards for UAS missions
- information of the public about recreational UAS use and increase level of law enforcement (ECA Piloting Safety 2015).

Table 2.9 Current UAS regulations in Europe as published by the UVSI (Source: van Blyenburgh 2014b; Abbrev.: * UAS Use is facilitated and granted by National Aviation Administrations; VLOS: visual line of sight; BLOS: Beyond line of sight)

Member state	MTOW established	MTOW planned	Comment
Austria*	< 150 kg VLOS		
Belgium*		< 150 kg VLOS	2013, not in force
Bulgaria			
Croatia			
Cyprus			
Czech Republic*	< 150 kg VLOS, BLOS		05/2013
Denmark*	< 150 kg VLOS		01/2004
Estonia			
Finland		< 150 kg VLOS	Expected mid 2014
France*	< 25 kg VLOS, BLOS	< 150 kg VLOS, BLOS	Since 04/2012, update in preparation
Germany	< 25 kg VLOS		
Greece*			
Hungary*		< 150 kg VLOS	
Ireland*	< 20 kg VLOS		Since 05/2012
Italy*	< 25 kg VLOS		Since 12/2013
Latvia			
Lithuania*	< 25 kg VLOS	< 150 kg VLOS	Expected mid 2014
Luxembourg			
Malta*		< 150 kg VLOS	In preparation
Netherlands*	< 25 kg VLOS	< 150 kg VLOS	Since 2012, update in preparation
Poland*	< 150 kg VLOS, BLOS		Since 2013
Portugal			
Romania*			

Member state	MTOW established	MTOW planned	Comment
Slovakia			
Slovenia*			
Spain*		< 25 kg VLOS	In preparation
Sweden*	< 150 kg VLOS		Since 2013
UK*	< 20 kg VLOS		Since 2002
Iceland		< 150 kg VLOS, BLOS	
Norway*			Expected 2014
Switzerland*	Model aircraft rules for UAS	VLOS over people and crowds	Expected 2014

2.10.2 Airspace Regulation in Germany

In 2012, the air traffic law (Luftverkehrsgesetz – LuftVG) integrated UAS in its listing (§1). Now the authorities work on the integration of UAS into subsequent constitutive laws and regulations (Udovic 2012). The Air Traffic Order (Luftverkehrsordnung – LuftVO §15a) published in 2010, forbids the operation of UAS if their total mass exceeds 25 kg or when their flight is being operated outside unaided visual line of sight (Udovic 2012). Each civil/commercial use (beside recreation or sports use) of a lighter unmanned aerial system requires an ascent license issued from the respective federal agency legally retained by the Federal Ministry of Transport, Building and Urban Development (LuftVO §16 (1) number 7). Flights are only permitted in segregated airspace and outside aerodromes. In Rhineland-Palatinate this is the *Landesbetrieb Mobilität Rheinland-Pfalz, Fachgruppe Luftverkehr* situated at Hahn airport (LuftVG §31 (2) 16f and g and §31c). General ascent permits are only issued for UAS of less than 5 kg MTOW without fuel engines, flight altitudes of up to 100 m above ground or may be issued for repeated missions at one location, for Rhineland-Palatinate only. Flight permits for higher altitudes need to be especially requested for each case.

For ascents (LuftVO §16 (5)) the admission of the land owner is necessary and, when indicated, the protection of data privacy need to be maintained. All flights in controlled airspace additionally deserve an air control clearance granted by the respective regulato-

ry agency (LuftVO §16a (1) 5) which needs to be obtained by the person starting the drone (LuftVO §16a (2) 5), and the local control station for (rescue) flights need to be informed. Last not least, the proprietor or even the pilot need to contract general liability insurance either for several pilots for one drone or pilots for several drones.

Formerly, the LBM, the local regulatory agencies and the rescue coordination centre needed to be informed of intended UAS missions 24 hours before ascent. Now, only the police authority requires contacting prior to flight.

According to Udovic (2012), the German Ministry of Transport works on a common operation permit for all federal states.

2.10.3 Airspace Regulation in Luxembourg

Up until now, there are no regulations for UAS use in the Grand Duchy of Luxembourg. UAS therefore fall under the rules for full-size manned aviation. All research and commercial UAS activities taking photographs or videos are treated as “aerial works” and require a permission issued by the Directorate of Civil Aviation (DAC) (DAC 2014). To facilitate UAS operations a tax of ~ 620 € has to be paid to acquire a UAS photography permit for Luxembourg. No further documents like registration number, airworthiness certificates nor pilot licenses are requested. In general, only single ascent permits are issued and hold the following restrictions:

- maximum flight altitude 50 m,
- no flights over people and crowds,
- flights only above pre-defined areas,
- working area limited to public access,
- VLOS-flights only,
- auto-landing maneuvers in case of system failure, and
- public responsibility insurance (DAC 2014).

Derogations of these restrictions are possible if the applicant presents a safety case demonstration for the DAC. On their web-page is a link to ascent permission proposal form. Higher flight altitudes may then be asked for and are generally granted provided that the above mentioned safety rules are met (DAC 2014).

2.10.4 Airspace Regulation in Spain

A note published by the Spanish Air Navigation Safety Agency (AESA) on 7 April 2014, declared that any civil commercial or professional use of UAS are and had been illegal except for military, experimental or recreational use. The regulatory framework had been worked on in the meantime and on 8 July 2014, the AESA proposed a temporal regulatory framework for drones less than 150 kg MTOW (information collected from the web pages of AESA, 24/08/2015). To the author's understanding, this foresees for lightweight UAS of < 25 kg,

- drone must hold a license tag,
- a pilot license or authorization derived through pilot license for a micro light aircraft or by training obtained at EASA-Approved Training Organization (ATO), or agreement of ATO for drones < 25 kg, else
- the pilot must be older than 18 years,
- the Pilot must present a medical certificate to prove fitness of flying drones, and
- a proof of ability to fly and handle the drone issued by UAS producer or any training authority

Moreover, all drone operators further need to fulfill the following:

- Provide information on drone type to the AESA,
- Hold an operation manual,
- Demonstrate aviation safety,
- Conform to a maintenance program according to producer's recommendations,
- Hold an insurance license,
- Seize measures against system fallouts, and
- Hold minimum distance of 8 km to airports and aerodromes, 15 km if drone is operated by instrument flight (AESA 2015).

Drones of less than 25 kg MTOW do not need an operating permit but need to inform the AESA with the relevant documentations for a safe operation. Intended ascents need to be announced at the AESA 5 days prior to flights, and a receipt will be issued AESA 2015.

3 Remote Sensing of Vegetation in Vis/nIR Spectral Range

Vegetation mapping and analysis have been amongst the very first applications in multispectral remote sensing since the 1970ies. And as vegetation is the key component in this work, the chapter gives a short general overview of key spectral-radiometric characteristics of vegetation. Methods to derive biophysical parameters from multispectral narrowband remote sensing imagery are then described in more detail in the particular case study applications in chapters 7-9.

3.1 Multispectral Properties of Plant Foliage

The above-ground biomass of plants may further be described by amount, location, size and orientation of its structural components. Plant foliage comprises leaves, needles and other green materials of plants. From a remote sensing perspective, the plant organs leaves are the most significant above-ground plant organ as they present the largest part of the crop plant, whose main function is the photosynthesis and evapotranspiration (Kurz 2003, p.13). The spectral properties of leaves are steered by the leaf structure and its chemical components according to Asner (1998):

1. pigments
2. water
3. carbon
4. nitrogen.

At first, the basic leaf structure and possible light-leaf interactions are described, then the main chemical components are described in more detail.

3.1.1 Leaf Structure

Among the above-ground plant organs, leaves represent the largest part of crops. Their main function is photosynthesis and evapotranspiration (Kurz 2003). Based on the theory of Willstatter and Stoll (1928), a dicotyledonous leaf is typically defined by four layers (Figure 3.1), the upper and lower *epidermis*, coating the leaf against the outside environment and encasing the two inner layers, palisade and sponge parenchyma, the so-called *mesophyll*. The epidermis is generally translucent and shows a waxy cuticle which protects the leaf from dehydration and physical destruction. The cuticle may also

have hairs (trichomes). Mostly on the lower epidermis, the leaf stomata regulate the gas exchange of CO₂ entering and evapotranspiration. The inner part of the leaf, the mesophyll or *chlorenchyma* tissue, is where photosynthesis happens. For horizontal leaves (planophile), the palisade layer is located on the upper leaf side and consists of a collection of cylindrical cells which contain most of the chloroplast material to use incoming solar energy. Erectophile (upward-pointing) leaves may have palisade parenchyma on both sides. Beneath the palisade layer, the spongy layer consists of irregular structured cells with large intercellular air spaces where oxygen (O₂) and CO₂ are exchanged (Kurz 2003, Jensen 2007a). Leaf veins transport water and minerals from the roots into the leaf (xylem) or sap, i.e. dissolve sucrose out of the leaf (phloem) (Hodson and Bryant 2012).

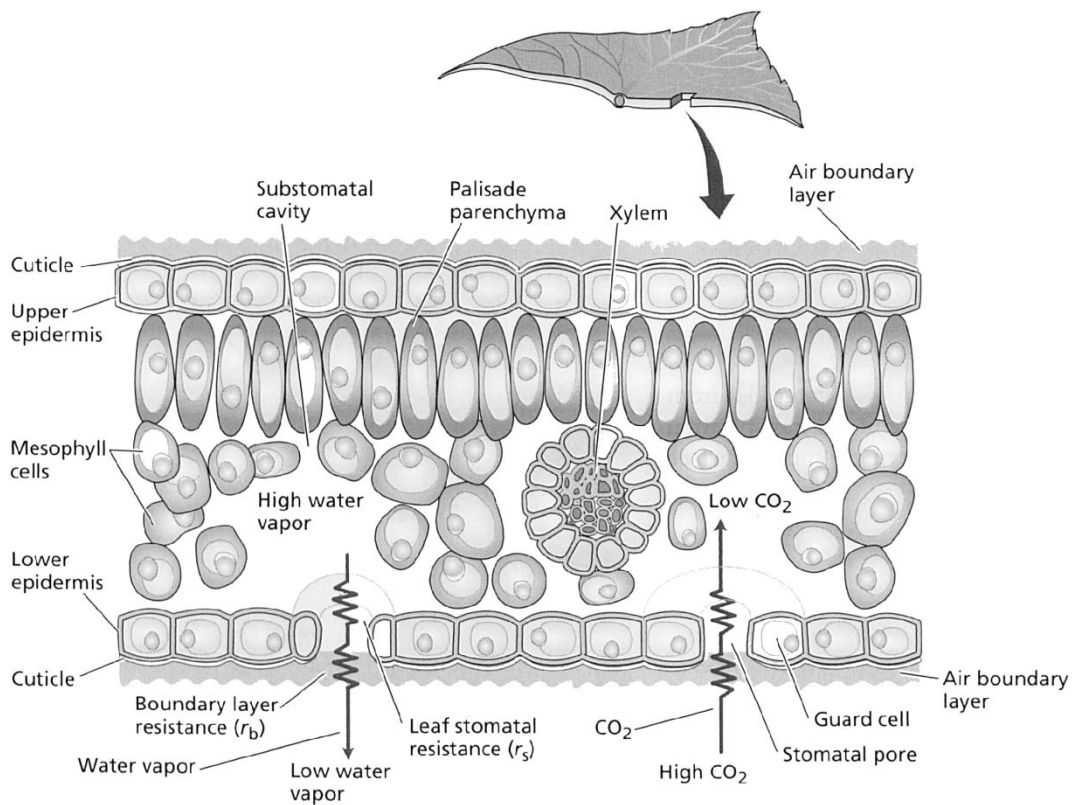


Figure 3.1 Water and gaseous pathway through a model leaf (Source: mod. from Taiz and Zeiger 2010 p. 97)

3.1.2 Biochemical Radiative Interactions with Leaves

Spectrally, the most significant leaf chemical component are the photosynthetically active leaf pigments, the chlorophyll (65%), carotenoids and flavonoids (Guyot 1990, Kurz 2003). The chlorophyll (Chl) pigments are located in the chloroplasts located in

the upper palisade parenchyma leading to the leaf's green colour (Jensen 2007b). They absorb incoming solar light in the visible (VIS: 350-700 nm) part of the electromagnetic spectrum, chlorophyll a (Chl_a) at wavelengths ranging from 430 to 660 nm with two peaks at 430 nm and 660 nm, and chlorophyll b (Chl_b) ranging from 400 to 650 nm with two peaks at 460 nm and 640 nm (Guyot 1990, Jensen 2007b).

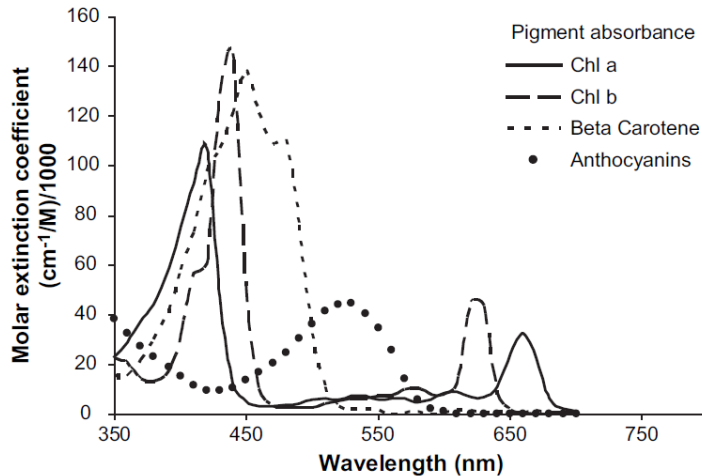


Figure 3.2 Leaf pigment absorption (Blackburn 2007, p. 857)

The carotenoids are also located in the chloroplasts and composed of hydrocarbons, the carotenes (lutein and β -carotene with yellow-orange colour) and yellow xanthophyll pigments also containing oxygen (Jensen 2007a). Xanthophyll pigments violaxanthin and zeaxanthin absorb light in the blue-green wavelengths (Jones and Vaughan 2010). Carotenoids absorb solar energy in the blue wavelength ranges (450 nm) for photosynthesis and chlorophyll protection from photodamage. For healthy green vegetation, their absorption is generally masked by the chlorophyll absorption. That's why in the VIS, only a small amount of light is reflected and transmitted by the leaf (Jensen 2007b). Flavonoids are pigments responsible for the leaf colour, e.g. anthocyanins gives fruits, berries and leaves their characteristic red colour in autumn (Jones and Vaughan 2010).

Leaf water is the dominant absorber in the IR electromagnetic spectrum. In the nIR, there is a minor water absorption bands at 970 nm, in the middle-infrared (mIR) domain of 1300-2500 nm wavelengths, water content steers leaf reflectance as there are several water absorption bands at 1450, 1950 and 2500 nm (Jensen 2007a, Jones and Vaughan 2010). Table 3.1 lists the absorption feature wavelengths for cellulose and sugar, protein and nitrogen, oil and lignin which reside mainly in the nIR-shortwave infrared (SWIR).

Table 3.1 Absorption features of leaf constituents in VIS – mIR (modified from Jones and Vaughan 2010, p. 41). Bold numbers show strongest absorption.

Constituent	Absorption Wavelength [nm]
Chlorophyll	430, 460, 640, 660
Water	970, 1200, 1450, 1950, 2500
Protein, nitrogen	910, 1020, 1510 , 1690, 1940, 1980, 2060, 2130, 2180 , 2240, 2300, 2350
Oil	930, 1020, 2310
Lignin	1120, 1420, 1690 , 1940
Cellulose/sugar	1780

In contrast to the VIS (Figure 3.3), in the near-infrared (nIR: 700-1300 nm) part, leaf pigments and cell walls are transparent resulting in high reflectances (40-60%), transmissions (40-60%) and only little absorption (under 10%).

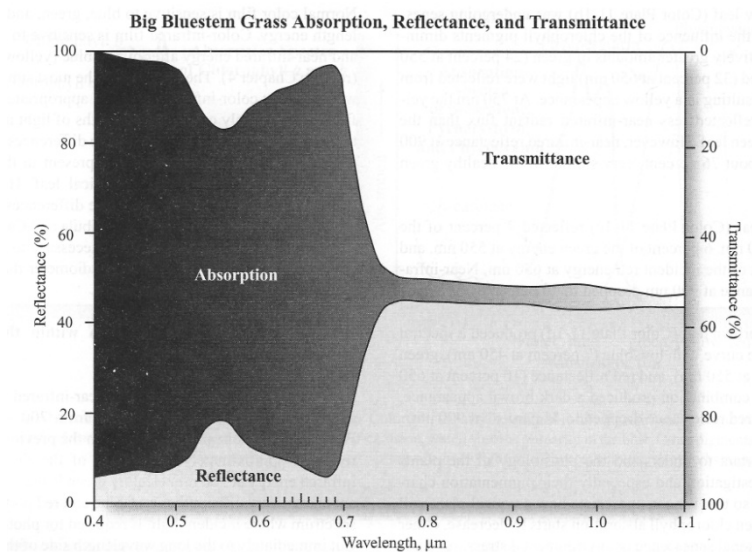


Figure 3.3 (Source: Jensen 2007a, p.362)

In the VIS most radiation is absorbed in the chloroplasts, but in the nIR light is mainly reflected and to a minor part scattered by the mesophyll air/cell wall interfaces (Asner 1998, Jensen 2007a, Jones and Vaughan 2010). The strength depends on number of cell layers, cell size, and the thickness of spongy mesophyll wall-orientation and cell heterogeneity (Gausman and Allen 1973, Guyot 1990, Jensen 2007b).

When the incident angle of light is off normal, specular reflectance of light on the cuticle will be combined with diffuse, spectrally dependent reflectance from within the

leaf. In the near-infrared (nIR), leaves may be considered as Lambertian diffusers, in the visible domain, reflectance is strongly directional (Guyot 1990).

3.1.3 Light interactions within the Photosystem II: Fluorescence and Non-Photochemical Quenching

Within the thylakoid membrane of the chloroplasts, reside the reaction centre of the Photosystem II (PSII) which steer oxygen generation and water splitting. PSII is sensitive to light levels and quality, water and nutrient availability, a.o., and therefore of major interest for remote sensing. Excess light energy not being required for photosynthesis and carbon-fixation is partly re-emitted as sun-induced chlorophyll fluorescence at longer wavelengths, showing two well-defined peaks at the red 685 nm and nIR 740 nm (Zarco-Tejada et al. 2003; Campbell and Wynne 2011; Damm et al. 2011, Jones and Vaughan 2010). Altogether, only 2-5 % (Figure 3.4) of the overall reflected radiance may be attributed to sun-induced fluorescence (Meroni et al. 2009, Jones and Vaughan 2010; Damm et al. 2011). The re-emission of excess energy occurs mostly in 10^{-9} s.

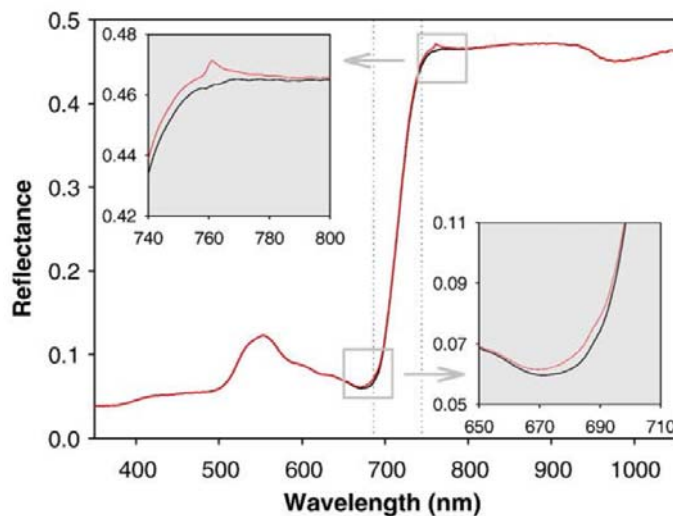


Figure 3.4 Reflectance of a green sugar beet leaf: without fluorescence in black; with fluorescence in red (Source: Meroni et al. 2009, p. 2038)

With senescence, fluorescence emission peaks (Figure 3.5) move towards lower wavelengths peaking at 500-600 nm (Campbell and Wynne 2011).

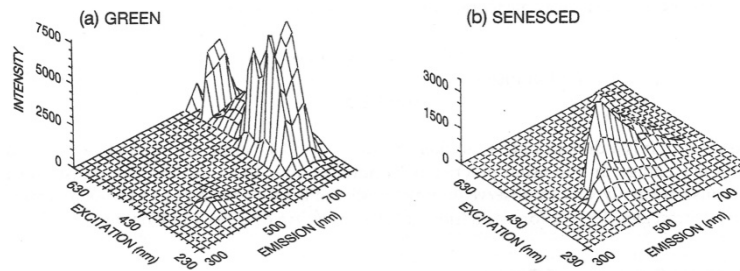


Figure 3.5 Fluorescence of healthy green and senesced vegetation (Source: Campbell and Wynne 2011, p. 51)

Another mechanism of chloroplasts to dispose of excess light energy is non-photochemical quenching (NPQ), a conversion of carotenoid violaxanthin into zeaxanthin into heat within the xanthophylls cycle (Gamon et al. 1990; Demmig-Adams and Adams 1996).

Canopy derivative fluorescence and reflectance measurements have shown to be directly related to temperature and humidity stress (Zarco-Tejada et al. 2003; Berni et al. 2009, Zarco-Tejada et al. 2013a; Zarco-Tejada et al. 2013b). How sun-induced fluorescence may be depicted from the overall reflectance is being reviewed in more detail in chapter 8.

3.1.4 Factors Influencing Leaf Reflectance

3.1.4.1 Leaf Architecture

Leaf anatomy has a great impact on nIR reflectance. Guyot (1990) summarises the following factors altering leaf optical properties: the number of cell layers and their cell size, and the thickness of the spongy parenchyma tissue. He further describes the leaf asymmetry when upper cuticle is compared to the lower side. Due to the higher chloroplast density in the palisade mesophyll, the upper leaf side reflects less than the lower part. Hairs on the cuticle, increase reflectance in the VIS and mIR, but are transparent in the nIR (Guyot 1990, p. 22).

3.1.4.2 Leaf Age

Depending on chlorophyll content, the spectral properties of plants change significantly from young to mature leaves, yet until senescence, for deciduous plants, the chlorophyll level remains relatively constant during the mature state (Guyot 1990, p. 23, Poni et al. 1994).

Figure 3.6 shows the reflectance of senescent vegetation in comparison to green vegetation. At the beginning of the seasonal cycle, young leaves show a blue-shift of the red-edge for a short period. With further development, the red-edge is shifting slowly to longer wavelengths. When Chl pigments wane in autumn, more light is reflected in the green and red VIS spectrum letting the leaves appear yellowed. The reflectance level in the nIR decreases slightly and the red edge shifts towards the VIS (Miller et al. 1991; Jensen 2007a). Non-photosynthetic vegetation - dried out vegetation – shows an increase in the nIR and mIR and the green peak becomes resolved into a step rise of reflectance towards shorter wavelengths. Also, smaller variations due to water/temperature stress during the season lead to blue-shifting fluctuations (Miller et al. 1991).

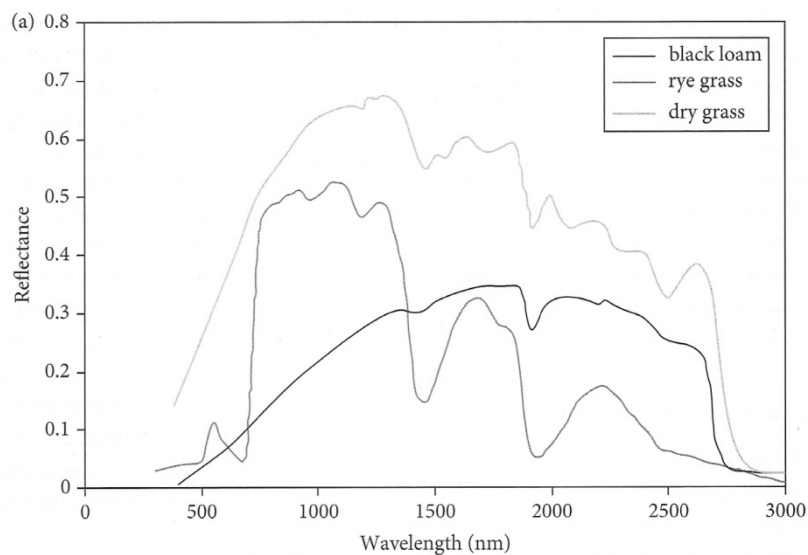


Figure 3.6 Reflectance spectral of healthy and dried vegetation and soil (Source: Jones and Vaughan 2010, p. 46)

3.1.4.3 Leaf Water Content

Water enters leaves through the petioles is transported mainly to the spongy mesophyll by the veins. There are five absorption bands within the nIR to mIR spectral range: 970, 1190, 1450, 1940 and 2700 nm (Jensen 2007a). Leaf moisture changes by evapotranspiration till wilting and death are dominant in the mIR and effect reflectance at the VIS, nIR due to water turgor (Guyot 1990, p. 24). When leaf water decreases, spectra increase in reflectance in the nIR-mIR.

3.1.4.4 Leaf Nutrients and Diseases

Iron deficiency causes chlorosis affecting VIS reflectance. Nitrogen is, amongst others, contained in the chlorophyll pigments, nitrogen deficiency therefore is directly linked to chlorophyll content, increasing VIS reflectance and decreasing nIR and mIR reflectance (Guyot 1990, Jensen 2007a).

Fungi and diseases may cause leaf aging/yellowing altering the VIS reflectance or introduce other changes, necrosis will look similar to leaves senescence.

3.2 Multispectral Properties of Canopies

Vegetation canopy reflectance is an interaction of sensor-characteristics, viewing- and illumination geometry, tissue reflectance resulting from light interactions within plant parts and canopy as well as background substrate, summarized in Table 3.2 (Asner 1998, Jensen 2007a).

Table 3.2 Main Impact Factors on Canopy Bidirectional Reflectance (modified from Jensen 2007a, p. 368)

Sensor	<ul style="list-style-type: none"> • sensor viewing geometry (viewing angle from nadir and azimuth position of sensor) • IFOV (Instantaneous field of view) • spectral sensitivity
Illumination	<ul style="list-style-type: none"> • sun position (zenith, azimuth) • wavelength region
Vegetation canopy	<ul style="list-style-type: none"> • canopy type (crown shapes, roughness and closure) • canopy orientation • visibility of trunks & stems • LAI • Leaf angle distribution (LAD)
Background	<ul style="list-style-type: none"> • understory • soil

3.2.1 Sensor- and Illumination Geometry

3.2.1.1 Bidirectional Reflectance Effects of Canopies

Lambert's emission law states that the radiation of a Lambertian – a perfectly diffusely reflecting surface - is proportional to the cosine of the angle θ between a sensor's line of

sight and the surface normal, so that the object shows the same radiance from any viewing position. Depending on the canopy structure, dense grass may resemble a Lambertian surface whereas a maize field canopy will show a combination of both specular and diffuse reflection components (Figure 3.4).

The at-sensor reflectance varies with a) the location (azimuth) of the sun and its height over the horizon (zenith) and depends on b) the sensor position and viewing angle (Jensen 2007a), *i.e.* the bidirectional reflectance distribution. Objects receiving back-scattered radiance - sensor and sun are positioned at similar azimuth values - seem brighter (see figure) than forward-scattered radiances - sensor is positioned opposite the sun (Sandmeier 2000). When object – sensor – sun are aligned on the “solar principal plane” (Jensen 2007a, p.368), a hot-spot effect occurs, *i.e.* a bright area on the image without any shadows. At nadir imagery, the hot-spot effect appears when the solar zenith angle is smaller than the FOV.

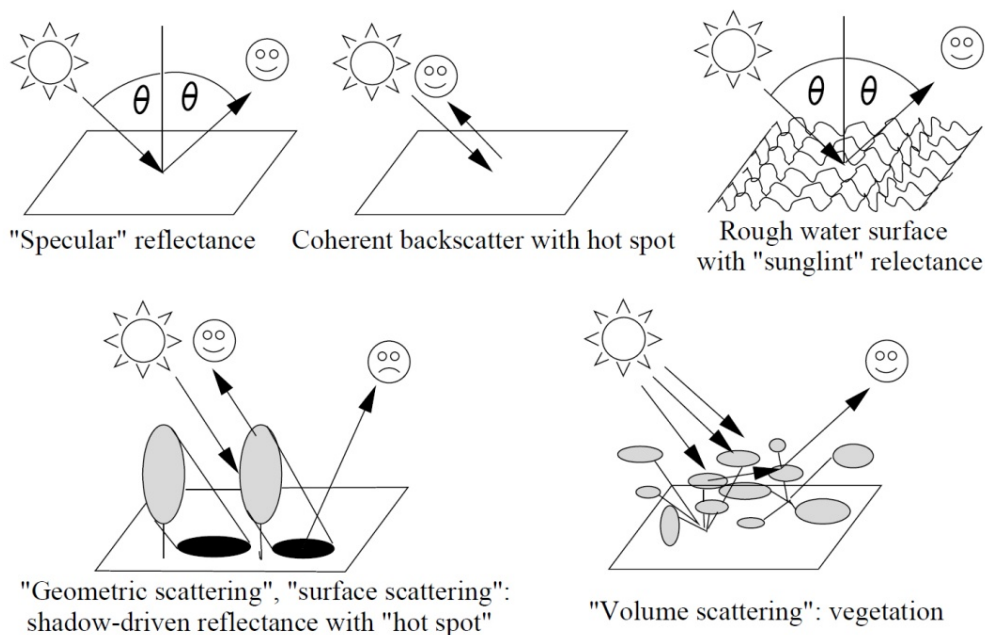


Figure 3.7 Sources of anisotropic reflectances in the environment (mod. from Beisl and Woodhouse 2004, p. 1684)

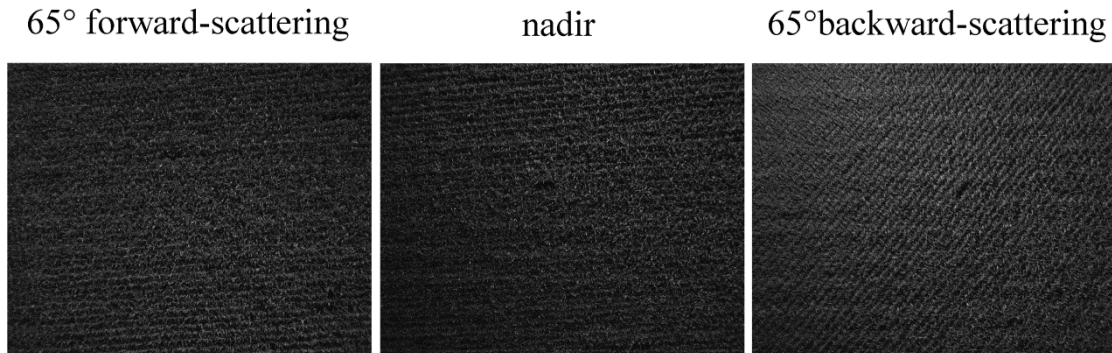


Figure 3.8 Bidirectional reflectance differences for a maize field along the solar principal plane (570 nm, sun azimuth $\sim 135^\circ$, sun altitude 51°)

3.2.1.2 The Bidirectional Reflectance Distribution Function

Sandmeier and Itten were the first to build a transportable field goniometer (FIGOS) to use with a spectroradiometer (GER-3700, nominal range of 300-2450 nm) studying the bidirectional reflectance distribution by a stepwise variation of sensor zenith and azimuth angles in relation to sun azimuth and zenith (Sandmeier and Itten 1999). The ratio of reflected radiance to incident irradiance in relation to sun – sensor – target geometry is described by the bidirectional reflectance distribution function (BRDF), first defined by (Nicodemus et al. 1977):

$$\text{Spectral BRDF } f_{v_{\theta_i, \varphi_i, \theta_r, \varphi_r, \lambda}} = \frac{R_{\theta_i, \varphi_i, \theta_r, \varphi_r, \lambda}}{I_{\theta_i, \varphi_i, \theta_r, \varphi_r, \lambda}} [\text{sr}^{-1}] \quad (3.1)$$

With:

- R: reflected radiance [$\text{Wm}^{-2}\text{sr}^{-1}\text{nm}^{-1}$]
- I: solar incident radiance [$\text{Wm}^{-2}\text{sr}^{-1}\text{nm}^{-1}$]
- θ_i : sun zenith
- φ_i : sun azimuth
- θ_r : sensor/view zenith
- φ_r : sensor azimuth
- λ : respective wavelength

The spectral bidirectional reflectance (BDR) factor describes the wavelength-dependent reflected radiance from a surface to a specific direction in relation to the reflected radiance from a Lambertian reference panel under equal irradiance conditions.

BRDF are spectrally dependent, effects are larger in the VIS than in the nIR (Guyot 1990; Sandmeier and Itten 1999). To illustrate wavelength dependent effects, bidirec-

tional reflectance data may be normalized by nadir reflectance, obtaining an anisotropy factors for each wavelength (Jensen 2007a). Figure 3.9 shows the anisotropy factor obtained by forward and backward scattering processes for a sun zenith angle of 35° for different wavelengths. BRDF effects are largest on the blue and red chlorophyll absorption spectral regions, and generally lower for the nIR where multiple scattering is strong and reduces BDR effects (Sandmeier and Itten 1999).

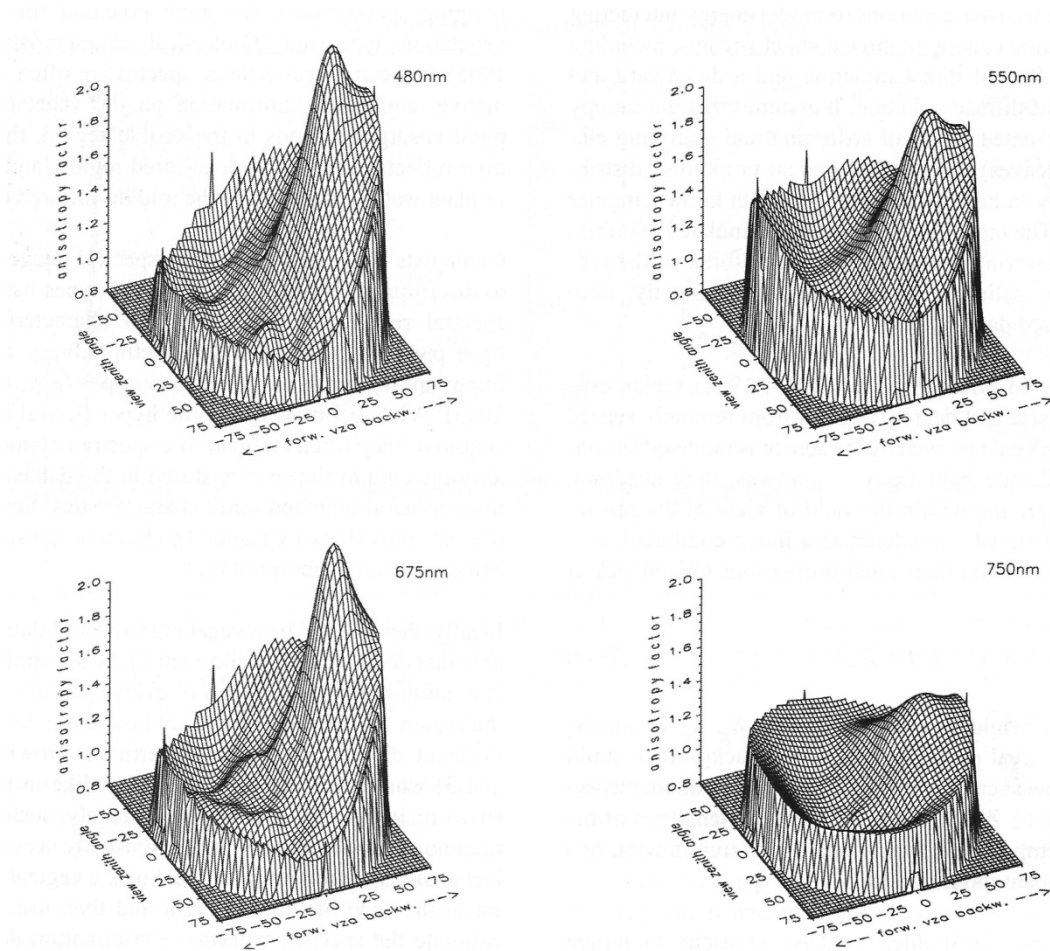


Figure 3.9 Anisotropy factors (nadir-normalized BRDF) of ryegrass for different wavelengths and a sun zenith angle of 35° (mod. Sandmeier and Itten 1999)

When sensor viewing angles vary from normal, BRDF may help to understand how the signal is affected by sensor viewing geometry in relation to sun position and, also, how respective wavelengths are affected. The BRDF also varies seasonally with sun azimuth/zenith variations (Sandmeier 2000). However, when multi-angular images are compared for a specific point in time, the side-looking imagery yield further information on the canopy and its biophysical properties than nadir imagery sensing solely

the top canopy layer (Qi et al. 1995; Jensen 2007a). Great care needs to be taken to accurately correct for atmospheric differences when biophysical parameters are estimated from multi-temporal imagery (Qi et al. 1995). A comprehensive overview over BDR correction models is given by Beisl 2001. They may be grouped into

- physical models mainly applied for information gain; these are generally based either on ray-tracing or radiative transfer function methods;
- semi-empirical models. They understand BDR as a number of isotropic and volume scattering kernels and are mostly applied for correcting brightness gradients for line scanner data (Beisl and Woodhouse 2004, Schiefer et al. 2006); and
- empirical models based on viewing geometry (Schiefer et al. 2006).

3.2.2 Canopy parameters

The canopy signal as a combination of “leaf additive reflectance” as rays transmitted by a leaf may again be reflected and transmitted by understory leaves. Thus, nIR reflectances for healthy leaves reach up to ~ 50% (Jensen 2007a). When the incident angle of light is off normal, specular reflectance of light on the cuticle will be combined with diffuse, spectrally dependent reflectance from within the leaf and canopy. In the near-infrared (nIR), leaves may be considered as Lambertian diffusers, in the visible domain, reflectance is strongly directional (Guyot 1990).

Canopy reflectance spectra were simulated using PROSAIL (explained in more detail in chapter 6) to illustrate the influence of leaf biophysical parameters (Wantzenrieder 2011). Figure 3.10 shows spectral variations of maize reflectances.

3.2.2.1 Leave’s pigments, leaf water and structure

For Chl_{a+b} (C_{ab} in the model), the most striking changes are as already described (Figure 3.2) to be found within the green peak area and the level of the minimum reflectance at the red spectral region. Similarly, the carotenoids (C_{ar}) induce changes of the level and shift the green peak from lower to higher wavelengths. Variations of the brown pigment content (C_{bp}) lead to an extinction of the green peak and a shortening of the red edge to the longer wavelengths with flattening slopes. The moisture content in maize leaves, introduces great shifts on the spectral signatures, increasing equivalent water content (EWT) fortifies the water absorption minima and the reflectance plateaus between these absorption areas. Dry matter content (C_m) and the leaf structure parameter (N) show opposing patterns: decreasing overall reflectance levels for C_m , and an overall increase of reflectance peaks for N .

3.2.2.2 Leaf area index

In dependences of the development and amount of biomass, the underlying soils influence the canopy reflectance quite strongly. Greatest impact on the spectral signature is therefore found by LAI at the green peak to short nIR and at midwave IR regions. When canopies are not closed as for vineyards or beginning stages in crop development, a substantial part of the reflected energy comes from background soils which adds to the reflectance curve especially in the nIR (Figure 3.10). With an increasing leaf area index towards a value of 3, the canopy is supposed to cover the underground and saturate the VIS signal, in the nIR a LAI of 5 is required (Guyot 1990).

Huete and Jackson (1988) showed that soil brightness strongly affected path radiance, leading to a greater atmospheric influence on darker soils, and rather greater atmospheric extinction on brighter soils. The soil background also varies with shaded cover, moisture state and litter fraction (Huete and Jackson 1988). Huete then introduced the soil-adjusted vegetation index to compensate that effect (Huete 1988, Huete et al. 1992).

3.2.2.3 Plant Geometry Effects

The orientation of leaves in relation to the stem may be categorised as follows:

- *planophil* i.e. horizontal inclination,
- *erectophil*, i.e. vertical inclination,
- *plagiophil*, i.e. mostly medium-sloped leaves,
- *extremophil*, i.e. only few leaves with medium inclination, and
- *uniform*, i.e. most leaves show are similar inclination (Kurz 2003, p.12).

Maize, for example, shows mostly erectophil leaves depending on the respective variety. Yet, not all leaves are oriented uniformly and leaf-angle-distribution may even vary during one day, e.g. when the plant orient towards the sun (sunflowers) when wilting occurs when moisture stress increases (Guyot 1990; Jensen 2007a). These attributes have been modelled by leaf inclination distribution functions (LIDF, Guyot 1990) or leaf-angle-distribution (LAD, Jensen 2007a) which model reflectance in relation to LAI. With increasing LAI, reflectance differences in the red/nIR domain increase considerably for different leaf angle distribution (Figure 3.10).

The phenological stages of crops and vegetation contribute to seasonal reflectance differences. When leaves develop they are of a lighter green and generally moister than mature leaves. The chlorophyll content develops within 80-90 days and then levels off just until harvest times, when senescence develops and leads to a yellowing or colouring

of the leaf (Poni et al. 1994, Jensen 2007a). Crop flowers also contribute to the reflectance signal as well as fruits. Depending on the viewing angle not all plant components will always be detected by the sensor.

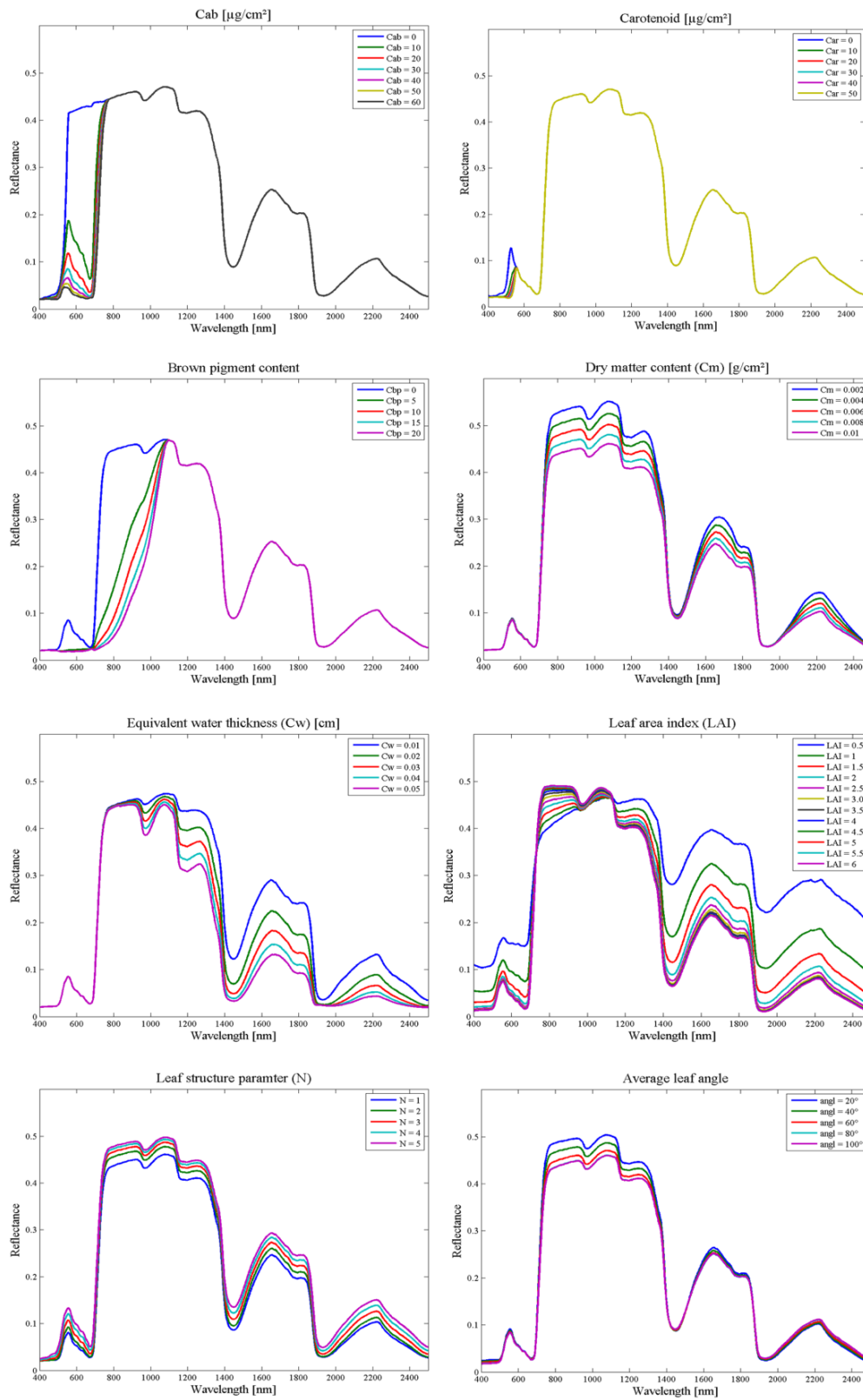


Figure 3.10 Effects of variation of Prosail biophysical input parameters on spectral signatures of maize

3.2.2.4 Soil Background Effects

Depending on the canopy closure, soil background is a major contributor to a vegetation stand's reflectance signal. Typically, soil reflectance is generally increasing from VIS to nIR/mIR wavelengths (see figure) and may well be discriminated from vegetation by utilizing the sharp increase along the red edge. However, senescent/dry vegetation also increases from VIS to IR wavelengths. Soil reflectance spectra vary with their water content, i.e. appearing of darker reflectance than dry soils, similarly organic content leads to darker signals. The mineral composition of soils also contributes to reflectance changes, clayey soils appear darker than more sandy, thus light-coloured soils and iron oxides give the typical red colour in the VIS. Similarly to plants, soil surface roughness strongly influences the bidirectional reflectance effects of soils (Jones and Vaughan 2010). Hyperspectral remote sensing can successfully discriminate mineral and organic components for dry soil samples (van der Meer et al. 2012).

3.2.2.5 Row Orientation and Density

Row structures of crops introduce additional variability on the reflected signal. Depending on the sensor – sun viewing geometry, bi-directional reflectance differences (see chapter 7), illumination and shading and part of visible soil may vary considerably. Here the row orientation, canopy height and inter-row-distance will influence the amount of canopy, shadow and background visible in the image (Zhao et al. 2010, Yan et al. 2012).

This effect has been analysed as early as the 1980ies, where Suits (1983) showed how the reflectance of wheat is affected by row structure modulations to uniform canopy models (Figure 3.11). As the contrast of soil background reflectance and the green reflectance within the chlorophyll absorption ranges is highest, it is there that the strongest BDR-effect is found.

Several row-models describing radiation transfer were developed in the past: The Geometric-optical model of BDRF (GO-model) by Li & Strahler (1985), Kuusk (1995) developed the Markov-Chain Canopy Reflectance Model (MCRMrow) which has been applied by coupling it with PROSPECT-SAIL-FLIM to predict grapevine canopy Chl (Zarco-Tejada et al. 2004), España et al. (1999) generated a plant and canopy 3D maize model and combined it with a ray tracing model to obtain canopy reflectances.

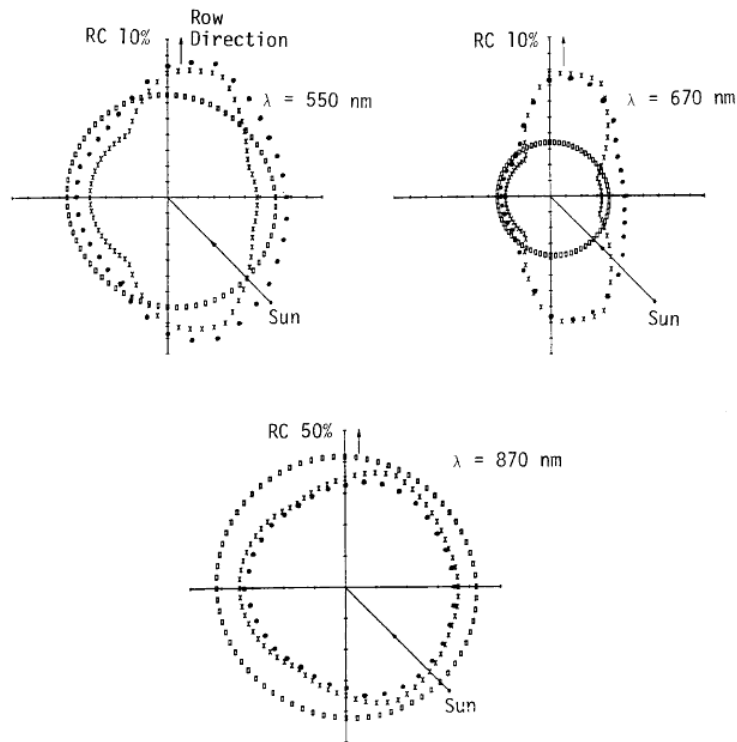


Figure 3.11 Reflectance (RC) polar plots of a uniform canopy model (o), a row model (•) and the Verhoef-Bunnik rectangular prism model (x) of wheat (Suits 1983, p.123)

Zhao and co-authors only recently developed a 3D row reflectance model to study bi-directional reflectance for hedgerow geometries (Zhao et al. 2010). Within the rectangular design of the rows, the row model, requires input on sun-sensor viewing geometry, canopy parameters (row distance, width, height, and orientation, foliage dimension, LAI, LIDF), and optical parameters such as the hemispherical leaf reflectance, transmittance, the hemispherical reflectance of soils and the ratio of direct to overall irradiance (Zhao et al. 2010).

Figure 3.12 illustrates the bi-directional reflectances for the red (left) and nIR (right) wavelengths and N-S-oriented wheat rows of different development stages. As expected, the effects in the VIS are greater than in the nIR, clearly indicating a bright stripe parallel to the row orientation for the well-defined row structures at early wheat development stages at the red and a darker stripe in the nIR, an influence that decreases with canopy closure (Zhao et al. 2010).

Recently, Yan et al. (2012) extended the GO model of BDR by using a leaf clumping index which may not only be applied to discrete but also to continuous vegetation covers of various types as the BDRF is shown to be driven by the areal component of a) illuminated versus shaded leaves and b) visible illuminated versus shaded background.

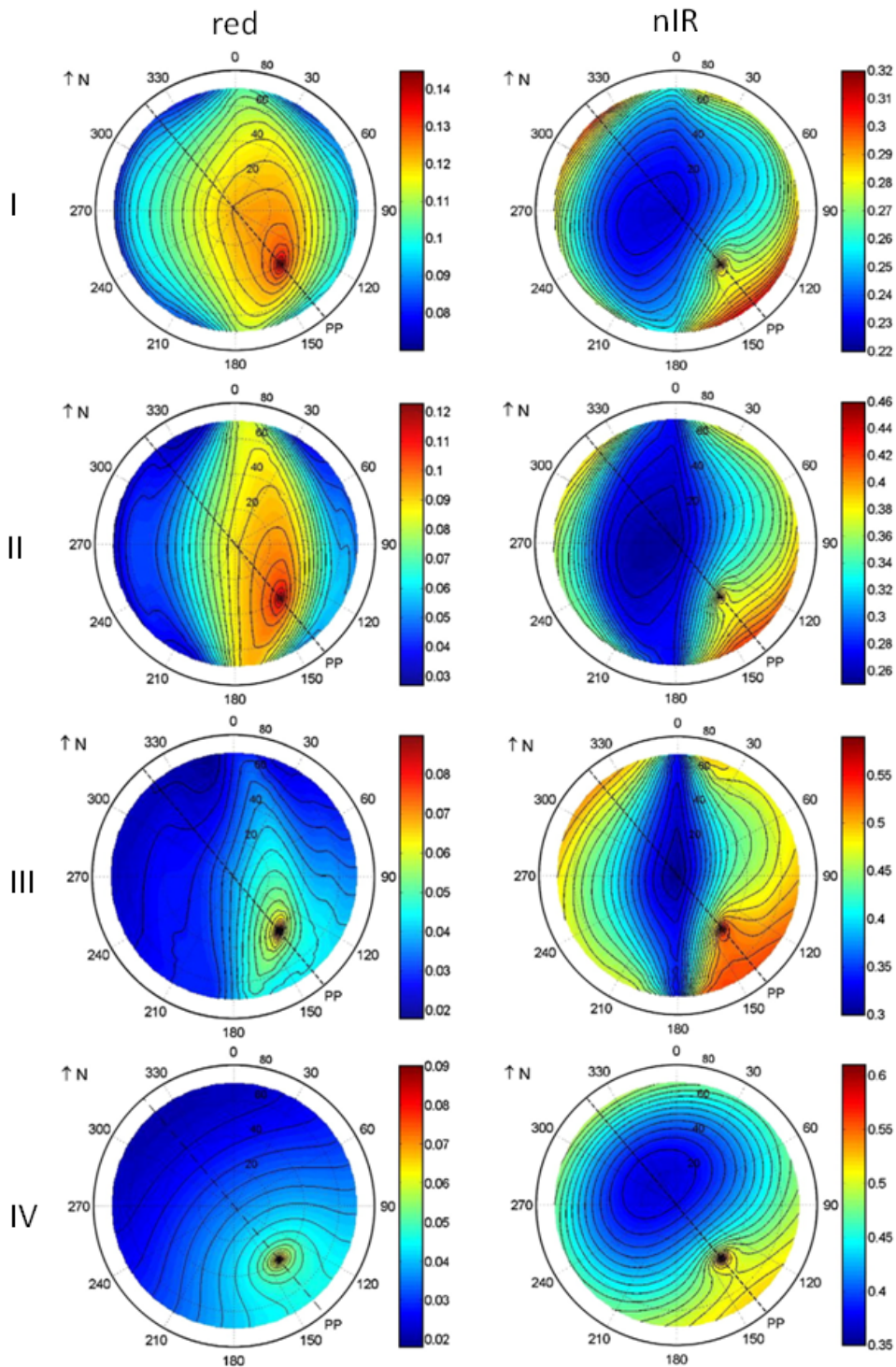


Figure 3.12 Polar plots of directional reflectances in the red (left) and nIR (right) retrieved by the row model for four wheat growth stages (I: sparse, II: low, denser canopy, III: well-developed canopy with less inter-row soil cover, III: homogenous canopy) (modified by Haho e Zhao et al. 2010)

3.3 Thermal Remote Sensing of Vegetation

Thermal infrared (TIR) radiation emits from 7 to 18 μm wavelengths and is also called emissive infrared or far infrared. For these wavelengths information on the thermal properties and surface temperatures may be derived (Campbell and Wynne 2011). As thermal remote sensing in this work was applied only qualitatively, only a brief summary of broad-band thermal sensing (8-13 μm) is given here. For a more detailed overview please refer to Jensen 2007a; Jones and Vaughan 2010, and Campbell and Wynne 2011.

3.3.1 Thermal Properties of Vegetation

According to the Stefan-Boltzmann-Law, thermal radiation of a surface depends on its emissivity and temperature:

$$E = \varepsilon\sigma T^4 \quad (3.2)$$

With:

E: thermal energy [Wm^{-2}]

ε : emissivity

σ : Stefan-Boltzmann constant $5.67 \cdot 10^{-18}$ [$\text{Wm}^{-2}\text{K}^{-4}$]

T: absolute temperature

The kinetic temperature is the relative warmth of an object and is measured by thermometers. Thermal sensors measure the radiant or apparent temperature (Campbell and Wynne 2011).

3.3.2 Canopy Emissivity

Natural and vegetation surfaces are neither blackbodies ($\varepsilon = 1$) nor greybodies (objects emitting thermal radiation equally at all wavelengths with an $\varepsilon < 1$). Typically ε of vegetation features range between 0.94 – 0.99 and its knowledge is crucial for the determination of an object's temperature. In the field, ε is derived by accurately measuring a surface's temperature and either also the background radiation or eliminating the background radiation by putting the object into a highly reflecting box (Rubio et al. 2003). The authors also generated an emissivity database for the range of 8-13 μm for various vegetation samples. The emissivity of a total canopy is generally greater than that of a leaf sample due to multiple reflection of thermal radiation.

$$L = \varepsilon\sigma T_{leaf}^4 + (1 - \varepsilon)\sigma T_{leaf}^4 = \sigma T_{leaf}^4 [\text{Wm}^{-2}] \quad (3.3)$$

With:

- L: thermal radiation [Wm^{-2}]
- ε : Stefan-Boltzmann constant $5.67 \cdot 10^{-18}$ [$\text{Wm}^{-2}\text{K}^{-4}$]
- T: absolute temperature

Following equation (3.3), emissivity approaches 1 and as Rubio et al. (2003) have shown, ε varies between 0.98 and 0.99 when dense canopies are measured.

However, several other effects may affect emissivity values:

- Dryness and age of vegetation (see above)
- LAI and leaf angle distribution (Guoqan and Zhengzhi 1992)
- IFOV (Ribeiro da Luz and Crowley 2007, Jones and Vaughan 2010).
- Viewing angle and directional effects of varying amounts of objects with potentially different ε

The impact of LAI and LAD on emissivity has been studied by Guoqan and Zhengzhi (1992), the authors found that with increasing canopy density, the apparent emissivity increases, too (Figure 3.13).

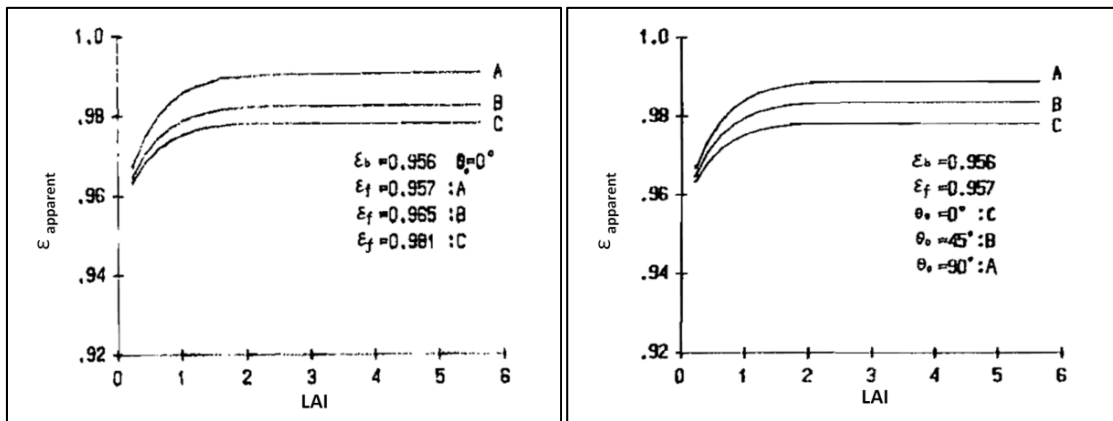


Figure 3.13 Affect of LAI (left) and leaf angle distribution (right) on apparent emissivity of a vegetation canopy (mod. from Guoqan and Zhengzhi 1992)

Similarly, when increasing the IFOV (Figure 3.14), the amount of canopy components seen by a thermal sensor increases, collecting a mixed signal of leaves, cavities, and stems which also lead to an assimilation of apparent ε towards an emissivity of a black-body (Ribeiro da Luz and Crowley 2007, Jones and Vaughan 2010).

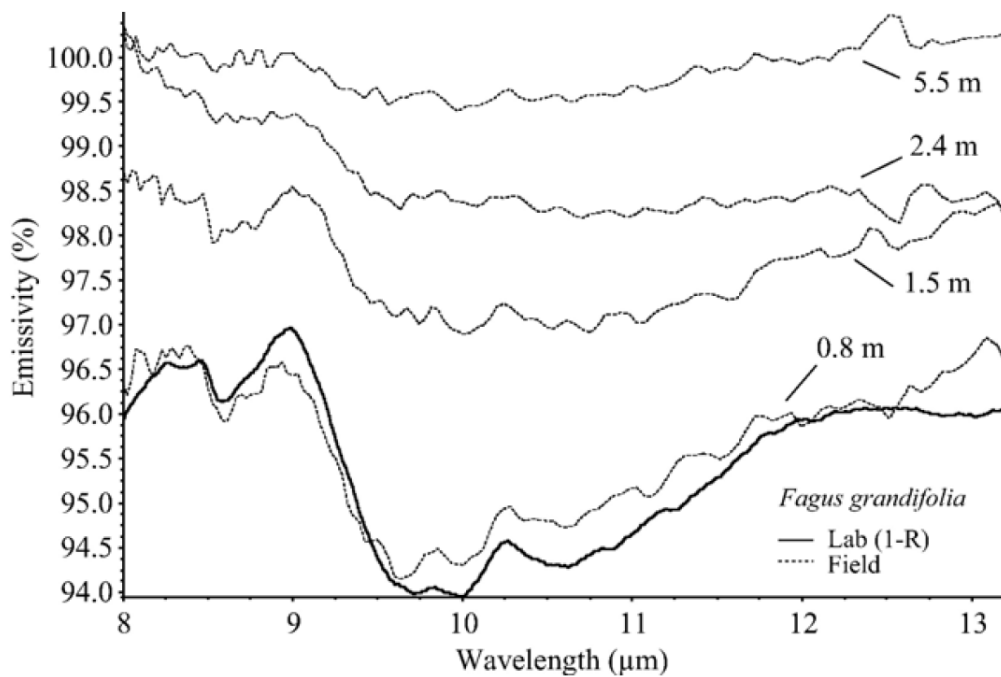


Figure 3.14 Changes in apparent emissivity with viewing distance [m] in relation to wavelength (Ribeiro da Luz and Crowley 2007)

Otterman et al. (1995) note that “sun and wind directions and the thermal and structural characteristics of the plants” (1995, p. 170) alter canopy thermal temperatures. Thermal radiation is strongly anisotropic and for agricultural crops may vary with viewing azimuth from 4 K to 13 K for sunflowers due to varying amounts of soil background radiation in the TIR signal (Jones and Vaughan 2010). Sun azimuth location has been reported to vary canopy temperatures up to 2°C under calm wind conditions (Kimes 1983,

Emissivity also changes with plant age, as can be visualised from the MODIS UCSB Emissivity Library (Zhang 1999). Vigorous vegetation has a high ϵ due to its water content and cell structure, when senescing, the emissivity becomes more variable (Figure 3.15)

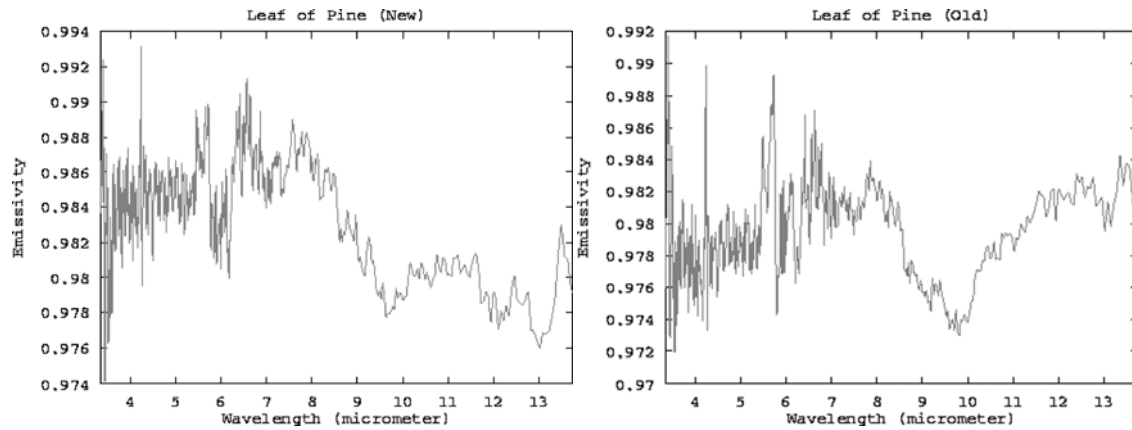


Figure 3.15 Emissivity spectral of young and old pines (MODIS UCSB Emissivity Library, <http://www.ices.ucsb.edu/modis/EMIS/images/pinenew.gif> and [pineold.gif](http://www.ices.ucsb.edu/modis/EMIS/images/pineold.gif), access date 28/04/2015)

3.3.3 Influence of Background

In environmental applications, a thermal sensor detects not only the target's energy but also the reflected component of emitted background energy, its alterations by transmitting atmosphere as well as radiation from the intermediate atmosphere itself (Jones and Vaughan 2010).

$$L = \tau[\varepsilon\sigma T_{target}^4 + (1 - \varepsilon)L_{background}] + L_{atmosphere} \quad (3.4)$$

With:

- τ : transmissivity
- ε : emissivity
- σ : Stefan-Boltzmann constant $5.67 \cdot 10^{-18} [\text{Wm}^{-2}\text{K}^{-4}]$
- T_s : absolute temperature

The thermal inertia P of objects is given as

$$P = \sqrt{K Cp} \quad (3.5)$$

With:

- K : Thermal conductivity [$\text{cal} \cdot \text{cm}^{-1} \cdot \text{sec}^{-1}$]
- C : Heat capacity [$\text{cal} \cdot \text{gram}^{-1} \cdot ^\circ\text{C}^{-1}$]
- p : density [$\text{gram} \cdot \text{cm}^{-3}$]

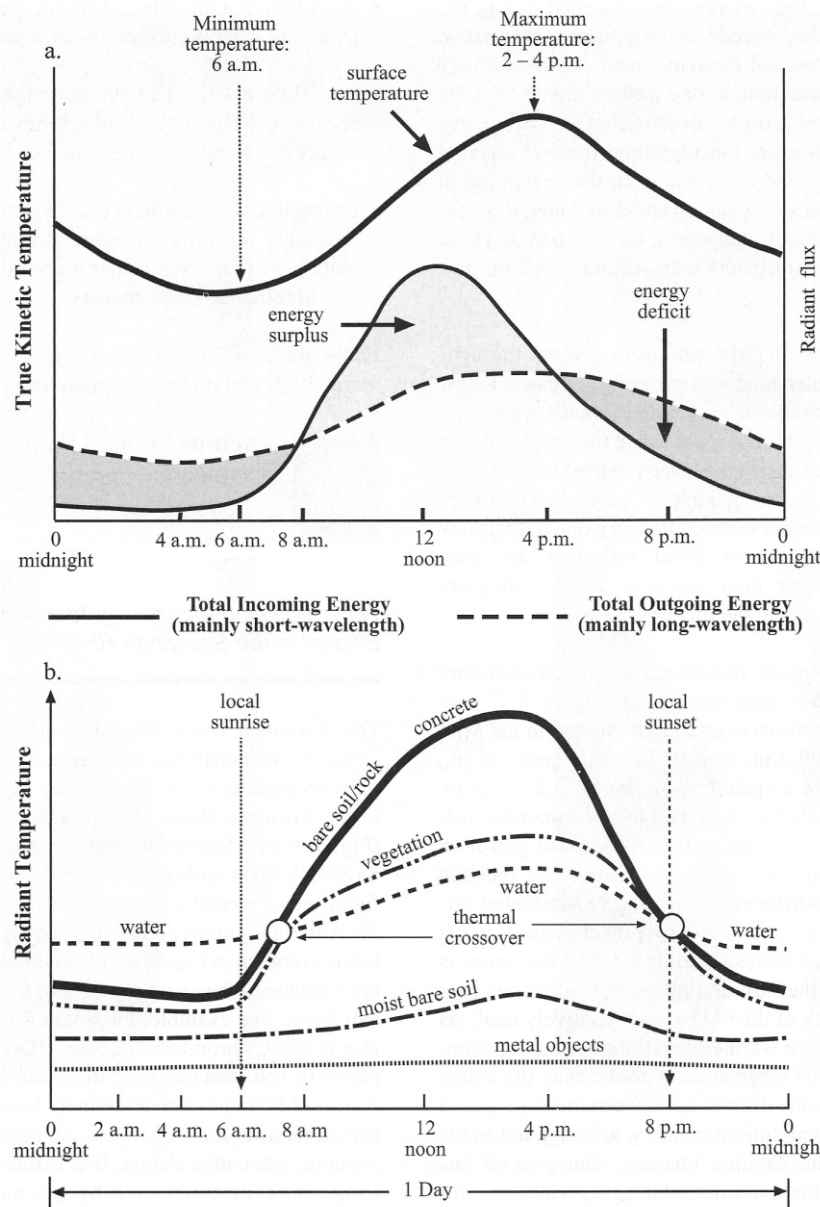


Figure 3.16 Diurnal course of radiant and kinetic temperature for different surfaces (Source: Jensen 2007a, p.725)

Figure 3.16 illustrates the diurnal thermal behavior of key surface materials. There is a lag of maximum temperature reached in relation to noon due to thermal inertia and similarly for the minimum temperatures. By differencing thermal images from the hottest (2-3 hours after maximum sun position) and coolest (just before dawn) diurnal times, thermal inertia P may be derived (Campbell and Wynne 2011).

4 UAS, Sensors and Data

This section will focus on equipment selected for this work. The used UAS will be described in more detail as well as the sensors used with this vehicle. For the agricultural applications, a hyperspectral sensor small enough (<1 kg) was not yet operationally available, so a multispectral six-band camera array had been acquired with the UAS. Furthermore, a thermal camera, and for archaeological studies, additionally a standard digital single lens reflex (DSLR) camera were applied in this work. The section ends with a description of other data sources and field devices.

4.1 UAS: The md4-1000 Quadcopter

At the end of 2010, the Department of Environmental Remote Sensing and Geoinformatics purchased a light-weight UAS which should be able to hover over sites of specific interest. As a stable and operational VTOL-system, a md4-1000 quadcopter (microdrones GmbH) with a carrying capacity of ~ 1.5 kg and a take-off weight of 5 kg was chosen. The size of the vehicle is about 170 cm x 170 cm x 50 cm with extended rotors (Schübeler and Eickhoff 2010).



Figure 4.1 The md4-1000 with base station (photos: J. Besold 2011)

The UAS consists of a carbon-fibre built vehicle, a base station and a remote control. The md4-1000 has four brushless rotors that move pairwise with counter-rotation (Figure 4.2).

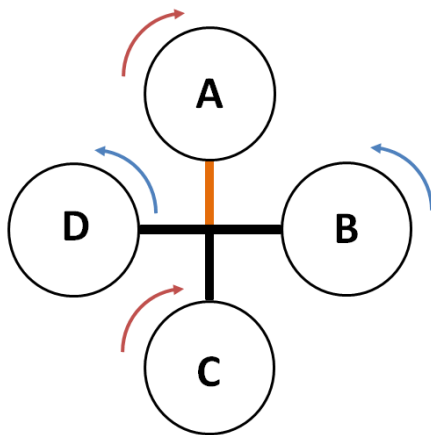


Figure 4.2 Rotor movement with the md4-1000 (microdrones GmbH 2008-2010)

The vehicle mounts with acceleration of all motors, hovers by equal speed at all rotors, flies forward by tilting along the lateral axis (pitch) and slowing down the front motor, and moves sideways by a change of speed between the motors aside of the longitudinal axis and vice versa. Power is supplied by a 22.2 V Lithium-Polymer battery allowing flight duration of about 20 minutes with camera weights of approximately 1 kg.

The drone position is steered by GPS based on the Global Navigation Satellite System (GNSS) and an IMU with a barometric height stabilization by fusioning different position sensors through a Kalman-filter.

The drone and camera triggering is carried out by a Multiplex remote control (Royal Pro 9) using a 35 MHz band for communication with the vehicle. Alternatively, the pilot may use waypoint navigation by programming flight routes and camera tasks using the proprietary software mdCockpit (Figure 4.3), which is also used for

- Waypoint editing,
- Downlinking of telemetry data
- Flight data recorder and analysis
- Communication with and parameterizing of the UAS.

Waypoint editing with the current version uses NASA/ESA's Shuttle Radar Topography Mission (SRTM) data for terrain input and either Google or user-defined georeferenced maps as the basis for route editing (microdrones GmbH 2007-2013).

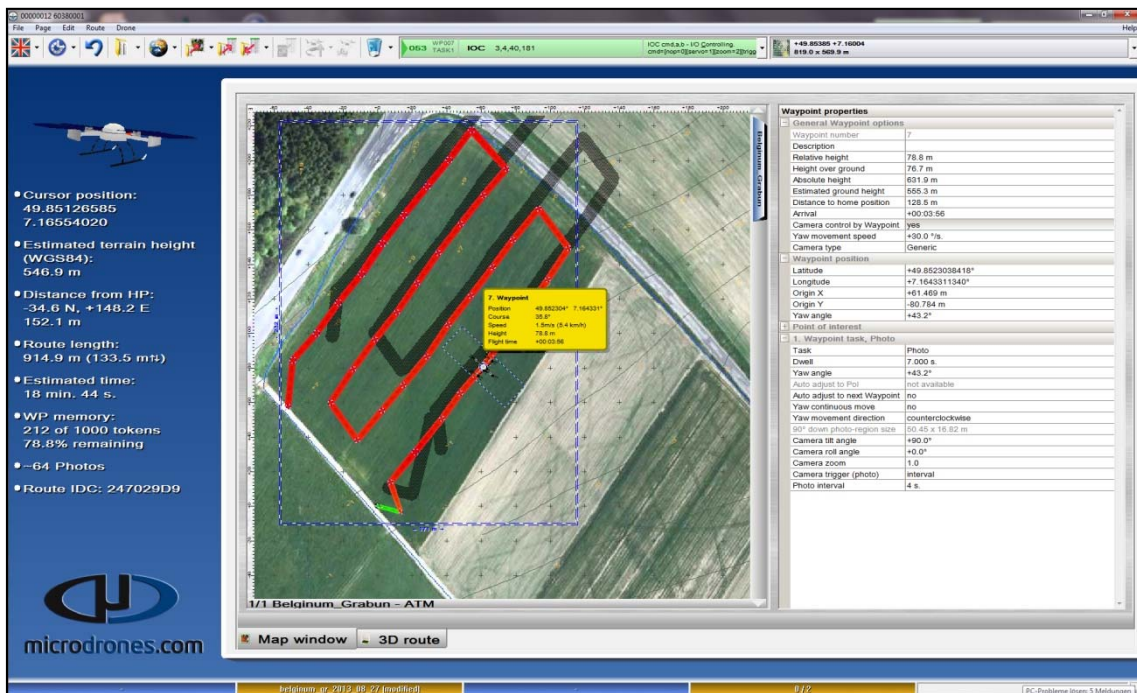


Figure 4.3 mdCockpit 3.2 Waypoint editor (microdrones GmbH 2007-2013)

Downlink decoding during the flight enables the ground crew to check on vehicle movement (positioning, height, speed, wind speed, etc.) and functioning (route, energy supply, motors, RC, payload, wind, GNSS, a.o.) and corresponding alerts and control of video signals (Figure 4.4).



Figure 4.4 Ground station device

Flight recorder data is written to a microSD-card functioning as a kind of “blackbox” supporting flight parameter analysis. The photo positions and attitude parameters as well as the GNSS and IMU data may then be exported to text/spreadsheet files for further references (Figure 4.5), the flown route may be exported to KML files for visualising flights on the terrain. Horizontal positioning accuracy varies with flight speed and number of GNSS satellites availability and mostly lied within 1.5 to 3 m accuracy.

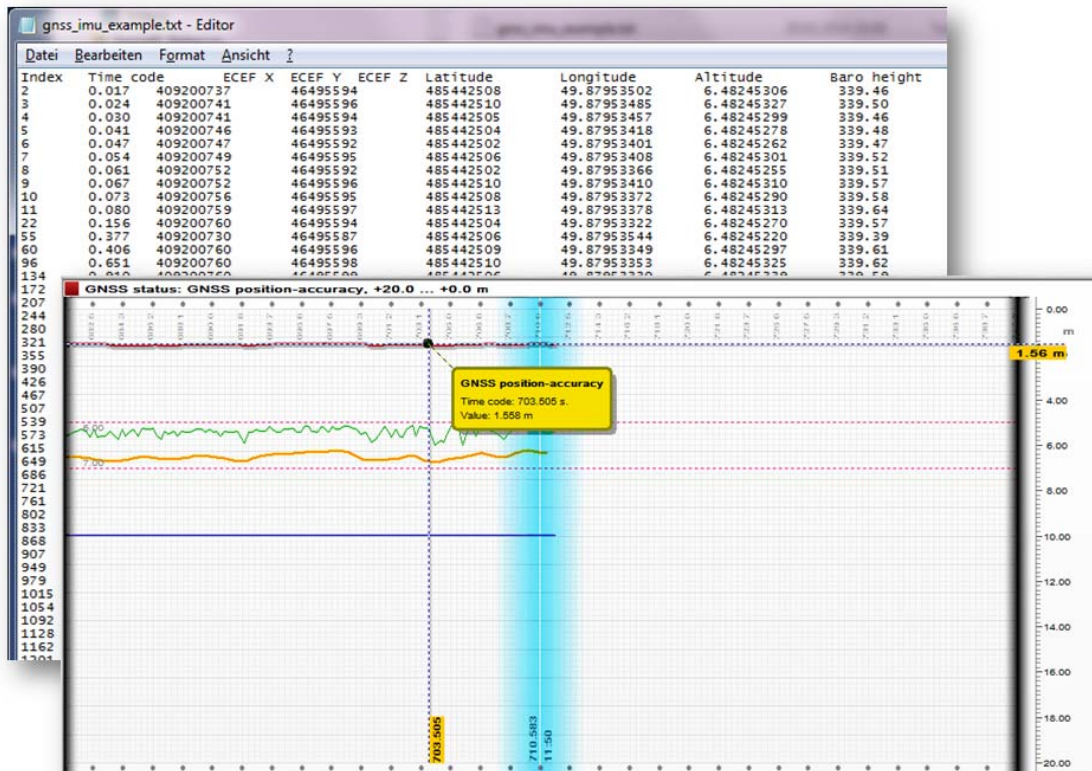


Figure 4.5 GNSS and IMU data text files and positional accuracy as given by flight recorder data

4.2 UAS Cameras

4.2.1 Digital Single Lens Reflex Camera: D3100

The Nikon D3100 was obtained in 2010 and has a resolution 14.2 megapixels (4608 x 3072 pixel). The sensor is an APS-C size CMOS sensor (Complementary Metal Oxide Semiconductor) with a size of 23.1 x 15.4 mm (Nikon Inc. 2011). Light is filtered into the primary colours red, green and blue onto the sensor by colour filters (Bayer or interference filters) and stored as 8-bit x 3 radiometric values (Figure 4.6).

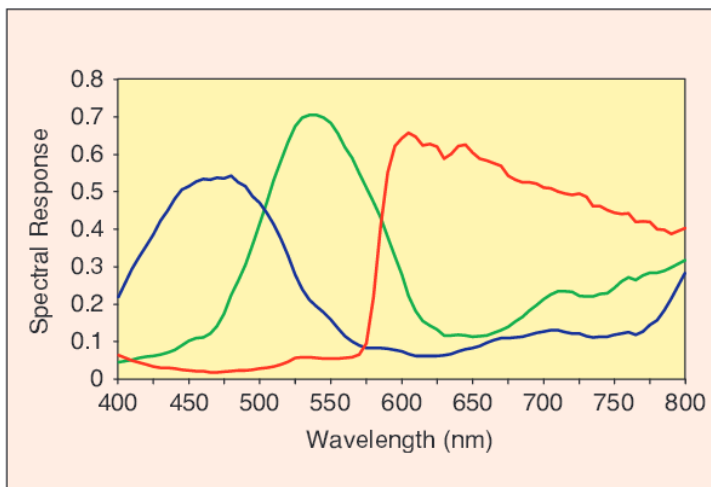


Figure 4.6 Spectral response of a CMOS sensor (mod. El Gamal and Eltoukhy 2005)

The camera is mounted by a carbon-frame (Figure 4.7) with two servo-motors which may be rotated in pitch direction (0° looking horizontally in flight direction, 90° nadir viewing) and along a roll axis to balance positional inclinations of the drone. The camera has an instant return lens aperture, exposure times may range from 1/4000 to 30 s.



Together with the wide angle lens AF-S DX NIKKOR 10-24 mm (1:3.5-4.5G ED) it weighs about 970 g (Nikon Inc. 2011). Images are stored as RGB either RAW or JPEG of varying resolution.

Figure 4.7 Nikon D3100 with wide angle lens

4.2.2 Multispectral Sensor: Mini-MCA-6

A multispectral sensor was to be selected in autumn 2010, when the Department of Environmental Remote Sensing & Geoinformatics bought the quadcopter. At that time, the weighing-off between camera weights (< 1 kg), reasonable spectral resolution and costs resulted in obtaining a multiple camera array system, the Mini-MCA6, developed by Tetracam Inc., USA.

The low-cost multiple camera array has been developed in 1993, weighs approximately 780 g and consists of six individual x-mount lenses equipped with 25 mm (1") diameter spectral band-pass filters (Tetracam Inc. 2011). In 2010, the camera was delivered with a front-filter mounting system (Figure 4.8).



Figure 4.8 The Mini-MCA6 with front-filter mounting (photo: © Tetracam Inc.)

The camera lenses then had a focal length of 8.3 mm (f/3.2) and were equipped with spectral 10 nm-bandwidth filters. The sensors used are CMOS sensors with a respective size of 6.66 mm x 5.32 mm with 1280 x 1024 pixels resulting in approximately 5.2 μ m x 5.2 μ m effective pixel size. The radiometric resolution may be user-defined to 10-bit or 8-bit data. The sensor's spectral response culminates about 800 nm with a total range from approximately the visible (Vis) blue to nIR wavelengths. Figure 4.9 illustrates the sensor's monochrome response and the location of filters applied in this context. The curve shows a rather steep sensitivity drop-off to the lower and higher filter wavelengths of transmissions ranging from 50-70%. Yet, the camera's exposure rates may be adjusted accordingly in relation to the master channel.

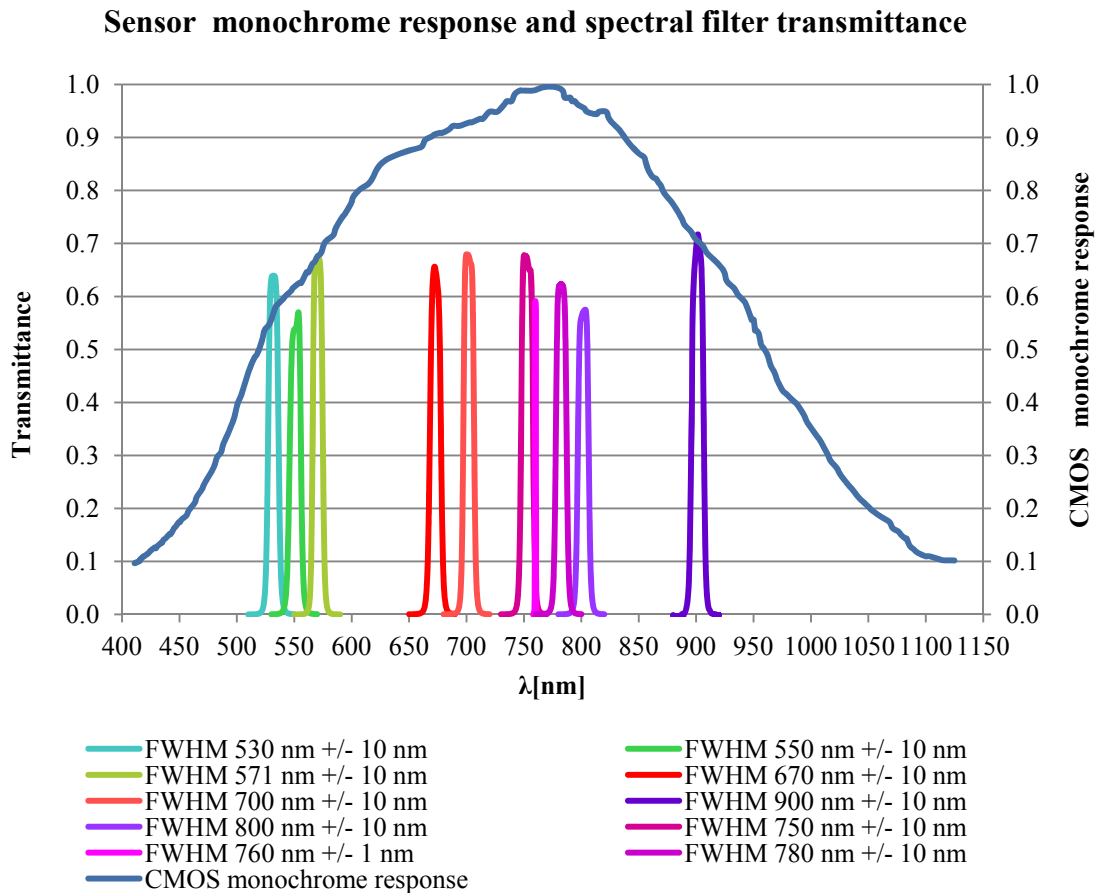


Figure 4.9 Spectral sensitivity of the Mini-MCA-6' CMOS sensor (modified from Tetracam Inc.) and filters (filter transmission as supplied from producer)

After a front-to-rear filter change at the end of 2011, the Mini-MCA6 had a focal length of 9.6 mm with a slightly elevated luminous intensity of f/2.8 (Figure 4.10).

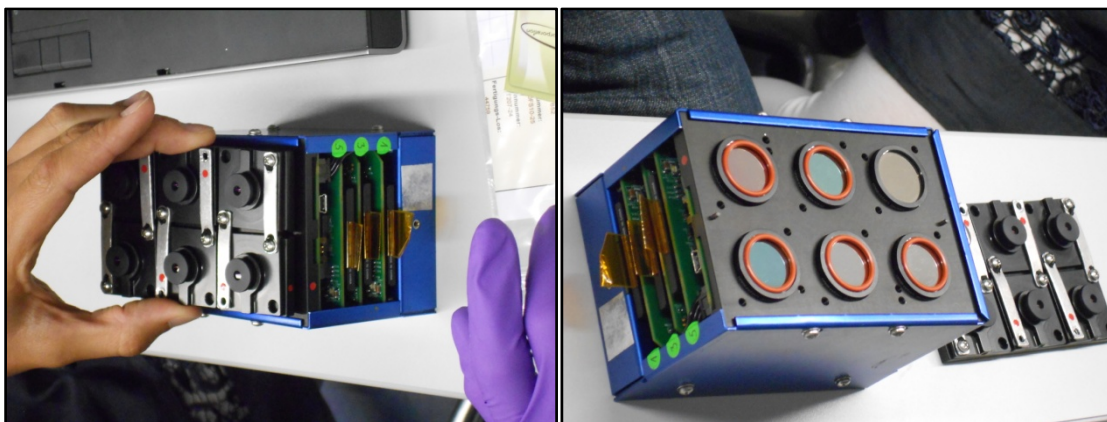


Figure 4.10 Mini-MCA-6 with front-to-rear filter rebuilt (left) with filters put behind the lens plate to facilitate filter access and change (right) (Photographs: M. Perez Saíz)

Each camera stores its images on standard 2 GB ScanDisk Compact Flash memory cards and may be downloaded by USB connection. The image capture rate takes 3-5 sec for the single shot mode, and 1.3 frames/sec in burst mode (Tetracam Inc. 2011). Exposure settings are either carried out by control box and video device or through a USB interface within the processing software PixelWrench supplied with the camera.

Thus, for automatic or fixed exposure, the progressive shutter allows exposure ranges from 0.5 to 20 msec. Time to save images to disc requires 2 sec for 10-bit RAW images and up to 5 sec for DCM mode. Further settings allow the alteration of sensor gain and/or relative exposure of individual cameras in relation to the master band. In this case, the master band is camera no. 0 equipped with the 570 μm 10nm-FWHM Andover filter.

4.2.3 Thermal Camera: Un-Cooled Module (UCM)

The UCM (UnCooled Module, Figure 4.11) had been bought at the end of 2011 as a light-weight, robust thermal camera to be used with the md4-1000 quadrocopter. The camera had been developed by Carl Zeiss Optronics as an easy-to-use and fast thermal microbolometer for mostly military operations. It records in the longwave infrared region from 7-14 μm with a thermal sensitivity of 90 mK and an image size of 640 x 480 pixels. The camera was delivered without housing so that a casing had to be built at the department. The UCM is 95 x 48 x 48 mm large and weighs 170g (Carl Zeiss Optronics GmbH 2011).



Figure 4.11 The thermal camera UCM (photo: G. Rock 2011)

Before image acquisition, all pixel values need to be calibrated to ensure identical gain and offsets by taking a picture of a homogenous background (*i.e.* lens-lid). The thermal

camera's lens has a focal length of 10 mm with quite strong barrel distortion (Figure 4.12). The image capture rate is 50/60 Hz and the storage comprises only up to 20 images per flight, at snapshot mode 50 images. Images are either stored to BMP or JPG format (Carl Zeiss Optronics GmbH 2008).

During image capture, the grey-value stretch is automatically optimized for each image. This renders image processing somewhat cumbersome as image-to-image equalization techniques need to be used in post-processing.

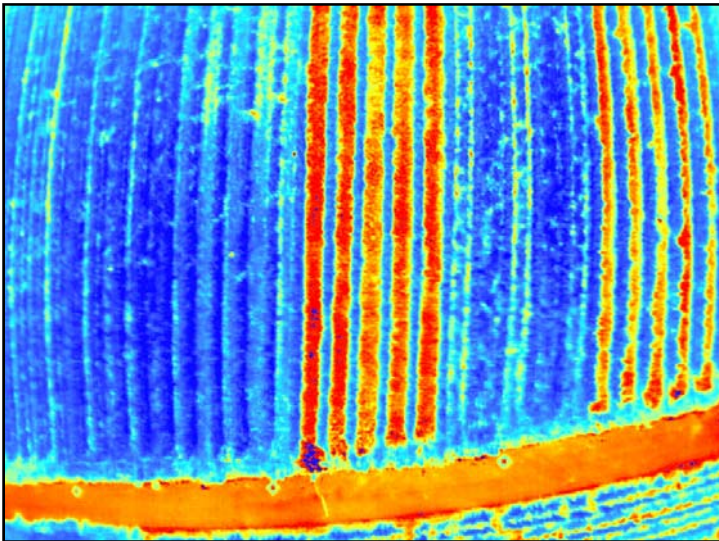


Figure 4.12 Thermal image (7-14 μm) of a vineyard taken with UCM

In this work, the UCM was mainly used for qualitative thermal description of study sites.

4.3 Reflectance Measurements: Spectroradiometer

In addition to the UAS data, reference reflectance measurements of grayscale reference panels and vegetation parameters were made using a FieldSpec Pro 3 Max spectroradiometer (ASD Inc., Boulder, CO, USA) kindly supplied by the Luxembourg Institute of Science and Technology (LIST), Luxembourg.

The FieldSpec acquires spectral measurements within the range of 350-2500 nm with sampling intervals of 1.4 nm up unto 1000 nm and 2 nm for the following wavelengths. The spectral resolution is ~ 3 nm @ 700 nm. A fibre optic collects the data with a 23° FOV. Reflectances are calibrated by using a 10 x 10 inch Spectralon[®] device with a known reflectance of almost 100% (Figure 4.13).

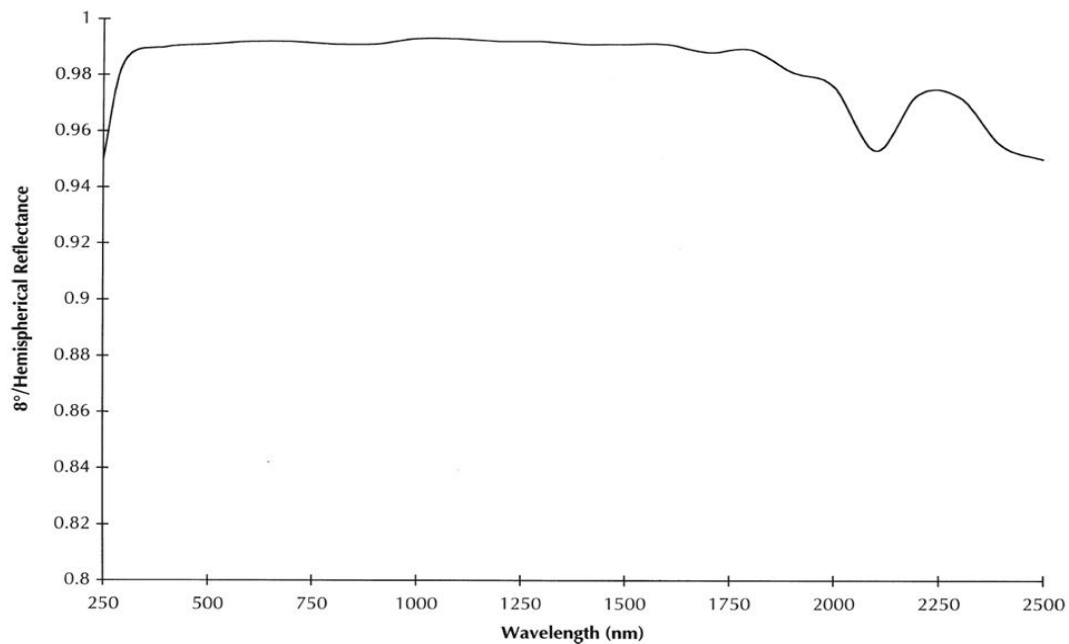


Figure 4.13 Spectralon reflectance (white reference) developed by Labsphere Inc., North Sutton, NH, USA.

For leaf measurements, a leaf-clip device was used. Laboratory measurements were carried out using a ProLight video lamp. Generally, 3-15 spectra were averaged for each target (with 50 measurements for dark noise, 50 measurements for the target and ...). These individual spectra were later averaged to a mean spectrum. To compare the FieldSpec reflectances to data derived from the multispectral camera, spectra were resampled to the FWHM spectral band widths x spectral response of the miniMCA-6 cameras using ATCOR4 (Richter 2010).

4.4 Field Measurements of Plant Parameters

4.4.1 Leaf Area Index

LAI or rather foliage area index measurements were carried out with a LAI-2000 Plant Canopy Analyzer (LI-COR Inc. 1992, p.2-9) which measures the amount of foliage within a FOV (below canopy) compared to a fully unlimited FOV (above canopy). The optical sensors measure light attenuation within five concentric rings from the zenith 0-13° to 18-28°, 32-43°, 47-58°, 61-74° (LI-COR Inc. 1992). The above-canopy sensor is typically set up in remote mode and measure the sky each 30 seconds. At the beginning

both sensors are connected to one data logging device, started simultaneously, and calibrated to ensure similar measurement values.

Depending on the measurement environment, parts of the FOV may be masked by use of view caps put onto the sensors to avoid false readings. Measurements should be carried out at cloudy conditions or without exposition to direct sun light to avoid underestimation of LAI. Measurements were recomputed to means per location for the respective amount of concentric rings required using the appropriate canopy model in the FV2000 processing software (LI-COR Biosciences).

4.5 Chlorophyll Measurements

4.5.1 Wet-chemical Analysis

For the sensitivity analysis, the following plant physiological parameters were derived: dry weight, water content and Chl content. For Chl analysis, leaves were taken in-situ, wrapped into aluminum foil and transported to the laboratory in a cooling bag. From each leaf, standardized punch discs of known size were retrieved and of each leaf 200 mg fresh matter mixed with 5 ml methanol. The solution was heated for 25 minutes within a 60°C water bath to solve Chl_{a+b} . Once solved, the liquid is put into a photometer UV-160A (Shimadzu, Japan) to estimate Chl content by relating absorption at $\lambda = 665$ nm and $\lambda = 650$ nm. Chl content [mg/g] was then calculated as follows:

$$Chl_{total} = \frac{MeOH (A_{665\text{ nm}} * 4) + (A_{660\text{ nm}} * 23.5)}{weight_{freshmatter}} \quad (4.1)$$

With:

MeOH: methanol content [mg]

A: absorption at specific wavelength

4.5.2 Chlorophyll Meter SPAD-502

The SPAD-502 () is a relative chlorophyll meter developed by Konica Minolta (Konica Minolta Sensing Inc. 2009). It has been used as a comparative measurement device to laboratory wet-chemical analysis. Two LEDs emit light in the red (650 nm) and NIR (940 nm) and of the incoming transmitted light, their ratio is being calculated as an indicator of chlorophyll content (eq. 4.2). Data in this study were not calibrated any further.

$$M = \log [t_{940} * t_{v,650}/t_{650}*t_{v,940}] \quad (4.2)$$

Where t_{nm} is the transmission of light through a leaf at that wavelength, and $t_{v,nm}$ is the control light beam stored as DN (Markwell et al. 1995).



Figure 4.14 The SPAD-502 chlorophyll meter

4.6 GPS Measurements

For georeferencing ground control points and sampling sites, two types of GPS were used: a differential Trimble GPS, and in some cases hand-held Garmin GPS, both using the GPS satellites.

The Trimble GPS GeoXT is part of the GeoExplorer 2008 Series and comes with a beacon and a GPS antenna. The ArcPad-based hand-held receiver is connected to the beacon via LAN or Bluetooth and is ideally receiving signals from an external correction source (radio). If no external emitting station is available, post-processing differential correction in the office was carried out by replicating source signals with measurement times. The GPS antenna was generally worn with a pole on a backpack with a known height difference. Generally, 50 to 200 measurements per location were averaged to one position by trading off accuracy versus number of measurements (Trimble Navigation Limited 2008). Using EVEREST multipath rejection technology, sub-metre accuracy may be retrieved.

For orientation purposes and navigation to sampling sites, hand-held Garmin 60CSx GPS with an accuracy of up to a couple of metres were used (Garmin Ltd. 2007). All measurements were made in WGS84 coordinates. As in this work no photogrammetric

objectives with highest spatial accuracy were neither aspired or required, the GPS set-ups with their rather rough geocoding capabilities within several decimeters (Trimble) to a couple of meters (Garmin) were adequate for georeferencing aerial image mosaics.

5 Radiometric and Photogrammetric Preprocessing of Aerial Image Data

The last chapter gave an overview over UAS sensors as well as spectral data sensors used for this work. Following camera calibration, time series of aerial imagery require the correction of radiometric differences in illumination and atmospheric conditions. Common preprocessing steps necessary for format conversion from raw to other DIP formats, radiometric calibration and correction of atmospheric effects used in this study are presented. Subsequent to the radiometry issues, ways forward for georeferencing and (ortho-)mosaicing of aerial images will be given.

5.1 Systematic Camera Errors

Common camera error sources which have been tackled in this context will be described focusing on the UAS sensors used. As a complete survey of all error sources surrounding aerial cameras is out of scope in this context, the reader is referred to photogrammetric literature for further reference (Kraus 1996; Mikhail et al. 2001; Kraus 2004, Aber et al. 2010).

Kelcey and Lucieer (2012) have in detail described the radiometric characteristics and error sources with respect to the MiniMCA-6 and described ways forward in correcting the respective sensor errors. The following sections documents how the MiniMCA-6 and Nikon DSLR data were calibrated and corrected for further processing and analysis for this study.

5.1.1 Camera Interior Orientation

Ideally, a photograph is a centrally projected image of an object. The interior orientation is the internal geometry of a camera at image capture (Figure 5.1), and is commonly described by the principal point (PP), the focal length f or camera constant c , if any, fiducial marks, originating in the fiducial centre (FC) and lens distortion parameters. Its projection centre is supposed to lie in the distance c (or focal length f) in front of the principal point on the image or focal plane (Mikhail et al. 2001; ERDAS Inc. 2010).

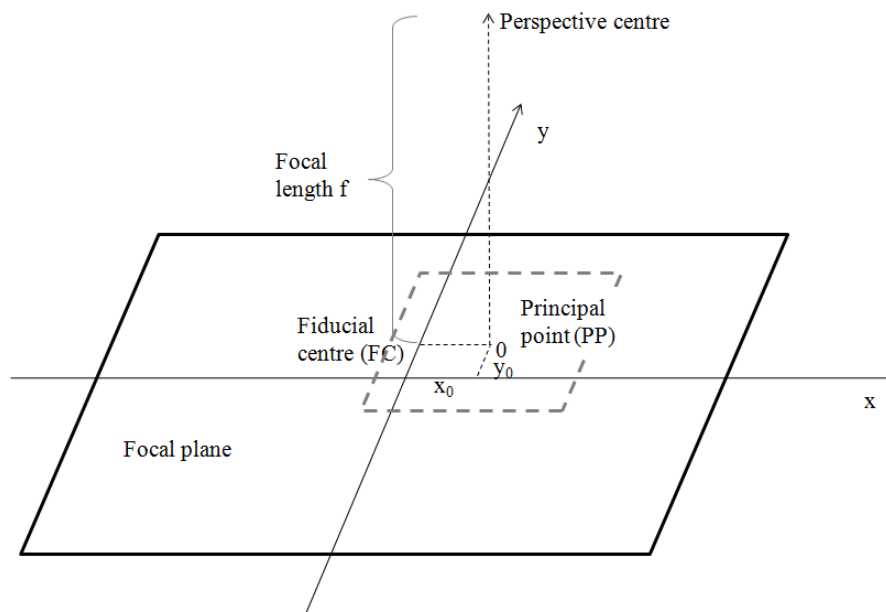


Figure 5.1 Interior orientation parameters (modified from Mikhail et al. 2001, p.21)

When image coordinates are shifted to the principal point ($x - x_0, y - y_0, -f$), the coordinates retrieved are the image space coordinates or sensor coordinates, generally given in μm or mm , and describe projected positions inside the camera. These are to be related to the object space or ground coordinate system, describing the regional coverage of an aerial photograph on the ground. They are Cartesian systems and may be latitude, longitude, height-based or datum-based (Mikhail et al. 2001, ERDAS Inc. 2010).

5.1.2 Lens Distortion

Camera lenses are prone to various lens distortions. Ideally, the central ray in Figure 5.2 shows the same angle between object point | optical axis and image point | perspective centre. In reality, modern lenses mostly show a symmetric quadratic radial distortion around the optical axis and the mechanical image size deviates from the optical image size. This leads to mapping of straight lines in nature as curved lines in the image (Kraus 2004, p. 48, ERDAS Inc. 2010), the radial distortion Δr .

$$\Delta r = r - f \tan \alpha \quad (5.1)$$

With:

r: radial distortion

f: focal length

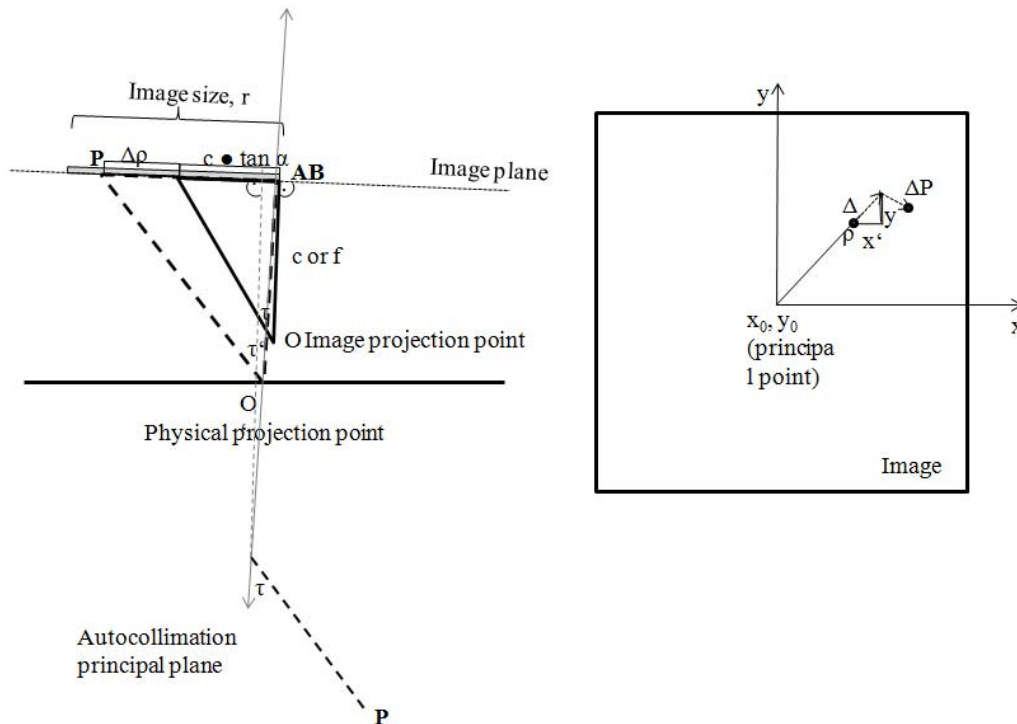


Figure 5.2 Radial $\Delta\rho$ and tangential lens distortion ΔP . Image projection point is orthogonal to main autocollimation beam (AB) (mod. from Kraus 2004, p. 49).

Depending on the lens and its focal length (Figure 5.3), several lens distortion may be found:

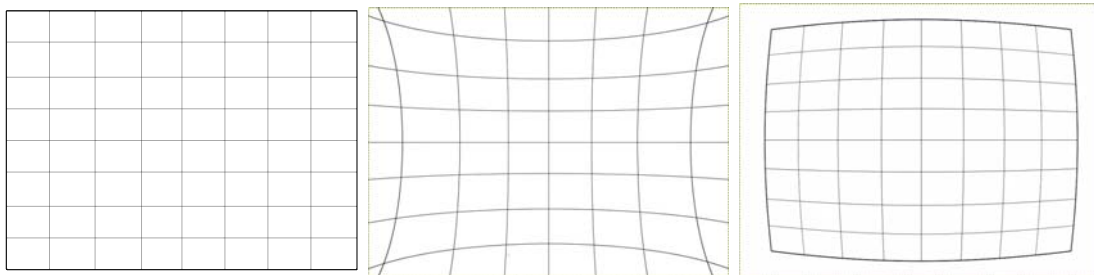


Figure 5.3 Lens distortion types: original pattern (left) pincushion distortion (middle), barrel distortion (right)

These are:

- pincushion distortion: magnification increases with increasing distance from the image centre, *i.e.* straight lines bend towards the lens centre/image centre, positive distortion parameters are found; or
- barrel distortion: magnification is highest in the image centre, *i.e.* straight lines bend away from the image centre, negative distortion parameters are found, or
- moustache distortion: a mixture of barrel and pincushion distortion.

Barrel distortion generally occurs at the wide angle ranges, and pincushion at longer focal lengths.

Deviation resulting from lens centering errors additionally lead to both tangential distortion and asymmetric radial distortion which in modern lenses usually is of a magnitude smaller than the radial distortion (Kraus 2004). Lens distortion may be corrected by camera calibration including the definition of

- the three camera coordinates x_0 , y_0 (image centre coordinates in x and y) and c (image z or focal length) of the sensor,
- the radial distortion Δr , and
- the tangential or asymmetrical distortion P_1 , P_2 (Kraus 2004, p. 462).

A commonly used correction method is based on the Brown-Conrady model (Conrady 1919, Brown 1966). It is based on the so called ‘plumb-line-calibration’ indicating that straight lines in reality should be imaged as straight lines in images (Brown 1971). To derive the distortion parameters a multiple-view approach is used where several images are taken of a calibration target and resulting multiple point correspondences are then used to estimate distortion.

For visualization purposes, lens distortion was retrieved with Agisoft Lens v. 0.4.1 (Agisoft LLC 2013) using a pinhole model for lens calibration based on Brown’s distortion model (Brown 1966), and specifying the transformation parameters in pixel coordinates in the image frame. Here X , Y and Z are the local camera coordinates with Z pointing towards the viewer (focal length). The image origin lies in the top left pixel centre. Image coordinates may then be calculated as follows:

$$x = X/Z \quad (5.2)$$

$$y = Y/Z \quad (5.3)$$

With:

X , Y , Z : local camera coordinates (origin upper left centre of pixel, Z towards viewing direction)

x : the x-value normalized to viewing direction axis, as projected by an ideal pin-hole camera

y : the y-value normalized to viewing direction axis, as projected by an ideal pin-hole camera

Radial distortion Δr is then retrieved by:

$$\Delta r = r^2 = \sqrt{(x^2 + y^2)} \quad (5.4)$$

The projected coordinates in x- and y-direction are determined by eq. 5.5-6. The first part accounts for radial, the second part for tangential distortion.

$$x' = x(1 + k_1 r^2 + k_2 r^4 + k_3 r^6) + P_2 (r^2 + 2x^2) + 1P_1 xy \quad (5.5)$$

$$y' = y(1 + k_1 r^2 + k_2 r^4 + k_3 r^6) + P_1 (r^2 + 2y^2) + 1P_2 xy \quad (5.6)$$

With:

k_i : radial distortion coefficients

P_i : tangential distortion coefficients

In addition, transversal distortion is accounted for by

$$u = c_x + x' f_x + y' \text{skew} \quad (5.7)$$

$$v = c_y + y' f_y \quad (5.8)$$

With:

u, v : projected image point coordinates/principal point, distortion centre (pixels)

c_x : principal point coordinate x

c_y : principal point coordinate y

x' : projected image coordinate in x-direction

y' : projected image coordinate in y-direction

f_x : focal length in x

f_y : focal length in y

skew: skew coefficient between x- and y-axis

Distortion parameters were estimated from screenshots of a checkerboard pattern (Figure 5.4) and are summarized in Table 5.1, Figure 5.5 and Table 5.2.

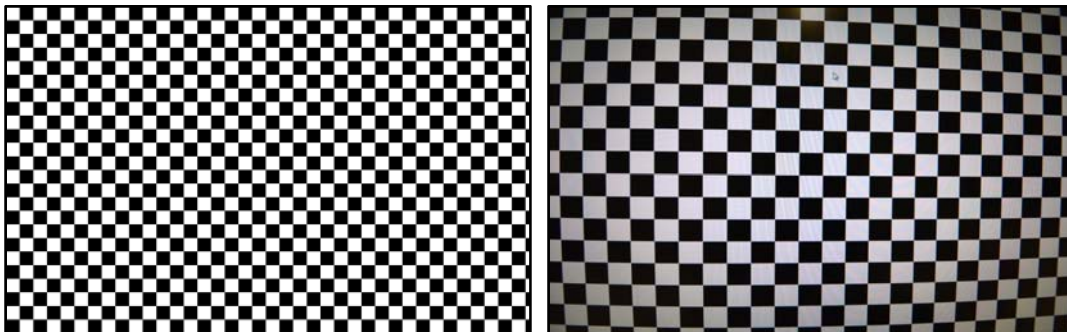


Figure 5.4 Calibration checkerboard pattern (left) and screenshot with DSLR for estimating lens distortion

The lens distortion parameters may then be fed into the Structure from Motion (SfM) software (chapter 5.3.4) as preliminary values for photo alignment.

As in this study, flight altitudes were less than ~ 150 m above ground, no corrections for atmospheric refraction were carried out. And as only Cartesian WGS84 coordinates were applied no correction for Earth curvature had to be applied to the image coordinates. These corrections may, however, easily be integrated into the triangulation procedure (Mikhail et al. 2001).

Table 5.1 Lens Distortion Parameters for Nikon D3100 Lens

Lens	F [mm]	C_x	C_y	K1	K2	K3	P1	P2	Fx	Fy
AF-S NIKKOR 10-24mm	10 (fixed)	2304.71	1534.8	0.00822958	-0.0477388	0.0213876	-0.000266117	-0.000463729	2045.34	2045.76

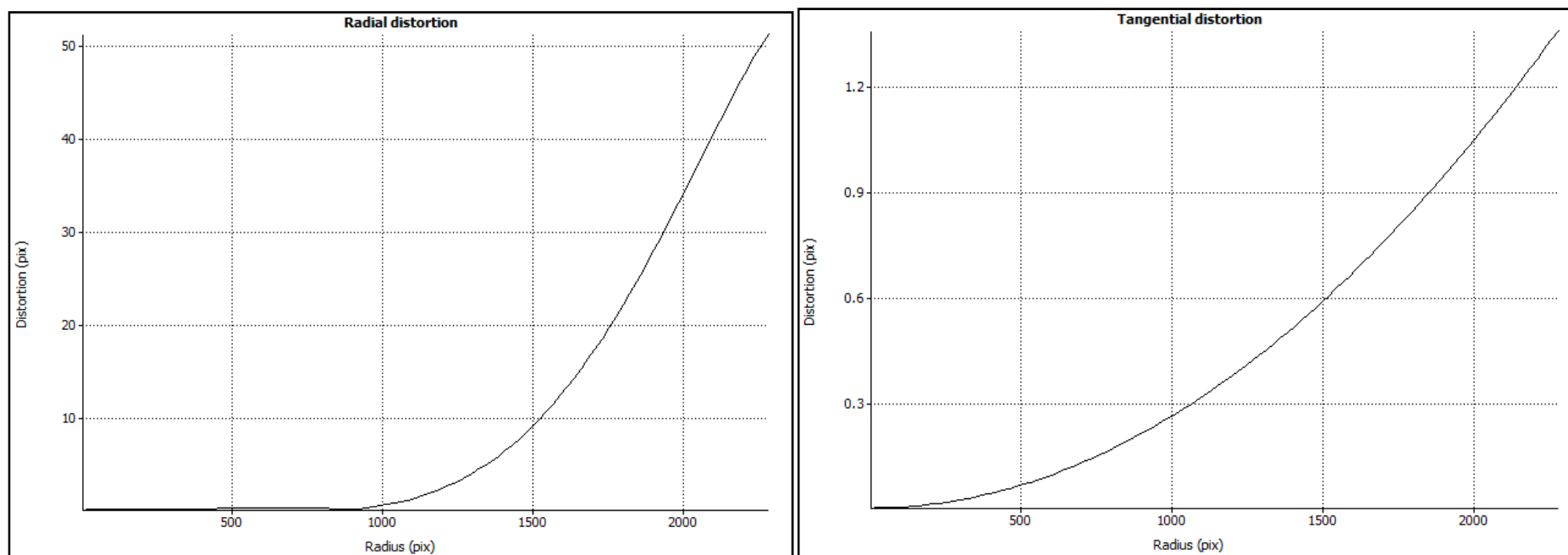


Figure 5.5 Radial and tangential distortion for Nikon D3100 lens used with 10 mm focal length

Table 5.2 Lens Distortion Parameters for Tetracam MiniMCA-6 cameras with filters

Band	fx	fy	cx	cy	skew	k1	k2	P1	P2
M (570 nm)	1986.17	1984.67	658.171	458.097	10.6111	-0.73393	12.0512	-0.00994079	0.00421855
1 (670 nm)	1897.43	1899.29	637.972	535.796	8.9840	-0.167045	0.420227	-0.00411402	0.00337485
2 (800 nm)	1982.35	1982.19	626.467	515.989	12.0740	-0.273991	1.62724	-0.00533414	0.00283517
3 (700 nm)	1961.66	1962.39	661.165	536.154	10.8274	-0.340178	4.18424	-0.00475422	0.00377564
4 (530 nm)	1954.36	1949.36	642.888	532.706	13.9461	-0.30112	2.54061	-0.00782972	0.000863469
5 (550 nm)	1883.01	1883.59	627.822	531.12	8.61918	-0.169352	1.12574	-0.00404646	0.00149796

5.1.3 Vignetting Correction

The MiniMCA-6 and, to a lesser extent, the Nikon DSLR display a radial greyvalue drop-off towards the image corners. To correct for this vignetting effect, several images of homogeneous white surfaces were taken for each respective filter combination. In this study, a white reference panel, a white wall or white paper had been photographed.

After averaging of several photographs, the maximum DN value was then used to define a mean per-pixel multiplicative corrections mask in accordance to equation (5.9).

$$VCF_{\lambda;i;j} = \frac{DN_{\lambda,max}}{DN_{\lambda;i;j}} \quad (5.9)$$

With:

VCF: vignetting correction factor

λ : wavelength/filter subscript

i, j: pixel subscript for columns and rows

Figure 5.6 shows example vignetting mask generated for the Nikon DSLR.

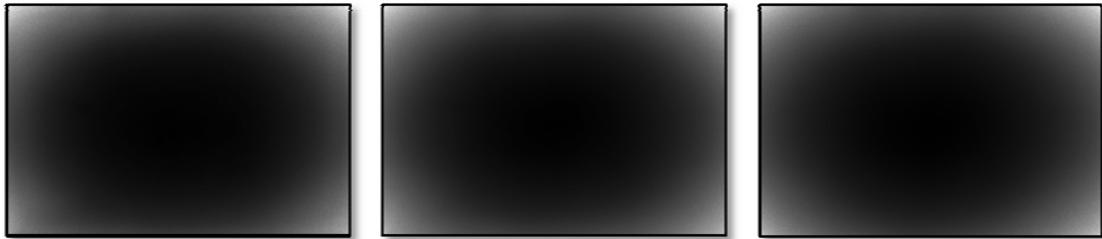


Figure 5.6 Nikon D3100 vignetting correction masks for RGB (left to right)

5.1.4 Correction of Systematic Camera Errors for MiniMCA-6Data

Kelcey and Lucieer (2012) have in detail described the radiometric characteristics and error sources of the MiniMCA-6 and described ways forward in correcting the respective sensor errors. The following sections document correction procedures required for the MiniMCA-6 only.

5.1.4.1 Band Alignment

The camera location on the lens plate introduces displacements of the individual band images in relation to the master camera. The camera was originally shipped with a global alignment file consisting of x- and y-shifts, rotation and scaling values which may

further be adapted for flight altitude using a Field of View Optical Calculator within the PixelWrench software. However, any handling of the camera, vibrations during the UAS flights and take-off and landings as well as changes of filters and focussing lead to fine alterations of this predefined camera alignments parameters. As a consequence, the band images do not match up within sub-pixel accuracy introducing a pixel-shift within the multispectral imagery (Figure 5.7).

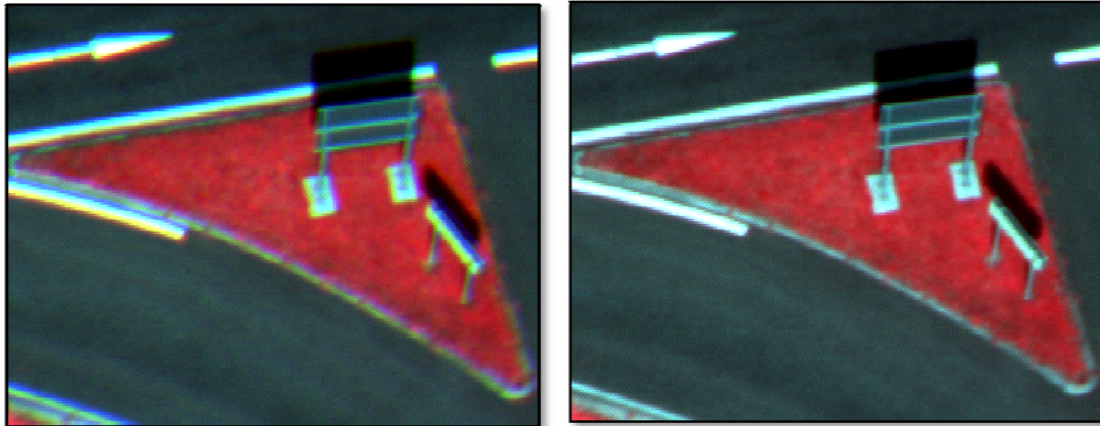


Figure 5.7 Multispectral image with misaligned bands after use of global alignment parameters showing colour halos (left) and corrected band alignment (right)

Therefore, in practice, the band alignment was modified for each flight by searching for features possibly recognizable in all bands at the corner of the images to estimate rotation and scaling followed by a shifting of pixels in x- and y-directions in relation to the master scene (example given in Table 5.3).

Table 5.3 Example camera alignment values

Camera	X-Shift	Y-Shift	Rotation	Scaling
Master	0	0	0.00	1.0000
Slave 1	-5	-5	0.10	1.0078
Slave 2	-1	-3	0.20	1.0008
Slave 3	-2	-5	-0.15	1.0026
Slave 4	-5	-6	0.10	1.0079
Slave 5	1	-3	0.00	0.9962

5.1.4.2 Data Conversion of 10-bit Data and Exposure Corrections

The MiniMCA-6 stores the individual camera images as either real 8-bit raw data or when 10-bit resolution is chosen, as a combination of three 8-bit image planes. Thus, after the band alignment, band images have to be converted to 10-bit radiometric resolution by multiplying the image planes as follows:

$$DN_{10bit} = DN_{green} * 4 + (DN_{green} - DN_{blue}) \quad (5.10)$$

Furthermore, respective relative exposure changes in relation to the master camera were corrected by introducing a correction factor (eq. 5.11).

$$DN_{\lambda} = DN_{10bit} * \frac{1}{T_{\lambda}} * \frac{1}{MR_{\lambda}} \quad (5.11)$$

With:

- c: correction factor [%]
- T: filter transmissivity (0-1)
- MR: monochrome response (0-1)
- λ : wavelength subscript

Similarly, correction factors for filter transmissivity and spectral sensor response need to be included (Table 5.4).

Table 5.4 Sensor and Filter Correction

Wavelength [nm]	Sensor response efficiency (SR)	SR correction factor	Filter transmission (FT)	FT correction factor	Total correction factor
530	0.56	1.80	0.63	1.58	2.83
550	0.62	1.61	0.54	1.86	2.99
570	0.68	1.48	0.66	1.52	2.24
670	0.90	1.11	0.60	1.67	1.86
700	0.93	1.08	0.68	1.47	1.59
750	0.99	1.01	0.68	1.48	1.49
760	0.99	1.01	0.59	1.69	1.71
780	0.99	1.01	0.61	1.63	1.65
800	0.96	1.04	0.56	1.79	1.86
900	0.71	1.41	0.69	1.45	2.04

The latter were only corrected when mere DN values were being analysed or in case of atmospheric correction. When an empirical line correction method based on reference

panels of known reflectance was applied, these offsets and gains were adapted within the regression model.

5.1.4.3 Lens Distortion Estimation from Structure from Motion Software

Ideally, lens distortion correction is executed first (see chapter 5.1.2). However, when image mosaics are built, lens distortion correction parameters are estimated from multiple views of aerial imagery prior to point cloud modeling in the respective Structure from Motion or photogrammetrical software (*i.e.* Agisoft). At the beginning, estimates of focal lengths, location of image principal point and radial distortion parameters for the master band may be put in. By aligning image pairs, the camera calibration is then estimated for the master channel (Figure 5.8).

```
fx 2831.31, fy 2831.31, cx 683.047, cy 539.702, k1 0.352617, k2 -1.61943, k3 22.1335
```

Figure 5.8 Lens calibration parameters retrieved for the MiniMCA-6: camera focal length in x- and y-direction (fx, fy), principal point on image plane (cx, cy), followed by radial distortion as retrieved by Agisoft software

From an operational point of view, this presents also a more accurate procedural method as the camera has been built to take photographs from greater heights and focus is generally set to infinity. This renders close-up image acquisition of calibration targets for lens distortion correction software difficult.

5.1.4.4 Noise

The MiniMCA-6 dark offset behavior has been analyzed in detail by Kelcey and Lucieer (2012) and three types of noise were found: (1) a global checkered pattern, (2) horizontally striped noise and (3) periodic noise, occurring with varying contribution in each band.

- (1) Global checkered pattern: a pseudo-texture is introduced by a bimodal alternating distribution of noise state within a band. Once bands are composed to a multispectral image, the noise texture may produce a checkerboard pattern across the image adding with 0-40 DN variations.
- (2) Horizontally striped noise: its source remains unknown and the authors found a DN variation of 0-32 DNs. This noise structure may be eliminated by digital image processing, *i.e.* by Fourier analysis and transformations (Oppenheim and Schaffer 1975).

- (3) Periodic noise introduced by the camera's progressive shutter results in a brighter horizontal strip (0-30 DN) whose location moves with raising exposure times (Kelcey and Lucieer 2012, p. 1473-1479).

Overall averaged noise was found to rise from minimum 5-6 (+/- 1) DN to a maximum of 12-13 (+/- 3-4) DN with exposure lengths from to 1000 μ sec to 20000 μ sec.

As image acquisition in this study generally was carried out during peak solar irradiance and images during orthophoto mosaicing were resampled to averaged resolutions, and statistical analysis were based on regional areas of interest (AOI), noise was not corrected. Finally, for each location several images were acquired with the UAS and best images selected for further processing.

5.1.4.5 Vignetting Correction

As Kelcey and Lucieer (2012) have illustrated, the radial DN fall-off from the centre becomes smoother and also lessens with longer exposure times, images for vignetting correction masks were taken at midday during sunny conditions to obtain similar illumination conditions as for flight campaigns. For each filter set, several images were taken and averaged to avoid random noise (Figure 5.9).

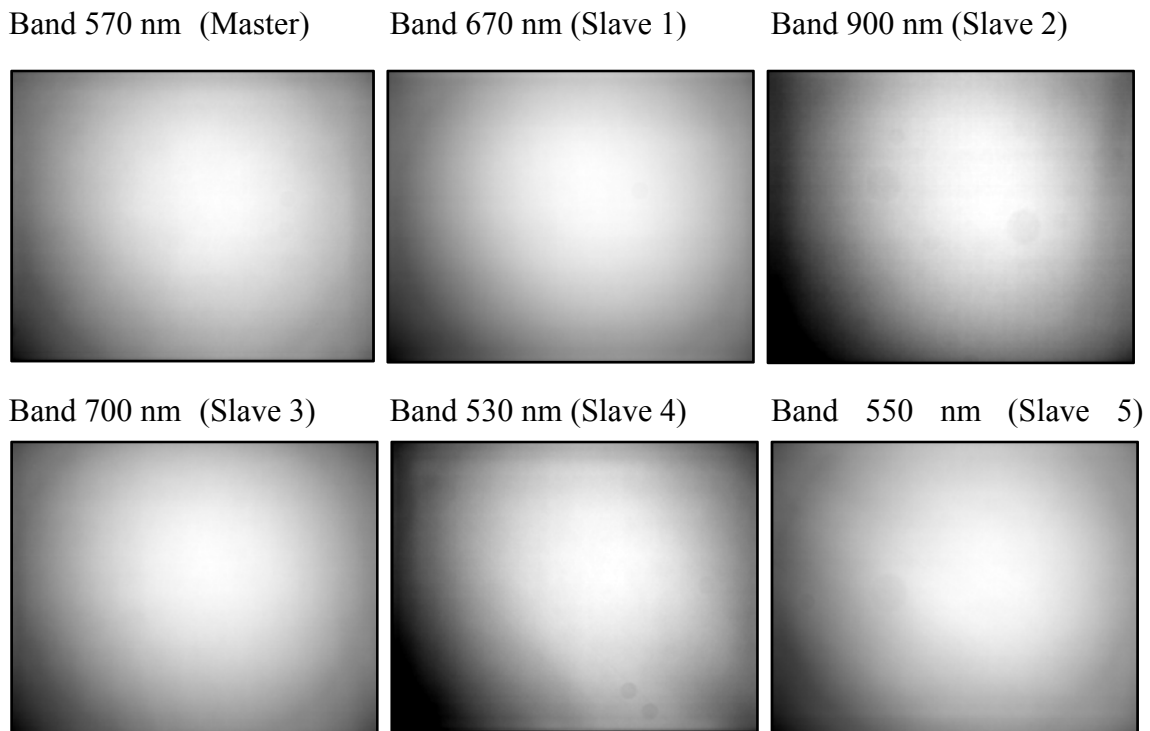


Figure 5.9 Vignetting with dust particles visible for the MiniMCA-6 lenses with respective filter

The highest radial drop-off was found for camera slave 2 (550 nm) and slave 4 (530 nm) and the smallest vignetting effect was obtained for the master camera (570 nm). Also the radial drop-off is not evenly distributed across the image. Vignetting was then corrected by the formula given in eq. 5.9 for each band respectively. Vignetting correction for a maize scene is illustrated in Figure 5.10.

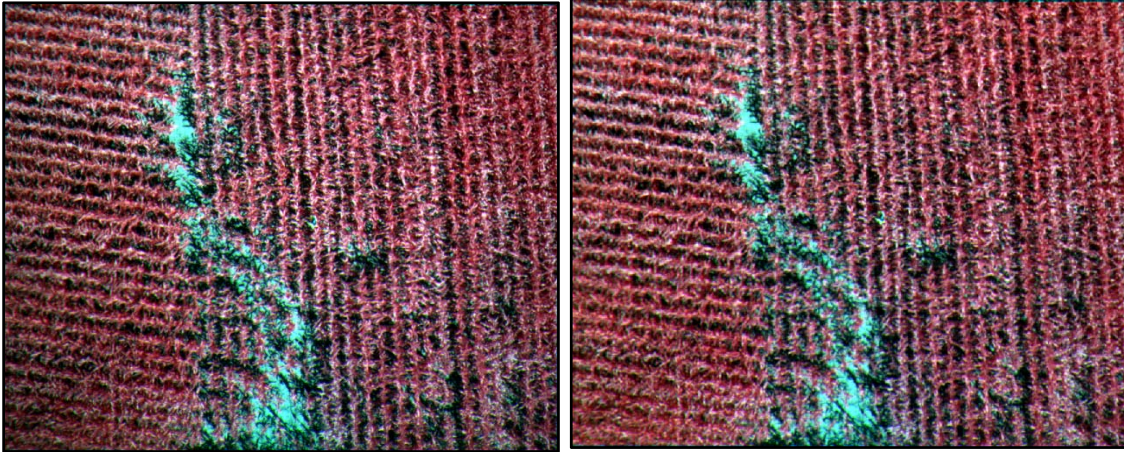


Figure 5.10 False colour composite (R: 900 nm, G: 570 nm, B: 550 nm) of a maize field with vignetting (left) and corrected image (right)

In practice, lens calibration was carried out within the SfM software and noise correction during image processing if required. Figure 5.11 summarizes the multispectral data preparation prior to radiometric/atmospheric processing or analysis. The processing steps from 8bit RGB images to layerstacked images were batch-processed within Matlab (MathWorks®) and ERDAS Imagine (Intergraph Corporation).

**MULTISPECTRAL
IMAGE
PREPARATION**

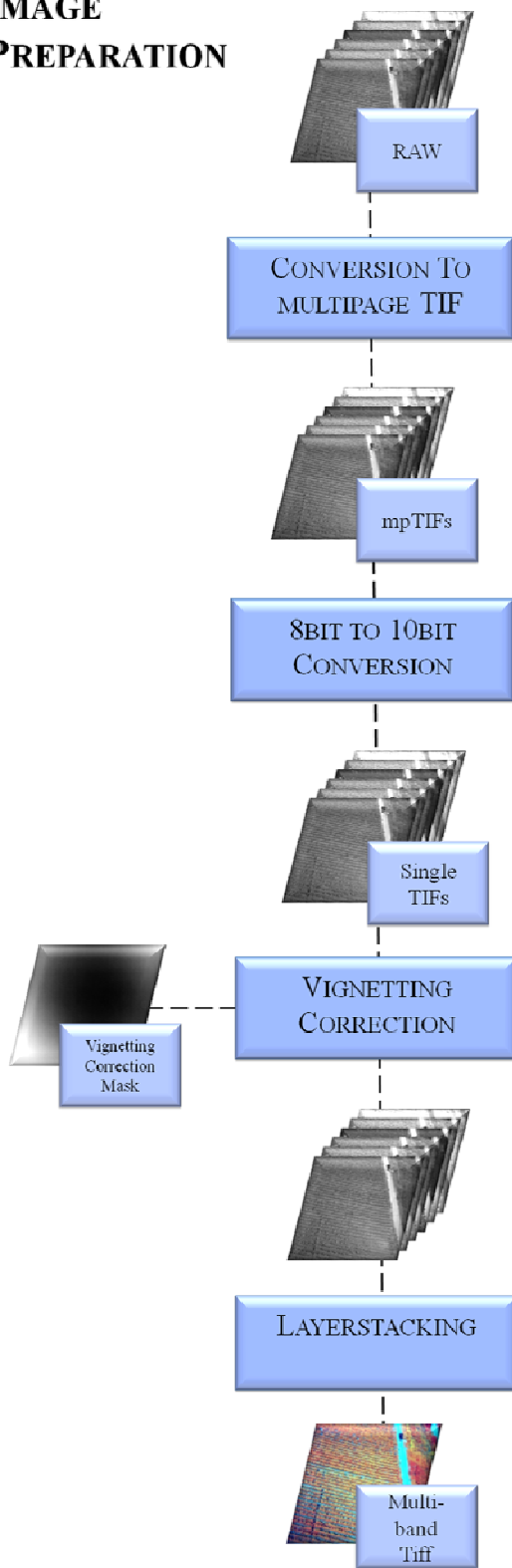


Figure 5.11 Pre-processing flowchart for Mini-MCA6 data: from raw single images to multiband images

5.2 Radiometric Correction of Atmospheric Effects

5.2.1 The radiation paths between solar irradiance, atmosphere and at-sensor radiance

Any image taken from the air is affected by the air mass and its radiative, absorbing and scattering processes (Figure 5.12). When aerial images of multiple times are being evaluated, images need to be either corrected or calibrated with respect to atmospheric effects. The following gives a summary of the atmospheric-target-sensor matter interactions described in detail by Hill and Sturm (1991), Jensen (2007), and Richards (2013).

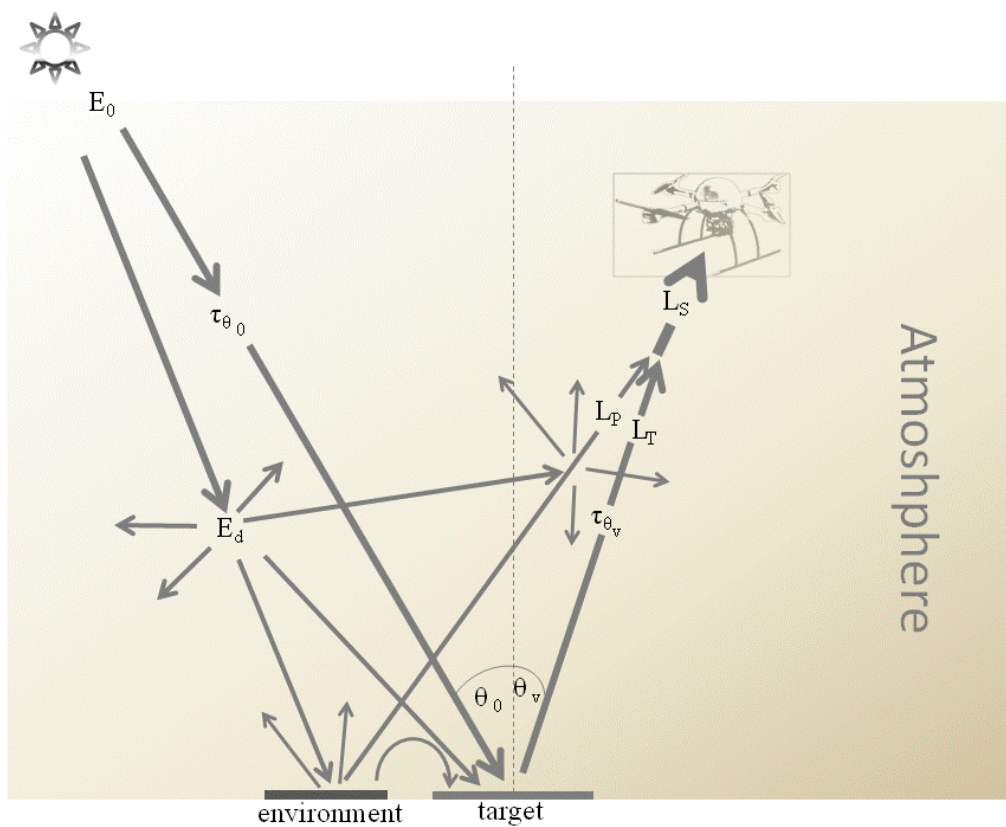


Figure 5.12 Radiance paths from sun to sensor (E_0 : solar irradiance, E_d : diffuse sky irradiance, θ : sun zenith angle, τ_{θ_0} : atmospheric transmittance, θ_v : exit angle towards sensor, L_P : path radiance, L_T target radiance/reflectance, L_S total at-sensor radiance, mod. from Jensen 2007, p. 59)

The spectral solar irradiance for any given ground area is:

$$E_{G,\lambda} = \int_{\lambda_1}^{\lambda_2} (E_{0,\lambda} \tau_{\theta_0} \cos \theta_0 + E_{d,\lambda}) \Delta \lambda \quad [W m^{-2}] \quad (5.12)$$

With:

- $E_{G,\lambda}$: The total solar irradiance at the earth's surface per wavelength λ
- $E_{O,\lambda}$: The total solar irradiance at the top of the atmosphere at wavelength λ
- τ_{θ_o} : atmospheric transmittance at the solar zenith angle θ_o
- $E_{d,\lambda}$: spectral diffuse sky irradiance

The energy emitted by the sun on its ways towards the target pixel is diminished by particle scattering through atmospheric molecules (τ_R) and aerosols (τ_A) and by gaseous absorption (τ_G , e.g. O₃, CO₂, water vapour):

$$\tau = \tau_R + \tau_A + \tau_G \quad (5.13)$$

Molecular Rayleigh scattering for a standard atmosphere depends on the wavelength λ and may be approached by (Hill and Sturm 1991):

$$\tau_R = 0.00879 * \lambda^{-4.09} \quad (5.14)$$

Aerosol optical thickness is defined by the so-called Ångstrom relation where the exponent describes the aerosol size and the variable β the aerosol content of the atmosphere:

$$\tau_{\text{Å}} = \beta * \lambda^{(-n)} \quad (5.12)$$

With:

- λ : wavelength
- n : Ångstrom exponent
- β : aerosol content

Gaseous absorption happens in specific wavelength-dependent absorption bands and is except for water vapour relatively constant and may be inferred from look-up tables.

Assuming the target to be an Lambertian diffuse reflector, the radiance emitted from a target area then is:

$$L_T = \frac{1}{\pi} \int_{\lambda_1}^{\lambda_2} \rho_{\lambda} \tau_{\theta_T} (E_{O,\lambda} \tau_{\theta_o} \cos \theta_o + E_{d,\lambda}) \Delta \lambda \quad [W m^{-2} sr^{-1}] \quad (5.13)$$

With:

- L_T : radiance from target area
- ρ_{λ} : reflectance at given wavelength λ
- τ_{θ_T} : atmospheric transmittance from target towards sensor at angle θ_T

The sensor additionally senses radiance from the atmosphere (diffuse irradiance and scattering processes), the path radiance L_P and from multiple reflections of neighbouring pixels L_{env} . Thus the total radiance recorded is:

$$L_S = L_T + L_P + L_{env} \quad [W \ m^{-2} \ sr^{-1}] \quad (5.14)$$

Ideally, for each spectral band, there is a known relationship between radiation and greyvalue:

$$L_S = c_0 + c_1 DN \quad [W \ m^{-2} \ sr^{-1}] \quad \text{with} \quad (5.15)$$

$$c_1 = \frac{(L_{max} - L_{min})}{DN_{max}} [W \ m^{-2} \ sr^{-1}]$$

And the target reflectance then is (Hill and Sturm 1991):

$$\rho_T = \frac{\pi \{d^2(c_0 + c_1 DN) - L_P\}}{\tau E_g} - \rho_{env} \quad (5.16)$$

With:

- E_g : global irradiance at ground level
 d : correction factor for sun-to-earth distance

Thus for precise correction of atmospheric effects, according to Richter (2010, p. 16), the user needs

1. to know the sensor calibration, and
2. to estimate the key atmospheric parameters such as aerosol type, aerosol optical thickness (AOT), visibility, and water vapour.

5.2.2 Topographic effects

Radiation transfer so far described radiance paths for flat surfaces. Topography adds to illumination differences as irradiance is directly proportional to the cosine of the angle of incoming solar irradiance in relation to the normal of the local surface (Hill et al. 1995, p. 145).

$$\cos \gamma = \cos \theta_0 \cos \theta_n + \sin \theta_0 \sin \theta_n \cos(\phi_n - \phi_0) \quad (5.17)$$

With

- θ_0 : solar zenith angle
 θ_n : zenith angle of normal to surface
 ϕ_0 : solar azimuth angle
 ϕ_n : topographic aspect angle

Hill et al. (1995) have therefore incorporated the correction of topographic effects into the atmospheric correction based on the 5S code - Simulation of the Satellite Signal in the Solar Spectrum – introduced by Tanré et al. (1990).

5.2.3 Bidirectional Reflectance

Viewing and illumination geometry further affect radiation paths (see also chapter 3.2.1). An aerial photograph is a central projection of the target area and depending on sun azimuth and sun zenith, each object in relation to the camera is detected by different viewing angles, and depending on sun-object-sensor geometry introduces different shading (Figure 5.13). BDR effects for different viewing geometries are analysed in more detail in chapter 6.

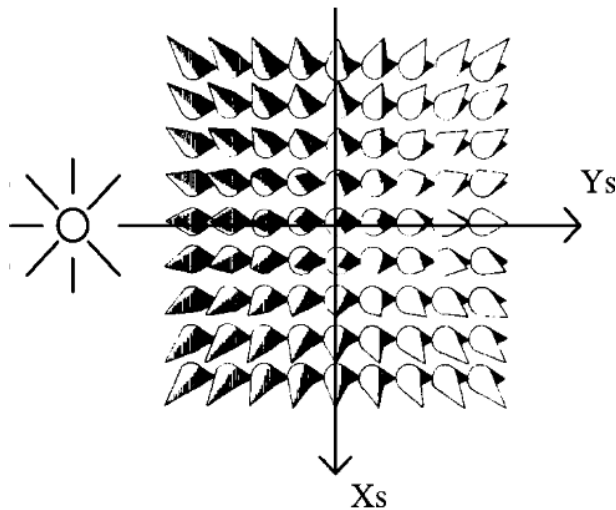


Figure 5.13 Bidirectional illumination differences for a tree stand with nadir viewing (Source: Holopainen and Wang 1998, p. 682)

The correction of bidirectional reflectance differences for UAS aerial imagery is possible when high resolution digital terrain models are available and sensor/sun positions at image acquisition are known. For flat terrain, a simple nadir normalization may be sufficient (Richter 2010).

5.2.4 Atmospheric Correction Using ATCOR-4

In this study, atmospheric correction of multispectral data was carried out using ATCOR-4 (v. 5.1), developed by Richter (2010), as to that time no other software was readily available. The version was built for airborne scanner instruments with FOV between 60°-90°. The MiniMCA-6 has a FOV of ~ 43° in x-direction, hence the value was changed in the sensor setup.

The underlying monochromatic atmospheric database uses the MODTRAN-4 radiative transfer code (Berk et al. 1998, 2003, Richter 2010) which requires resampling for each sensor and filter using Gaussian fitting curves.

For a given image acquisition time, location and sensor position in relation to the sun, ATCOR-4 predicts the radiation path through the atmosphere. As descriptors for the atmosphere, visibility, optical thickness and water vapour are used.

The visibility is defined by “the maximum horizontal distance a human eye can recognize a dark object against a bright sky” (Richter 2010, 13).

$$\text{Vis} = \frac{1}{\beta} \ln \frac{1}{0.02} = \frac{3.912}{\beta} \quad (5.18)$$

With:

β : extinction coefficient at 550 nm

Where available, visibility measures [km] and water vapour content [g/cm^2] were derived from meteorological records or MODIS data or based on season. A plausibility check for the visibility was obtained by fitting estimated reflectances to that of reference targets.

The aerosol type was chosen by selecting a suitable atmosphere (*i.e.* continental midlatitude summer rural or urban) or by in-flight calibration, an interactive estimation from reference targets of known reflectances present in the scene. The veneer plywood panels are 50 cm x 50 cm large and were painted with mat acrylic colours from black to white (Figure 5.14).

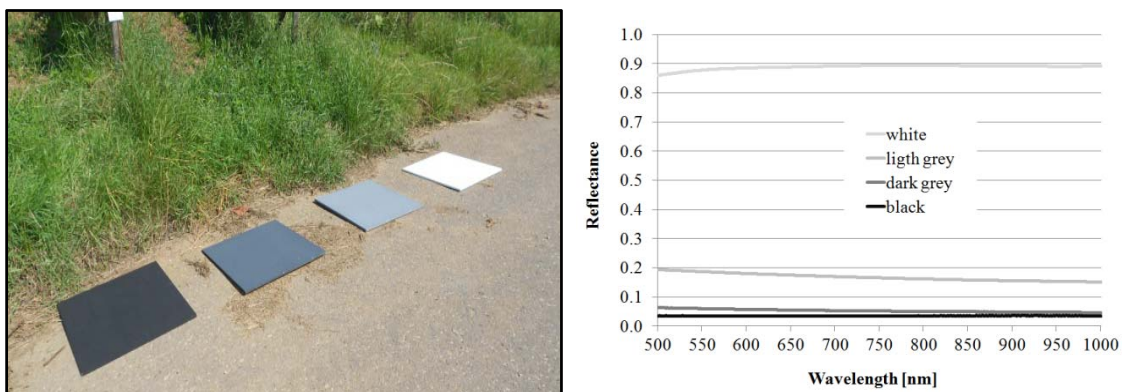


Figure 5.14 Reference targets (left) and respective reflectance measurement with spectroradiometer (right)

Their reflectance was measured with the ASD FieldSpec both in laboratory and, where possible, in the field during image acquisition. Spectral calibration was then carried out by using a dark and bright reference target:

$$L_{bright} = c_0 + c_1 DN_{bright} \quad \text{and} \quad L_{dark} = c_0 + c_1 DN_{dark} \quad (5.19)$$

Then

$$c_1 = \frac{L_{bright} - L_{dark}}{DN_{bright} - DN_{dark}} \quad (5.20)$$

And

$$c_0 = L_{bright} - c_1 DN_{bright} \quad (5.21)$$

ATCOR-4 also corrects for bidirectional reflectance differences across track illumination correction where the pixel greyvalue is multiplied with a correction factor of the inverted function of the scan angle (Richter 2010).

5.2.5 Empirical Line Method for Atmospheric Correction and Calibration

Due to lack of meteorological data, also data-driven methods for atmospheric correction were applied in this context. A widely applied approach is the so-called empirical line calibration (ELC), where the radiance detected by the sensor is assumed to be linearly correlated with the respective target reflectance ρ when solar irradiance is homogeneous and for flat terrain (Roberts et al. 1985; Smith and Milton 1999; Karpouzli and Malthus 2003; Gege et al. 2009; Richards 2013).

At least two or more targets of known reflectance are selected in the images. As reference targets, pseudo-invariant features ranging from low to high albedo are used. These may be obtained from targets like concrete, bare soil/substrate, dark vegetation or water, or reference panels are laid out in the image area prior to the overflight. Reference reflectances are either measured in the field or under laboratory conditions. In this study, generally three to four grey scale reference panels (Figure 5.14) were used, as more than the minimum required two targets reduce errors in the empirical line computation (Karpouzli and Malthus 2003; Baugh and Groeneveld 2007).

The image DNs are band-wise linearly regressed to the target's reflectances to obtain the empirical line (Figure 5.15), the EL offset thereby accounts for atmospheric scatter-

ing processes involved in the path radiance L_p (Schott et al. 1988), the multiplicative term incorporates all other atmospheric processes. The calibration is then applied to all image pixels at the specific wavelength. Despite the time and effort spent on field reference reflectance measurements, the ELC method results in comparable, noise-reduced reflectances (Roberts et al. 1985).

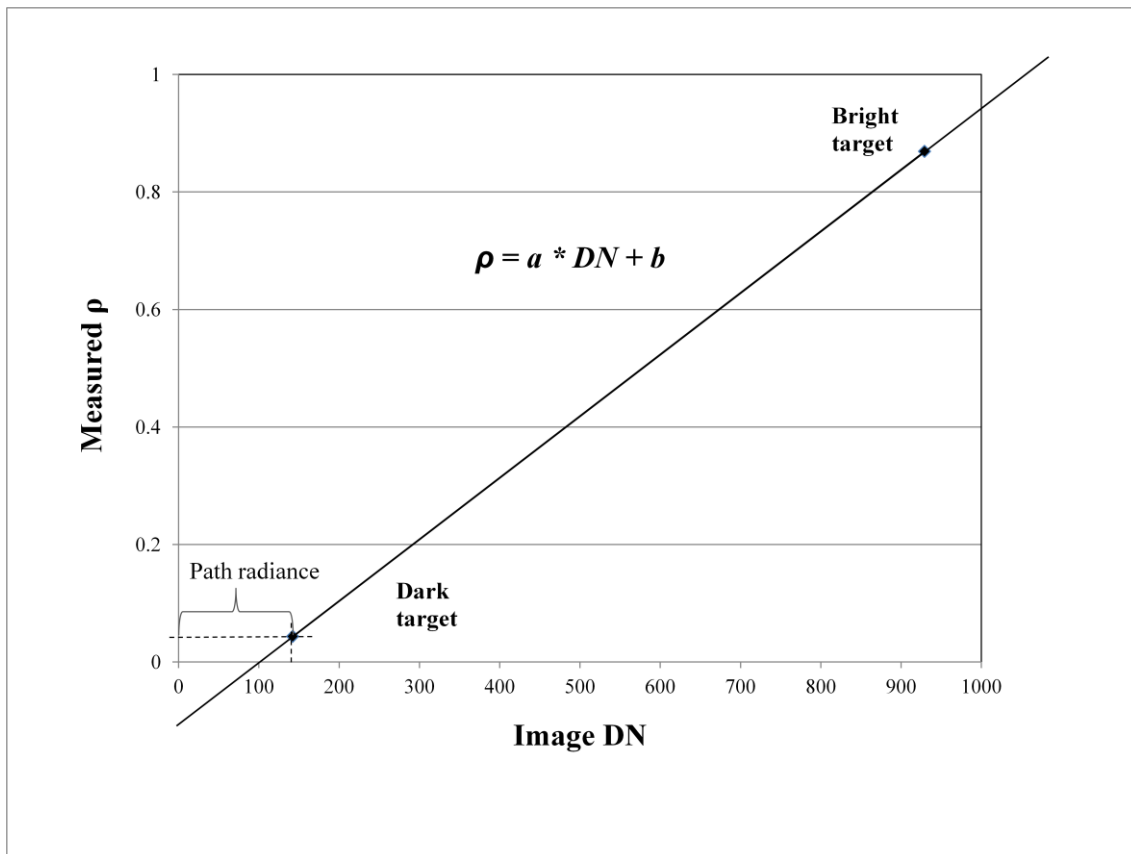


Figure 5.15 The empirical line calibration

Figure 5.16 shows results from an empirical line calibration of an image taken of a vineyard. As vegetation generally ranges from 3-7% in the red wavelength spectrum to 40%, maximum $\sim 70\%$ reflectance in nIR wavelengths, the aim was to enhance the DN distribution among the smaller reflectances values. Exposure settings were thus slightly extended, which then caused an overexposure of the white reference panel. As a result, in most cases only the three darker panels (Figure 5.14) were employed for empirical line calibration. The graphs in Figure 5.16 show the original in-situ measured reflectances (dashed line) and the resulting reflectances of the respective reference panels after the ELC. Absolute differences in reflectance are listed in Table 5.5 and show a maximum of three percent of reflectance. The obtained errors are still well in range with

those found in the literature (Smith and Milton 1999; Karpouzli and Malthus 2003, Baugh and Groeneveld 2007).

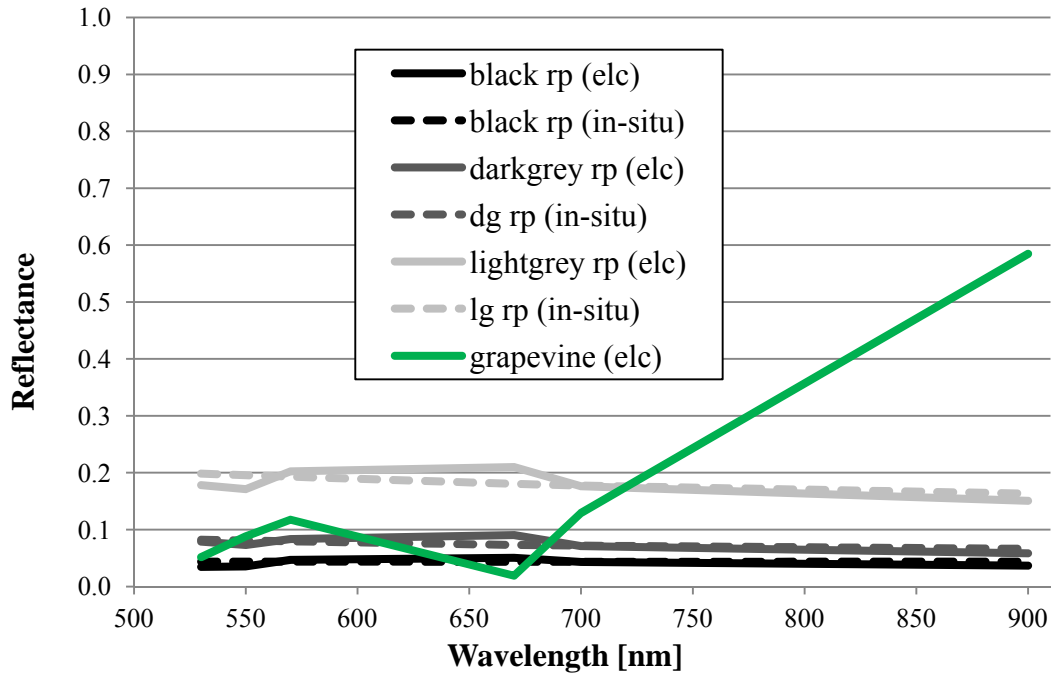


Figure 5.16 Absolute reflectance differences for reference panels after ELC

Table 5.5 Absolute $\Delta\rho$ in percent of reference panels after ELC compared to in-situ measurements for given wavelength ρ

ρ [nm]	Lightgrey reference panel	Darkgrey reference panel	Black reference panel
530	-0.020	-0.003	-0.009
550	-0.025	-0.008	-0.009
570	0.009	0.004	0.003
670	0.030	0.017	0.007
700	-0.001	-0.001	0.000
900	-0.013	-0.008	-0.007

5.3 Geometric Processing

Depending on the task, UAS images in this work were either used non-registered, i.e. as single frames of aerial photographs without linkage to a ground coordinate system, or when and where required, mosaiced to orthophotos by aerial triangulation based on bundle block adjustment. A description of the image space and ground coordinate systems, as well as a definition of interior orientation has been given in section 5.11, now the resection (definition of the position and orientation of a photo during image acquisition), and intersection (calculation of ground space coordinates from the rays of two or more overlapping photos) are explained which are combined in the bundle block adjustment.

5.3.1 Exterior Orientation of Camera during Image Acquisition

The exterior orientation describes the local position and the orientation of a camera/photo during the image acquisition (Figure 5.17). This includes the position (X_o, Y_o, Z_o) of the perspective centre or camera station (O) in relation to the ground coordinate system (X, Y, Z) with Z_o being the camera altitude above sea level or ground level. The angular orientation between image (x, y, z or $-f$) and ground coordinate system are described by kappa (κ) – “rotation about the photographic z -axis”, phi (ϕ) – “rotation about the photographic y -axis”, and omega (ω) – “rotation about the photographic x -axis” (ERDAS Inc. 2010, p.23). The photographic z -axis follows the focal length optical axis of the camera, and $x', y',$ and z' are parallel to the ground coordinate system (ERDAS Inc. 2010).

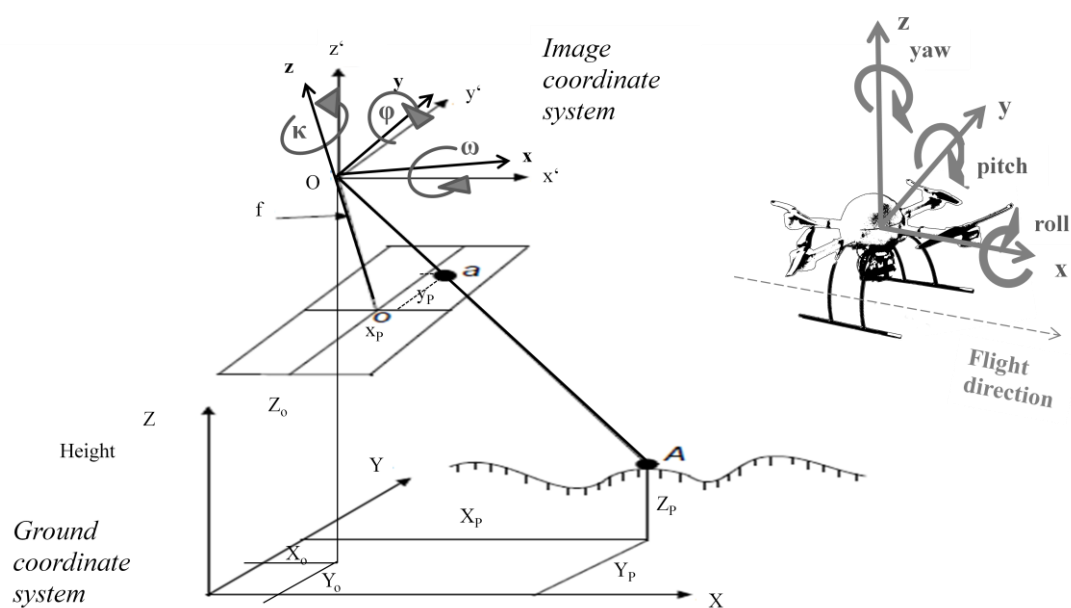


Figure 5.17 Exterior orientation (mod. from Intergraph Corporation 2013, p. 552)

The quadcopter drawing (Figure 5.17) illustrates the orientation of the UAS/camera during the image acquisition. Positions are given by the GPS coordinates. The roll angle is the rotation angle around the principal x-axis of the UAS in flight direction, pitch is the rotation angle around the y-axis (nodding movement), and yaw the rotation angle around the vertical z-axis (ERDAS Inc. 2010).

The exterior orientation may thus be described as a bundle of rays' position and orientation in relation to the ground coordinate system (Mikhail et al. 2001):

$$\begin{bmatrix} x \\ y \\ z \end{bmatrix} = k M \begin{bmatrix} X - X_0 \\ Y - Y_0 \\ Z - Z_0 \end{bmatrix} \quad (5.22)$$

With:

x, y, z	image coordinates
k:	scaling factor
M:	3x3 rotation matrix of three sequential rotations
X, Y, Z:	ground coordinates
X ₀ , Y ₀ , Z ₀ :	coordinates of camera station

The rotation matrix is derived as follows (ERDAS Inc. 2010 p. 25-28, Mikhail et al. 2001, p. 91):

The rotation matrix may be derived by “three sequential rotations: ω around the X-axis, ϕ about the once-rotated Y-axis, and κ about the twice-rotated Z-axis” (Mikhail et al. 2001, p. 91).

$$\begin{aligned}
M_\omega & \begin{bmatrix} 1 & 0 & 0 \\ 0 & \cos \omega & \sin \omega \\ 0 & -\sin \omega & \cos \omega \end{bmatrix} \\
M_\varphi & \begin{bmatrix} \cos \varphi & 0 & -\sin \varphi \\ 0 & 1 & 0 \\ \sin \varphi & 0 & \cos \varphi \end{bmatrix} \\
M_\kappa & \begin{bmatrix} \cos \kappa & \sin \kappa & 0 \\ -\sin \kappa & \cos \kappa & 0 \\ 0 & 0 & 1 \end{bmatrix}
\end{aligned} \tag{5.23}$$

Leading to the rotation matrix M

$$M = M_\kappa M_\varphi M_\omega \tag{5.24}$$

Being

$$M = \begin{bmatrix} \cos \varphi \cos \kappa & \cos \omega \sin \kappa + \sin \omega \sin \varphi \cos \kappa & \sin \omega \sin \kappa - \cos \omega \sin \varphi \cos \kappa \\ -\cos \varphi \sin \kappa & \cos \omega \cos \kappa - \sin \omega \sin \varphi \sin \kappa & \sin \omega \cos \kappa + \cos \omega \sin \varphi \sin \kappa \\ \sin \varphi & -\sin \omega \cos \varphi & \cos \omega \cos \varphi \end{bmatrix} \tag{5.25}$$

Or expressed by its elements

$$M = \begin{bmatrix} m_{11} & m_{12} & m_{13} \\ m_{21} & m_{22} & m_{23} \\ m_{31} & m_{32} & m_{33} \end{bmatrix} \tag{5.26}$$

Each bundle therefore requires six parameters for exterior orientation: three positional and three orientations (Mikhail et al. 2001).

5.3.2 Absolute Orientation of Camera during Image Acquisition

Relatively oriented models may be mapped to the ground coordinate system by a seven parameter transformation including a scaling factor, three translations, and three rotations (Mikhail et al. 2001).

$$Y = k M X + T \tag{5.27}$$

With:

Y: vector of world coordinates

k: scale factor

M: rotation matrix from model space to world coordinate system

X: vector of model coordinates

T: Translation vector

5.3.3 Bundle Block Adjustment

UAS flight campaigns are typically planned with an overlap of 60 % in x-direction and 40 % in y-direction for the neighbouring stripe (Figure 5.18), the resulting images each consist of a bundle of rays converging at the perspective centre or principal point with a certain position and orientation in space.

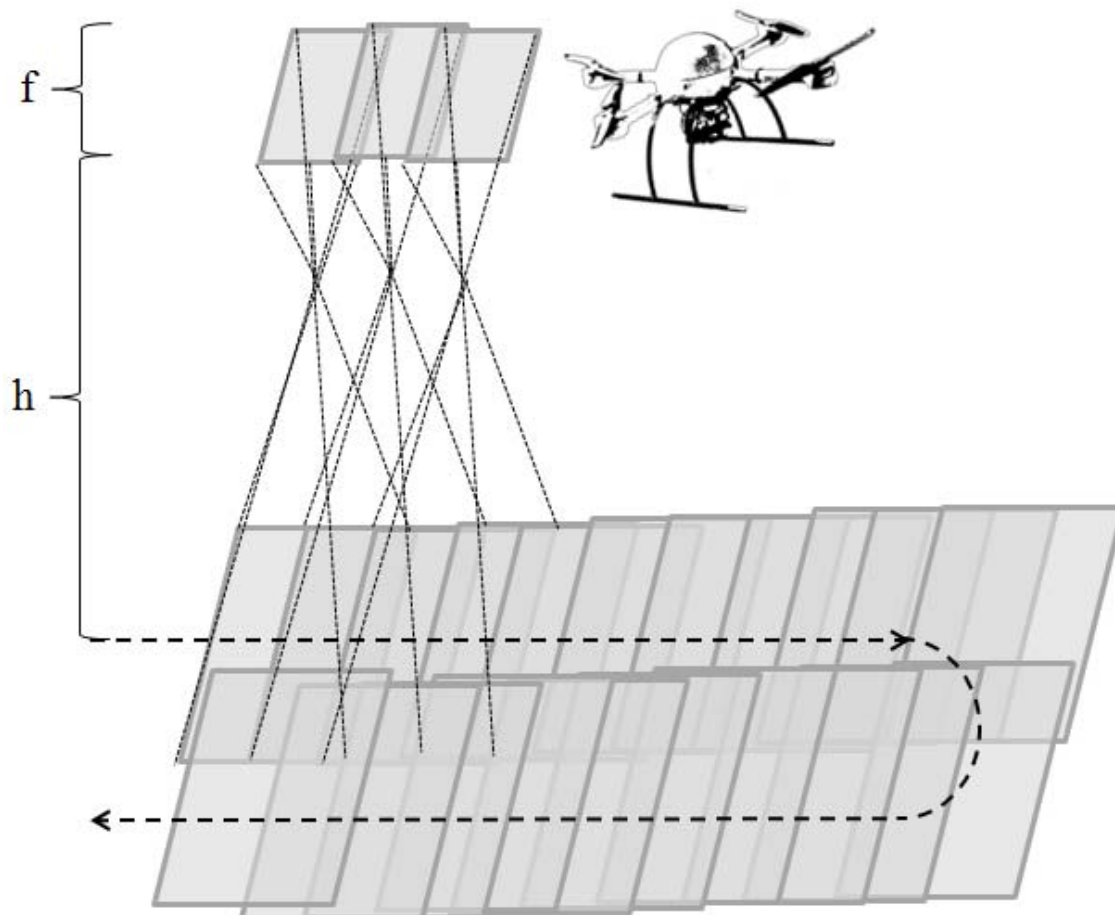


Figure 5.18 Flight plan geometry and bundle rays

Bundle block adjustment is the computational optimization of simultaneously refining the 3D scene geometry from different viewpoints and its parameters of exterior orientation and simultaneously calibrating the camera and accounting for lens distortion (i.e. self-calibration). Each image consists of a bundle of rays. By comparison and finding of image pairs (the exterior orientation of cameras in space by tie-point matching and simultaneously intersecting rays of images, reprojection errors are minimized and image locations modeled (Triggs et al. 1999; Mikhail et al. 2001). The whole process is based on the collinearity condition which assumes that the camera station, ground point and its corresponding image point location must lie along a straight line:

$$x - x_0 = -f \left[\frac{m_{11}(X - X_o) + m_{12}(Y - Y_o) + m_{13}(Z - Z_o)}{m_{31}(X - X_o) + m_{32}(Y - Y_o) + m_{33}(Z - Z_o)} \right] \quad (5.28)$$

$$y - y_0 = -f \left[\frac{m_{21}(X - X_o) + m_{22}(Y - Y_o) + m_{23}(Z - Z_o)}{m_{31}(X - X_o) + m_{32}(Y - Y_o) + m_{33}(Z - Z_o)} \right] \quad (5.29)$$

For each location on the ground one such set of equations is computed (Mikhail et al. 2001; ERDAS Inc. 2010).

The retrieved model then may be georeferenced for further accuracy by the use of ground control points.

5.3.4 Structure from Motion Software for 3D Model Generation, Mosaicing of Orthophotos and Generating DEM

In this study, Agisoft PhotoScan Professional has been used to calibrate and align the aerial photographs. As the 3D structure is being inferred from 2D aerial image sequences, the process is also called *Structure from motion*. Either image centre GPS coordinates are fed into the software for a first alignment, or image pairs are retrieved solely by feature matching algorithms. First tie-points are searched that are found in correspondence across the input photos, then by feature matching several thousand matching points are retrieved. With error minimization, the ground, image plane and camera model parameters are simultaneously modeled, thus solving exterior and interior orientation and lens calibration in one modelling approach. The result is a 3D point cloud model (Figure 5.19) GCPs may then help to fix the model to the respective reference system. For multispectral images, computations are based on the user-defined master band (for MiniMCA-6 data the master camera equipped with the 570 nm filter) (Figure 5.19).

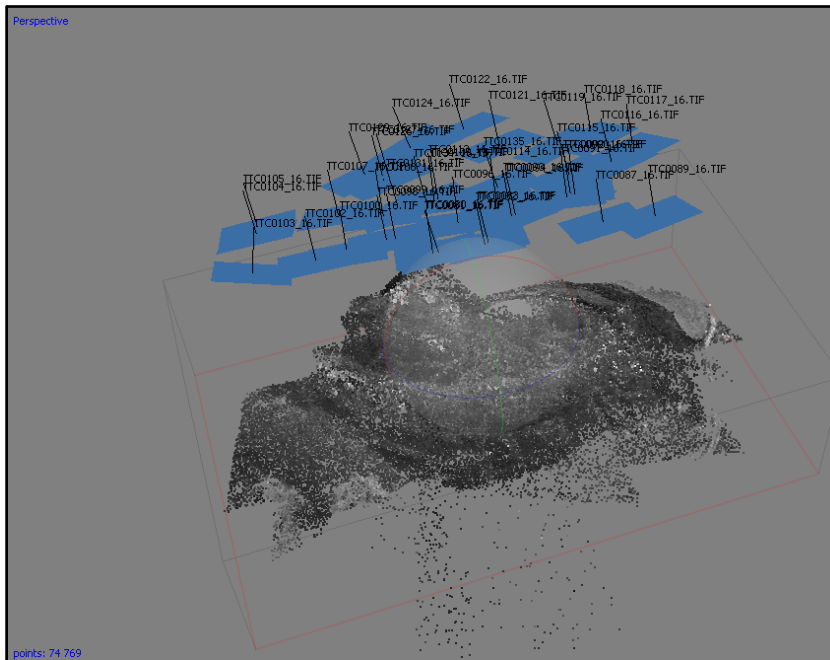


Figure 5.19 Example of a 3D point cloud model with stray points requiring further editing

The resulting 3D point cloud may then be edited before a dense point cloud is generated. The dense point cloud may also be filtered to obtain sharp or mild edges were depths are showing abrupt changes. The next processing step is the creation of a mesh model (triangulation) of the points and a maximum number face counts may be set. Following this, the triangles may be textured with image greyvalue resampling (Figure 5.20).

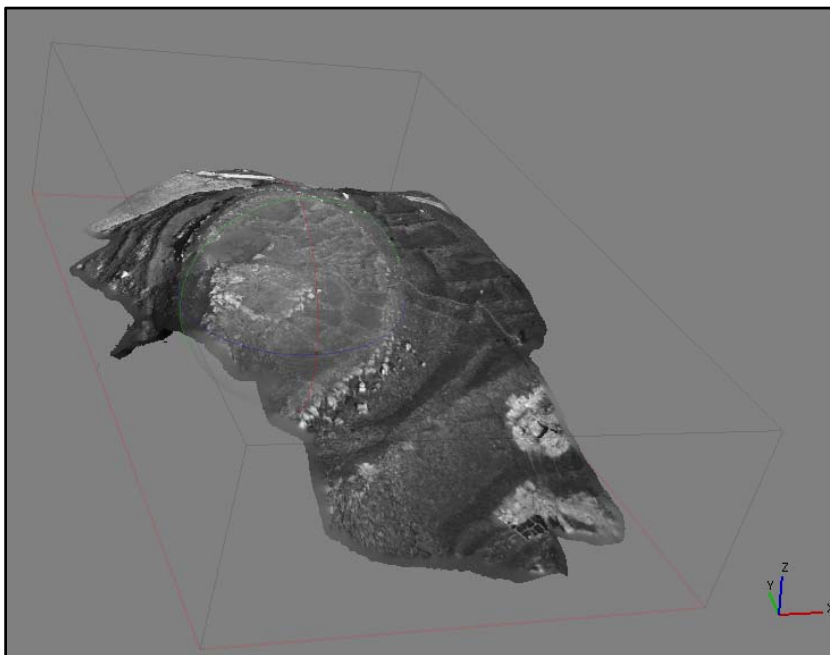


Figure 5.20 Textured 3D model representation of a site and its image locations obtained with Agisoft PhotoScan Professional

Four resampling methods exist:

- 1) mosaicing blends low frequency components of overlapping images, taking picture detail from high frequency components of the nearest single image;
- 2) averaging weighs pixel by distance from centre and calculates a weighted average DN using bilinear interpolation;
- 3) minimum DN of closest image or
- 4) maximum DN of closest image is used (Ovod 2015).

Finally, an orthophoto mosaic and DEM may be exported (Figure 5.21). The white areas within the model are holes, which have not been filled but may be interpolated.

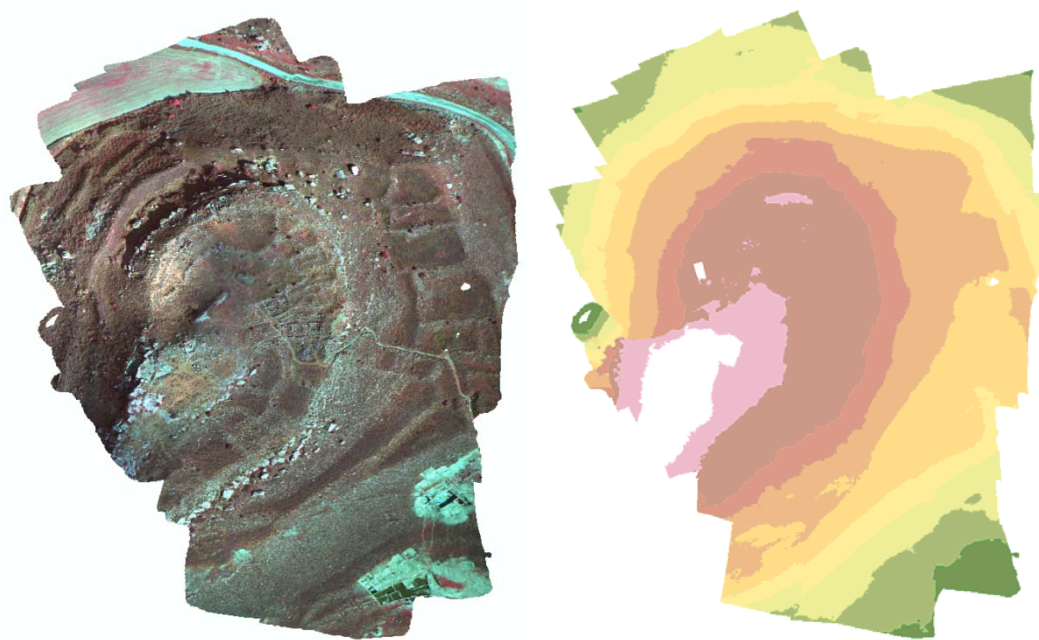


Figure 5.21 Orthophoto-mosaic and DEM retrieved by structure from motion software

Figure 5.22 summarizes the pre-processing chain for the multispectral MiniMCA-6 data from raw data to orthophoto mosaics applied in this work.

RADIOMETRIC
PRE-PROCESSING

USE OF VIGNETTING
CORRECTED,
ALIGNED PHOTOS

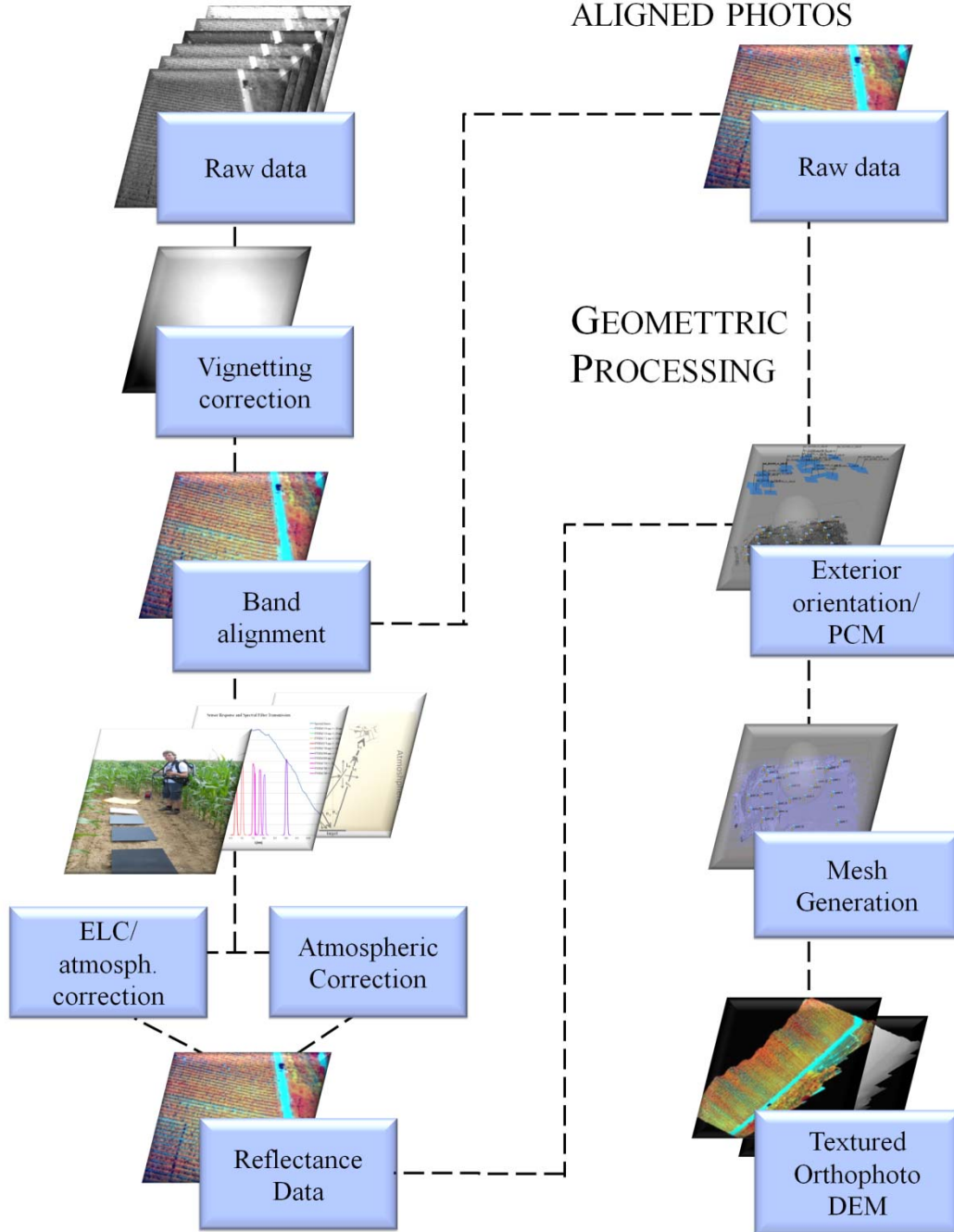


Figure 5.22 Pre-processing chain applied to multispectral data

5.4 Discussion of Pre-processing Steps

Band-to-band image alignment is supposed to be tackled by a calibration file which is ideally created after each filter change or camera focusing. Tetracam Inc. suggests to use objects at infinite distances. Another approach is to use a target pattern (provided for example, by the SfM software calibration tools) which should be photographed to compute lens calibration. The MiniMCA-6 is generally set to be focused for infinite objects, thus rendering focused image acquisition of close calibration patterns difficult. Alternatively, the Tetracam Inc. approach of iteratively solving for rotation/scaling and off-set was chosen for each image campaign. Other authors have programmed feature-matching algorithms to tackle band alignment (Laliberte et al. 2011).

ELC for correction of radiometric effects during image acquisition is widely used (Smith and Milton 1999; Baugh and Groeneveld 2007; Laliberte et al. 2011; Del Pozo et al. 2014) and has shown to retrieve reliable results as Figure 5.16 and Table 5.5 have shown. To account for non-linear radiometric effects atmospheric correction is required. ATCOR-4 has been developed for airborne scanner data, yet UAV images are central projections. So, correction of illumination geometry and BDRF are not strictly correct. However, errors remaining from lack of consideration of the central projection geometry, have shown to be of minor magnitude and have therefore been accepted for this study. Beside, DTM describing the terrain with required accuracy for that scale can only be retrieved from the UAV images themselves by e.g. SfM procedures (see the following sections) which still need to be derived from the point cloud modeling. Ideally, this demands a future processing chain of a) correction and calibration of camera errors, b) model a point cloud by SfM techniques to obtain a DTM to feed into c) an atmospheric and topographic correction procedure incorporating camera attitudes and reference targets followed by d) dense point cloud modelling and orthomosaicing to reflectance images.

6 Filter Wavelength Selection, Sensitivity Analysis and Scale Issues of the Multispectral Camera

In this chapter, the sensitivity of the UAS-based multispectral remote sensing of vegetation parameters in relation to appropriate filter wavelengths and viewing and illumination geometries are scrutinized. Bidirectional reflectance measurements of maize, grassland and barley were randomly simulated varying different levels of LAI or Chla+b and other parameters, followed by wavelength selection algorithms to derive appropriate filter wavelengths. For the canopy reflectance simulations, the PROSAIL model has been selected (Feret et al. 2008; Jacquemoud et al. 2009). Additionally, bidirectional reflectance derived from the UAS were compared to modeled canopy reflectances, and common vegetation indices used in this thesis and in the literature were computed for the same canopy to get an indication of the BDR effects when using the multispectral data. BDR effects and other factors influencing the spectral signature of crop canopies have been described in detail in chapter 3. Finally, “atmospheric effects” for the low-altitude UAS flights were investigated by recording multispectral images from different heights.

6.1 The PROSAIL Canopy Reflectance Model

For row-structured crops, recently a number of row structure reflectance models were developed or further adapted to gain further insight to BDR effects for inhomogeneous crop canopies of which only some are mentioned here: Yao et al. (2008) introduced a bi-directional gap probability model. Yan et al. 2012 (2012) showed that even more simple geometrical object models (GO models) treating the row crop as a function of leaves clumping may well be used to model BDR. Combinations of geometrical object models including radiative transfer within the canopy (GORT models) are applied (see Zhao et al. 2010 for a more detailed overview) treating row crops as geometric opaque rectangular solid objects, 3D computer simulation models such as the 3D radiosity-graphics model (RGM) adapted by Qin and Gerstl (2000), and the hybrid geometric optical and radiative transfer row model based on SAIL developed by Zhao et al. (2010). Although row crops were analyzed, there were not, to the author’s knowledge, any publicly available adequate reflectance models available yet. The promising row

model of Zhao et al. (2010) which tends to assimilate the SAILH model with closing canopies is currently being inverted.

Within row crops, the clumping of leaves along the rows, the soil influence and multiple scattering will contribute significantly to the reflected signal (Zhao et al. 2010, Yan et al. 2012), yet, here, row crops were studied when the canopy was already more or less homogenous.

The aim of this experiment was to define sensitive filter wavelengths to the variation of plant biophysical and structural parameters such as Chl_{a+b} and LAI, and to estimate the impact of varying sun-sensor viewing geometries on the retrieved canopy reflectance and commonly used vegetation indices obtained from UAS-based multispectral images of a maize field. PROSAIL has been shown to be useful for designing and evaluating vegetation indices (Haboudane et al. 2002; Zarco-Tejada et al. 2004; Jacquemoud et al. 2009).

The PROSAIL simulation model was selected for this study. The model code is freely distributed and has been widely used in the remote sensing community resulting in an abundance of applications published in recent years (Jacquemoud et al. 2009; Barman et al. 2010; Thorp et al. 2012; Tripathi et al. 2012; Mobasheri and Fatemi 2013, a.o). The PROSAIL simulation model is a combination of PROSPECT leaf optical properties model and SAIL, a canopy bidirectional reflectance model (Jacquemoud 1993, Feret et al. 2008; Jacquemoud et al. 2009). PROSPECT assumes the leaf as a set of absorbing plates with isotropic scattering, and requires input about the leaf structure (leaf structure parameter N : number of compact layers and air/cell boundaries inside the mesophyll) and leaf biochemical contents (Table 6.1) to model directional-hemispherical reflectance and transmittance. (Jacquemoud et al. 2009).

SAIL (Scattering by Arbitrary Inclined Leaves) is a radiative transfer model for canopy reflectance. SAIL assumes a horizontal and homogenous infinite canopy layer (Lambertian reflector) with uniform leaf optical properties (Verhoef 1984, Jacquemoud 1993). Canopy morphology is described by leaf area index, discretized leaf inclination distribution function (LIDF) describing leaf inclination and azimuth, and layer thickness (Verhoef 1984). Other parameters used are leaf reflectance and transmission, background/soil reflectance and fraction of incident diffuse/direct solar radiation, sun and sensor zenith, and azimuth between these two (Verhoef 1984, Jacquemoud 1993). In this study, SAIL5B was used which additionally incorporates a hotspot parameter as a function of leaf size and canopy height.

The PROSAIL_5B version for Matlab was selected for this work and couples the SAIL and PROSPECT models for simulations of spectral canopy hemispherical and directional reflectance in forward and inverse directions (Figure 6.1).

Table 6.1 Required input parameters for coupled PROSAIL model

Parameter	Symbol	Unit
SAIL		
Leaf area index	LAI	-
Leaf inclination distribution function	LIDF	-
Hot spot parameters	s_L	-
Soil reflectance factor	ρ_{soil}	-
Ratio of diffuse to total incident radiation	SKYL	-
Solar zenith angle	θ_{solar}	$^{\circ}$
Sensor/observer zenith angle	θ_{sensor}	$^{\circ}$
Relative azimuth between sun and sensor or observer	$\Phi_{\text{solar-sensor}}$	$^{\circ}$
PROSPECT		
Leaf structure parameter	N	-
Chlorophyll a+b content	Chl_{a+b}	$\mu\text{g cm}^{-2}$
Carotenoid	C	$\mu\text{g cm}^{-2}$
Equivalent water thickness	C_w	cm
Dry matter content	C_m	g cm^{-2}
Brown pigment content	C_{bp}	-

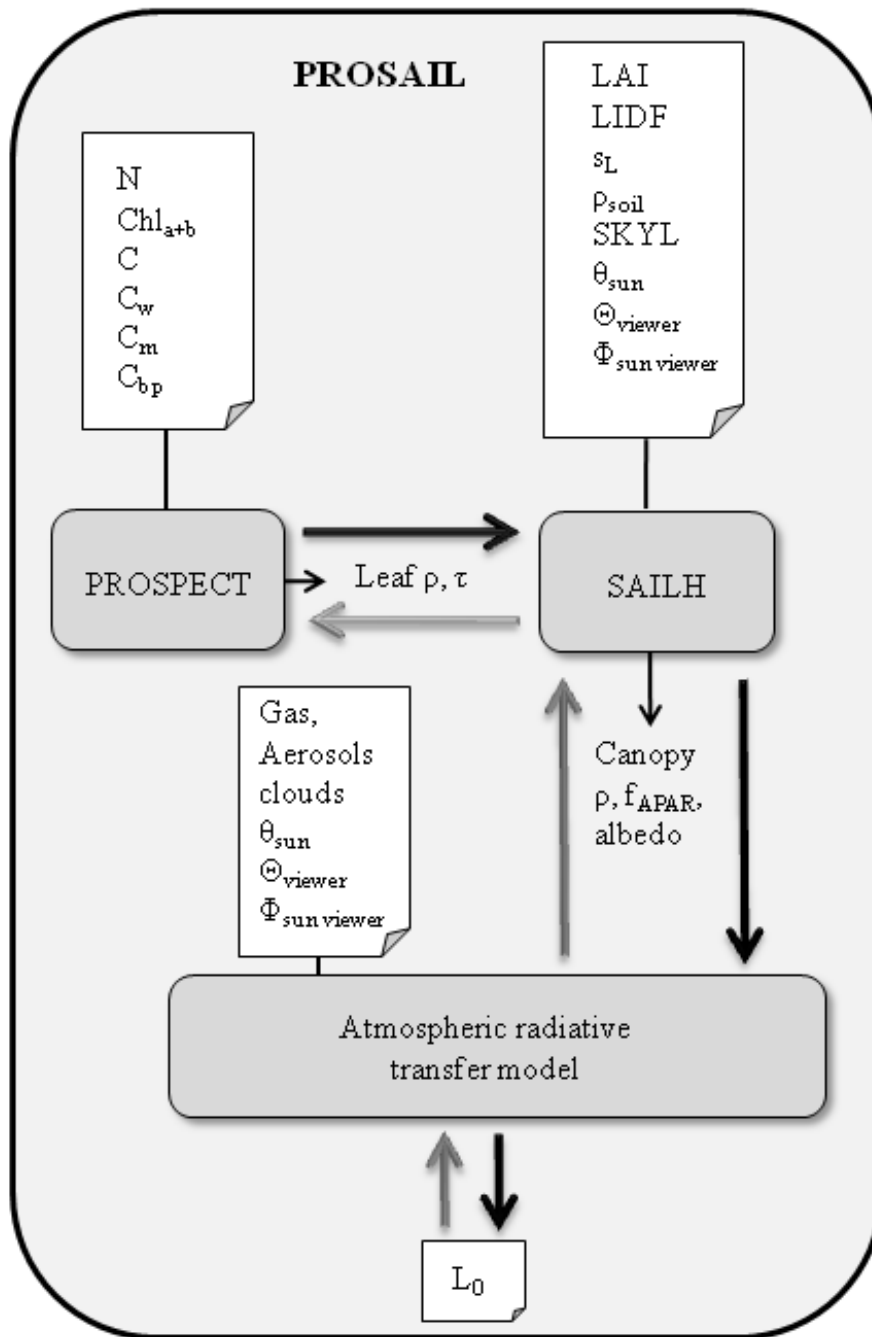


Figure 6.1 PROSAIL coupled model: black arrows indicate forward modelling mode, grey arrows indicate inverse modelling mode (mod. from Jacquemoud et al. 2009)

6.2 Filter Wavelength Selection

6.2.1 Introduction

As has been described in chapter xxx, the MiniMCA-6 has a spectral monochromatic response in the VIR/nIR range between 400 nm to 1000 nm of the electro-magnetic spectrum. The objective was to select sensitive filter wavelengths to adequately retrieve differences of key plant parameters such as Chl, LAI, carotenoids, leaf water content, etc.. The variation of canopy reflectance spectra has been discussed in detail in chapter 3. Several band selecting techniques have been introduced since the upcoming of hyperspectral remote sensing data. Prior to the millennium, the definition of optimal wavelengths has mostly been carried out by linking vegetation spectral (leaf- and canopy-level) to biochemical parameters by selecting appropriate band combinations for band indexing.

Hansen and Schjoerring (2003) checked “broadband” (30 nm) and narrow-band (10 nm) combinations of normalized differenced vegetation indices within the range of 438nm to 883 nm (1 nm-width) canopy spectrometer measurements of winter wheat to derive optimal wavelengths for the prediction of green biomass (GBM), LAI, Chl-concentration (Chl_{conc}), Chl-density ($\text{Chl}_{\text{density}}$) leaf nitrogen concentration (N_{conc}), leaf nitrogen density ($\text{N}_{\text{density}}$). The linear regression analysis between canopy reflectance and plant parameters for each wavelength obtained for winter crop canopies is illustrated in Figure 6.2.

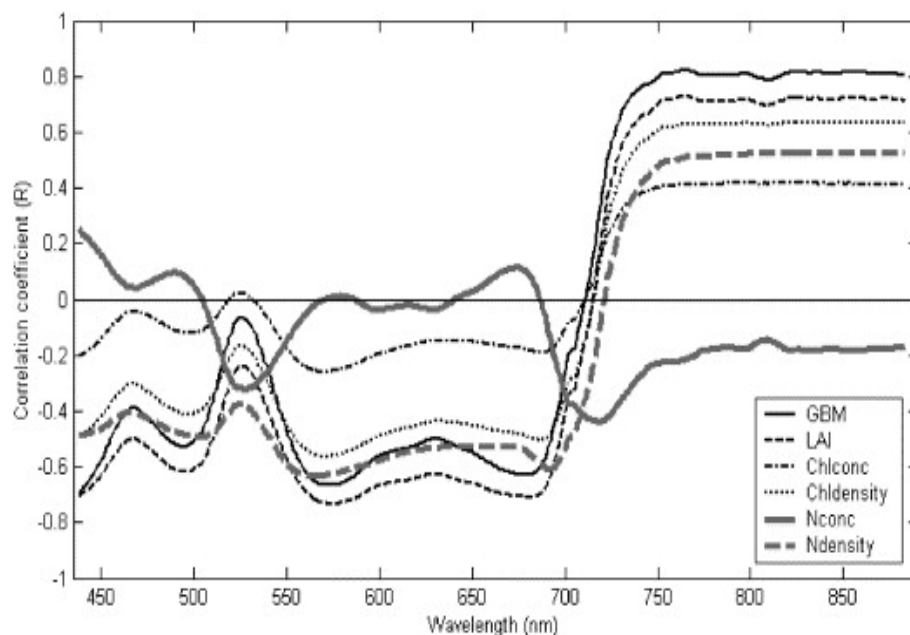


Figure 6.2 Coefficient of determination (R^2) for linear regression of canopy reflectances and plant parameters for the given wavelengths. Abbreviations: GBM: green biomass, Chl_{conc} : Chl_{a+b} , N: leaf nitrogen conc: concentration (Source: Hansen and Schjoerring 2003, p.545)

Bands located within the red and red-edge region were mostly retrieved for NDVIs for GBM, LAI, $Chl_{density}$, and $N_{density}$. GBM and LAI also were successfully estimated by NDVIs with wavelengths around the red edge (690-760 nm) and green area (521-565nm). For Chl_{conc} and N_{conc} the blue and green or red bands were most effective. The authors additionally found that narrow bands outperformed the broadbands.

Around the millennium, the multivariate calibration method based on bilinear partial least squares regression (PLS) found its way into the remote sensing community (van den Broek et al. 1996; Hansen and Schjoerring 2003; Udelhoven et al. 2003). Hansen and Schjoerring (2003) used it for the optimal wavelength detection. The method reduces the high amount of measured collinear spectral variables to few non-correlated principal components (PC). The authors found two PCs for the prediction of LAI and six for the prediction of GMB and N_{conc} , and PLS increased all R^2 values for these parameters.

For leaf water and namely EWT, the MiniMCA-6 monochromatic response is not ideal, as leaf water content is best estimated by including bands located in the SWIR region of the electromagnetic spectrum and nIR wavelengths (Gao 1996; Ceccato et al. 2001; Ordonez et al. 2011; Mobasheri and Fatemi 2013). This is due to the fact, that reflectance in the nIR is mainly influenced by internal structure and dry matter, yet, the SWIR is additionally influenced by the vegetation water content (Ceccato et al. 2001, Song et al. 2011). Mobasheri and Fatemi (2013) used the least square method of linear relationships between EWT with the measured reflectance in different parts of the spectrum between 400 nm to 2500 nm. Highest R^2 values were found for the 1030 nm to 1380 nm region, although the peaks and depressions for the R^2 within the VIS/nIR region also may also be useful, and in the study potentially useful local maxima were found at 425 nm (R^2 0.223) and 750 nm (R^2 0.284) and local minima of 686 nm (R^2 0.056) and 979 nm (R^2 0.158) (Figure 6.3).

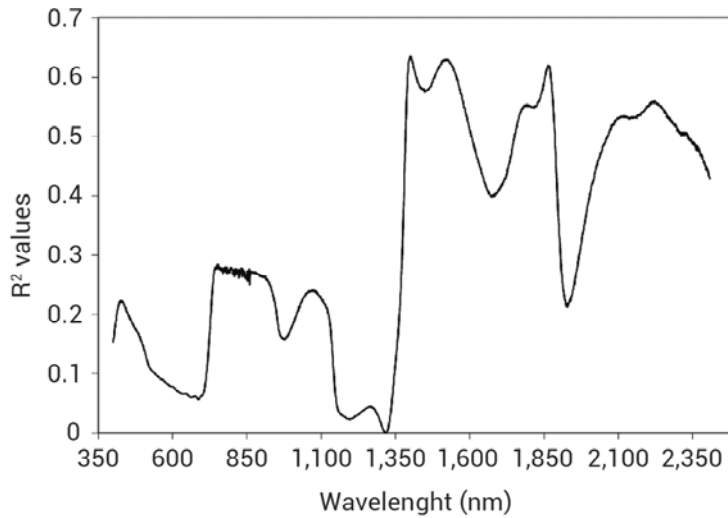


Figure 6.3 R^2 values of linear relationships between EWT and leaf reflectances values (Mobasheri and Fatemi 2013, p.198)

Song et al. (2011) used a PLS following a principal component analysis (PCA), to determine wavelength combinations suitable for predicting biochemical parameters of Chl, nitrogen of paddy rice leaves. They found higher numbers of band combinations (215) to produce the largest coefficient of determination compared to two-band combinations, but that 4 wavelengths increased the coefficient of determination to 0.82 for the prediction of nitrogen cultivation levels (552, 675, 705 and 776 nm).

Among all the wavelength selection techniques, no single best method may be suggested as they all depend on training sample size, number of desirable components and spectral ranges used (Hansen and Schjoerring 2003; Song et al. 2011).

In this work, the aim is to support suitable filter wavelengths prior to vegetation assessment, possibly applicable to a range of biochemical parameter analyses.

6.2.2 Spectra Simulations

Again using the PROSAIL model, random hemispherical reflectances were simulated for grassland, barley and maize within plant parameter value ranges obtained by either measurements or found in the literature (Table 6.2). Within each run, 10000 reflectances were simulated within the given ranges. Brown pigment (C_{bp}) were uniformly set to 0, carotenoids to $10 \mu\text{g}/\text{cm}^2$. A sun zenith angle of 45° was set and a clear sky was being simulated with a ratio of diffuse and direct radiation of 0.1 (SKYL) (Atzberger and Richter 2012).

Table 6.2: Range limits, and fixed values of input plant variables for different crops used for the PROSAIL model

Input variable	Unit	Minimum	Maximum	Fixed Value
Maize Schneider and Manakos 2003; Duan et al. 2014				
Chlorophyll content (Chl_{a+b})	$\mu\text{g}/\text{cm}^2$	23	101	68
Dry matter content (C_m)	g/cm^2	0.002	0.03	0.009
Equivalent water thickness (C_w)	g/cm^2	0.008	0.045	0.016
Leaf area index (LAI)	m^2/m^2	0.1	6	4.379
Leaf structure parameter (N)	unitless	1	2	1.3
Average leaf angle (angl)	degrees	43	77	50
Hot spot size (s_L)	mm^{-1}	0.05	1	0.2
Soil brightness parameter (ρ_{soil})	unitless	0.5	1.5	1
Grassland Dorigo et al. 2009, Darvishzadeh et al. 2011				
Chlorophyll content (Chl_{a+b})	$\mu\text{g}/\text{cm}^2$	15	45	30
Dry matter content (C_m)	g/cm^2	0.005	0.0135	0.009
Equivalent water thickness (C_w)	g/cm^2	0.0188	0.0231	0.015
Leaf area index (LAI)	m^2/m^2	0.5	7	2
Leaf structure parameter (N)	unitless	1.5	1.9	1.3
Average leaf angle (angl)	degrees	40	77	60
Hot spot size (s_L)	mm^{-1}	0.05	1.5	0.2
Soil brightness parameter (ρ_{soil})	unitless	0.5	1.5	1
Barley Berjón et al. 2013; Yu et al. 2014				
Chlorophyll content (Chl_{a+b})	$\mu\text{g}/\text{cm}^2$	7	8	30
Dry matter content (C_m)	g/cm^2	0.002	0.012	0.009
Equivalent water thickness (C_w)	g/cm^2	0.004	0.024	0.015
Leaf area index (LAI)	m^2/m^2	0.1	8	2
Leaf structure parameter (N)	unitless	1.1	1.9	1.3
Average leaf angle (angl)	degrees	40	77	40
Hot spot size (s_L)	mm^{-1}	0.05	1.5	0.2
Soil brightness parameter (ρ_{soil})	unitless	0.5	1	1

Furthermore, to obtain sensitive filter wavelengths for the most commonly retrieved parameters from remote sensing data, Chl_{a+b} and LAI, additional 10000 reflectance spectra were generated while only varying Chl_{a+b} and LAI values within the given ranges (Table 6.2), respectively. Other parameters were then set to fixed values. The simulated spectra were divided into training and validation data, both samples with $n = 5000$.

6.2.3 Wavelength Selection Algorithms

The R Toolbox Subselect package was applied for the statistical analysis. Four different search algorithms were compared for grassland spectra: (1) Genetic Algorithm (GA), (2) Simulated Annealing (SA), (3) Multiple least square regression analysis and (4) step-wise multiple linear regression analysis (stepwise MLR). The algorithm fitting best between training and validation data were to be applied. As the MiniMCA-6 camera used in this study has six cameras, the target was to retrieve six filter band central wavelengths (CWL). Additionally, for grassland it was to be tested how filter wavelength locations varied when only three and four filters were to be selected.

GA is an evolutionary algorithm or stochastic search algorithm mimicking natural selection in biological evolution. For each cardinality k (6), i.e. the number of targeted wavelengths, the evolution starts with an initial random population of size $n = 5000$ which is divided into two couples and subsequently generates an offspring, a new k -variable subset, inheriting properties from the parents. A criterion value ranks parents and offsprings and the best parent/offspring pair in relation to wavelengths will present the next generation. The evolutionary process is steered by exploration and exploitation. “Exploration is the creation of population diversity by exploring the search space, and is obtained by genetic operators”, i.e. “mutation and crossover” (Scrucca 2013, p.3). Exploitation reduces the population diversity by survival of the fittest (i.e. wavelengths). Convergence criteria terminates the evolutionary process (Scrucca 2013). The termination rule is given by the number of generations (please refer to Cerdeira et al. 2014, p.29-33 for further details).

SA describes a heuristic optimization algorithm for solving unconstrained and bound-constrained optimization tasks like e.g. the traveling salesman problem (Kirkpatrick et al. 1983). It models the physical process of heating a metal and slowly cooling it down (i.e. “annealing”) so that metal atoms have time to rearrange themselves to stable crystals at low system energy (please refer to Cerdeira et al. 2014, p.2-6 for further details). An initial k -variable subset is randomly selected and put into the SA algorithm. A random subset within the neighbourhood of the current subset is selected and according to

the SA rule and updates the current (wavelength) subset when its subset variables improve the criterion.

The **RLI** algorithm searches for a k-variable subset serving as a representative for the whole set. Initially, a k-variable subset is randomly defined from the full set, and other variables are put aside into a queue. Then one variable from the queue is taken and the enhancement of the criterion value, when replacing each individual k-value, is tested. When the criterion value is improved, the current subset will be updated (please refer to Cerdeira et al. 2014, p.47-50 for further details).

For all algorithms described so far, the τ^2 -criterion had been selected. It is related to the Wilk's lambda statistic (λ), a measure of multivariate coherence, (Cerdeira et al. 2014):

$$\tau^2 = 1 - \lambda^{(1/r)}$$

where r is the rank of effect matrix.

Last not least, a stepwise forward **MLR** was carried out to retrieve the six wavelengths that best predict the biophysical parameters Chl and LAI. As criterion the Akaike's An Information criterion (AIC) was taken (The R Core Team 2014, p.1160). The algorithm starts with one wavelength and depending on the decision criterion keeps the wavelength variable if it improves the model. The modelling is finished when there is no further improvement.

6.2.4 Results

6.2.4.1 Comparison of Wavelength Selection Algorithms

The correlation spectra for simulated Chl_{a+b} values and simulated mean grassland reflectance show two distinct minima at around 550 nm and around 720 nm with a peak in-between at around the red region (Figure 6.4).

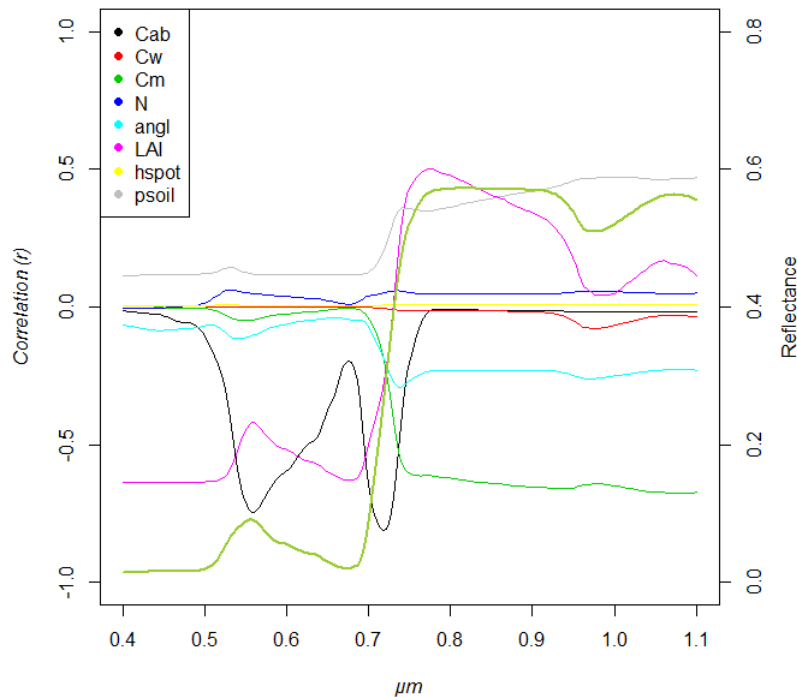


Figure 6.4 Correlation spectra between simulated reflectance spectrum and plant variable (bold green line: simulated Chl_{a+b} spectrum for grassland)

LAI values show distinct features around the red/red edge and nIR. Although not further studied in this context, leaf water content (Cw) only shows a weak correlation minimum at around the water absorption around 970 nm. Dry matter content (Cm) showed higher negative correlation from the red edge to the nIR region. N shows only weak correlations at around 550 nm and from the red edge to the nIR.

Among the wavelength selection algorithms, GA, RLI and SA generally yielded the best correspondence between measured (training) and predicted (validation) data, although all selection algorithms predicted variables with an adjusted R^2 of ≥ 0.9 (Figure 6.5).

Except for the stepwise MLR, the wavelength selection algorithms do not retrieve one single but rather a set of solutions, the best fit is defined by minimizing the τ^2 criterion. Therefore, there is not one single solution, yet from the plot showing the range of selected wavelengths, one may infer sensible filter wavelength locations or ranges (Figure 6.7). Here, the filters should be located along the slopes of the green reflectance peak and at the red absorption minimum. The blue squares hereby indicate ten different solutions of the search algorithms, the red squares show the selected wavelengths with the highest overall R value.

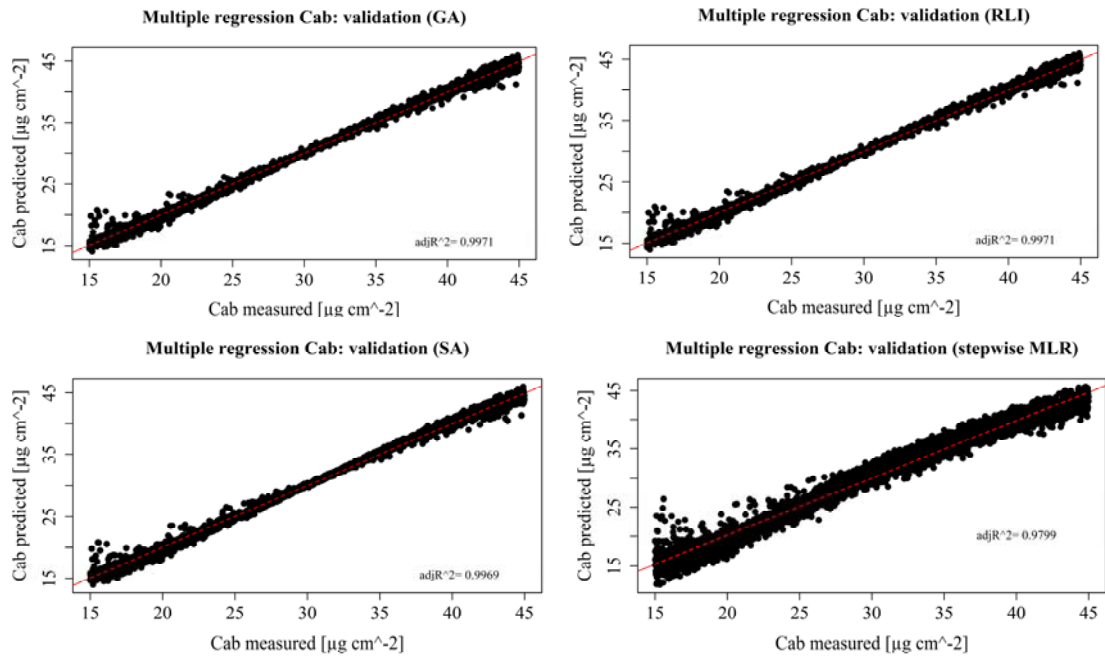


Figure 6.5 Scatter plots for wavelength selection algorithms to predict Chl_{a+b}

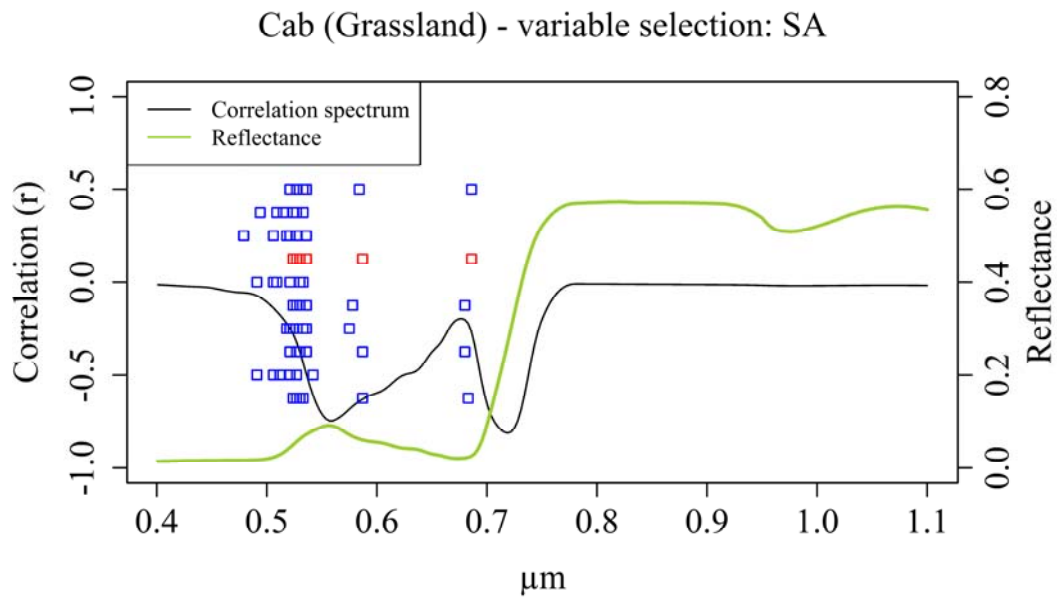


Figure 6.6 Selected optimal filter locations for the prediction of grassland Chl_{a+b}

As a summary, Figure 6.7 shows for grassland the leaf pigment Chl_{a+b} (here Cab in figures) and LAI, the retrieved wavelengths for all selection algorithms. GA, SA and RLI show almost similar wavelengths regions for the prediction of Chl_{a+b} located along the slopes of the green peak and in the red region of the visible spectrum.

For the assessment of LAI, filter centre wavelengths were selected from short visible wavelengths (RLI) to only nIR wavelengths for GA, SA and stepwise MLR.

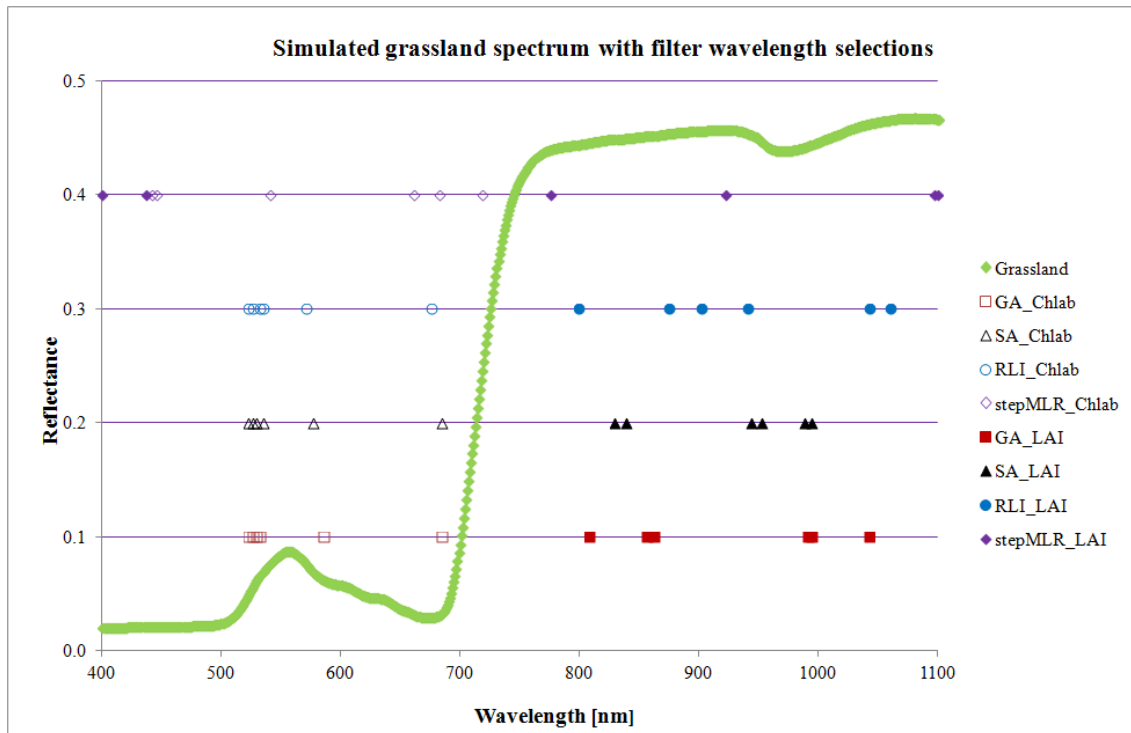


Figure 6.7 Simulated grassland spectrum with selected filter wavelengths for Chl_{a+b} and LAI

6.2.4.2 Crop-type Dependent Wavelength Selection

The respective wavelengths selected in Figure 6.7 are listed in for the crop types and wavelengths selection algorithms.

Table 6.3 Filter wavelength selection for Chl_{a+b} and LAI for each selection algorithm

Selected Wavelengths [nm]	1	2	3	4	5	6	Multiple R^2
Grassland							
GA_ Chl_{a+b} λ	523	526	529	532	586	685	0.9971
SA_ Chl_{a+b} λ	523	526	529	535	577	685	0.9969
RLI_ Chl_{a+b} λ	523	526	532	535	571	676	0.9971
Stepwise MLR_ Chl_{a+b} λ	442	445	541	661	682	718	0.9799
GA_ LAI λ	808	856	862	991	994	1042	0.9714
SA_ LAI λ	829	838	943	952	988	994	0.9707
RLI_ LAI λ	799	874	901	940	1042	1060	0.9769
Stepwise MLR_ LAI λ	400	436	775	922	1096	1099	0.8964
Barley							
GA_ Chl_{a+b} λ	520	523	526	529	532	535	0.9769
SA_ Chl_{a+b} λ	490	505	511	523	526	532	0.9769
RLI_ Chl_{a+b} λ	520	523	526	529	532	535	0.9769
Stepwise MLR_ Chl_{a+b} λ	541	664	715	742	976	982	0.9269
GA_ LAI λ	802	874	898	940	1042	1057	0.9507
SA_ LAI λ	865	880	910	976	997	1024	0.9554
RLI_ LAI λ	808	835	865	1030	1033	1069	0.9489
Stepwise MLR_ LAI λ	400	775	913	1063	1066	1075	0.8236
Maize							
GA_ Chl_{a+b} λ	523	529	532	544	553	715	0.9777
SA_ Chl_{a+b} λ	523	526	535	544	553	715	0.9757
RLI_ Chl_{a+b} λ	505	508	511	526	529	532	0.9678
Stepwise MLR_ Chl_{a+b} λ	445	451	535	685	721	724	0.9047
GA_ LAI λ	484	862	931	1063	1069	1081	0.9524
SA_ LAI λ	484	865	931	1063	1069	1081	0.9525
RLI_ LAI λ	490	928	931	1063	1081	1093	0.9521
Stepwise MLR_ LAI λ	664	685	775	811	829	841	0.8000

For the other crop types, barley and maize similar results were obtained (Table 6.3). Looking at Chl , again, GA, SA, and RLI yielded similar results with high R^2 values of ~ 0.97 , and least residuals for the green part of the electromagnetic spectrum, for barley, a red/nIR spectrum was only selected for the stepwise MLR. For maize, another band within the red edge region was introduced (715-724 nm). The LAI is mainly predicted with wavelengths within the nIR, for barley. The stepwise MLR selection algorithm additionally retrieved a blue band at 400 nm. For maize also nIR bands were selected, and an additional band in the blue/green (GA, SA and RLI) or red region (stepwise MLR).

The GA iterations confirm the concentration of selected wavelengths next to the green peak, red (grassland) and red edge for Chl_{a+b} for grassland, barley and maize (Figure 6.8 - Figure 6.9).

Filter wavelengths for defining LAI are rather situated along the nIR plateau and located on both sides of the water absorption minimum at 970 nm (Figure 6.9), and in some cases below the green peak and blue region. Similar results were found by Schlerf et al. (2005), who analyzed the potential of narrowband ratio and orthogonal VI for hyperspectral Vis-shortwave IR (SWIR) and found them to be close to water absorption features.

If only three bands (Figure 6.10 top row) were to be selected, the filter locations vary around the red and blue region for grassland and the prediction of Chl_{a+b} ($R^2 = 0.9774$) and with four bands are situated along the green peak ($R^2 = 0.9898$). For LAI, the GA terminates with filters situated next to the water absorption feature for three bands ($R^2 = 0.9139$) and again along the nIR plateau and next to the water absorption for four bands ($R^2 = 0.9536$).

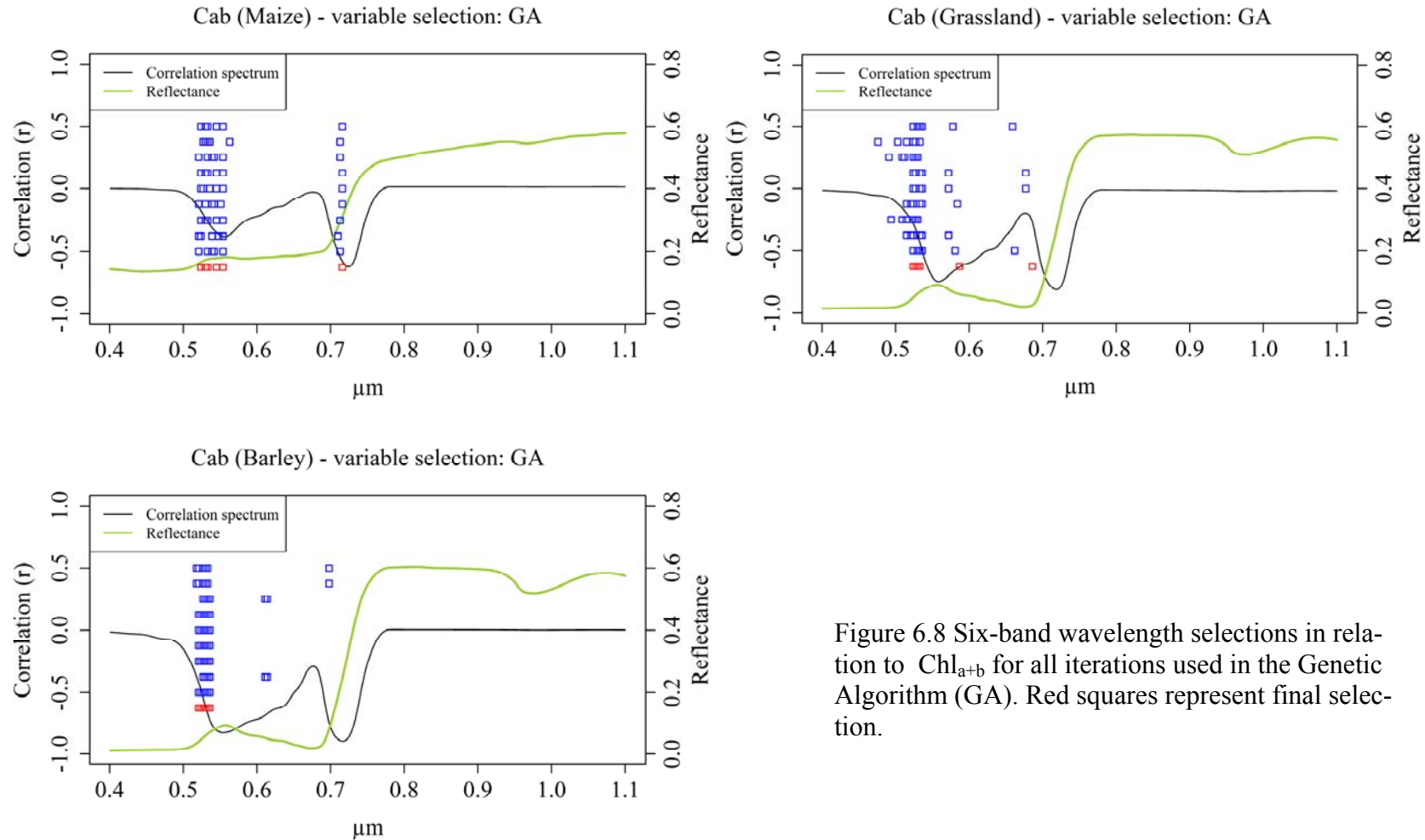


Figure 6.8 Six-band wavelength selections in relation to Chl_{a+b} for all iterations used in the Genetic Algorithm (GA). Red squares represent final selection.

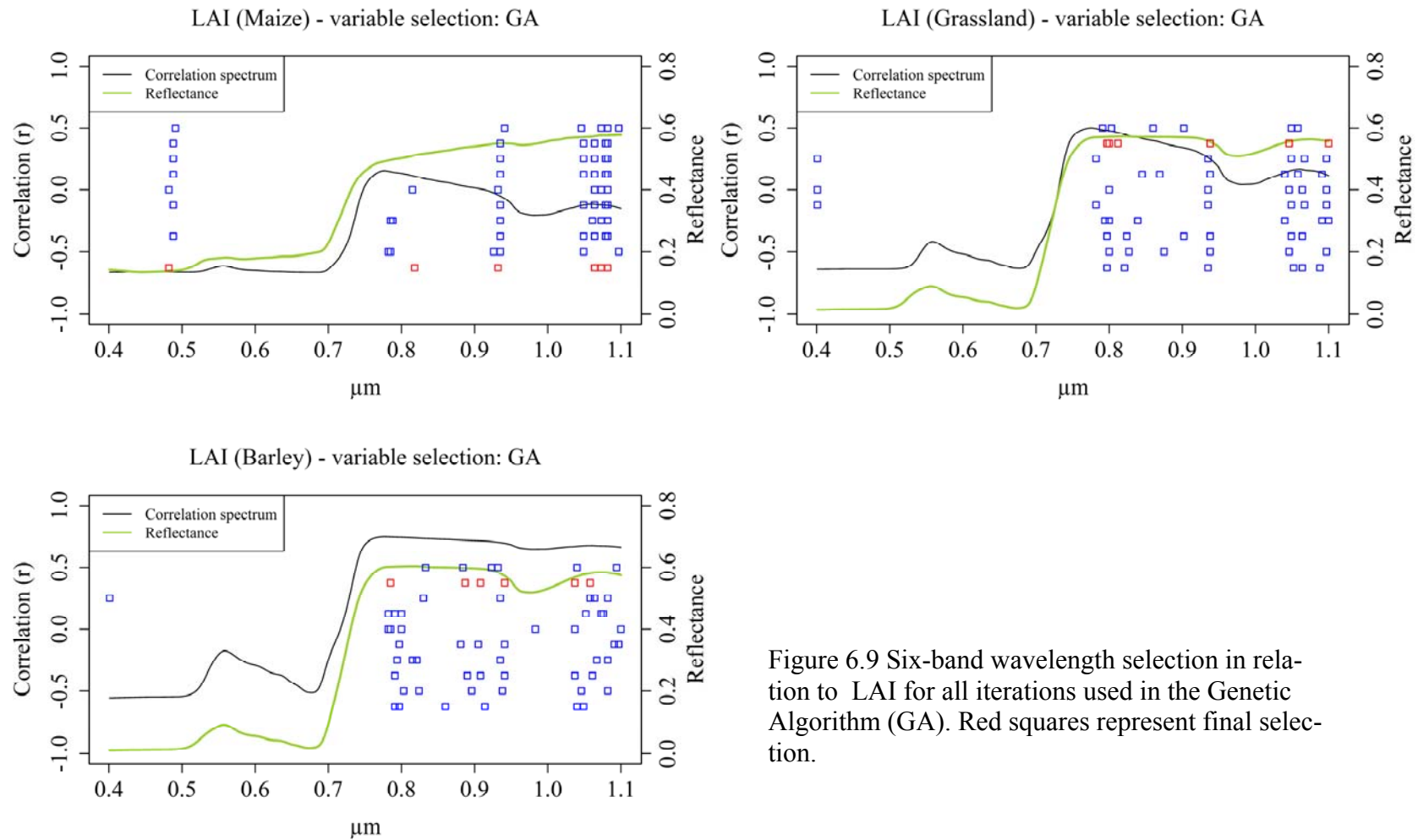


Figure 6.9 Six-band wavelength selection in relation to LAI for all iterations used in the Genetic Algorithm (GA). Red squares represent final selection.

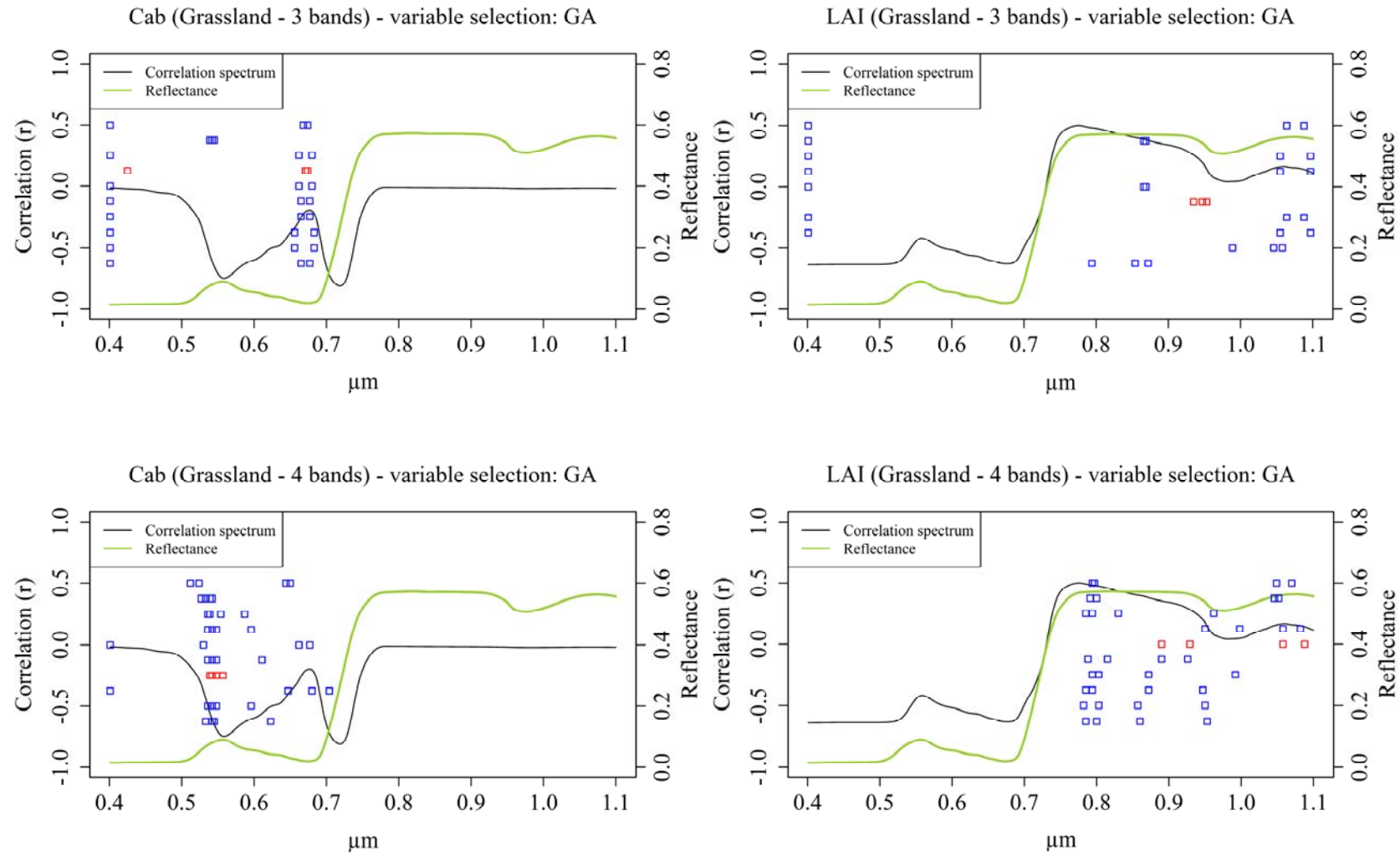


Figure 6.10 Three- (top) and four-band (bottom) filter wavelength selections retrieved by Genetic Algorithm (GA) for grassland. Red squares represent final selection.

6.2.5 Discussion

General sensitive wavelength locations had been illustrated graphically by Wantzenrieder for maize and grassland (2011) and in Figure 6.4 for grassland. The interpretation of these graphs already allows the determination of obvious spectrally sensitive ranges to biophysical parameters and put forward key sensitive ranges for vegetation: the green peak and its slopes, the red absorption minimum, the red edge and its slope, the nIR plateau and short-wave to mid-wave IR for water content. The filter wavelength selection algorithms altogether retrieved similar critical wavelength ranges for the predicted plant variables Chl and LAI for grassland where six bands were to be selected. Especially, GA, SA and RLI delivered nearly matching filter centre wavelengths (Figure 6.8 Table 6.3) with an R^2 of well over 0.97. For the other crops, barley and maize, the filter locations varied slightly so that for barley only wavelengths along the shorter wavelength slope of the green peak were retrieved and for maize, right along the green peak and additionally a red-edge band was selected (Table 6.3). When smaller numbers of bands are selected (three and four-band combinations), filter CWL vary slightly more and lie at different locations (Figure 6.10): for grassland the three-band wavelength selection retrieved also blue. Filters in that range are neither possible for the MiniMCA-6 as its monochromatic response in that area is too low, and the signal would also be affected by strong atmospheric influences. For four bands optimal filters range along the green peak for Chl and for LAI, similar to the six-band combinations, along the nIR plateau (three filter wavelengths) and at both sides of the water absorption feature for four filters. The differences result from the fact, that there is no fixed solution to the search algorithms as can be seen by the respective blue squares in Figure 6.8-Figure 6.10.

To overcome the problem of retrieving varying band selections especially known from the step-wise MLR, Feilhauer et al. (2015) suggest to use a multi-method ensemble selection consisting of PLS-, random forest- (RFR) and support vector machine regression (SVMR). They found spectral locations in accordance with known absorption features.

For differentiating crops under nitrogen stress, Song et al. (2011) found for laboratory-derived hyperspectral leaf reflectances within the VIS/nIR region of the electromagnetic spectrum for paddy rice, the band CWLs 552 nm, 675 nm, 705 nm and 776 nm most appropriate for four-band combinations. For fluorescence analyses of green vegetation, intensive work on sensitive wavelengths and filter widths has been carried out within the ESA-FLEX program (Damm et al. 2010, Damm et al. 2011).

The results show that the filter CWLs chosen for the MiniMCA-6 (10 nm-FWHM: 531 nm, 551 nm, 571 nm, 673 nm, 702 nm, 753 nm, the 1 nm-FWHM 760 nm, 782 nm, 803 nm, 901 nm, 971 nm and 1 nm-FWHM 760 nm) are well suited for analyzing crop physical parameters Chl, LAI, N, leaf water and fluorescence, a.o. Filter had also been selected for these spectral ranges to conform to common vegetation indices used in the remote sensing community.

Further crops could be included in the ideal filter wavelength selection and also more plant parameters (leaf water, dry matter, structure a.o.) could have been varied to consolidate the findings. But a first overview with variations of all parameters except for the fixed proportion of diffuse to direct radiation, hot spot parameter and viewing angles, led to similar reflectance ranges. The choice between three to six target filters may also help to understand the ideal filter centre wavelengths and filter combinations to tackle more than one plant parameter at a time for quantitative analysis of key vegetation parameters.

6.2.6 Conclusion

All filter search algorithms used in this study (GA, SA, RLI and stepwise MLR) predicted the plant variables Chl and LAI with high R^2 values of $> 0.9 - 0.98$, best results were obtained with GA and SA (R^2 0.95 to > 0.99). The filter wavelength selection retrieved potentially ideal filter centre wavelengths to retrieve the key plant parameters Chl_{a+b} and LAI. These are

- for Chl_{a+b} : green peak from 520–570 nm, red absorption minimum (670 nm)
- for LAI: mainly nIR-plateau 800-900 nm, shoulders of water absorption feature (~ 970 nm).

Further crops could be included in the ideal filter wavelength selection and also more plant parameters (leaf water, dry matter, structure a.o.) could have been varied to consolidate the findings. But a first overview with variations of all parameters except for the fixed proportion of diffuse to direct radiation, hot spot parameter and viewing angles, led to similar reflectance ranges. The choice between three to six target filters may also help to understand the ideal filter centre wavelengths and filter combinations to tackle more than one plant parameter at a time for quantitative analysis of key vegetation parameters.

6.3 Bidirectional Reflectance Simulations and Measurements of a Maize Canopy Using a UAS Goniometer-Flight

6.3.1 Introduction

Bidirectional reflectance effects encompass the variation of the at-sensor received signal of non-Lambertian targets and alterations of viewing and illumination geometry depending on the target object characteristics, sensor and solar position at image acquisition. Huete and co-workers compared the NDVI with the soil-adjusted vegetation index (SAVI) for 5°-stepwise variations of viewing angles from 0-40° off-nadir and could show that SAVI behaved symmetrically with increasing VZA towards both shaded and illuminated sides, the NDVI behaved anisotropically (Huete et al. 1992). Epiphonio and Huete (1995) further investigated the indices' behaviour for different densities of alfalfa crops and showed that SAVI seemed more sensitive to nIR changes with higher amounts of vegetation, and increasing NDVI/decreasing SAVI values from antisolar to solar viewing geometries, the SAVI being of generally higher sensitivity to changing viewing angles.

Lelong et al. (2008) developed a method to balance received light quantity for UAS-derived multispectral images of a trial wheat plot. As their system was lacking an IMU, they employed an image-driven adaption of the Local Range Modification: 1) They started subsampling the image to 1/200 of the original pixels by bilinear interpolation; 2) they performed a Gaussian 3x3 filtering, 3) then over-sampled the image to its original size by bicubic interpolation; 4) inverted and scaled the image to 5) obtain a BDR-filter to be applied on the original image. However, this intensive pre-processing is not feasible for multitudes of aerial images for one flight. Hakala et al. (2010) used the Rahman Pinty Verstraete surface model (RPV) to correct UAS images derieved on a snow field. The semi-empirical model uses three parameters to obtain the bidirectional reflectance factor (BRF): incident illumination and observation directions, reflectance intensity, level anisotropy of the surface reflectance (here reference panels were used) and the amount of back- and forward scattering (Rahman et al. 1993).

These studies though, have worked on relatively homogenous, structure-poor, more or less flat target features. Only few studies so far, have focused on heterogeneous canopy structure where additionally row orientation, row gaps and soil background contribute to the signal (Guillen-Climent et al. 2012). The 3D radiative transfer Forest Light Interaction model (FLIGHT) has been used to study the influence of background substrate on the NDVI in orchards under varying daytime illumination to obtain the fraction of

intercepted photosynthetically active radiation (fIPAR) by scaling-up and model inversion of image NDVI values (Guillen-Climent et al. 2012).

Grenzdörffer and Niemeyer (2011) looked into BDRF-measurements of agricultural surfaces obtained also with a md4-1000. A hemispherical flight pattern of screw-shaped circular flight lines with increasing height and narrowing radii was conducted and the anisotropic reflectance behavior derived for a wheat plot. They found the anisotropic behavior in the principal plane to be minimal. They now look into how these factors may be incorporated into image analysis.

The main aim was to assess bidirectional reflectance effects on the signal obtained with the multispectral MiniMCA-6 in relation to changing sun-observer viewing geometries. Furthermore, the bidirectional performance of some selected, commonly used vegetation indices was to be studied in relation to the respective image acquisition geometries.

6.3.2 Data and Methods

Test site was a maize field at the Ehranger Flur, Germany situated at 49.8087° N, 6.697° E. The rows are oriented SSW-NNE, and the phenological development of the individual plant at stage \sim BBCH 38 (Lancashire et al. 1991) with a height of approximately 2 m (Figure 6.11).

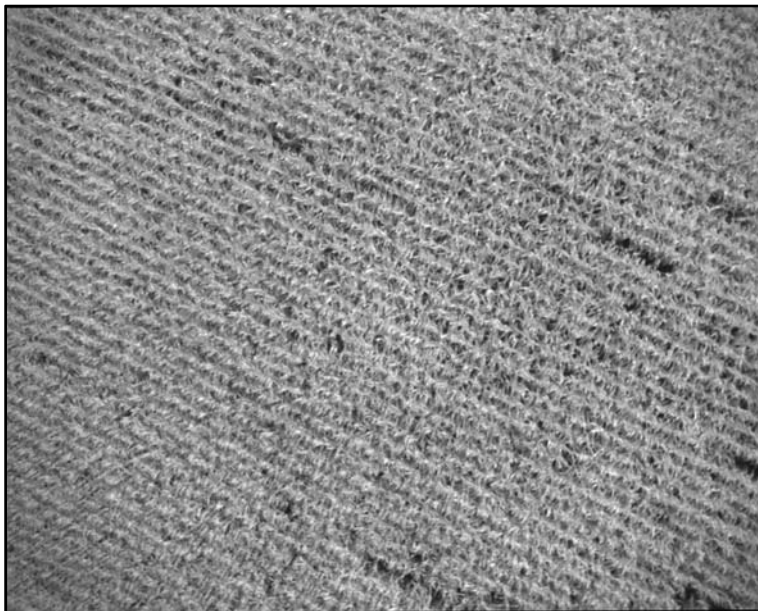


Figure 6.11: Raw UAS image of maize canopy (Tetracam MiniMCA-6 band 900 nm)

On 20/08/2011, a UAS flight at approximately 50 m above ground was carried out, following a circle of about 40 m in diameter around its centre and W-E, N-S cross sections

(Figure 6.12). Images were acquired at 11.45 h local MEST prior to solar noon at 12:27 h local MEST with a sun elevation of 46° and a sun azimuth position of 136° SE. The sky was clear and sunny. The multispectral MiniMCA-6 was set up to look at the central point of interest (POI) with viewing angles between 75° at the outer circle to 90° (nadir) in the centre position and 5° steps for the sensor zenith angle. Azimuth sensor positions in relation to N (0°) were taken at 30° steps. Filter wavelengths were selected to cover main vegetation reflectance characteristics with 530 nm, 550 nm, 570 nm, 670 nm, 700 nm, and 900 nm (see chapter 4.22 for filter description). Image pixel resolution was about 3 cm.



Figure 6.12: Goniometer-flight plan for maize field on the Ehranger Flur, Germany, presented on Google Earth data, image is oriented to the N (Google Earth: 28/04/2014)

Photo preprocessing was following the procedures described in chapter 5. The respective six band images were corrected for vignetting effects and aligned to retrieve multi-spectral images. With the help of in-situ derived reflectance measurements of reflectance panels with an ASD FieldSpec, the individual photo DNs were converted to reflectances by empirical line correction (chapter 5.2.5). A more detailed description of preprocessing may be found in Wantzenrieder (2011). Image reflectances were obtained by averaging the reflectances of an area of approximately 3 m in diameter around the POI situated at the centre of the respective image.

For modelling maize reflectance, field sample of top layer leaves were collected. Around the projected circle centre on the ground five maize plants were selected at the centre and about 1 m to the N, E, S and W via GPS and five leaf samples were cut of each plant a couple of days after the UAS flight. From these samples, fresh matter and dry weight were measured in the laboratory, to obtain the equivalent water thickness C_w and dry matter content C_m . Chl_{a+b} was retrieved with UV-160A Shimadzu photometer

wet-analysis (see chapter 4.5.1). Furthermore, LAI was measured at breast and knee-height at the same positions as sampling was taken.

Mean LAI, Chl_{a+b} content, C_w and C_m were used as parameter input for PROSAIL simulations of the particular viewing angles at the respective 26 UAS photo positions for the goniometer exercise. From drone position and attitude during the flight, observer zenith angle and azimuth values in relation to the sun position were retrieved for each image. Other parameters were retrieved from literature analysis (Schneider and Manakos 2003; Duan et al. 2014), *i.e.* carotenoid content of $10 \mu\text{g}/\text{cm}^2$, brown pigment content C_{brown} of 0, N of 1.3, p_{soil} coefficient of 1, diffuse/direct radiation factor SKYL of 0.1, and a hot spot effect S_L of 0.2; a leaf angle of $\sim 50^\circ$ was estimated in the field.

To illustrate the effect viewing geometry has on vegetation indices, additionally some widely used vegetation indices were computed to show their behavior with varying observer and azimuth angle (AA) (Table 6.4).

Table 6.4: List of vegetation indices used for Prosail simulations (subscripted λ in nm)

Vegetation index	Formulation	Author	Application
Simple Ratio Index	$\text{SR} = R_{\text{nIR}}/R_{\text{red}}$	Jordan 1969	Structural index, plant vitality
Normalized Difference Vegetation Index	$\text{NDVI} = (R_{\text{nIR}} - R_{\text{red}}) / (R_{\text{nIR}} + R_{\text{red}})$	Rouse et al. 1974	Structural index, plant vitality
Transformed Chlorophyll Absorption in Reflectance Index	$\text{TCARI} = 3[(R_{700} - R_{670}) - 0.2(R_{700} - R_{550})(R_{700} / R_{670})]$	Haboudane et al. 2002	Chl index, less influence of LAI
Optimized Soil-Adjusted Vegetation Index	$\text{OSAVI} = (1 + 0.16) (R_{\text{nIR}} - R_{\text{red}}) / (R_{\text{nIR}} + R_{\text{red}} + 0.16)$	Rondeaux et al. 1996, Haboudane et al. 2002	Chl index, less sensitive to soil background
Photochemical Reflectance Index	$\text{PRI} = (R_{531} - R_{570}) / (R_{531} + R_{570})$	Gamon et al. 1992; Gamon et al. 1997	Carotenoids/Chl index, Chl fluorescence, radiation use efficiency, water stress
Renormalized Difference Vegetation Index	$\text{RDVI} = (R_{\text{nIR}} - R_{\text{red}}) / (R_{\text{nIR}} + R_{\text{red}})^{0.5}$	Roujean and Breon 1995	Structural index related to fAPAR
Red Edge Ratio Index	$\text{RE} = R_{700}/R_{670}$	Part of TCARI; Zarco-Tejada et al. 2013, Zarco-Tejada 2013	Chl content
Normalized PRI	$\text{PRI}_{\text{norm}} = \text{PRI}/(\text{RDVI} * \text{RE})$	Zarco-Tejada 2013	Chl content, less sensitive to crown architecture, water potential, stomatal conductance

Average biophysical leaf parameters retrieved from field sampling and laboratory analysis are summarized in Table 6.5. The selected UAS images' viewing parameters are summarized in Table 6.6. 26 images were selected for simulation process.

Table 6.5: Measured field parameters for maize leaves as input to PROSAIL simulations

Sample	LAI	Chl _{a+b} [$\mu\text{g}/\text{cm}^2$]	C _m [g/cm^2]	C _w [g/cm]
1	4.13	67.524	0.095	0.016
E2	4.22	58.086	0.089	0.015
E3	4.28	69.166	0.098	0.015
E4	4.27	73.487	0.061	0.016
E5	5.01	69.238	0.046	0.015
Mean	4.38	67.500	0.078	0.016

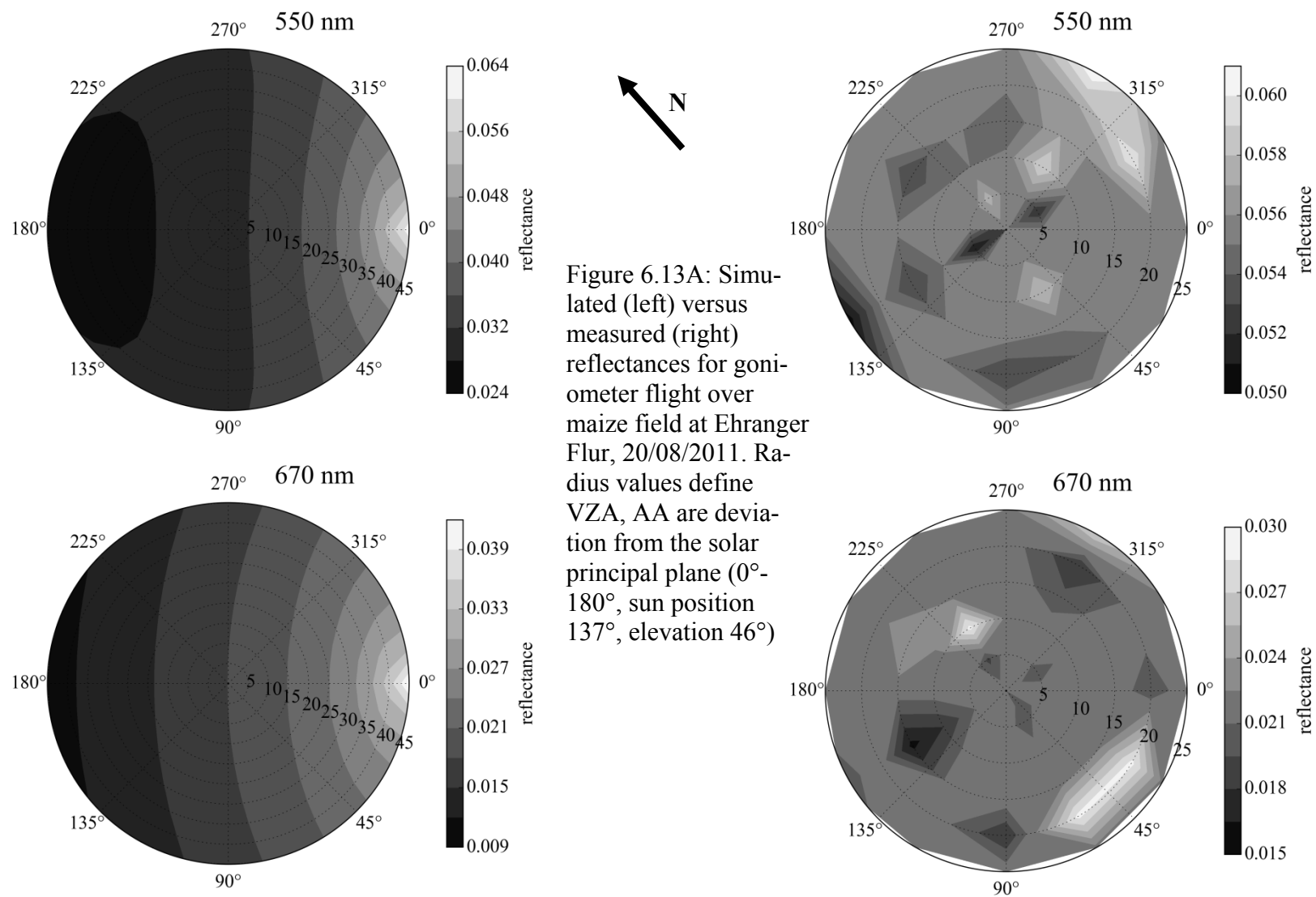
6.3.3 Results

The following polar plots (Figure 6.13A and B) show the differences for simulated hemispherical reflectances as obtained by PROSAIL and the actual reflectances retrieved from the maize canopy. The polar plot centres represent nadir viewing and the radius axis represents increasing viewing zenith angles (VZA). The circular/polar angles define the azimuth angles (AA) with deviation from the sun position, hence, the solar principal plane is defined along the 0°-180° axis. For all angle combinations where no UAS images were taken, the mean reflectance of all other photo samples of that respective band were used for interpolation. Image viewing and sun position geometries are listed in Table 6.6.

Table 6.6: Photo attitude parameters and derived observer and AA for PROSAIL input (as derived from the ATCOR4 solar position calculation tool)

Photo-number	UTC	Latitude	Longitude	GPS-Altitude [m]	Height [m]	Observer zenith [°]	Sun zenith [°]	Sun azimuth[°]	Azimuth (sun-observer) [°]
2	09:38:15	49.80894191	6.69708064	225.0	49.0	41.3	44.40	135.1	135
6	09:38:40	49.80893117	6.69694185	225.3	48.8	41.2	44.30	135.3	162
8	09:38:59	49.80885968	6.6968274	224.7	48.9	41.1	44.30	135.4	192
10	09:39:19	49.80876343	6.69680216	223.9	48.7	41.3	44.20	135.5	132
12	09:39:39	49.80867672	6.69684302	222.9	48.5	41.5	44.20	135.6	103
14	09:39:59	49.80860908	6.69694125	223.1	48.3	41.7	44.20	135.7	75
16	09:40:18	49.80858857	6.69709113	223.4	49.0	41.0	44.10	135.8	46
18	09:40:38	49.80862605	6.69722372	223.8	48.8	41.2	44.10	135.8	21
19	09:40:51	49.80866824	6.6973038	223.3	48.2	41.8	44.10	135.9	10
22	09:41:14	49.8087725	6.6973674	224.3	49.0	41.0	44.00	136.1	36
24	09:41:33	49.80886235	6.69733841	223.5	48.7	41.3	44.00	136.2	69
26	09:41:52	49.80892452	6.69721981	223.5	49.0	41.0	43.90	136.3	103
28	09:42:11	49.80891244	6.69706509	223.8	48.8	41.2	43.90	136.4	138
31	09:42:39	49.80885706	6.69706532	224.3	49.1	40.9	43.90	136.5	138
32	09:42:44	49.80883851	6.69708724	222.7	48.2	41.8	43.90	136.5	141
33	09:42:56	49.80882316	6.69707285	222.9	48.8	0.3	43.80	136.6	144
34	09:43:01	49.80880113	6.69707678	222.6	48.5	41.5	43.80	136.6	138
35	09:43:10	49.80878592	6.69708186	223.0	48.8	0.0	43.80	136.7	123
38	09:43:30	49.80873596	6.69707526	223.2	48.8	41.2	43.80	136.8	26
40	09:43:41	49.80871313	6.69707212	223.0	48.9	41.1	43.70	136.8	46

Photo-number	UTC	Latitude	Longitude	GPS-Altitude [m]	Height [m]	Observer zenith [°]	Sun zenith [°]	Sun azimuth [°]	Azimuth (sun-observer) [°]
43	09:44:01	49.80867229	6.69709152	223.8	48.5	41.5	43.70	136.9	39
45	09:44:15	49.80862894	6.69708174	224.1	48.8	41.2	43.70	136.9	45
48	09:44:49	49.80877128	6.69688458	222.4	48.9	41.1	43.60	137.2	130
50	09:45:04	49.80877139	6.69694392	223.6	48.8	41.2	43.60	137.3	126
52	09:45:19	49.80876978	6.69700345	223.0	48.6	41.4	43.60	137.3	121
55	09:45:41	49.80877873	6.69713279	222.9	48.8	41.2	43.50	137.5	23
58	09:45:57	49.80876464	6.69720409	223.5	48.5	41.5	43.50	137.5	47
62	09:46:20	49.80877405	6.69728009	223.8	48.5	41.5	43.40	137.7	50



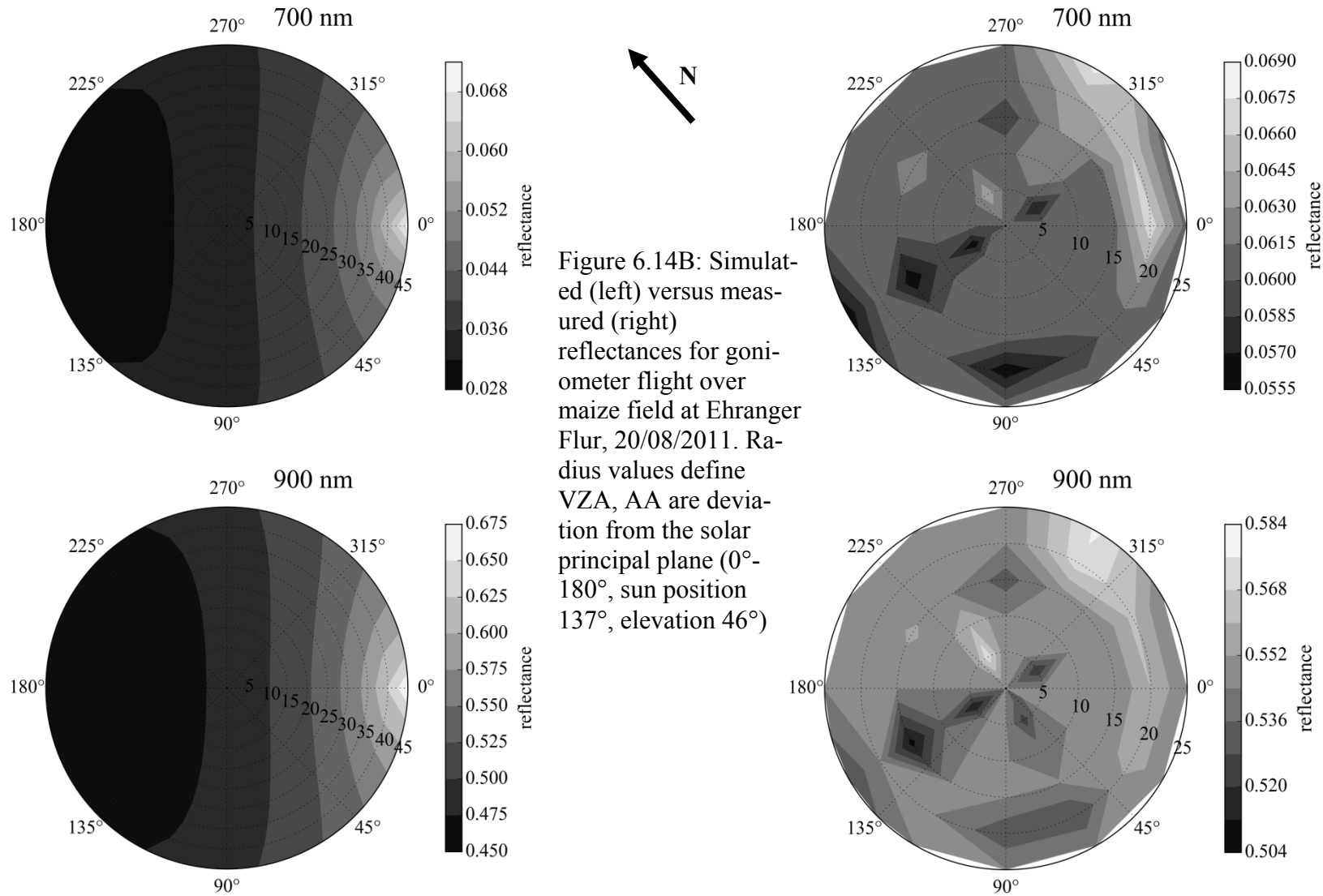


Figure 6.14B: Simulated (left) versus measured (right) reflectances for goniometer flight over maize field at Ehranger Flur, 20/08/2011. Radius values define VZA, AA are deviation from the solar principal plane (0°-180°, sun position 137°, elevation 46°)

The simulated reflectances show parts of the hot spot effect at 0° AA and higher viewing zenith angles (VZA) and lower reflectances for opposite observer-sun locations and with departure from the principal plane with higher AA. As expected, values retrieved from the principal plane show generally higher reflectances in the simulated data. Opposite sensor positions in relation to the sun (left hemicircle) show slightly lower reflectance. However, for VZA around nadir $\pm 5^\circ$, and also observer azimuths perpendicular to sun location (90° and 270°) reflectances obtained show more or less homogenous values of absolute differences 0.6% to 0.8% in the VIS to 2.75% in the nIR.

Table 6.7 lists the absolute and relative differences for the individual simulated reflectances ($\Delta\rho$) between VZA ranging from nadir (0°) to 25° for each AA and Figure 6.14 illustrates the course of simulated relative $\Delta\rho$ for VZA comparable to the goniometer flight (0° - 25°) for all AA.

Table 6.7: Absolute and relative differences in reflectances ($\Delta\rho$) between VZA 0° to VZA 25° for all AA as derived from PROSAIL simulations

Wavelength [nm]	ρ_{\min} [0-1]	ρ_{\max} [0-1]	$\Delta\rho_{\text{absolute}}$ [0-1]	$\Delta\rho_{\text{relative}}$ [%]
530	0.0001	0.0083	0.0082	20
550	0.0001	0.0081	0.0080	20
570	0.0001	0.0081	0.0080	20
670	0.0003	0.0059	0.0056	23
700	0.0001	0.0087	0.0086	20
900	0.0018	0.0558	0.0540	10

Relative $\Delta\rho$ across all AA amount to approximately one fifth of the signal obtained for the respective filter except for the nIR which is slightly lower at 10% (Table 6.7). Absolute $\Delta\rho$ for the VIS are under 1% reflectance. When the reflectance distribution along all AA is considered, Figure 6.14 shows highest $\Delta\rho$ for band 670 nm, lowest for nIR, and altogether, a global minimum around AA of 90° and 270° which represents the along row observations.

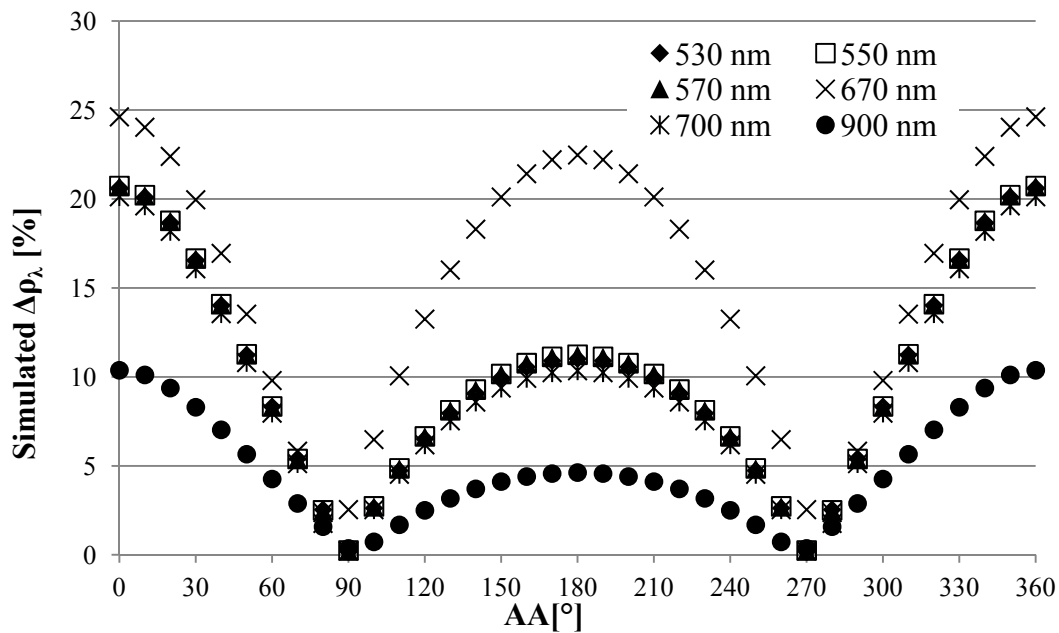


Figure 6.14: Simulated relative reflectance differences ($\Delta\rho$) for VZA ($0\text{-}25^\circ$) across all AA derived from PROSAIL model

This is not the case for the measured reflectances which show a quite different area distribution for the goniometer circle (Figure 6.12A and B right part). Illumination effects are not as homogeneous as for the simulated data, altogether reflectances are slightly higher close to sun position ($0^\circ \pm 90^\circ$), yet higher reflectances may be observed from the $180^\circ\text{-}270^\circ$ quadrant. As the row orientation is perpendicular to the solar plane, i.e. from $90^\circ\text{-}270^\circ$ AA, may be specular reflectance effects from leaves. keeping in mind that the goniometer flight did not reach observer zenith angles of greater than 25° , the absolute values of reflectances retrieved from UAV flights, are within similar reflectance ranges.

Figure 6.15 illustrates the real mean UAS-derived reflectances obtained from the goniometer flights for each AA. Their course following along the AA does not depict the respective AA dependency from the simulated reflectances (NB: less AA/VZA have been obtained for the goniometer flight altogether).

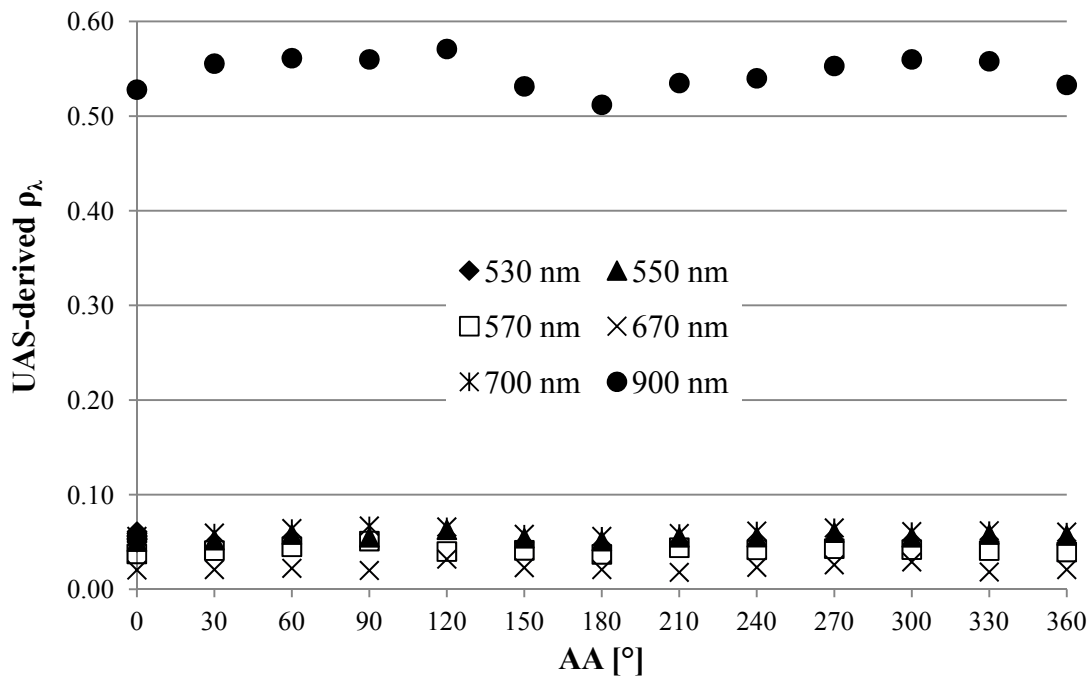


Figure 6.15: Absolute reflectances (ρ) for VZA (0-25°) across all AA derived from UAS flight

The next figures illustrates the reflectances across the the VZA for the PROSAIL simulations (lined points) and as derived from the goniometer flight for the red (Figure 6.16) and nIR bands (Figure 6.17). The simulations show the hot spot effect at 45° for the reflectances along PP, the CP shows less variation with increasing reflectances towards the sun position. Nadir measurements deviate $\sim 0.5\%$ reflectance for the red and up to 8% and for the nIR ranges for the UAS images. The UAS-derived value distribution is again noisier with a hardly detectable higher reflectance variation for the PP than the CP direction.

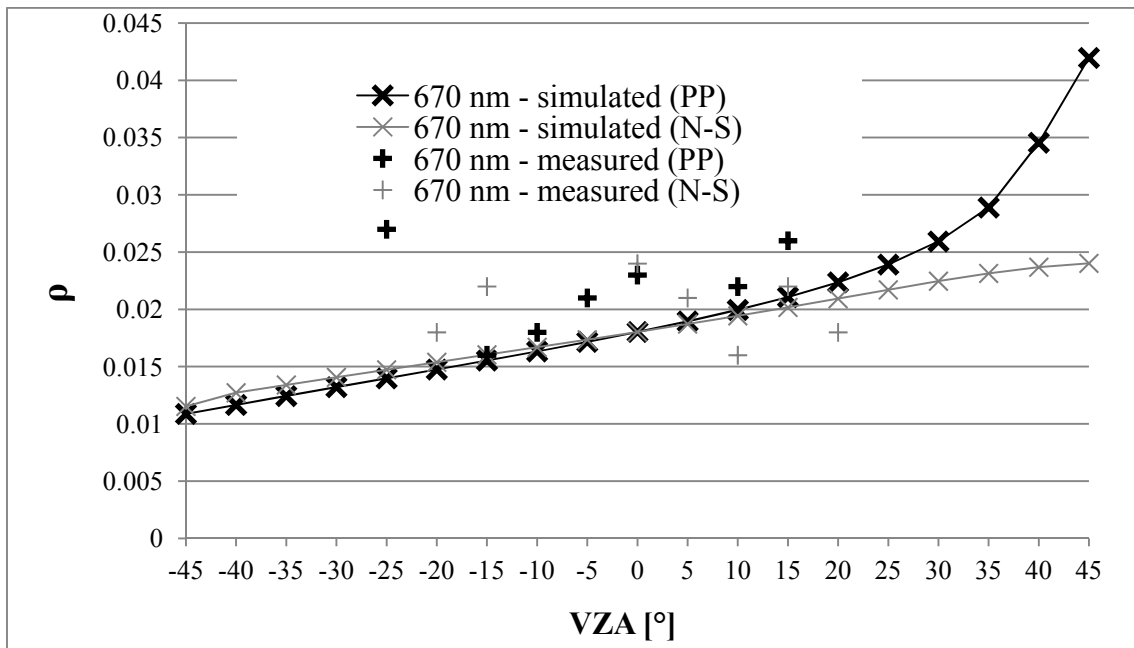


Figure 6.16: Simulated and UAS-derived reflectances (ρ) at 670 nm for solar principal plane (PP) and N-S transect (Sun elevation 46° , sun azimuth 137°)

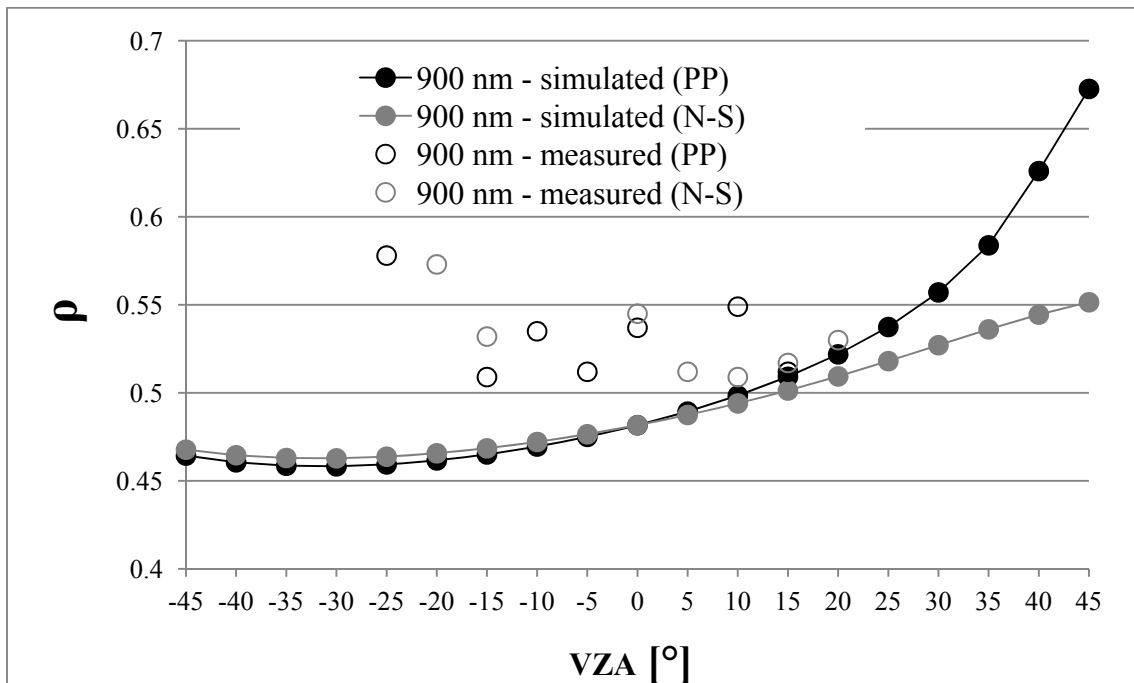


Figure 6.17: Simulated and UAS-derived reflectances (ρ) at 900 nm for solar principal plane (PP) and N-S transect (Sun elevation 46° , sun azimuth 137°)

PROSAIL simulations of selected vegetation indices are illustrated in Figure 6.18 and also show a dependence on viewing geometry.

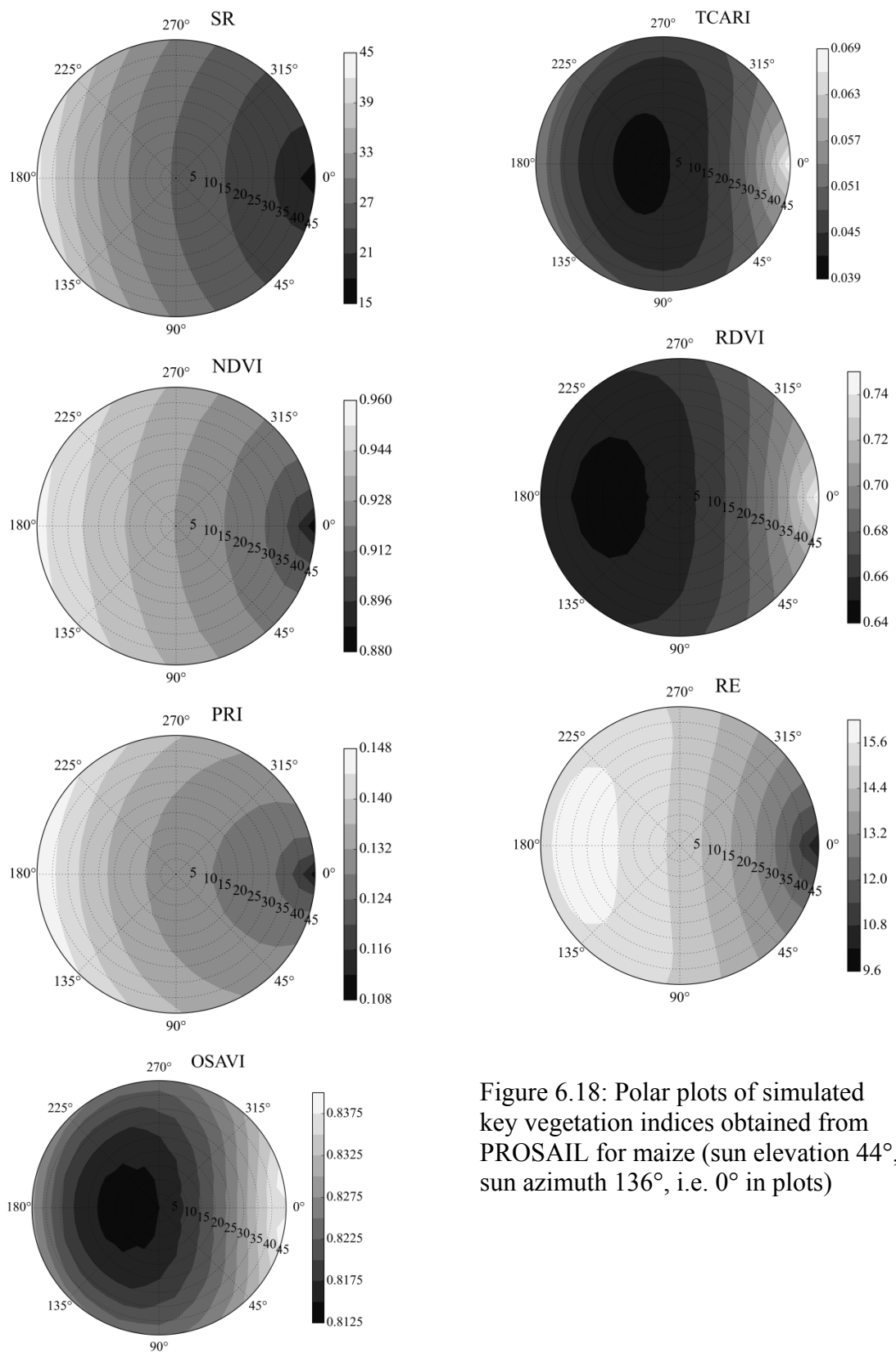


Figure 6.18: Polar plots of simulated key vegetation indices obtained from PROSAIL for maize (sun elevation 44°, sun azimuth 136°, i.e. 0° in plots)

PROSAIL simulations of selected vegetation indices are illustrated in Figure 6.18 and also show a dependence on viewing geometry. All indices produce value differences with altering viewing geometries. The SR, NDVI and PRI are especially affected by azimuth changes of sun-sensor positions and VZA, with opposite behavior along the principal plane. NDVI shows higher values when the sensor is opposite to the sun location. Observer zenith angles are of minor influence when the sensor-sun azimuth is around 90° . Similar results are found for the RE, although it shows a hot spot when the sensor looks $20\text{-}40^\circ$ off nadir opposite to the sun. PRI also illustrates a considerable influence of the azimuth angle on the signal obtained with higher viewing angles opposite to the sun. TCARI and OSAVI are more sensitive to observer zenith angle variations and only to a lesser degree to azimuth variations. The RDVI also produces differences in relation to the azimuth angle, the effect being smaller though for opposite sun-sensor positions which also illustrate less influence by observer angles. Except for SR, NDVI, TCARI and OSAVI, the indices for the simulated sun-sensor positions show similar reflectance for nadir positions ($0^\circ\text{-}5^\circ$ observer angles) across all azimuth locations.

6.3.4 Discussion

As expected, the PROSAIL goniometer simulation showed quite considerable BDR effects of sensor-object-sun viewing geometries on the signal derived. Errors amount to $\sim 20\%$ relative differences (Table 6.6, Figure 6.14) and are highest for the red band and lowest for the NIR. The absolute differences in simulated reflectances from nadir to about 25° VZA, lay under 1% in the VIS and under 6% in the NIR which is still within the noise ranges of the Tetracam multispectral camera (Kelcey and Lucieer 2012).

Although, PROSAIL has not been developed for row crops (Atzberger and Richter 2012), the simulated reflectances along the PP and CP for all VZA agree well with results obtained for a 3D model published by Zhao et al. (2010). The hot spot effect at the PP is clearly displayed as well as the higher variations along the PP compared to the CP which again points towards using flight directions perpendicular to the solar illumination direction. The deviations of the measured (right part in Figure 6.13) versus simulated maize reflectances (left part in Figure 6.13) may be attributed to the row-structure of maize and its non-homogenous canopy. The maize rows where the goniometer flight took place were oriented WNW-ESE, almost perpendicular to the sun position of AA $136\text{-}7^\circ$ (Table 6.6: Photo attitude parameters and derived observer and AA for PROSAIL input (as derived from the ATCOR4 solar position calculation tool)) and by

flying a circle and diameters across the field, different row orientations and sides of the row canopy are viewed. This may explain the contradicting reflectances along the positive and negative semi-circle in relation to the simulated reflectances, as well as the rather random reflectance variations along the PP and CP in Figure 6.16 and Figure 6.17. However, except for the peculiar effect of higher reflectance along the $180^\circ - 270^\circ$ AA quadrant, one may infer more shaded components with lower reflectances along the locations opposite the sun which has indeed been measured by the photographs. Grenzdörffer and Niemeyer (2011) found the anisotropic reflectance behavior of winter wheat to be less strong for the PP and higher for CP.

Within recent years, reflectance models for row-structured crops have been introduced and point the way for further studies of this kind (Zhao et al. 2010). Zhao et al. (2010) also obtained only a poor agreement between simulated and measured directional reflectances along the solar principal plane and its cross plane with increasing deviation from nadir. Generally, simulated along-row reflectances were most homogenous across all VZA than cross-row observations as the canopy appears denser. Cross-solar plane observations curves were smoother, too.

Except for the SR, NDVI, TCARI and OSAVI, the vegetation indices have shown to produce similar values for nadir to 5° observer angles (Figure 6.18). When higher angular views are being applied the value behavior of each index should be given thought prior to flight planning. For almost all indices, i.e. SR, NDVI, RE, RDVI and to a lesser extent, OSAVI, an azimuth position of 90° off the solar position (yields similar values across observer zenith angles. When row crops are being analysed that have not yet reached canopy closure, flight planning should indeed include 3D or row structure reflectance models to account for the variable background contribution to the signal not only related to row structure and their orientation but also to flight day time and sun elevation: Guillen-Climent et al. (2012) showed a bowl-shape behavior of the NDVI with lowest values at noon through scaling up the 3D radiative transfer model FLIGHT (Forest Light Interaction Model).

6.3.5 Conclusion

Ideally, further goniometer flights are required with more diametric flights, extending to higher VZA and denser AA positions. The hemispherical flight pattern applied by Grenzdörffer and Niemeyer (2011) over more homogenous canopies would yield further insight into retrieved signals. When the observer zenith deviates from nadir, flights perpendicular to the incident light for homogenous canopies and along row-orientation for

row crops could be favorable as they showed relatively homogenous simulated reflectances across the VZA. Yet, across-row observation may nonetheless gain more information on the crop as larger parts of the canopy may be seen (i.e. vineyards), and to obtain insight into the BDR effects, 3D simulation models should be applied to either select appropriate viewing geometries or for signal correction.

When row-structured crops are being analyzed it might indeed be advisable to use multi-views to either average illumination differences within the canopies as suggested by (Atzberger and Richter 2012; Duan et al. 2014) or use standardized viewing geometries with similar sun altitude/observer positions to avoid sun position dependencies on the retrieved signal. Lelong et al. (2008) presented an empirical BDR-correction approach which is feasible for small numbers of UAS photos, or the For UAS flights over alternating land covers, Schiefer et al. (2006) presented an empirical approach for class-wise correction of brightness differences of line-scanner data and correction by second-order polynomial equations.

When sites are to be monitored throughout the season, it might well be advisable to simulate potential sun-sensor-target geometries with least differences in BDRs prior to flight planning. Finally, the large-scale UAS images in the real world, remain a conglomeration of 3D structural effects of the ground (relief issues), of the crop row characteristics (width, depth, density), crop characteristics (leaf angle values and orientation, optical leaf properties) and the viewing geometry and thus BDR effects will remain a characteristic of aerial imagery.

Summarizing, for avoidance of BDR effects in UAS images, ideally flat sites/homogeneous crops:

- a detailed goniometer flight would be required for similar sun elevations as for the flight campaign, to obtain the anisotropy factors and derive correction factors; or
- Multiple viewings angles could be used to average BRD effects on DNs/reflectances.

However, as the real world in large-scale UAS images shows a complex 3D structure and seldomly are homogeneous, care should be taken to evaluate image areas affected by only minimally by BRD effects when biophysical parameters shall be retrieved for modelling or statistical analysis.

6.4 Sensitivity of Signal to Flight Altitude and Air Mass

The aim was to estimate the effect of the air mass between ground targets and sensor on the signal for low flight altitudes and if the correction is mandatory for further quantitative analysis.

6.4.1 Data & Methods

Subsequent to the goniometer flight, additionally a scaling flight from roughly 10 m to 90 m a.g.l. was conducted at the Ehranger Flur (49.8090776 °N, 6.6974405°E) around 9:50 a.m. UTC. The greyvalue panels presented in chapter 6.2.4 were used as reference panels and all images were taken with the reference panels in the centre of each image. Table 6.8 shows the camera position parameters acquired for the multispectral aerial images acquired with the MiniMCA-6. Reference panels were centred in the image and recorded with total pitch angles of a maximum of 2.2° deviation of nadir.

Table 6.8 Flight altitudes and camera position angles for scaling flight

altitude [m]	roll _{Qu} [°]	pitch _{Qu} [°]	yaw _{Qu} [°]	Pitch _{cam} [°]	Roll _{cam} [°]	Total pitch [°]
11	-1.1	-1.1	-83.1	89	45	90.1
20	-1.7	-0.6	-82.4	90	45	90.6
31	-2.2	0.4	-82.7	90	45	89.6
49	-2.8	0.3	-83.7	90	45	89.7
60	-2.1	2.2	-83.3	90	45	87.8
70	0.4	-0.7	-84.5	90	45	90.7
79	-1.4	-1.5	-82.9	89	45	90.5
86	-1.7	1.4	-82.5	90	45	88.6

Pre-processing again comprised band alignment and vignetting correction. Then DNs were extracted from the centre of the white reference panel on the image. The respective DNs of each image were then plotted against the flight altitude and the linear trend defined.

6.4.2 Results

The DN value differences between the reference panels in dependence to camera elevation are rather small and amount to a maximum of Δ 4% DN for the white reference panel, and Δ 0.5 - 3 % DN for the black reference panel (Figure 6.19).

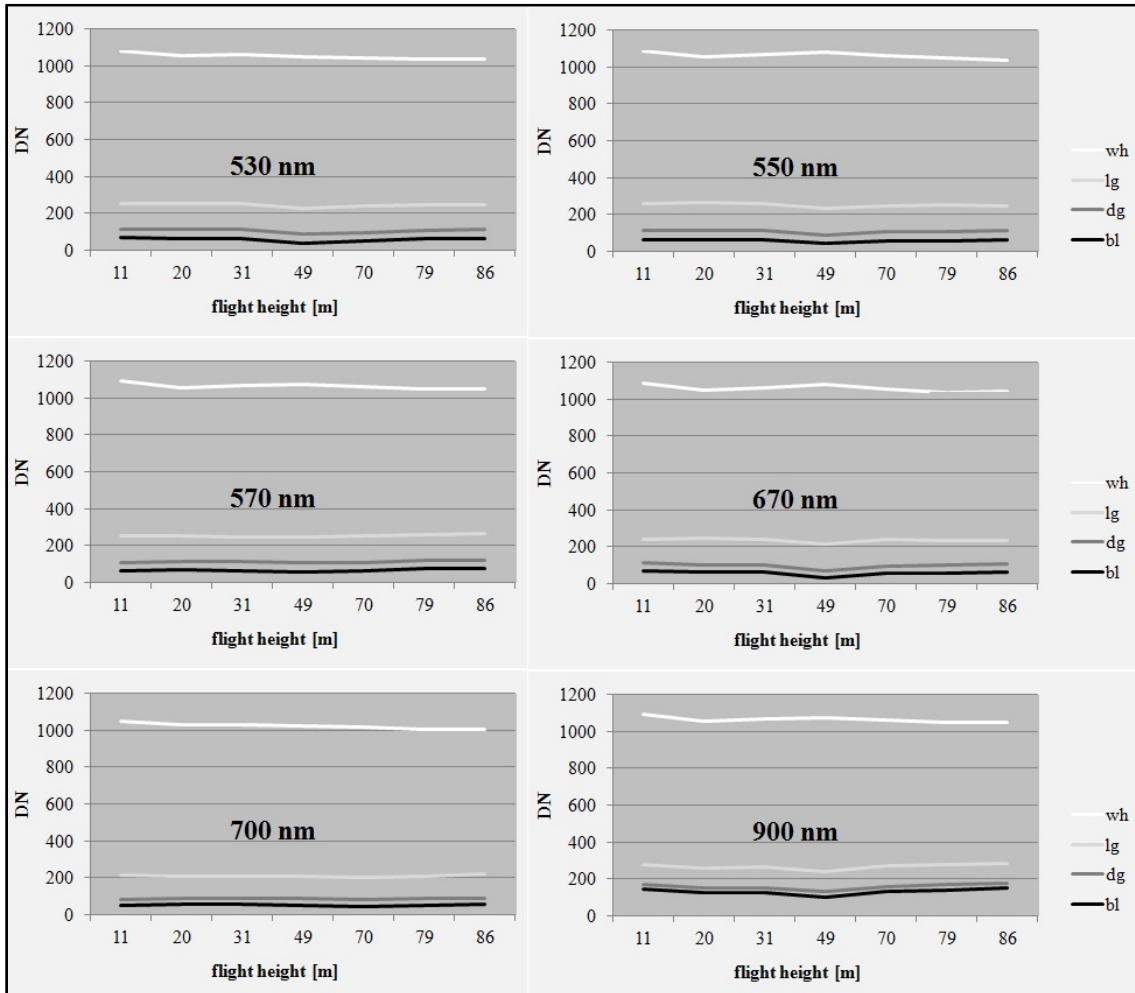


Figure 6.19 Reference panels in relation to flight altitude (in m a.g.l.) at Vis/nIR wavelengths

The DNs of the white reference panel were plotted against the flight altitudes (Figure 6.20).

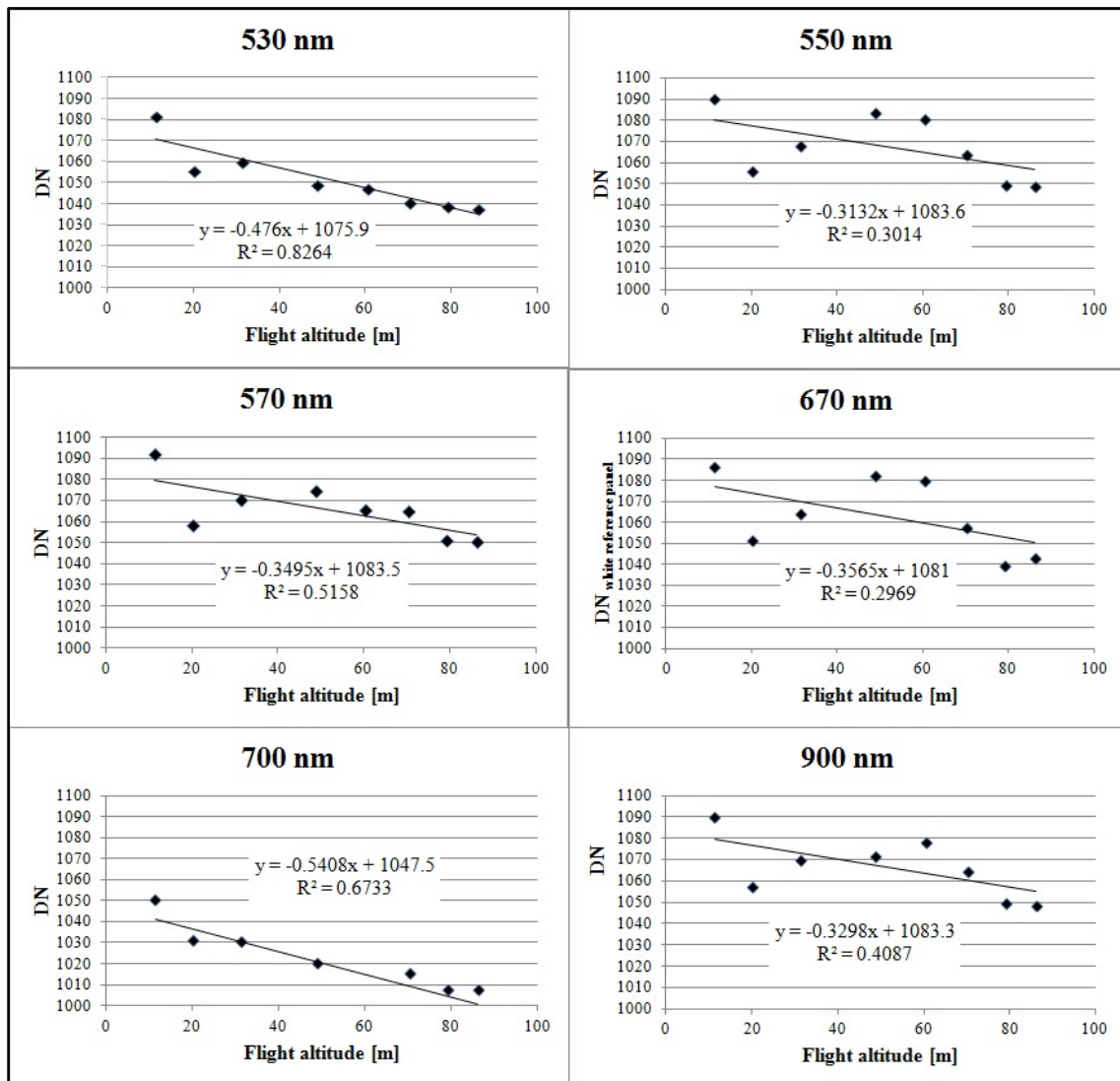


Figure 6.20 DN of white reference panel extracted for images of different flight altitudes (in m a.g.l.)

Figure 6.20 shows the minimal radiometric effect of overall Δ +/- 5% DN differences from low to high altitudes for the white reference panel. Altogether there is a decrease in DN values with increasing flight heights: values decrease about ~50 DN for the respective height difference of 80 m. The negative trend is stronger for 530 nm and 700 nm, the coefficient of determination ranging from $0.83 > R^2 > 0.67$.

For dark targets, i.e. the black reference panel, the effect is smaller, except for the nIR panel (Figure 6.21).

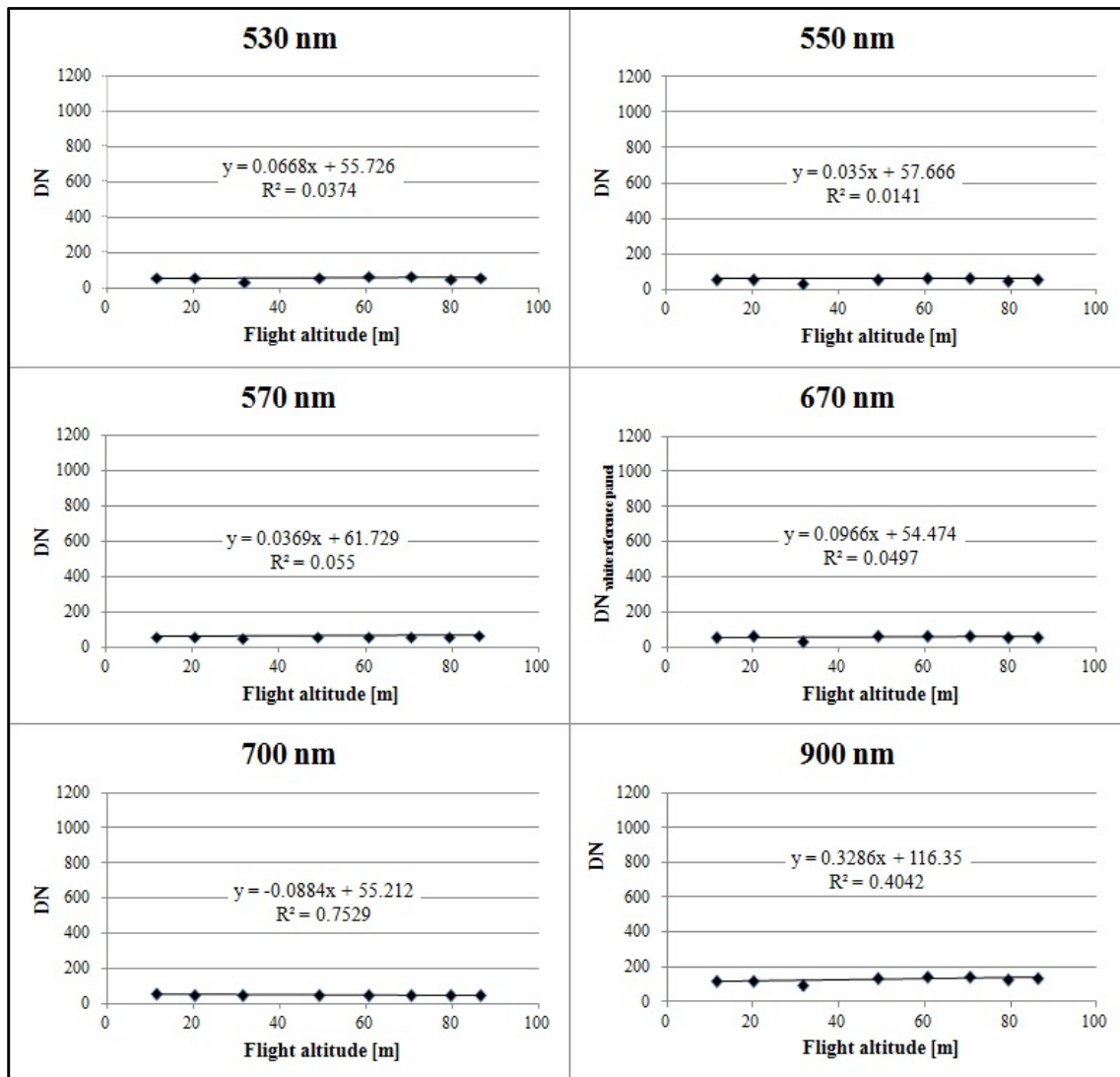


Figure 6.21 DN of black reference panel extracted for images of different flight altitudes (in m a.g.l.)

6.4.3 Discussion and Conclusion

There is, especially for the brighter targets, a radiometric effect on image DNs in relation to flight altitude: with increasing height, DNs of bright targets decrease. For darker targets, the found absolute differences are, however, within noise range of the MiniMCA-6 found by Kelcey and Lucieer (2012, p. 1478) with 5-13 DNs.

For regulated flight altitudes of 100 m a.g.l. in general ascent permits issued in Germany, radiometric differences are approximately within the noise range of the multispectral camera and a radiometric calibration by ELC should be appropriate for most applications. ELC also corrects for the spectral filter response and exposure time settings.

The experiment could be repeated for higher flight altitudes. The required following experiment setup would require repeated parallel reflectance measurement of reference targets and a spectralon® with the respective multispectral camera at varying heights and with a field spectrometer simultaneously, while measuring incoming solar irradiance at the same time to verify the camera's radiometric stability.

Part II

7 The Impact of Soil Management Effects on Grapevine Physiological Variables and Vigour Using Multispectral UAS-Data

7.1 Introduction

Several studies have shown that wine sensory attributes are driven by underlying soils and management, and possibly terroir (Schultz and Löhnertz 2002; Bramley et al. 2011a; Bramley et al. 2011b), and soil cover crops therefore are thought to have a major impact on grapevine growth and physiological parameters.

Soils ideally allocate moisture, affect nutrient uptake and influence the microclimate by their thermal budget and influence the taste of wine by their terroir characteristics and soil management (Jackson and Lombard 1993, Hall et al. 2002; Schultz and Löhnertz 2002; Meggio et al. 2010, Bramley et al. 2011a Bramley et al. 2011b). Thus, soil management has a direct influence on grape vegetative growth, fruit composition, and finally wine quality. Vineyard soil management comprehends the sowing of cover crops, tilling, mowing and chemical treatments aiming at the suppression of weeds, fostering of nutrient uptake, minimization of water loss and soil erosion, positive effects on soil fauna and avoidance of pests and diseases (Schultz and Löhnertz 2002; Tesic et al. 2007, Serrano et al. 2012). Cover crops play an important role for the carbon and water balance of vineyards (Schultz and Stoll 2010). In the late 80ies, however, viticulturists recognized that cover crops also increase competition for nitrogen (N) and water uptake and might contribute to the development of atypical aging (ATA), an off-flavour in white wines (Schultz and Löhnertz 2002, Schneider 2010).

The effect different floor cover types have on growth, yield and fruit composition in a mild and semi-humid climate Chardonnay vineyard in California, USA was analyzed by Clarke et al. (2006) and Tesic et al. (2007). Soil cover slowed down blossoming and yielded lower shoot length, pruning weight and canopy density. After two years into the experiment, also yield, cluster number and berry weight decreased for the complete soil cover, but no effect on fruit composition was measured (Clarke et al. 2006; Tesic et al. 2007).

Remote sensing constitutes a valuable tool to monitor vineyard properties and to retrieve physiological plant parameters. Due to vineyard architecture remote sensing of leaf and canopy variables requires large-scale imagery. Traditionally, high spatial resolution satellite imagery such as Ikonos (Johnson *et al.* 2003) and, more so, aerial imagery are used in this context utilizing multispectral (Smit *et al.* 2010), hyperspectral (Zarco-Tejada *et al.* 2005, Meggio *et al.* 2008, Gil-Perez *et al.* 2010, Smit *et al.* 2010) and thermal sensors (Berni *et al.* 2009b). Application of UAS are increasing considerably not only within the scientific community but also by farmers gaining rapid visual overviews over their vineyards, as frequently note within the UAS Vision Daily News Bulletin (<http://www.uasvision.com>, 18/11/2014). UAS have recently been applied for deriving biophysical parameters such as Chlorophyll (Chl) content, frequently directly linked to grape vigour, growth and yield (Gil-Perez *et al.* 2010, Hall *et al.* 2011a), Chl fluorescence (Zarco-Tejada *et al.* 2009, Primicerio *et al.* 2012; Zarco-Tejada *et al.* 2012) and LAI *a.o* (Mathews and Jensen 2013).

As chapter 3 has illustrated, the leaf pigments chlorophyll a and b (Chl_{a+b}) control the photosynthetic activity by absorbing solar energy and converting it to chemical energy (Guyot 1990; Walter-Shea and Norman 1991; Asner 1998, Mabrouk and Sinoquet 1998). The Chl content varies with leaf nutrient status (leaf N), water supply, light and temperature, and leaf age (Boochs *et al.* 1990, Haboudane *et al.* 2002; Steele *et al.* 2008, Cabello-Pasini and Macias-Carranza 2011). Poni *et al.* (1994) showed that chlorophyll content increased with leaf age, saturating after approximately 80-90 days and, hereafter, persisting until harvest times. Chl absorbs light at 450 nm (blue) and 670 nm (red) spectral region, hence, showing a negative correlation between Chl content and reflectance. Yet, with increasing Chl, the reflectance decreases at 550 nm (green), 715 nm (red edge) and >750 nm (nIR) (Schultz 1996; Daughtry *et al.* 2000, Zarco-Tejada *et al.* 2005). Photosynthetic activity of *Vitis vinifera* is further driven by temperature, leaf age and variety, Zufferey *et al.* (2000) found that at higher temperature (27-32°), the primary shoots showed a maximum of photosynthetic rate, secondary shoots had their maximum during the berry ripening period.

Also, vegetation indices (VIs) have been employed to map grapevine Chl content and vigour properties. The normalized difference vegetation index, NDVI (Tucker 1979; Huete and Jackson 1988), has been applied to map wine quality, grapevine vigour (Meggio *et al.* 2010; Primicerio *et al.* 2012), long-term water deficits and stem water potential (Baluja *et al.* 2012a). The division of the transformed chlorophyll absorption ratio index, TCARI (Haboudane *et al.* 2002) and optimized soil-adjusted vegetation index, OSAVI (Rondeaux *et al.* 1996), TCARI/OSAVI appropriately estimate stomatal

conductance (Baluja et al. 2012a). The abundance of (narrow-band/hyperspectral) spectral vegetation indices for mapping Chl and plant pigments has been described in detail by Haboudane *et al.* 2002, Zarco-Tejada *et al.* 2004, Zarco-Tejada *et al.* 2005, Gil-Perez *et al.* 2010.

Water stress as well as photosynthetic efficiency may be measured by the narrow-band photochemical reflectance index PRI and UAS application in vineyards and tree plantations have been published plentifully by Berni et al. 2009a; Berni et al. 2009b; Berni et al. 2009c, Berni et al. 2009c; Suárez et al. 2009; Suárez et al. 2010; Baluja et al. 2012a; Zarco-Tejada et al. 2013a. However, the PRI has also been proven to be sensitive to differences in crown-structure, viewing and illumination geometry, showing the strongest response in illuminated hot spot conditions and shadowed canopy (Hilker *et al.* 2008, Hall *et al.* 2008, Zarco-Tejada *et al.* 2013b). Therefore, recent studies combined the renormalized difference vegetation index, RDVI (Roujean and Breon 1995), and the red edge ratio (ρ_{700}/ρ_{670}) as a normalization factor to the PRI obtaining an indicator sensitive not only to water stress but also to canopy Chl content (Zarco-Tejada *et al.* 2013a). Other hyperspectral physiological indices sensitive to the carotenoids and anthocyanins foliar pigments were able to predict grape quality deficiencies due to iron chlorosis (Meggio et al. 2010), but will not further be considered due to the multispectral sensors used in this study. Further narrow-band, hyperspectral indices have been developed within the past decades which have been presented and tested elsewhere (Haboudane et al. 2002; Zarco-Tejada et al. 2005, Wu et al. 2008, Xue and Yang 2009).

Other authors used aerial temperatures and thermal indices to predict leaf stomatal conductance and stem water potential (Baluja et al. 2012b). Yet, the study revealed that spectral indices such as the NDVI and TCARI/OSAVI were also well related to the vineyard's water conditions, assuming to reflect longer term water status regimes. In contradiction to Baluja et al. (2012) though, NDVI were found less sensitive to leaf stomatal conductance and stem water potential (Zarco-Tejada et al. 2012). Thermal inertia (maximum temperature deviations between day and night time imagery) has been applied as another proxy for soil moisture variations and potentially water stress (Soliman et al. 2013).

In terms of viewing geometry, the retrieval of biophysical parameters is supposed to be improved for vertically trained crops, as more canopy is being recorded as Kempeneers et al. (2008) successfully proved for for hyperspectral (AHS) airborne data. Best results were obtained for perpendicular sun-object orientations (Kempeneers et al. 2008).

For cool climate conditions, the impact of different soil management strategies (SMS) on grapevine physiology and vigour has not yet been studied in more detail by means of multispectral and thermal UAS remote sensing. Thus, the objectives were:

- (i) to test if different SMS may be separated by means of multi-angular multi-spectral UAS aerial imagery,
- (ii) to derive optimal viewing directions for such vertically trained crops in relation to the prediction of physiological and vigour parameters (e.g. Chl, nitrogen, nitrogen balance index, percentage of canopy gap, yield), and
- (iii) to follow seasonal changes of grapevine physiology and yield in relation to soil management. The chapter is a more detailed version of a conference contribution (Retzlaff et al. 2013) and a paper version (Retzlaff et al. 2015).

For the first two objectives, UAS multispectral images from three viewing geometries were derived in 2011 (17/08/2011). The last objective used data from four points during the 2012 growing season were used.

7.2 Material and Methods

7.2.1 Study Site

The study was carried out in a commercial vineyard in Grevenmacher/Luxembourg (49.69 N, 6.45 E, ~180 m a.s.l.) on the white *Vitis vinifera* L. variety Pinot blanc. The vertical shoot positioning trained vineyard (108.7 are) was planted on 125 AA rootstock in 1992. The distance between the rows is 2 m and between single plants 1.2 m. The experimental vineyard is east exposed with an inclination of around 20% and a west-east orientation of the rows.

Pruning as well as canopy management measures were conducted in the same way in all strategies. Herbicides were used to suppress weed development. Crop protection applications against *Plasmopara viticola*, *Erysiphe necator* and *Botrytis cinerea* were carried out from the air (helicopter) and from the ground (tractor-driven fungicide sprayers by the farmer) (Retzlaff et al. 2015).

7.2.2 Soil Management Strategies

Four SMS were compared using a randomized block design, consisting of 4 replicates (plots) of five rows each (Figure 7.1). SMS were:

1. multi-species cover crop mixture, commercial name “Wolff mixture”,
2. natural greening,
3. summer soil tillage with rotating harrow and winter greening, and
4. natural greening with disturbance in dry conditions.

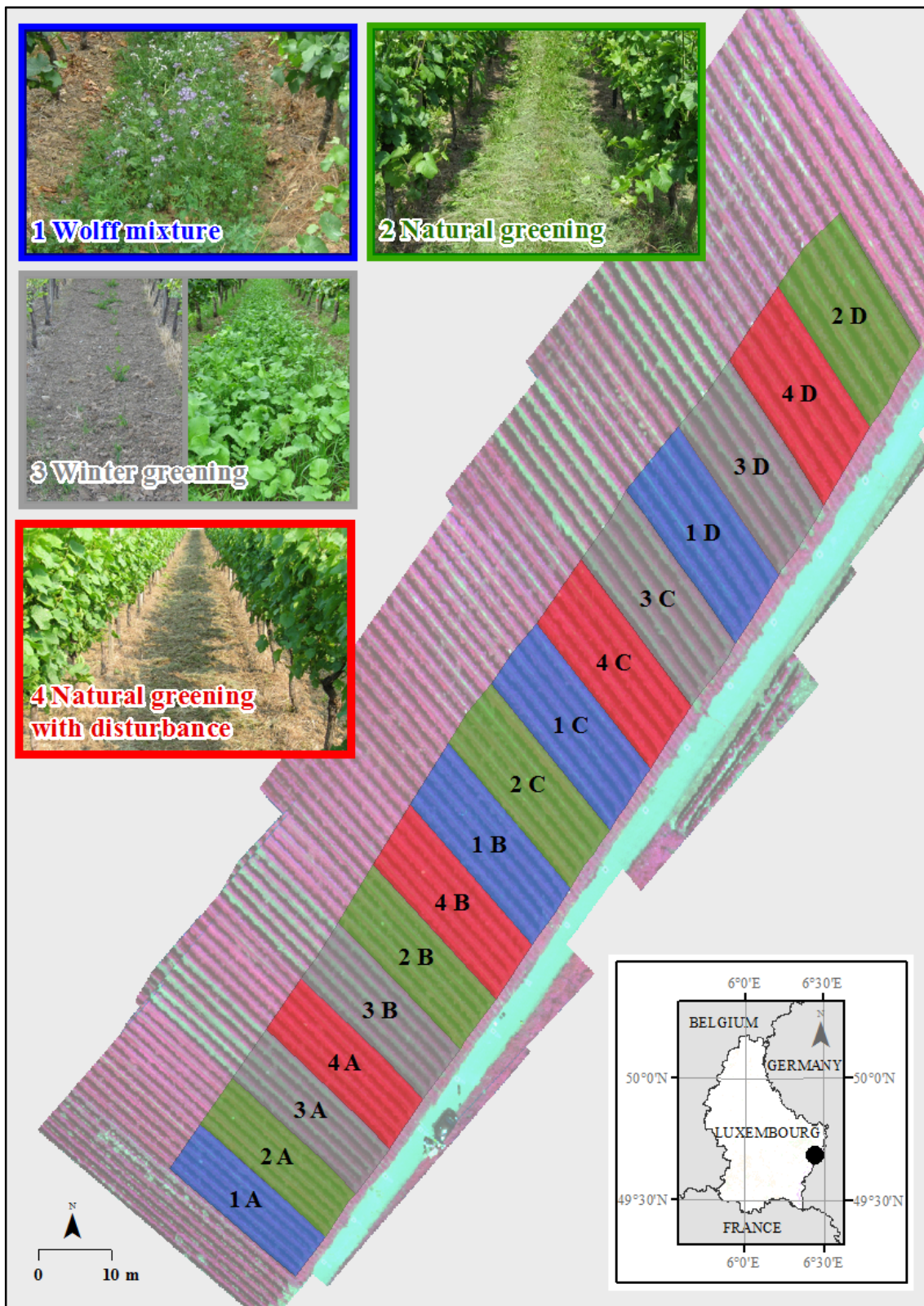


Figure 7.1 Location of studied vineyard in Grevenmacher, Luxembourg, with soil management strategy plots (1-4) and replicates (A-D). Data source: UAS image (R: 900 nm, G 670 nm, B 550 nm; ESRI Data & Maps for ArcGIS® 2012)

Prior to the start of the experiment, all rows had been covered by natural greening plants for several years. In spring 2010, this natural greening layer was tilled in the strategies (1) and (3). At the beginning of the trial, the Wolff mixture consisting of *Vicia* sp., *Trifolium* spp., *Phacelia* sp., *Onobrychis* sp., *Melilotus* sp., *Medicago* spp. and further herbs was sown in plots of strategy (1). In this strategy the greening plants were not mulched but rolled 3 times per season. Natural greening plants (mainly grass) in strategy (2) were mulched 3 to 4 times per season. In strategy (3), the soil was kept open between April and August using a rotary harrow. In both years, a winter greening mixture consisting of *Vicia* sp., *Lolium* sp., *Trifolium* sp., *Raphanus* sp. and *Malva* sp. was sown in August and plowed in in April. In strategy (4) one interruption of the greening layer was conducted by rotary harrow in May or June (Retzlaff et al. 2015).

7.2.3 Field Sampling and Analysis

All parameters were assessed in the central row of each plot (five rows each) in pre-defined “assessment regions” consisting of 12 plants each in the lower part of the experimental vineyard. Field sampling was carried at five characteristic BBCH-code (Biologische Bundesanstalt, Bundesortenamt und Chemische Industrie; Hack et al. 1992, Meier 2001) stages illustrated in Figure 7.2: after flowering BBCH 69, developing of fruits BBCH 71-73, berries beginning to touch BBCH 77-79 and at ripening of berries BBCH 81-85 (Lorenz et al. 1995). Yield and pruning wood weight per plant were measured after harvest in November.

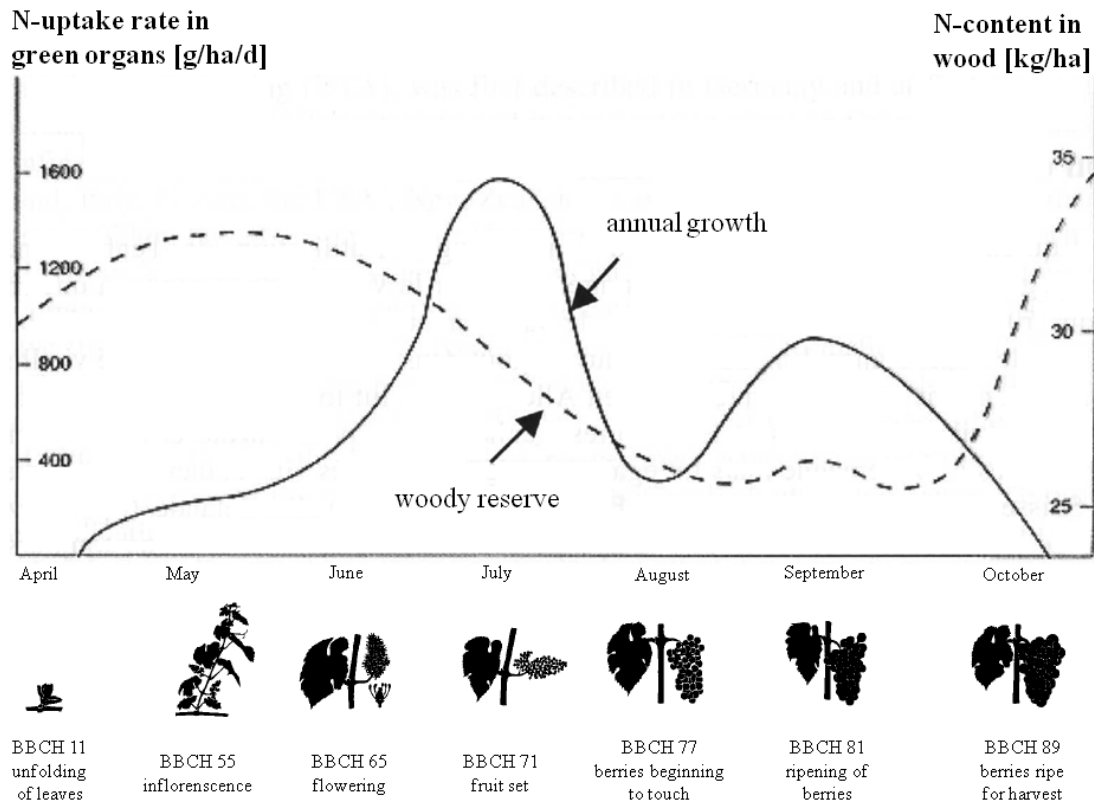


Figure 7.2 Seasonal nitrogen uptake and content for grapevine in relation to growth stages (modified from Schultz and Löhnertz 2002, p.20)

The impact of the different SMS on the canopy structure in the cluster-zone was assessed on 27 and 28 July 2011 using point quadrat analysis (PQA) according to (Smart and Robinson 1991). To this end, a rod was inserted into the cluster-zone every 10 cm from the south side of the row on the height of the upper fruiting wire. Here, PQA was carried out at 1.5 m height above the ground in the middle of the canopy instead of the cluster-zone as suggested by Smart and Robinson (1991). All contacts of the rod were recorded distinguishing between leaves (L), clusters (C) and gaps (G) on 48 insertion points per plot. The leaf layer number (LLN) and the percentage of gaps (PG) was calculated according to Meyers and Van den Heuvel (2008).

Chl content and N were measured between fruit set and harvest (distance between sampling dates in each case five weeks): the Chl content in the leaves and the Nitrogen-balance-index (NBI) were measured four times using the Dualex[®] equipment (Force-A, Paris, France) (Goulas et al. 2004). For this, 40 leaves were pricked from the main shoot from the upper canopy (fifth leaf from the top) at BBCH stages 71, 77-79, 85 and 89 (Lorenz et al. 1995) on 09/06/2011 (2011 – I), 12/07/2011 (2011 – II), 17/08/2011

(2011 – III) 21/09/2011 (2011 – IV), 21/06/2012 (2012 – I), 18/07/2012 (2012 – II), 20/08/2012 (2012 – III) and 26/09/2012 (2012 – IV). Leaves were transported to the laboratory in cooling boxes. Here, Dualex measurements were performed. Leaf discs were punched from the same leaves, dried at 60°C for 24 hours and ground. Nitrogen (N) contents were quantified with a TruSpec elemental analyser (LECO Corporation, St. Joseph, MI, USA) (Mayer *et al.* 2013). Additionally, the nitrogen balance index (NBI) was assessed by the ratio of the Dualex® derived Chl and flavonol content (Martinon *et al.* 2010).

As UAS flights were not carried out on the same day, additional Chl measurements were made according to the Dualex measurements using a Konica Minolta SPAD-502 chlorophyll meter (see chapter 4.5.2).

Leaf area measurements were carried out using a Li-COR® LAI-2000 Plant Canopy Analyzer. LAI was measured just before dusk on 30/08/2011 with a 50% view cap averaging measurements underneath the grapevine's first layer of leaves, and in the middle of the row interspace. For each row 10 such measurements were averaged to one LAI value. To comply with routine LAI measurements at the Luxembourg Institute of Science and Technology (LIST), this set up was changed following Ollat *et al.* (1998) in 2012 (28.06.2012): a 45° view cap was used and measurements were made facing W perpendicular to the first layer of leaves and facing 45° NW at the side of the respective row. Again, 10 measurements were averaged to one LAI.

The plants in the assessment regions of each plot were harvested separately at 20/09/2011 and 10/10/2012. The total yield per plant was calculated by dividing the total weight at harvest recorded per plot by the number of plants.

After leaf fall (30/11/2011, 21/11/2012), grapevines were pruned and the total pruning wood weight per plant as an indicator of vegetative growth, was calculated by dividing the weights recorded per plot by the number of plants (Retzlaff *et al.* 2015).

7.2.4 UAS Image Acquisition

Flights were covering the entire management site (1) taking multispectral imagery with the miniMCA-6 camera (Tetracam Inc. 2010, CA, USA) in 2011 and 2012. In 2011, three camera pointing angles were applied: nadir and slant-range (45° off-nadir) viewing directions on both illuminated and shaded sides of the vine canopy (Figure 7.3 Flight route along the vineyard at Grevenmacher for 17/08/2011). In the following year,

only VZA of nadir and 45° on illuminated canopy were applied. Flight height was at approximately 70 m a.g.l. and resulted in a pixel resolution of about 4 cm x 4 cm.



Figure 7.3 Flight route along the vineyard at Grevenmacher for 17/08/2011

In early summer, also thermal data was acquired with the broadband camera UCM (Zeiss) at 70 m above ground, too. Cameras were described in detail in chapter 4.

Table 7.1 lists the UAS flights, sensors and respective weather conditions and BBCH stages (Lorenz et al. 1995) for 2011 and 2012 (Ministère de l'Agriculture, de la Viticulture et du Développement Rural, 2011). It is important to note that image acquisition could not always be carried out at the same dates when field parameters were assessed due to weather or other reasons (availability of UAS and sensors, pilot) leading to a time-shift between the respective data sets.

Table 7.1 Flight dates, sensors weather conditions and grape phenological stages at UAS flights in 2011 and 2012 (mod. Retzlaff et al. 2015)

Date	UTC	Sensor	Weather	BBCH stage (Lorenz et al. 1995)
17/08/2011	10:00h – 10:30h	miniMCA-6, nadir and 45° VZA	23.3°C, 58% relative humidity (RH), 788 Wh/m ²	81 Beginning of ripening
28/06/2012	11.03h – 11:05h	UCM, nadir	26.7°C, 61% RH, 698 Wh/m ²	71 Fruit set
03/07/2012	13:05h - 13:15h	miniMCA-6: 45° illuminated side and nadir	24.3°C, 47% relative humidity, 716 Wh/m ²	ditto
23/07/2012	11:22h - 11:29h 12:24h - 12:30h	miniMCA-6: nadir° 45° illuminated side	23.3 -24°C, 45% RH, 740 Wh/m ²	77-79 Berries touching
03/09/2012	10:01h – 10:07h 11:06h – 11:12h	miniMCA-6: 45° illuminated nadir	21.8°C - 22.6°C, 60% - 53% RH, 750-700 Wh/m ²	85 Softening of berries
30/09/2012	12:23h – 12:28h 13:00h – 13:05 h	miniMCA-6: 45° illuminated nadir	16.5°C – 17.2°C, , 58-51% RH 748-780 Wh/m ²	89 Berries ripe for harvest

For the multispectral imagery 10 nm (FWHM) standard filters centred at 530 nm, 550 nm, 570 nm, 670 nm, 700 nm, and 900 nm were used. Radiometric resolution was set to 10-bit (1024) greylevels (*i.e.*, digital number: DN). Example images of different viewing angles are presented in Figure 7.4.

Thermal images were taken within a spectral range of 7-14 μm and a thermal sensitivity of 90 mK at 30°C. As only about 20 images may be stored on the internal memory, generally two flights were required to cover the vineyard.

Ground control points highlighted each assayed row, and their geographic position was measured using a Trimble GPS. For radiometric calibration four reference grey-scale panels (chapter 5.2.4) with known reflectance were put in the field.

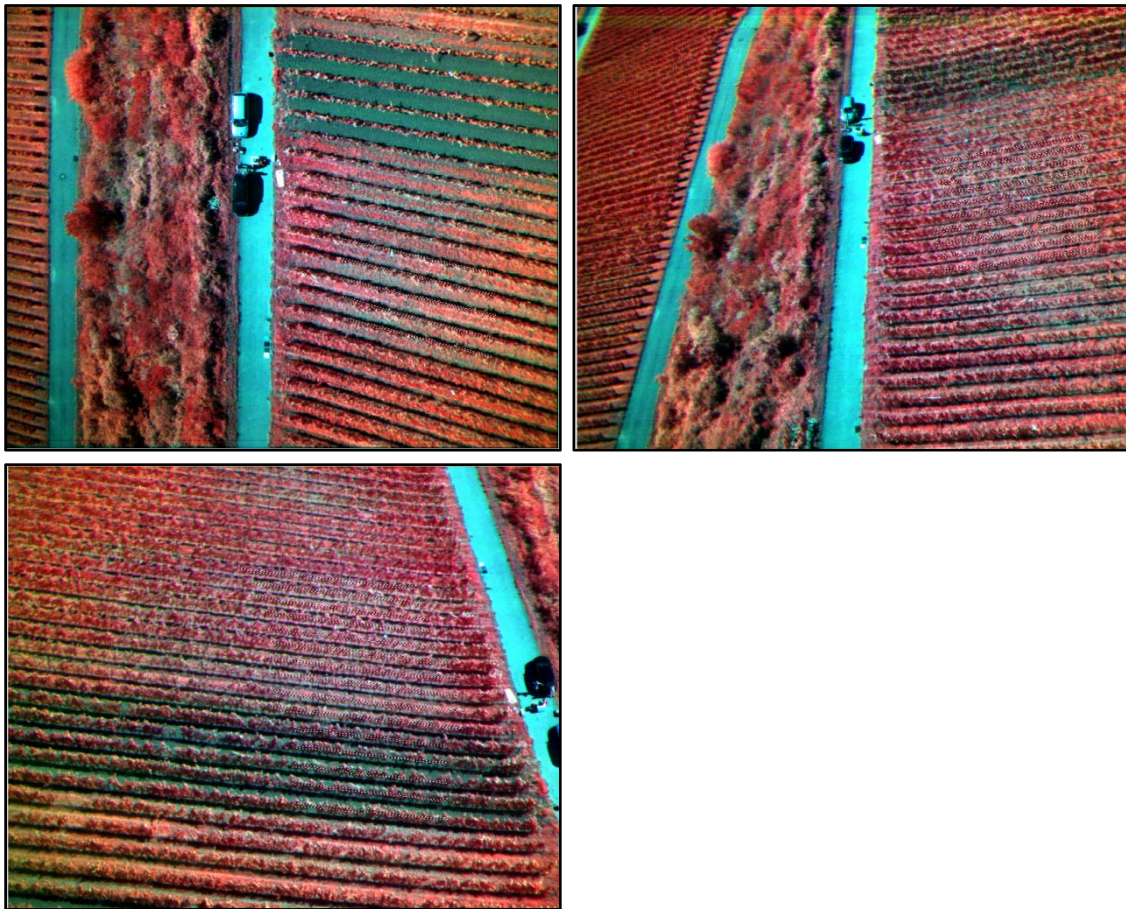


Figure 7.4 Multispectral images from study vineyard (17/08/2011) taken with different viewing angles: top left: nadir; top right: 45° VZA illuminated; bottom: 45° VZA shaded canopy (RGB: 900 nm, 550 nm, 530 nm).

7.2.5 Data Preparation

7.2.5.1 Multispectral Image Data

Following the preprocessing chain explained in chapter 6, after vignetting correction, the six individual band images (1280x1024 pixels) were aligned to a principal plane by x-, y-translation, rotation and scaling and combined to multispectral images. As for the 2011 data, vignetting was not fully corrected, some darkening around the image edges persisted and could not be corrected retrospectively as the camera had already been sent to the producer for a rear-to-front filter change, only the central imagery parts were further analysed.

Radiometric corrections included an empirical line (EL) based regression of image digital values obtained from four reference panels (white, light-grey, dark-grey, black) to in-

situ derived reflectances using a FieldSpec Pro spectro-radiometer (ASD) as was explained in more detail in chapter 4.3. Reference images to determine the EL parameters were chosen with reference panels lying close to nadir position.

For the 2012 data, the 30/09/2012-flight was chosen as reference. All other flights were calibrated relatively to this flight. As exposure was typically optimized for vegetation reflectance, the white reference panel tended to be overexposed and only the three dark-reference panels were used for empirical line calculation. Resulting negative reflectance values were set to Null/NoData and excluded from further analysis. Table 7.2-Table 7.3 show the respective empirical line parameters.

Table 7.2 Empirical line and coefficient of determination (R^2) for radiometric correction of 2011 UAS flight

17/08/2011 Nadir		
Band [nm]	Empirical line	R²
530	$\rho = 0.0009x - 0.0209$	0.9999
550	$\rho = 0.0009x - 0.0191$	0.9993
570	$\rho = 0.0008x - 0.0113$	0.9993
670	$\rho = 0.0008x - 0.0109$	0.9966
700	$\rho = 0.001x - 0.0237$	0.9997
900	$\rho = 0.0011x - 0.128$	0.9719
45° illumin. canopy		
Band [nm]	Empirical line	R²
530	$\rho = 0.001x - 0.036$	0.9996
550	$\rho = 0.0009x - 0.0343$	0.9993
570	$\rho = 0.001x - 0.0395$	0.9994
670	$\rho = 0.0009x - 0.036$	0.9996
700	$\rho = 0.0011x - 0.0321$	0.9997
900	$\rho = 0.0011x - 0.1108$	0.9995
45° shaded canopy		
Band [nm]	Empirical line	R²
530	$\rho = 0.001x - 0.0335$	0.9990
550	$\rho = 0.0009x - 0.0344$	0.9991
570	$\rho = 0.001x - 0.0419$	0.9948
670	$\rho = 0.0012x - 0.0712$	0.9923
700	$\rho = 0.0011x - 0.0283$	0.9911
900	$\rho = 0.0012x - 0.1541$	0.9973

Table 7.3 Empirical line and coefficient of determination (R^2) for radiometric correction of 2012 UAS flights

03/07/2012 Nadir			03/09/2012 Nadir		
Band [nm]	Empirical line	R²	Band [nm]	Empirical line	R²
530	$\rho = 0.0009x - 0.0238$	0.9929	530	$\rho = 0.0002x - 0.0173$	0.9978
550	$\rho = 0.0008x - 0.0215$	0.9933	550	$\rho = 0.0003x - 0.0134$	1
570	$\rho = 0.0009x - 0.0279$	0.9942	570	$\rho = 0.0003x - 0.0226$	0.9999
670	$\rho = 0.0008x - 0.0324$	0.995	670	$\rho = 0.0002x - 0.0237$	0.9998
700	$\rho = 0.0008x - 0.0194$	0.9997	700	$\rho = 0.0003x - 0.0254$	0.9997
900	$\rho = 0.0029x - 0.1056$	0.9999	900	$\rho = 0.001x - 0.1069$	0.9999
45° illumin. canopy			45° illumin. canopy		
Band [nm]	Empirical line	R²	Band [nm]	Empirical line	R²
530	$\rho = 0.0009x - 0.0238$	0.9929	530	$\rho = 0.0003x - 0.0384$	0.9995
550	$\rho = 0.0008x - 0.0215$	0.9933	550	$\rho = 0.0003x - 0.015$	0.9995
570	$\rho = 0.0009x - 0.0279$	0.9942	570	$\rho = 0.0003x - 0.0177$	0.999
670	$\rho = 0.0008x - 0.0324$	0.995	670	$\rho = 0.0002x - 0.033$	0.9967
700	$\rho = 0.0008x - 0.0194$	0.9997	700	$\rho = 0.0003x - 0.03$	0.9978
900	$\rho = 0.0029x - 0.1056$	0.9999	900	$\rho = 0.0012x - 0.1281$	0.9907
23/07/2012 Nadir			30/09/2012 Nadir		
Band [nm]	Empirical line	R²	Band [nm]	Empirical line	R²
530	$\rho = 0.0003x - 0.013$	1	530	$\rho = 0.0003x - 0.0208$	0.9959
550	$\rho = 0.0002x - 0.0089$	1	550	$\rho = 0.0003x - 0.0137$	0.9987
570	$\rho = 0.0002x - 0.0113$	1	570	$\rho = 0.0004x - 0.0157$	1
670	$\rho = 0.0002x - 0.0124$	1	670	$\rho = 0.0003x - 0.0187$	0.9987
700	$\rho = 0.0003x - 0.0157$	1	700	$\rho = 0.0003x - 0.015$	1
900	$\rho = 0.001x - 0.0976$	0.9999	900	$\rho = 0.0009x - 0.0957$	1
45° illumin. canopy			45° illumin. canopy		
Band [nm]	Empirical line	R²	Band [nm]	Empirical line	R²
530	$\rho = 0.0003x - 0.0312$	0.9998	530	$\rho = 0.0003x - 0.0856$	0.9965
550	$\rho = 0.0002x - 0.0177$	0.999	550	$\rho = 0.0003x - 0.0313$	0.9933
570	$\rho = 0.0003x - 0.0488$	0.999	570	$\rho = 0.0003x - 0.0286$	0.9938
670	$\rho = 0.0002x - 0.0334$	0.9998	670	$\rho = 0.0003x - 0.0572$	0.9962
700	$\rho = 0.0003x - 0.0332$	1	700	$\rho = 0.0003x - 0.0545$	0.9963
900	$\rho = 0.0011x - 0.1489$	0.9998	900	$\rho = 0.0011x - 0.1645$	0.9925

According to field sampling, all rows within the SMS and replicates sampling area located at the lower end of the vineyard (Figure 7.5) were digitized to retrieve the respec-

tive canopy spectral values of the sampling horizon which was located within the upper leaf layer. Canopy gaps were generally avoided..

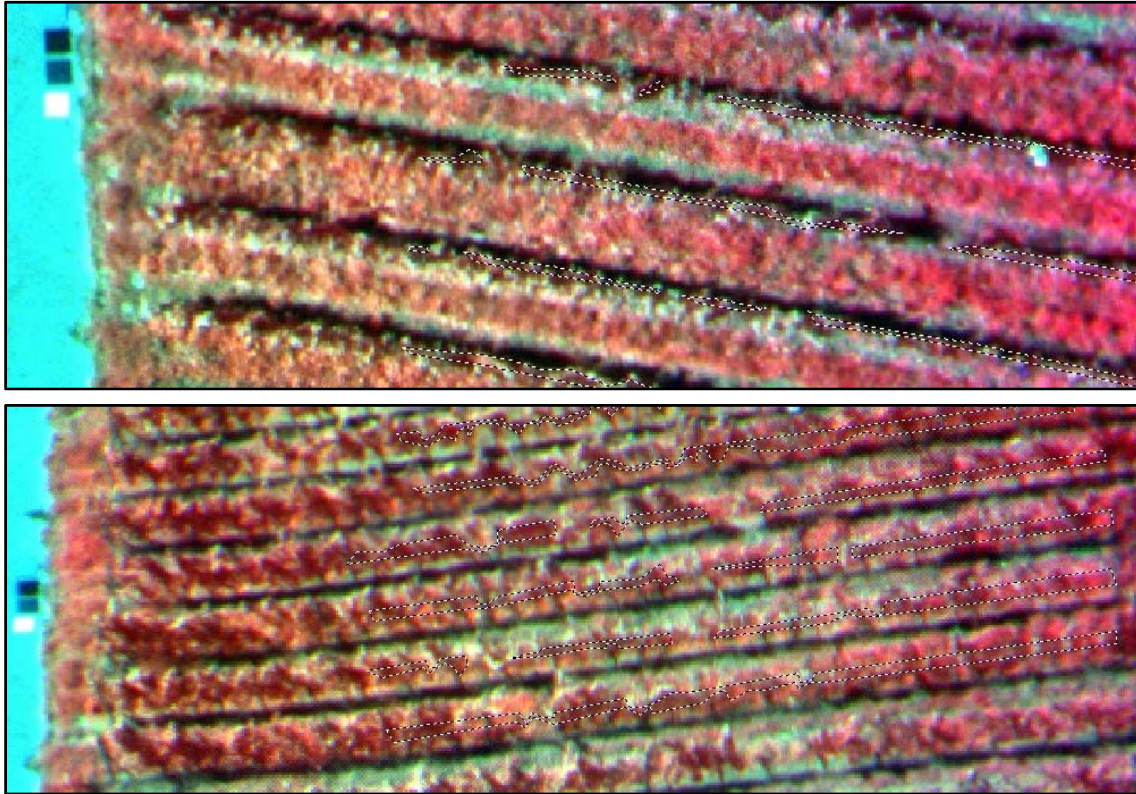


Figure 7.5 Polygons for retrieving canopy spectral value means (top: nadir VZA, bottom: 45° VZA)

In preparation for seasonal comparisons of Chl, a mask of the vine rows was created by an unsupervised classification following a principal component analysis: The Iterative Self-Organizing Data Analysis Technique (ISODATA) algorithm (Memarsadeghi et al. 2007, Intergraph Corporation 2013) was applied with the following settings: 10 spectral classes with 20 iterations and a convergence threshold of 0.95. Statistics were initialized from image statistics and classes obtained needed to fit the following criteria: minimum size of 0.1% of all pixels for a cluster, maximum standard deviation of 5, minimum Euclidian distance between clusters of 4 and a maximum of 1 cluster merging at the end of the procedure. The retrieved 10 classes were further assigned by visual interpretation to a binary map of strict vine canopy (1) and other (0).

For 2011, commonly used VIs were calculated (Table 7.4) and image statistics (mean, minimum, maximum, and standard deviation of DNs or reflectances) derived for the digitised sampling zones.

Table 7.4 Vegetation indices and their focus on physiological variables used in this study (subscripted wavelengths in nm)

Vegetation index	Formulation	Author	Application
Simple Ratio Index	$SR = R_{nIR} / R_{red}$	Jordan 1969	Structural index, plant vitality
Normalized Difference Vegetation Index	$NDVI = (R_{nIR} - R_{red}) / (R_{nIR} + R_{red})$	Rouse <i>et al.</i> 1974	Structural index, plant vitality
Transformed Chlorophyll Absorption in Reflectance Index	$TCARI = 3 [(R_{700} - R_{670}) - 0.2 (R_{700} - R_{550}) (R_{700}/R_{670})]$	Haboudane <i>et al.</i> 2002	Chl index, less influence of LAI
Optimized Soil-Adjusted Vegetation Index	$OSAVI = (1 + 0.16) (R_{nIR} - R_{red}) / (R_{nIR} + R_{red} + 0.16)$	Rondeaux <i>et al.</i> 1996, Haboudane <i>et al.</i> 2002	Chl index, less sensitive to soil background
Photochemical Reflectance Index	$PRI = (R_{531} - R_{570}) / (R_{531} + R_{570})$	Gamon <i>et al.</i> 1992	Carotenoids/Chl index, Chl fluorescence, radiation use efficiency, water stress
Renormalized Difference Vegetation Index	$RDVI = (R_{nIR} - R_{red}) / (R_{nIR} + R_{red})^{0.5}$	Roujean and Breon 1995	Structural index related to fAPAR
Red Edge Ratio Index	$RE = R_{700} - R_{670}$	Part of TCARI; Zarco-Tejada <i>et al.</i> 2013a	Chl content

7.2.5.2 2012 Thermal Data

As the UCM automatically performs a greyvalue stretch for each image acquisition, the 28/06/2012 thermal images were radiometrically aligned by histogram matching. Images were resampled to mosaics by ERDAS Imagine image-to-image registration with the help of the ground control points laid out in the field. Nearest neighbour resampling to 15 cm x 15 cm pixel resolution was chosen (Figure 7.6).

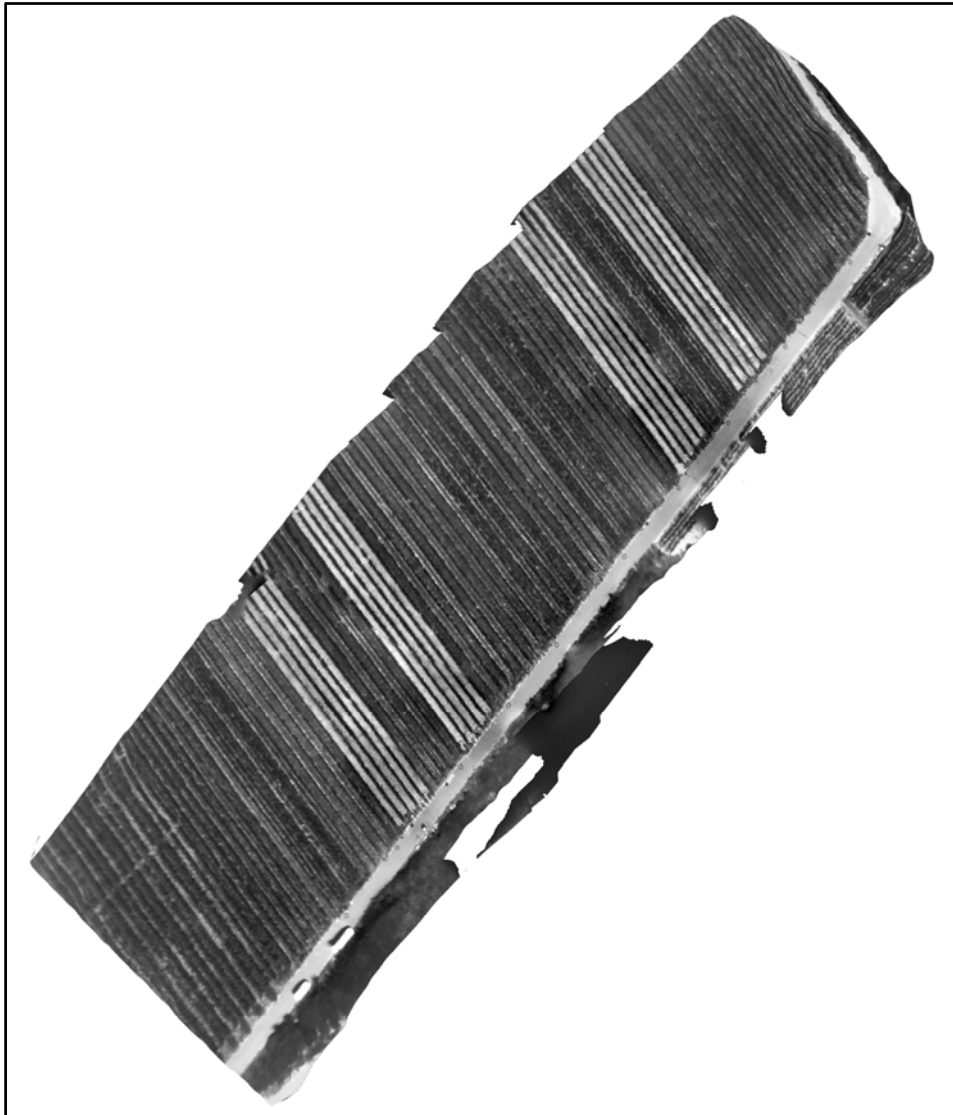


Figure 7.6 Mosaic of thermal histogram-matched images from 28/06/2012

As for the multispectral data, for each row, the mean digital values were retrieved from the canopy for each treatment and their replicates.

7.2.6 Statistical Data Analysis

Statistical analysis on the 2011 and 2012 data sets was carried out a) to assess the impact of the different SMS on canopy reflectance and their spectral separability in relation to VZAs, b) to analyse the correlation structure among the variables, and c) to establish quantitative prediction models for a spatial assessment of selected plant physiological properties based on the measured reflectance data.

A principal component analysis was computed from the DNs to show potential differences in VZA and canopy spectral behavior. The correlation structure among the measured reference and band values data of 2011 was visualized using a heat map of pairwise Pearson's correlation coefficients of all properties, considering all flight directions and physiological variables.

Differences among canopy reflectance caused by the different SMS were analysed using both linear discriminant analysis (LDA) and visual inspection (boxplots). The LDA was carried out for each viewing direction, with SMS as grouping factor and the VIs as explanatory variables. The following indices were used: SR, NDVI, TCARI, OSAVI, TCARI/OSAVI, PRI, RE, and RDVI (Table 7.4).

Further inspection included boxplots of the thermal radiation at fruit set (BBCH 71) to inspect if SMS induce thermal canopy differences, an ANOVA was computed of the thermal signal versus SMS.

The quantification of selected vegetation properties (Chl and N content, leaf layer number LLN, percentage of gaps PG in the upper canopy, LAI and yield) using grey value (i.e. DN, digital number) data was accomplished using forward stepwise multiple regression analysis. Different regression models were calibrated for the 2011 and 2012 data sets: The aim of the 2011 analysis was to understand the impact of the viewing direction on plant property estimations and to derive the most appropriate wavelengths in doing so. To this end the combined reflectance data set, including the data from all viewing directions were included in the stepwise regression models. The intention of the 2012 analysis was to calibrate global regression models for estimating key biophysical plant parameters and to exemplarily compare the resulting spatial estimations of Chl content. In this stepwise regression only data of the illuminated 45° viewing direction were considered since the performance of these data was better compared to the nadir and shaded 45° viewing direction. All regression models were internally validated using leave-one-out (LOO-) cross-validation. The statistical analysis was carried out using the R software package (Retzlaff et al. 2015).

7.3 Results

7.3.1 Field assessments

The results of field assessments in the season 2011 are summarized in Table 7.5. SMS 3 (winter greening and soil tillage in summer) showed highest values in LLN, Chl, N, NBI, the densest upper canopy, as well as the highest LAI, pruning weight and yield per plant.

Table 7.5 Field parameters assessed in the experimental vineyard 2011 (Sampling dates: LLN, PG [%], Chl_{Dualex®} contents, NBI_{Dualex®} at 17/08/2011; N [% dry weight] at 21/09/2011, yield [kg] at 20/11 and 10/10/2011, pruning weight [kg] 30/11/2011)

Parameter	LLN	PG [%]	Chl	N	NBI	LAI	Yield	PW
Mean	1.17	33.37	21.61	1.80	6.31	0.76	2.63	0.45
SMS1	(±0.31)	(±11.5)	(±3.26)	(±0.22)	(±1.26)	(±0.13)	(±0.29)	(±0.13)
Mean	1.11	35.50	19.61	1.77	5.75	0.69	2.69	0.39
SMS2	(±0.19)	(±6.81)	(±2.4)	(±0.27)	(±0.97)	(±0.21)	(±0.67)	(±0.10)
Mean	1.79	18.00	26.09	2.09	8.43	1.09	4.22	0.57
SMS3	(±0.3)	(±9.52)	(±2.52)	(±0.14)	(±1.19)	(±0.22)	(±0.38)	(±0.16)
Mean	1.64	23.00	21.41	1.82	6.51	0.70	3.03	0.51
SMS4	(±0.37)	(±10.89)	(±1.58)	(±0,21)	(±0.73)	(±0.15)	(±0.83)	(±0.13)

Table 7.6 lists the seasonally derived physiological parameters for the grapevine leaves in 2012.

For Chl, N, KBI, LAI, and yield SMS 3 “Winter greening” showed continuously the highest values and for pruning weight the lowest values in 2011 and 2012, followed by SMS 1 “Wolff mixture”.

Further information on retrieved grapevine parameters and analyses of vegetation data not relevant to this study may be found in Evers et al. (2012).

Table 7.6 Field parameters assessed in the experimental vineyard for 2012 (arithmetic mean and \pm standard deviation; DOY: day of year; BBCH after Lorenz et al. 1995, SMS: Soil management strategy; PG [%], Chl_{Dualex®} contents, N [% dry weight], NBI_{Dualex®}, yield [kg], pruning weight [kg])

Parameter	Chl I	SPAD	NBI I	N I	SPAD	Chl II	NBI II	N II	PG	LLN	Chl III	NBI III	N III	Chl IV	NBI IV	N IV	LAI	Yield	Pruning weight
DOY	173				185	200			220		233			270			274	284	326
BBCH	71					71-79			81	81	85			89					
Mean	18.8	26.0	6.4	2.8	27.2	22.7	7.6	2.4	9.4	1.7	21.4	7.2	2.3	19.1	6.4	2.2	2.0	2.3	
SMS 1	± 0.4	± 0.4	± 0.1	± 0.1	± 1	± 0.5	± 0.3	± 0.1	± 4.7	± 0.2	± 1.2	± 0.4	± 0.1	± 1.3	± 0.6	± 0.1	± 0.2	± 0.4	0.7 ± 0.1
Mean	17.8	24.8	6.0	2.6	27.8	20.3	6.7	2.2	18.2	1.6	16.5	5.2	1.9	12.9	4.1	1.8	1.9	2.0	
SMS 1	± 0.4	± 0.9	± 0.2	± 0.1	± 1.8	± 1.0	± 0.4	± 0.1	± 3.4	± 0.1	± 1.3	± 0.5	± 0.1	± 1.3	± 0.5	± 0.1	± 0.4	± 0.3	0.5 ± 0.1
Mean	21.9	29.3	8.0	3.6	28.8	28.1	10.8	3.3	3.1	2.2	30.3	11.3	3.0	26.1	10.1	2.4	2.0	3.2	
SMS 3	± 0.7	± 1	± 0.3	± 0.1	± 1.5	± 0.9	± 0.5	± 0.0	± 1.3	± 0.1	± 0.5	± 0.3	± 0.1	± 1.0	± 0.6	± 0.1	± 0.3	± 0.3	1.1 ± 0.1
Mean	18.8	25.9	6.4	2.7	27.7	20.6	6.9	2.4	12.0	1.7	15.9	5.1	2.1	13.1	4.2	2.1	1.7	2.1	
SMS 4	± 0.2	± 0.4	± 0.2	± 0.1	± 1.2	± 0.8	± 0.4	± 0.1	± 2.9	± 0.0	± 0.9	± 0.4	± 0.2	± 1.3	± 0.5	± 0.2	± 0.5	± 0.1	0.7 ± 0.1

7.3.2 Spectral Separability of Soil Management Strategies Observed by Different Viewing Angles (2011 Data)

The PCA score plot of PC 1 versus 2 (Figure 7.7) demonstrates a higher variability of reflectance values depicted by the oblique viewing geometries, and specifically at illuminated canopy parts (red) compared to the narrower ranges of nadir values (blue) and shaded canopy parts (green).

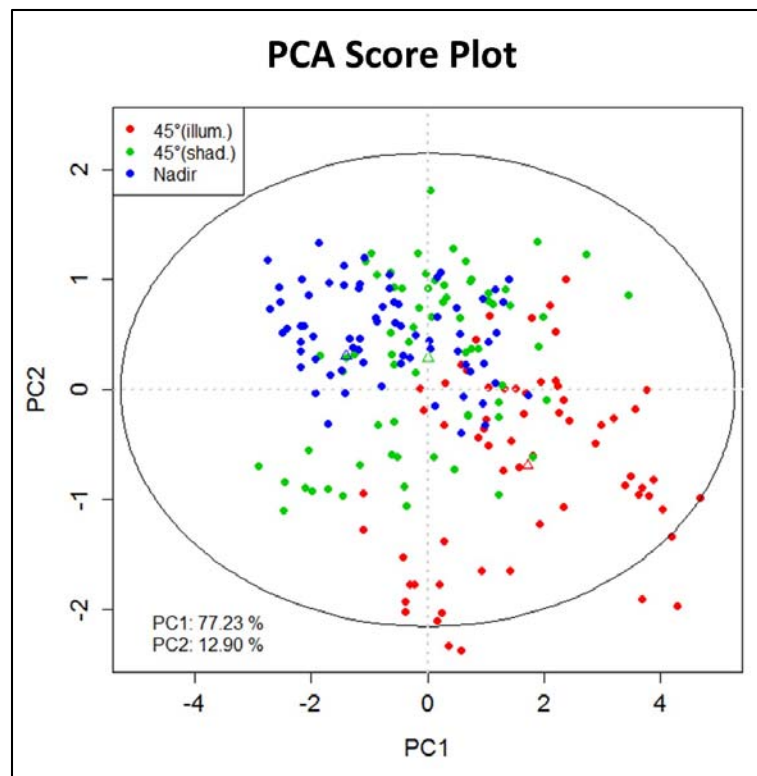


Figure 7.7 Plot of the principal component 1 and 2 for all rows and nadir and oblique viewing geometries (Retzlaff et al. 2015)

Figure 7.8 shows box-plots of different vegetation indices (SR, NDVI, PRI, RDVI, TCARI, and OSAVI) versus the SMS for the three considered viewing geometries (nadir, VZA 45° illuminated, VZA 45° shaded grapevine canopy). The central tendencies of all these vegetation indices show remarkable differences between the four different soil management systems for the oblique viewing directions and especially for the 45°-illuminated direction (SR, NDVI, RDVI, OSAVI), whereas for the nadir direction the soil management systems show very similar means and cannot be separated from each other.

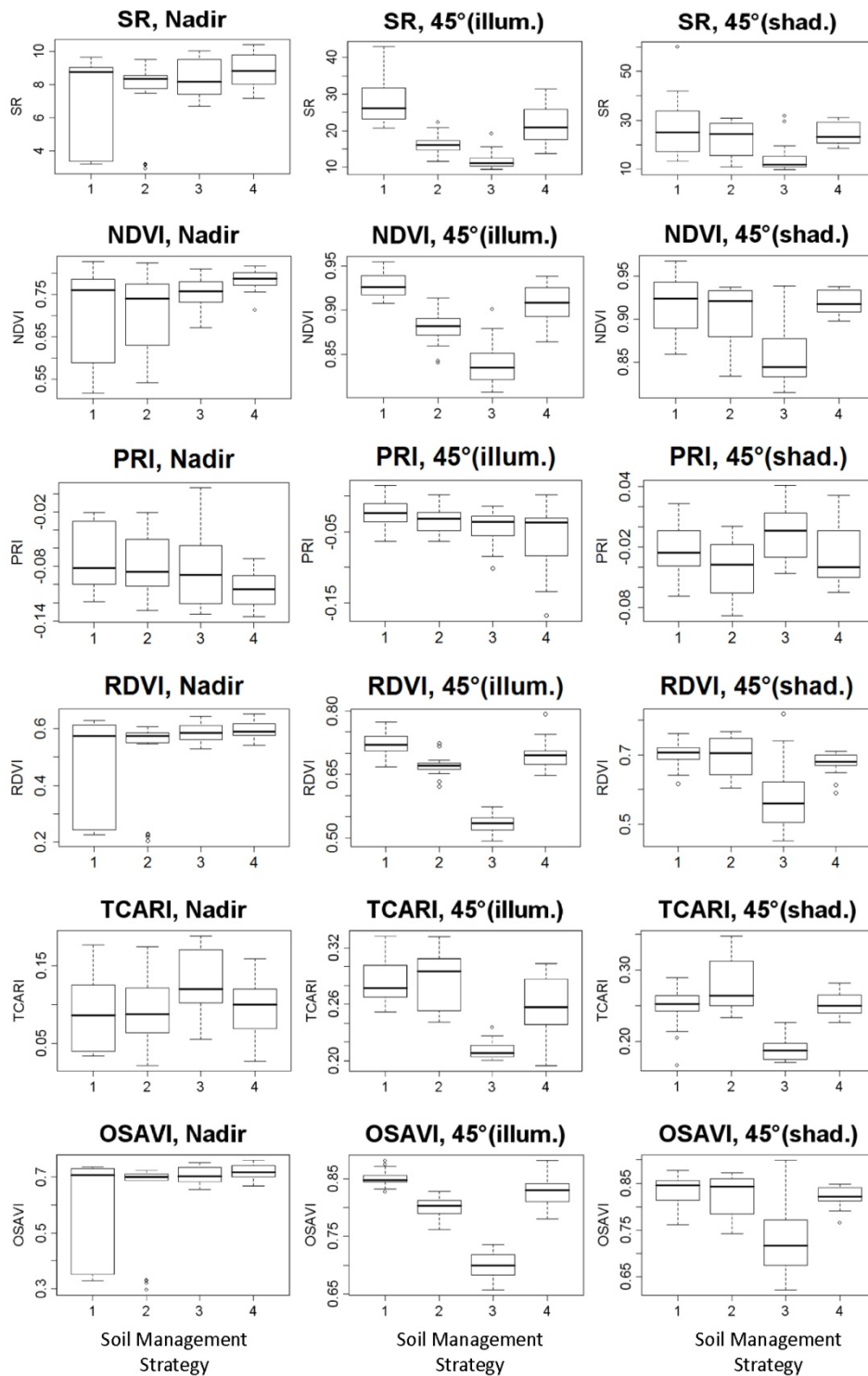


Figure 7.8 Box-plots of different vegetation indices versus SMS 1- 4 (x-axis) for the viewing geometries nadir, illuminated and shaded grapevine sides (black line: median, boxes minimum and maximum values, tails: non-outlier range, circles: outliers)

This was confirmed by linear discriminant analysis (Table 7.7) that was carried out for each viewing direction, with soil management as grouping factor and the vegetation indices as explanatory variables. Table 7.7 summarizes the (cross validated) total accuracies of the respective models and the standardized discriminant coefficients of the first two functions that represent the contribution of a variable to the discriminant function in the context of the other predictor variables in the model. The total accuracy of the model that is based on the nadir viewing direction is 48.77%, whereas in both oblique viewing directions >70% of the data could be correctly classified.

Table 7.7 Standardized discriminant coefficients of the first two discriminant functions, proportion of trace and cross-validated total accuracies for LDA models for different viewing directions (n=215, LD: linear discriminant)

	Nadir		45°(illum.)		45°(shade)	
	LD1	LD2	LD1	LD2	LD1	LD2
SR	-5.77	-1.35	0.67	3.74	3.4	-0.56
NDVI	0.45	0.93	5.19	0.66	0.65	-0.83
PRI	1.86	0.01	-0.19	0.27	0	0.27
RE	-0.96	3.16	0.05	-1.23	-3.15	2.21
TCARI	5.74	-8.94	17.4	20.72	4.37	5.32
OSAVI	-1.32	-12.22	-28.8	-15.64	-5.14	-11.66
TCARI/OSAVI	-3.82	4.85	-14.02	-15.68	-3.7	-4.42
RDVI	6.13	15.6	11.17	2.83	0.38	9.69
Prop. of trace	0.69	0.25	0.89	0.08	0.86	0.08
Total acc.(CV)	48.75%		70.77%		70.25%	

Furthermore, the discriminant coefficients in Table 7.7 reveals that the vegetation indices TCARI, OSAVI, TCARI/ OSAVI, RDVI and to a lower extent NDVI mostly contribute to the discrimination, especially for the illuminated canopies (Retzlaff et al. 2015).

7.3.3 Separability of Soil Management Strategies Observed by Thermal Radiation (2012 Data)

As the boxplots (Figure 7.9) and the ANOVA (Figure 7.10) of the LWIR radiation data against the SMS show, the SMS 3 (summer soil tillage with rotating harrow and winter greening) could again be separated from the other strategies and to a lesser extent SMS

1 (Wolff mixture) from 2 (natural greening). The SMS 4 (natural greening with disturbance in dry conditions) could at that point of time not be separated from 1 and 2.

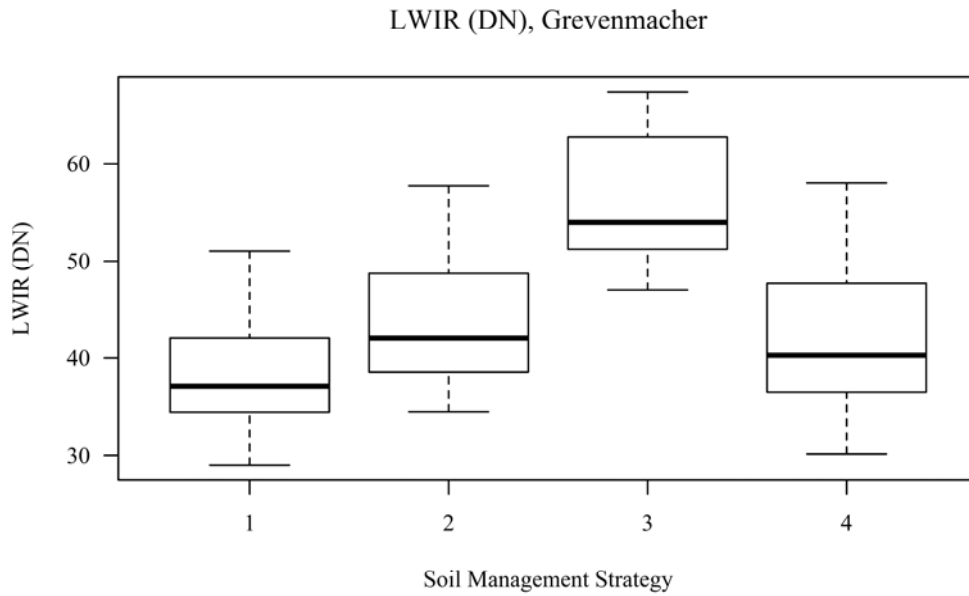
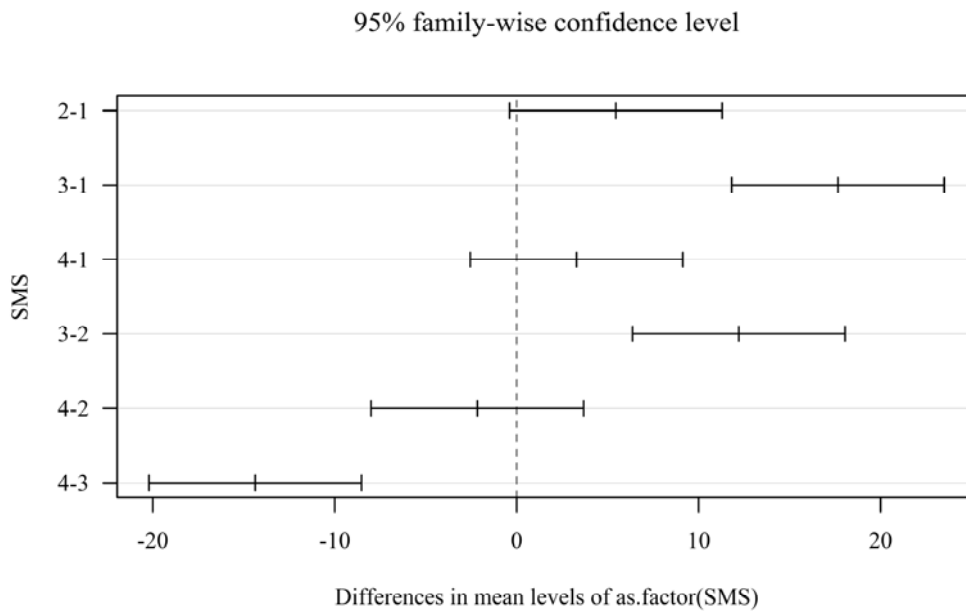


Figure 7.9 Box-plot of thermal radiation signal versus SMS for 28/06/2012



	Df	Sum Sq	Mean Sq	F value	Pr(>F)
as. factor(SMS)	3	3562	1187.5	24.02	4.91e-11***
Residuals	76	3757	49.4		

Signif. codes: 0 '***' 0.001 '**' 0.01 '*' 0.05 '.' 0.1 ' ' 1

Figure 7.10 ANOVA results of thermal radiation signal versus SMS for 28/06/2012

7.3.4 Ability to Predict Physiological Parameters and Yield for Grapevine Using Different Viewing Geometries (2011 Data)

Figure 7.11 shows a heatmap depicting the correlation among the measured plant parameters for the growing season and reflectance data. Plant parameters from all dates were included in the analysis. There is a group of variables that are positively correlated (Chl, N, LLN, yield). The variable PG is negatively correlated with this group. From the remote sensing perspective, among these variables, the chlorophyll content is the most interesting one, since chlorophyll can be predicted from multispectral remote sensing data and may be linked to yield. The heatmap also illustrates the increasing correlation between Chl and yield with image acquisition dates progressing to the end of season.

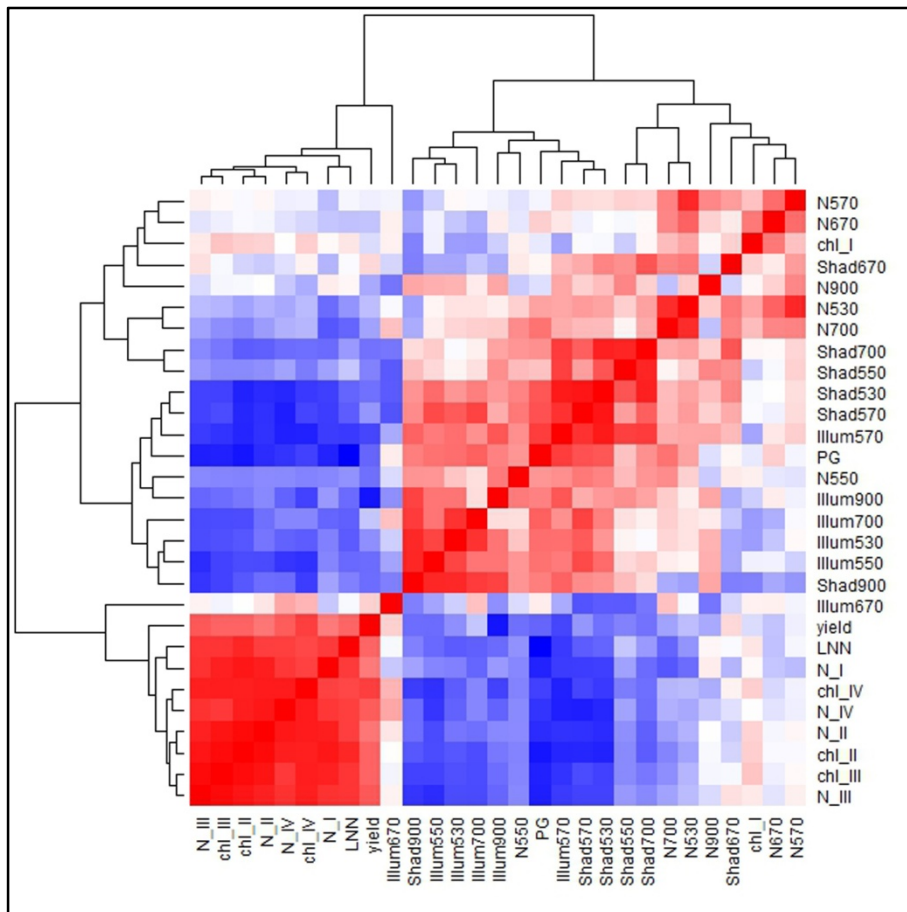


Figure 7.11 Heatmap of *in-situ* measured physiological variables in 2011 (red: high correlation, blue: low correlation, N: nadir; Shad: 45° VZA shaded; Illum: 45° VZA illuminated, I-IV are measurement dates of *in-situ* sampling from beginning of berry development to harvest)

Table 7.8 Derived regression models for the prediction of measured vine physiological variables of 2011 field samples for each VZA (X: Band; significance codes: 0 ‘***’, 0.001 ‘**’, 0.01 ‘*’, 0.05 ‘.’, 0.1 ‘.’ 1) (Retzlaff et al. 2015)

Chl	Nadir	45°(illum.)	45°(shad.)
Intercept	549.101	541.1043	529.7517
X ₅₃₀			0.000246 ***
X ₅₅₀	0.0403 *	0.00223 **	
X ₅₇₀		0.00318 **	
X ₇₀₀		0.05216 .	0.043850 *
N	16	14	13
R ² _{cv}	0.26	0.85	0.76
RMSE _{cv}	34.64	17.21	19.92

N	Nadir	45°(illum.)	45°(shad.)
Intercept	3.6251	3.39543	3.7748189
X ₅₃₀			9.93E-05 ***
X ₅₅₀	0.083350 .	0.000884 ***	
X ₅₇₀		0.004124 **	
X ₇₀₀		0.029463 *	0.00338 **
N	16	14	13
R ² _{cv}	0.24	0.85	0.76
RMSE _{cv}	0.184	0.11	0.126

PG	Nadir	45°(illum.)	45°(shad.)
Intercept	-30.1074	-25.22294	-31.609778
X ₅₃₀		0.017161 *	
X ₅₅₀	0.0184 *	0.151129	2.37E-06 ***
X ₅₇₀		0.000276 ***	
X ₆₇₀		0.002361 **	
N	16	14	13
R ² _{cv}	0.4	0.66	0.84
RMSE _{cv}	6.81	4.89	2.97

Yield	Nadir	45°(illum.)	45°(shad.)
Intercept	10.563235	6.28664	3.540241
X ₅₃₀		0.029139 *	
X ₅₅₀	0.010237 *	0.056265 .	0.185868
X ₅₇₀		0.095864 .	
X ₇₀₀		0.024746 *	0.000964 ***
X ₆₇₀			0.001972 **
X ₉₀₀	0.055355 .	0.000236 ***	
N	16	14	13
R ² _{cv}	0.51	0.84	0.68
RMSE _{cv}	0.57	0.34	0.46

For the 2011 data, the influence of different viewing directions on the quantitative predictions of selected vine physiological properties was tested: Chl, N, PG and yield. For this purpose stepwise linear regression models were computed for each VZA to identify

the most relevant wavelengths for estimation, using the Akaike information criterion (AIC). Validation was accomplished through leave one-out cross-validation (Table 7.8).

Table 7.8 demonstrates that for a given plant property different models were identified for the different viewing directions using the stepwise linear regression approach. In general, best results for each plant characteristics were obtained using the reflectance data from the oblique viewing geometries. Beside PG, the 45° sun-illuminated canopy parts showed higher coefficients of determination than the shaded sides. The cross-validated R^2 values in our case range from 0.66 (PG) to 0.85 (Chl, N). In contrast, spectral signatures taken from nadir did not, except for yield, lead to reliable quantitative estimations of the plant characteristics.

7.3.5 Predicting Seasonal Grapevine Physiological Parameters and Yield (2012 Data)

As in the previous year, the best separability was obtained from oblique imagery of the illuminated grapevine parts, therefore only these images were further processed for the 2012 data. Regression models were computed for Chl, N, and NBI including all dates. Compared to individual step-wise regression models for one date in 2011 with a $R^2_{cv} > 0.8$, the global predictive models' R^2_{cv} in 2012 were smaller but except for N with $R^2_{cv} = 0.52$ still ranged from $R^2_{cv} = 0.65$ for Chl, and $R^2_{cv} = 0.76$ for NBI (Figure 7.12). Table 7.9 lists the associated model coefficients which include the nIR band (900 nm) and the red edge (700 nm) as highly significant (p value < 0) for all parameters models, and for Chl also the Chl peak near 550 nm.

7.3.5.1 Chlorophyll Estimation (2012)

The following presents in detail the results for Chl for 2012.

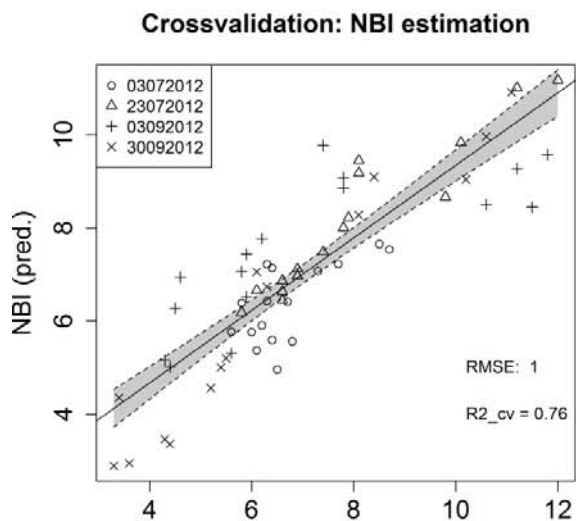
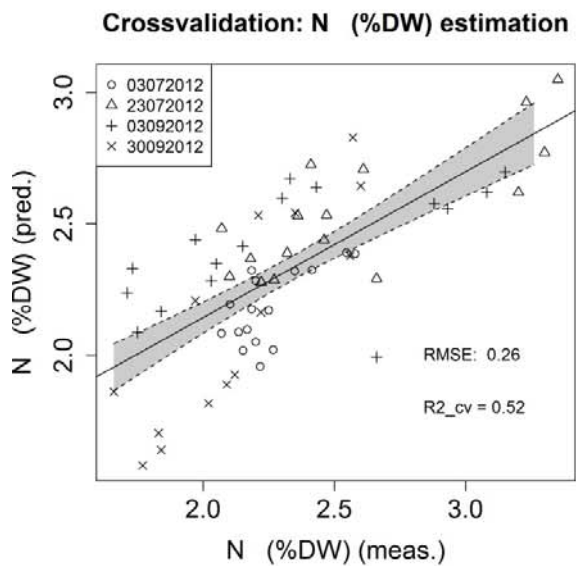
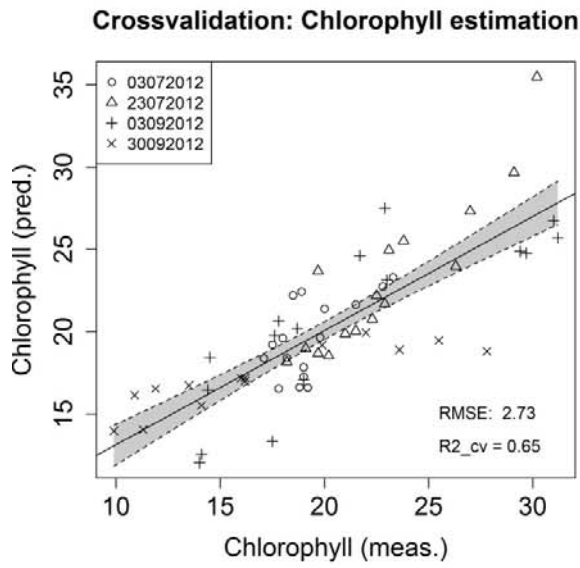


Figure 7.12 Cross-validated regression models and model coefficients for Chl Dualex® and N content [% dry weight] and NBI_{Dualex®} for 2012

Table 7.9 Model coefficients for cross-validated regressions models for Chl, N and NBI in 2012 of Figure 6 (Significance codes: 0 ‘***’, 0.001 ‘**’, 0.01 ‘*’, 0.05 ‘.’, 0.1 ‘ ’ 1)

Coefficients	Estimates	Standard	t value	Pr (> t)	Sign.
Chl					
Intercept	31.9502625	1.8207056	17.548	< 2E-16	***
X ₉₀₀	0.00325	0.0002935	11.074	9.96E-16	***
X ₇₀₀	-0.0182065	0.0030136	-6.041	1.30E-07	***
X ₅₃₀	0.0125341	0.004308	2.91	0.00518	**
X ₅₅₀	-0.0117183	0.002162	-5.42	1.31E-06	***
Multiple R ²	Adjusted R ²	Residual SE	F-Statistic	p-value	
0.7068	0.6859	2.822	38.76 on 4 and 56 DF	2.49E-14	
N					
Intercept	2.07E+00	2.06E-01	10.067	3.59E-14	***
X ₉₀₀	3.17E-04	4.77E-05	6.642 1.	1.35E-08	***
X ₇₀₀	-1.42E-03	2.53E-04	-5.632	5.99E-07	***
X ₅₃₀	5.29E-04	2.14E-04	2.467	0.0167	*
X ₆₇₀	9.77E-04	4.655E-04	2.1	0.0403	*
Multiple R ²	Adjusted R ²	Residual SE	F-Statistic 19	p-value	
0.5758	0.5455	0.271	on 4 and 56 DF	6.40E-10	
NBI					
Intercept	5.4260802	0.6973468	7.781	1.43E-10	***
X ₉₀₀	0.0020961	0.0001669	12.557	< 2E-16	***
X ₇₀₀	-0.0074283	0.0006788	-10.943	9.91E-16	***
X ₆₇₀	0.0053489	0.0012923	4.139	0.000114	***
Multiple R ²	Adjusted R ²	Residual SE	F-Statistic	p-value	
0.7895	0.7786	1.026	72.52 on 3 and 58 DF	2.2E-16	

Based on the derived seasonal regression models, Chl values were spatially estimated for each of the SMS and all replicate for the image acquisition dates in 2012 (Figure 7.13). For identification purposes, only replicate A was selected for visualization. The map illustrates clear differences among the reflectances between the BBCH stages (Lorenz et al. 1995).

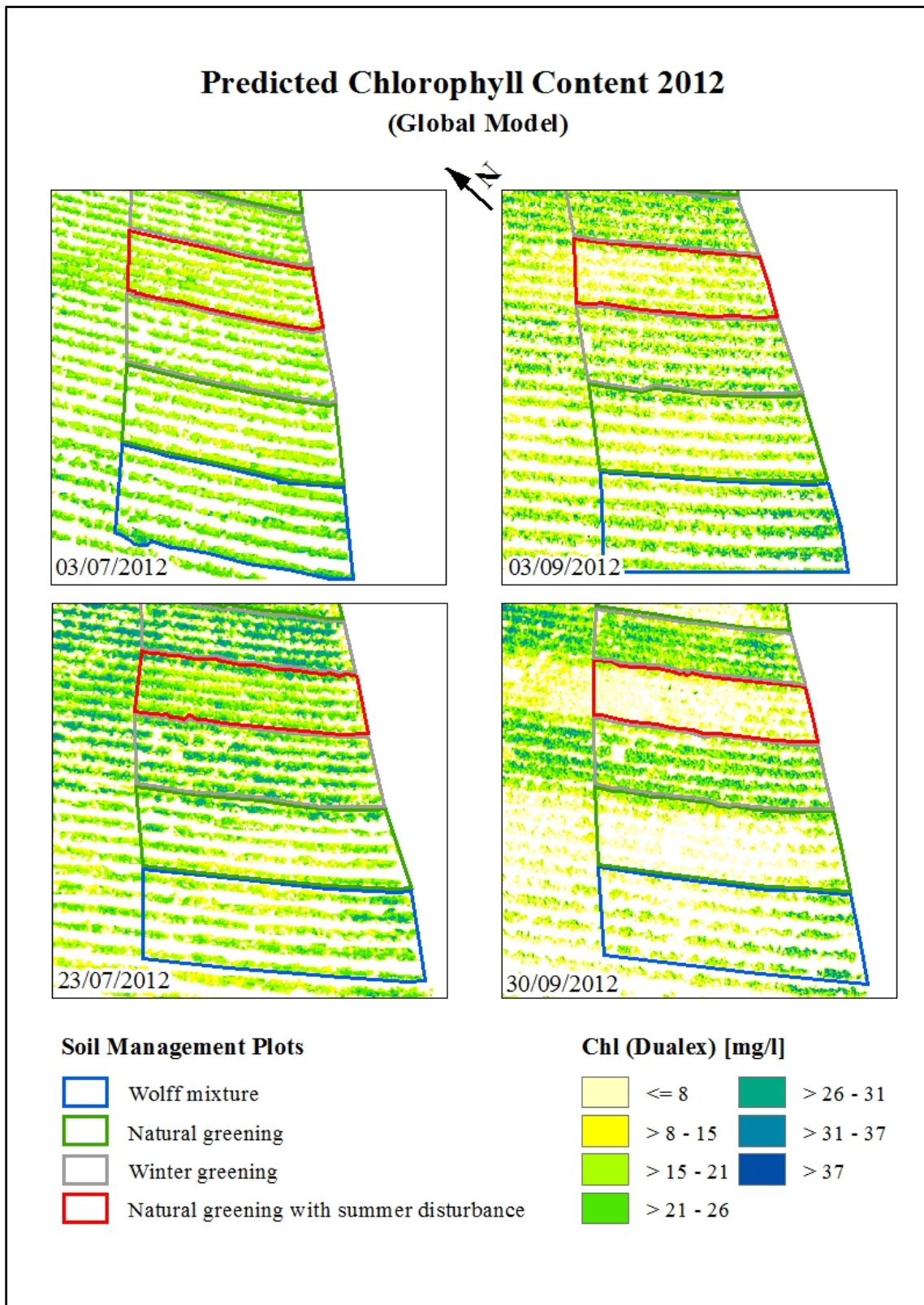


Figure 7.13 Chlorophyll estimation for image acquisition dates based on global regression model of in-situ derived Chl and reflectances in 2012 (replicate A)

The seasonal course of predicted canopy Chl illustrates that SMS (3) with winter greening and summer soil tillage, except for early summer, showed the highest values for all dates followed by the Wolff mixture (1). For the natural greening (2) and natural greening with disturbance during dry conditions (3), late summer/early autumn date Chl values diminish faster than for other SMS.

Measured Chl(Dualex) values for replicate A-D, confirm these results (Figure 7.14). The Chl values are generally highest and persist at higher levels even for September (DOY 270) compared to other SMS with respective correlation coefficient between measured and predicted Chl values being $R = 0.84$ for SMS (1), $R = 0.84$ for (2), $R = 0.94$ for (3) and $R = 0.99$ for (4).

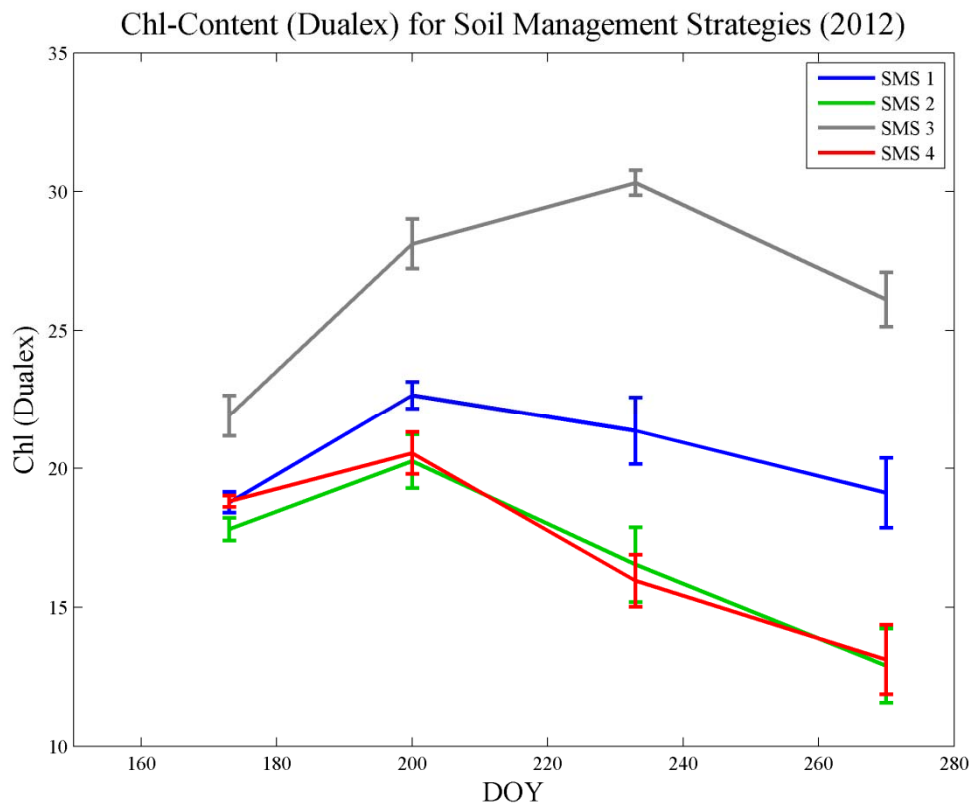


Figure 7.14 Mean seasonal course and standard deviation of measured Chl (Dualex) across all replicates in 2012 (SMS: soil management strategy; bars: standard deviation)

7.3.5.2 LAI (2011 versus 2012)

For 2011 (Figure 7.15), LAI values could be predicted with a R^2_{cv} of 0.71 by a step-wise regression model of the August multispectral reflectance data and measured LAI values at the end of August.

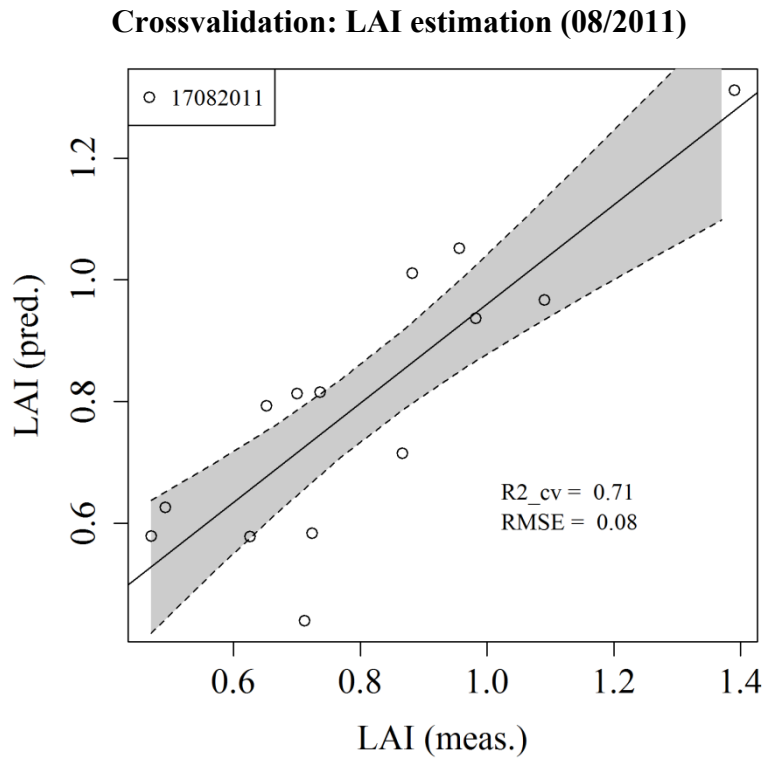


Figure 7.15 Cross-validated regression model for LAI

For comparison, similar regression analysis for 2012 using the 03/09/2012 images being closest in season stage to the 2011 data, yielded no correlation (multiple R^2 : 0.3687, adjusted R^2 : - 0.05209).

7.3.5.3 Yield Estimation (2012)

The individual step-wise regression models for each respective date and measured yield in 2012 showed deviating results: The prediction of yield was best achieved at BBCH stage 71 Fruit set (Lorenz et al. 1995) (03/07/2012) with a R^2_{cv} of 0.87 and for stage 81 Softening of berries (03/09/2012) with a R^2_{cv} of 0.73. There seems to be no correlation of the multispectral data at BBCH stage 77-79 Berries touching (23/07/2012) with R^2_{cv} of 0.2 as well as for the end of the growing season (30/09/2012) and a R^2_{cv} of 0.12.

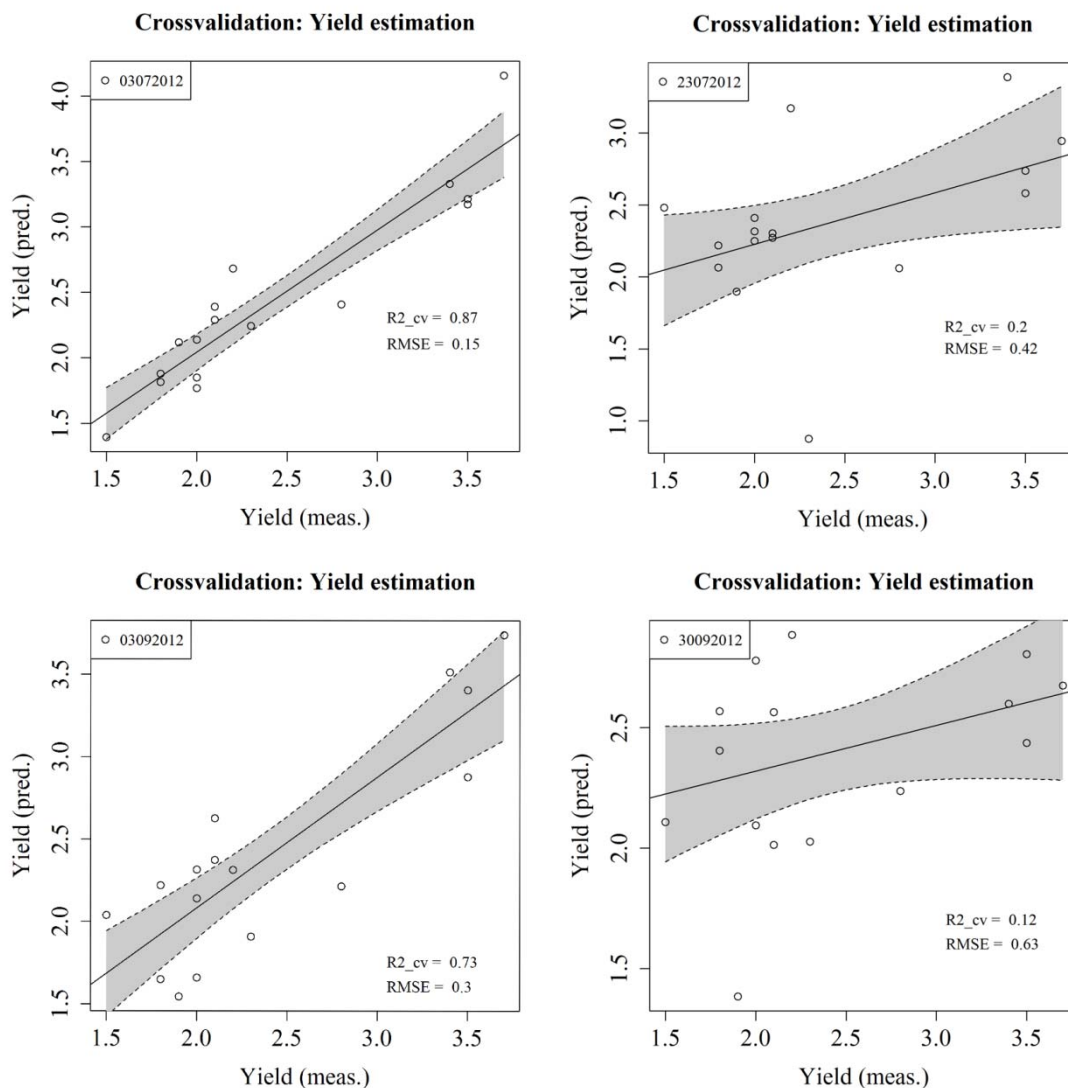


Figure 7.16 Cross-validated regression models and model coefficients for different within-season times in 2012 (top left: 71 Fruit set; top right 77-79 Berries touching; 85 Softening of berries, 89 Berries ripe for harvest)

7.4 Discussion

High quality wines highly depend on fertile soils and a sensible soil management (Gil-Perez et al. 2010, Bramley et al. 2011a, Tardaguila et al. 2011, Arnó et al. 2012). In this study, the utility of multispectral data acquired at nadir and oblique viewing geometries to distinguish among SMS was analyzed (objective (i)). It could be shown that different SMS result in variations in the Vis/nIR during the growing season and could well be separated by multispectral and to a lesser extent by broadband thermal data, although the latter only for one point in time and to a lesser degree (SMS 4 and SMS 2 were not separable, Figure 7.9).

Compared to nadir images, oblique viewing angles were found to significantly boost the spectral separation of grapevine canopy reflectance of different SMS (Figure 7.7). The multispectral images obtained from a UAS for August 2011 showed that the canopy reflectance of illuminated canopy fractions has a larger variance in the PC space of the 1st and 2nd principal component (PC) of all bands than the nadir image. The shaded canopy parts however, are rather a mixture of these two. This is in accordance with the findings of Kempeneers *et al.* (2008) and Meggio *et al.* (2008) who successfully modelled Chl concentration from hyperspectral reflectances perpendicular to the solar plane by inverting a 3D ray tracing canopy model. Possible signal contamination by spurious soil pixels included in the row polygons retrieving the image spectral signals, did not seem to affect the statistical separation. First, as arithmetic means were computed for each row, potential soil signal effects are supposed to become negligible. Also, one would expect the results for the oblique viewing geometries to be more affected by spurious soil pixels and should have performed worse as more soil signal is potentially included within the signal. This was, however, not the case.

Evaluating the performance of common vegetation indices (VI) listed in Table 7.4, we were able to confirm the higher suitability of oblique viewing angles on illuminated canopy (Table 7.7). Hyperspectral VIs such as OSAVI, TCARI, TCARI/OSAVI and PRI, have been described as being sensitive to Chl_{a+b} changes for *Vitis vinifera* L. leaves and canopies (Zarco-Tejada et al. 2005; Martín et al. 2007, Gil-Perez *et al.* 2010, Zarco-Tejada *et al.* 2013a), and indeed OSAVI, TCARI AND TCARI/OSAVI were able to precisely separate the SMS (Figure 7.8), separability being strongest for oblique viewing angles on illuminated canopies. Only poor discriminant power had been found for PRI and RE (Table 7.7). Among the simpler VIs and oblique viewing angles with the sun positioned behind the observer, the RDVI and NDVI also distinguish well among SMS. Hall *et al.* (2011b) enhanced the analysis of shaded canopies compared to the

sunny sides by normalization using a shadow fraction derived from multiple viewing geometries.

Similarly, the broadband thermal data (nadir) was partly able to separate the SMS 3 (summer soil tillage with rotating harrow and winter greening) from all other treatments and partly SMS 2 (natural greening) from 1 (Wolff mixture) as Figure 7.9 and Figure 7.10 illustrated. The good separation of SMS 3 is most likely due to the heated open floor and higher radiative signals compared to the other strategies. A different result may be expected if the grapevine suffered from water stress (Berni et al. 2009a; Berni et al. 2009c, Berni et al. 2009b).

The second objective (ii) in this study was, using the 2011 data, to determine the most appropriate viewing geometry for predicting physiological and canopy parameters, where again best results (Table 7.8) were obtained using multispectral reflectances of oblique viewing geometries for illuminated canopies for N and Chl (both R^2_{cv} 0.85), and yield (R^2_{cv} 0.84). For PG in the upper canopy, however, the shaded canopy parts were better suited for the estimation (R^2_{cv} 0.84). The better performance of oblique viewing angles compared to nadir imagery, is due to seeing a greater part of the vertically-oriented grapevine canopy. In spite of careful pixel selection using manual digitizing and unsupervised classification a possible signal contamination by spurious soil pixels could not be fully excluded in the statistical analysis. However as arithmetic means were computed for each row, a potential soil signal effect is suppressed. If this was not the case, the results for the oblique viewing geometries should have been more affected and expected to perform worse as more soil signal is potentially included in the area, which was not the case. In fact, the optimal retrieval of leaf chemical components was achieved from the oblique viewing directions.

Seasonal changes of grapevine physiological parameters (objective (iii)) were derived by global regression models. Chl and NBI content estimations throughout the season of 2012 showed slightly lower R^2_{cv} values (Figure 7.12: 0.65, and 0.76, respectively) than in 2011 (Chl and N $R^2_{cv} = 0.85$), for N even $R^2_{cv} = 0.52$ (Table 7.8, Table 7.9). Generally, the quantification of the N content from spectroscopic data using empirical models is mainly indirect via the positive correlation between N and Chl. In fact, Table 7.9 shows that apart from the wavelength 550 nm the stepwise multiple regression selected the same wavelengths (900 nm, 700 nm and 530 nm) for both variables and respective regression coefficients have the same signs. N is positively correlated with the Chl content as it is contained in the Chl pigments (Guyot 1990, Jensen 2007), which is the optically active parameter for remote sensing. Compared to Figure 7.12, Figure 7.17 shows

the linear relationship between N and Chl for the early flight at fruit set ($R^2_{cv} = 0.87$), and the latter three dates in 2012 ($R^2_{cv} = 0.83$).

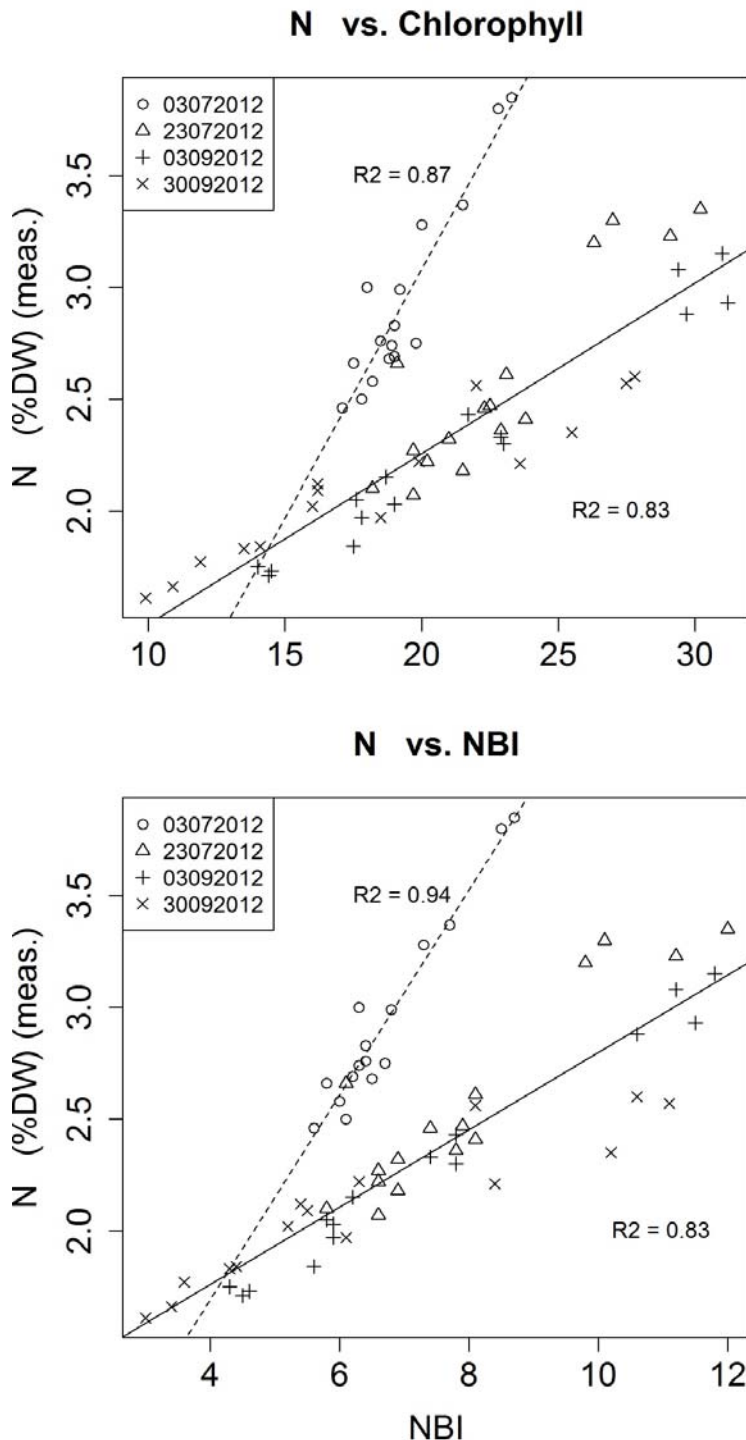


Figure 7.17 Plot of Chl_{Dualex} versus N (top) and NBI_{Dualex} versus N content for the field measurements early and the latter three dates in 2012

It illustrates that at early season, the relationship between Chl and N is different than for later development stages leading to an overall lower R^2_{cv} value of 0.52 for the prediction of N for the whole season. This again consolidates the importance of selecting appropri-

ate BBCH stages for image acquisition. The prediction's accuracy of N therefore increases if the first flight data was subtracted from the 2012 analysis. As Figure 7.17 additionally shows, the NBI is directly linked to Chl content as it is derived from the same optical measurement device (*i.e.* Dualex).

Furthermore, remaining bidirectional reflectance differences between *in-situ* spectral measurements and sensor-viewing and row geometry may add to that effect (Zarco-Tejada *et al.* 2005). Another reason for lower correlations in 2012 compared to 2011 may be attributed to time delay between field parameter derivation and image acquisition (Figure 7.18). Due either to weather conditions or logistic reasons (e.g. availability of instruments), image acquisition could not always take place at field measurement dates. However, the general progression is nevertheless following the measured Chl course.

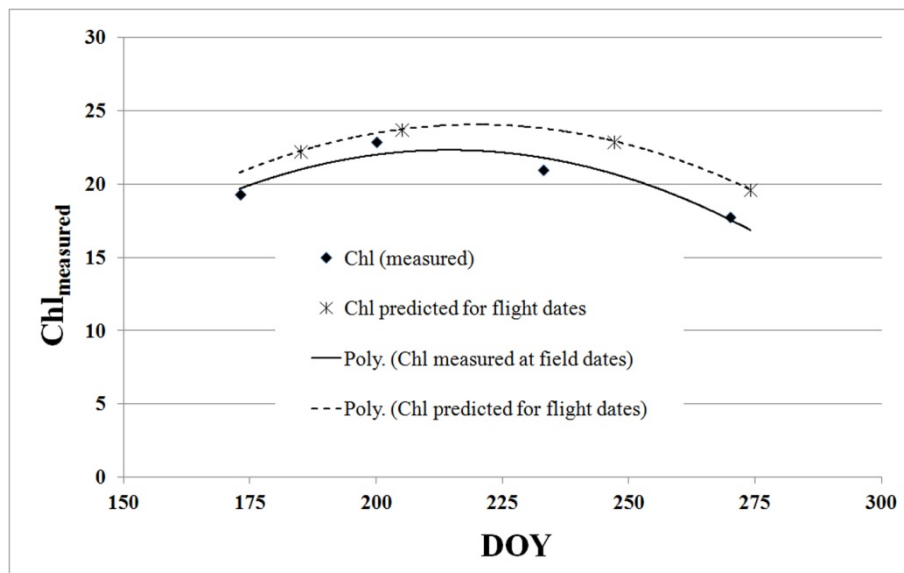


Figure 7.18 Time shift between seasonal field Chl measurements (arithmetic mean: black dots) and UAS image acquisition dates (grey asterix) in 2012

The SMS 3 (summer soil tillage with rotating harrow and winter greening) was observed being the most vigorous in terms of Chl, N, NBI and yield values followed by SMS 1 (Wolff mixture) (Table 7.5, Table 7.6, Figure 7.14). The graph also shows the greater late summer drop of mean measured Chl for SMS 2 (natural greening) and 4 (natural greening with disturbance in dry conditions). This suggests that grapevine vigour is fostered by lack of competing cover crops in summer. Similar results had been found for more Mediterranean type climate zones (Clarke *et al.* 2006; Tesic *et al.* 2007).

Both years have deviated from the long-term mean by $+1^{\circ}\text{C}$ and $+0.5^{\circ}\text{C}$ in temperature derived at 2m height, and 2011 had about 30-45% less rainfall than normally, 2012 had mean annual rainfall (data: Forschungsanstalt für Waldökologie und Forstwirtschaft 2015).

The grapevine structural parameter LAI could be predicted with reasonable accuracy for 2011 (Figure 7.15), yet not so for the subsequent year. This may be attributed to the changing measurement method to comply with other experiments. Experiments should be repeated throughout a season comparing measurement setups to retrieve any conclusions.

Predicting yield showed seasonal differences in the prediction quality of measured yield (Figure 7.16). Similar as for N and NBI (Figure 7.17), the early season shows higher correlation of multispectral data ($R^2_{cv} = 0.87$) than for later seasons. Although, in this case, at veraison, yield could be better predicted ($R^2_{cv} = 0.73$) than at the end of season image shortly before harvest ($R^2_{cv} = 0.12$). Negative correlations ($r \sim -0.2$) between canopy density and canopy area and yield until flowering and higher positive correlations ($r \sim 0.4-0.6$) around veraison have also been reported by Hall et al. 2011a. Hall *et al.* (2011a) therefore confirming the importance of selecting appropriate image acquisition times.

7.5 Conclusion

UAS-based imagery has proven to be a useful tool for rapid spatial information of vineyard vigour and precision viticulture. Viticulturists in the Anglican world increasingly fly own UAS to obtain quick overviews over their vineyard's state. SMS affect grapevine vigour and yield across different regions and climates and hence allow for targeted viticulturist attention (Poni et al. 1994; Bramley et al. 2011b; Hall et al. 2011a, Ripoche et al. 2011, Fourie 2011). Observed differences in vigour may be well depicted by means of multispectral UAS-based remote sensing and are best retrieved by oblique UAS data. In this work, reflectance of the illuminated parts of the grapevine canopy was most appropriate to distinguish among SMS using oblique UAS data using simple vegetation indices like the NDVI and RDVI. OSAVI, TCARI and TCARI/OSAVI were also well suited to discriminate SMS at angled views. From multiple UAS images taken at specific BBCH stages from fruit set to pre-harvest, reliable regression models could be derived to estimate Chl and NBI and yield. Thus, the presented methodology is a valuable tool for precision agriculture. Upcoming hyperspectral sensors should widen the scope of canopy and fruit properties even more. Further analyses should include UAS

imagery into 3D presentations of the vine row canopy (Corbane *et al.* 2012) to study in more detail viticultural canopy properties and bidirectional reflectance behaviour as has been exerted for PRI in forests (Hilker *et al.* 2008, Hall *et al.* 2008, Hall *et al.* 2011b).

The scope of thermal infrared data may best be used for water stress studies in vineyards as has been widely published within recent years (Sepulcre-Cantó *et al.* 2006; Berni *et al.* 2009a; Berni *et al.* 2009b; Berni *et al.* 2009c; Suárez *et al.* 2009, a.o.). Another issue for viticulturists could be the microclimatic regional cooling effects during day/night-times within the season, but this was out of scope in this study.

8 UAS-based Retrieval of Sun-Induced Fluorescence

8.1 Introduction

Chlorophyll fluorescence has been described in chapter 3.1.3. Photosynthesis is (a) the process of converting solar light to carbohydrates fuelling all plant processes and carbon fixation (Rascher et al. 2009). Of the solar energy absorbed by the plant pigments, within the photosystem II, (b) excess energy may be emitted from the chloroplasts at longer wavelengths (*i.e.* fluorescence) leading to a double peak at 690 nm (red) and 740 nm (nIR). Further surplus energy (c) is released by the non-photochemical quenching or heat dissipation (NPQ), which converts surplus energy into heat that is dissipated from the leaf and thus protects the chloroplasts from damages (Demmig-Adams and Adams 1996; Meroni et al. 2009; Damm et al. 2010a). The processes occur in competition and give insight into the photosynthetic activity. The used amount of incident light hence varies around 0-82%, for solar-induced chlorophyll fluorescence (F_s) $\sim 0.5\% - 2\%$, and $\sim 17.5\% - 98\%$ for NPQ (Demmig-Adams and Adams 1996; Frankenberg 2012, Murchie and Lawson 2013).

F_s measurements are an early indicator of plant stress (Lichtenthaler and Miehe 1997; Meroni et al. 2009, Calderón et al. 2013, Panigada et al. 2014) and may indirectly be used to estimate light use efficiency (LUE). LUE again is an important variable for the quantification of gross primary production (GPP) and, together with the fraction of absorbed photosynthetically active radiation (fAPAR), a key component in the definition of carbon fixation in the biosphere (Rascher and Pieruschka 2008; Rascher et al. 2009; Damm et al. 2010b).

Within the Flex 2012 Field Campaign at Campus Klein-Altendorf, the impact of N-fertilization on a sugar beet field on the F_s signal using narrow-band multispectral UAS data were to be determined (i). Furthermore, it was tested if UAS-based F_s may follow diurnal courses of photosynthetic activity of a sugar beet (*Beta vulgaris*) field compared to field-based spectro-radiometric measurements.

8.1.1 Remote Sensing of Sun-Induced Chlorophyll-Fluorescence

Multispectral remote sensing of F_s has been used with different sensors and for a variety of platforms ranging from the ground (Maier et al. 2003, Baluja et al. 2012, Guanter et al. 2013, a.o.) to airborne UAS (Berni et al. 2009b; Zarco-Tejada et al. 2012, Calderón et al. 2013, Zarco-Tejada et al. 2012; Zarco-Tejada et al. 2013d), airplanes (Zarco-Tejada et al. 2000, Damm et al. 2010a, Damm et al. 2014), and also space-borne campaigns (Guanter et al. 2007, quoted in Meroni et al. 2009, Guanter et al. 2014).

The sensor spectral resolution defines the location of the absorption maximum and has only recently been shown to vary from 760.4 nm at 0.1 nm spectral resolution to 762 nm at 5 nm resolution growing wider with decreasing band resolution (Damm et al. 2011, figure 8.2). Similar results were obtained with synthetic spectra derived by FluorMOD (Zarco-Tejada et al. 2012).

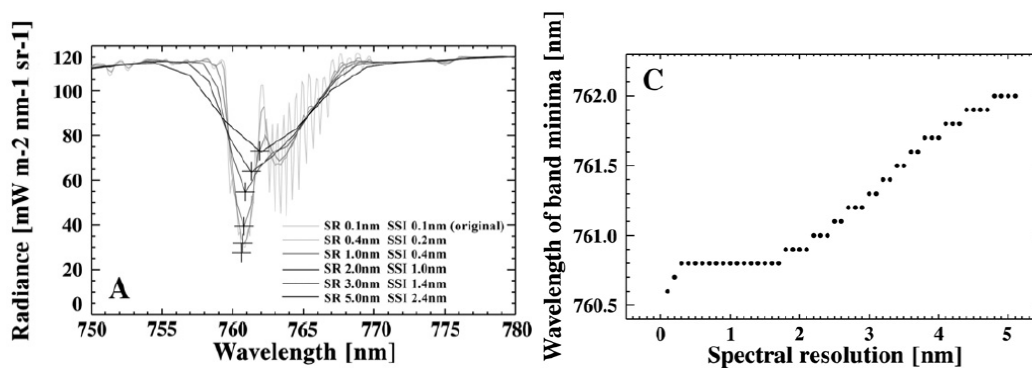


Figure 8.1 Location of Fraunhofer Line absorption maximum in relation to sensor band spectral resolution (mod. from Damm et al. 2011, p. 1886)

Physical or absolute values of F_s require accurate atmospheric correction of remote sensing data even for path lengths in meter-range (Alonso et al. 2008). Even minimal errors in estimating the aerosol depth and distribution within the atmosphere introduce errors in F_s retrieval and may be corrected by an effective transmission correction using non-fluorescing targets (Guanter et al. 2007; Guanter et al. 2010).

Yet, F_s has been derived without atmospheric correction from AISA airborne imaging spectrometer by Corp et al. (2006) and Middleton et al. (2008). Among the first applications of UAS for F_s detection was conducted by Berni et al. (2009) and Zarco-Tejada et al. (2009) who used the in-filling O_2 -A band method with soil as non-fluorescing target to derive spatial and diurnal fluorescence variations within orchards treated with water

stress. Consistent results between airborne multispectral and field-based measurements were found, and both, the in-filling method (3FLD) and in-filling ratios for modeled spectra showed high correlations ($R^2 > 0.82$). For hyperspectral UAS data obtained at ~ 6 nm band width, the in-filling ratios were not significant (Zarco-Tejada et al. 2012).

Meroni et al. (2009) classified and reviewed in detail the different approaches for multispectral data. Basically, there are two types of sun-induced fluorescence retrieval, (a) the radiance-based methods employing the Fraunhofer Line O₂ absorption bands or (b), the reflectance-based methods using indices.

A detailed description of the respective processes and ground-based measurement techniques of fluorescence may be found in Murchie and Lawson (2013). Passive multispectral remote sensing of (F_s) allows for spatial determination of photosynthetic activity in a non-destructive way (Meroni et al. 2009; Rascher et al. 2009; Guanter et al. 2010; Murchie and Lawson 2013). F_s is an additive term to the reflected energy at plant level. The incoming radiance is isotropic (E_0), and canopy reflectance (ρ_λ) as well as F_s may be assumed as Lambertian:

$$L_\lambda = L_\lambda^{path} + \frac{\left(E_0 \frac{\rho_\lambda}{\pi} + F_s\right) \times \tau_\lambda}{1 - \alpha_{atm} \times \rho_\lambda} \quad (8.1)$$

With:

- L_λ : target radiance at wavelength λ
- L_λ^{path} : atmospheric path radiance at wavelength λ
- E_0 : solar irradiance
- ρ_λ : canopy reflectance at wavelength λ
- F_s : solar-induced Chl fluorescence
- τ_λ : atmospheric transmittance at wavelength λ
- α_λ : atmospheric spherical albedo at wavelength λ

8.1.1.1 Radiance-based Method for Fluorescence Retrieval

Radiance-based methods generally utilize the so-called Fraunhofer lines, and in this case the molecular absorption bands of oxygen at 687 nm (O₂-B band) and around 760 nm (O₂-A band, see Figure 8.2) where solar light is absorbed by the atmosphere and radiances within the absorption maximum are compared to shouldering areas where no absorption takes place (Fraunhofer 1817; Malenowský et al. 2009, Meroni et al. 2009; Damm et al. 2010a).

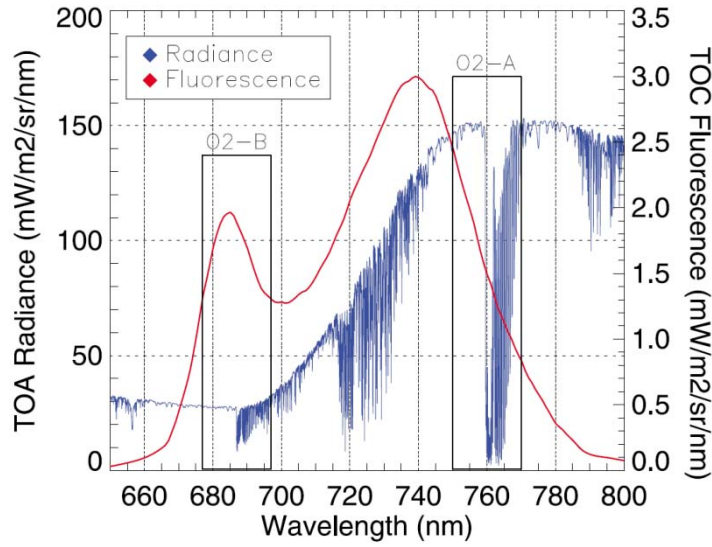


Figure 8.2 Top-of-atmosphere radiance and top-of-canopy F_s for green vegetation and location of O₂-absorption bands (from: Guanter et. al. 2010, D1903)

The Fraunhofer Line Discrimination (FLD) or in-filling method was first introduced by Plascyk (1975) and has long been accepted as the standard F_s retrieval method (Damm et al. 2011, Meroni et al. 2009). It is based on the assumption that F_s is an additive term to the reflectance within that spectral region and may be measured by flux measurements within the O₂-A band and a reference band outside the Fraunhofer line. It is assumed that reflectance fluxes ρ and F_s are constant for that spectral range.

To account for linear variations of ρ and F_s within and outside the O₂-A absorption band at 760 nm (Meroni et al. 2009) Maier et al. (2003) introduced the 3FLD method which includes two close shouldering bands to model an artificial reference band.

$$F_s = \frac{L_i - \frac{E_i}{(w_l E_l + w_r E_r)})(w_l L_l + w_r L_r)}{1 - \frac{E_i}{(w_l E_l + w_r E_r)}} \quad (8.2)$$

With

L : target radiance at wavelength λ

E : radiance upwelling from non-fluorescent target

$$w_l = \frac{\lambda_l - \lambda_i}{\lambda_r - \lambda_l}, \text{ and } w_r = \frac{\lambda_i - \lambda_r}{\lambda_r - \lambda_l}$$

i, r, l : subscripts indicate wavelengths (e.g. i : 760 nm within, l : outside the absorption band at 745-755 nm and r : at 770-785 nm)

Various improvements of the 3FLD method have been developed within the past years (Meroni et al. 2009). In this study F_s was retrieved by using the empiric modification (c3FLD) suggested by Damm et al. (2014). While assuming $\tau = 1$, path radiance $L_p = 0$ due to low flight altitude and $\alpha = 0$, F_s may be obtained by equation 4:

$$F_s = B \left[\frac{L_i E_o - \alpha L_o E_o}{B E_o - A E_i} \right] \quad (8.3)$$

With

$$\left. \begin{aligned} \rho_i &= A \rho_o \\ F_{s_i} &= B F_{s_o} \\ B &= 0.8 \end{aligned} \right\}$$

The factor A relates ρ_i and ρ_o by interpolation of the shoulder bands:

$$A = \frac{\rho_{750} w_l + \rho_{780} w_r}{\rho_{750}}, \text{ and}$$

B is an empirical factor relating F_s inside and outside the O_2 -A band (Damm et al. 2014, p. 259f).

The advantage of the radiance-based methods lies in the derivation of physical fluorescence units (Damm et al. 2011). Furthermore, the authors could show the robustness of the c3FLD method against noise.

8.1.1.2 Fluorescence Reflectance and Method for Fluorescence Retrieval

The fluorescence signal is a rather fine contribution to the overall plant reflectance with a general proportion of only 1 to 5% (see also chapter 3). Figure 8.3 illustrates reflectance and its fluorescence component for a sugar beet leaf.

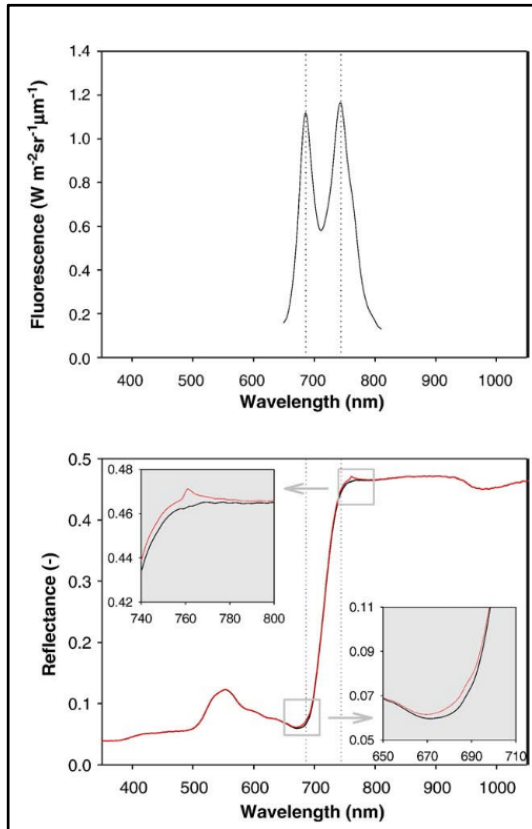


Figure 8.3 Sun-induced chlorophyll fluorescence for a sugar beet leaf (top) and its contribution to the reflectance signal (bottom) (from: Meroni et al. 2009, p. 2038)

As solar-induced chlorophyll fluorescence (F_s) contributes to the reflectance, Zarco-Tejada et al. (2000) first showed how the fluorescence signal may be derived from the reflectance signal (Meroni et al. 2009):

$$\rho_{\lambda}^* = \frac{\pi L_{\lambda}}{E_{\lambda}} = \rho + \frac{\pi F_{\lambda}}{E_{\lambda}} \quad (8.4)$$

With

- ρ_{λ} : reflectance
- ρ_{λ}^* : apparent reflectance
- L_{λ} : upwelling radiance
- E_{λ} : reflected energy
- F_{λ} : emitted energy/fluorescence

The reflectance-based methods were mostly developed for hyperspectral sensors but often use only up to three narrow-band indices. They may be categorized in (1) reflectance-based indices where at least one band is affected by fluorescence, (2) derivative indices, and (3) in-filling indices utilizing fluorescence and neighbouring bands. Their advantage lies in the simplicity of retrieving F_s from traditional EO data but yet do not yield data in physical units, and are often not only steered by fluorescence (Meroni et al. 2009).

Dobrowski et al. (2005) used ratios of ρ_{690}/ρ_{600} nm and ρ_{740}/ρ_{800} nm with field spectrometer data, and Zarco-Tejada et al. (2009) applied the in-filling ratios ρ_{690}/ρ_{630} nm and ρ_{761}/ρ_{757} , and found the latter least affected by Chl_{a+b} variations.

The measurement of the NPQ's pigment variations introduce reflectance changes in the green spectral ranges at 531 nm, and therefore Gamon et al. (1990, 1997) defined the photochemical reflectance index (PRI):

$$PRI = \frac{\rho_{531} - \rho_{570}}{\rho_{531} + \rho_{570}} \quad (8.5)$$

The index correlates well with NPQ and has shown to be well correlated with water stress (Evain et al. 2004, Berni et al. 2009a; Berni et al. 2009c; Suárez et al. 2009; Zarco-Tejada et al. 2012; Zarco-Tejada et al. 2013b).

The PRI has successfully been used to show differences in photosynthetic efficiency (see Nichol et al. 2006) and LUE (Hall et al. 2008). Some studies, however, showed PRI values to vary with species and phenology (Filella et al. 2004, Rascher and Pieruschka 2008; Damm et al. 2010b) and PRI of canopy is strongly affected by solar illumination angles, leaf angle distribution and viewing angles (Hall et al. 2008; Hilker et al. 2008; Malenowský et al. 2009). This could be confirmed by the sensitivity analyses carried out in the chapter 6. Momentary environmental conditions (irradiance, temperature, water supply, etc.) steer the photosynthetic activity of plants independently of the chlorophyll pigment content, canopy structure or fAPAR (Malenowský et al. 2009). Vegetation indices are thus supposed to be of limited use for estimating photosynthetic activity.

8.1.2 The Impact of N-Fertilization on UAS-based Sun-induced Chlorophyll Fluorescence Measurements

Airborne retrieval of F_s of corn crops using AISA multispectral data treated with different levels of N-fertilization has been analysed by Corp et al. (2006) using AISA multispectral data. Values ranged from 7-36 $\text{mWm}^{-2}\text{sr}^{-1}\text{nm}^{-1}$ and the fluorescence index $\rho_{688\text{nm}}/\rho_{760\text{nm}}$ was able to discriminate between N-fertilization levels. Airborne canopy F_s values were also shown to detect biophysical changes introduced by N treatments. On the leaf and top of canopy (TOC) level (1m) in-situ ASD spectrometer data yielded higher F_s levels with increasing N application rates (Middleton et al. 2008). The authors found lower F_s values for in-situ derived F_s values (Corp et al. 2006) using the FLD method which is in accordance with findings from Sobrino et al. (2011) who found F_s retrieval from sFLD and from improved FLD (Alonso et al. 2008) from airborne measurements to overestimate F_s with RMSEs of 0.4-0.5 $\text{mWm}^{-2}\text{sr}^{-1}\text{nm}^{-1}$. The latter however, used atmospherically corrected data.

8.1.3 UAS-Based Diurnal Observations of Sun-induced Chlorophyll Fluorescence

F_s have been derived from airborne micro-hyperspectral and multispectral UAS sensors by Zarco-Tejada et al. (2009), Zarco-Tejada et al. 2012, and Zarco-Tejada et al. (2013). A consistent course for airborne/UAS- and field-based F_s -measurements has already been outlined by several authors (Zarco-Tejada et al. 2009, Zarco-Tejada et al. 2012). In-situ based measurements of TOC- F_s radiances with a field-spectrometer (ASD FieldSpec) have been made by Zhao et al. generally, F_s was higher for the O2-A-band compared to the O2-B values and rise in the morning until midday and recline in the afternoon following the diurnal PAR (Figure 8.4).

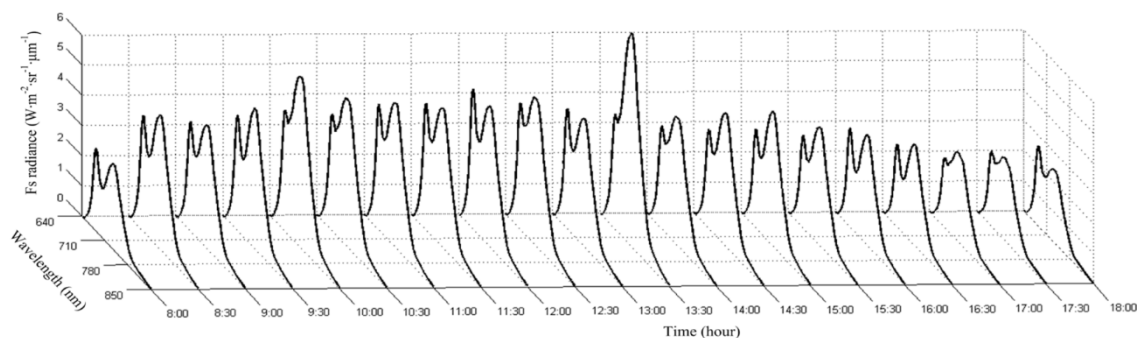


Figure 8.4 Diurnal F_s radiation for a maize-wheat field in China, 13/05/2010 (from Zhao et al. 2014, p. 10186)

The following sections present the two experiments. They start with a description of the study sites followed by the airborne data acquisition and field data collection, data processing and analysis methods for each experiment respectively.

8.2 Experiment Campus Klein-Altendorf 1 (CKA1): N-Fertilization Rate and Fluorescence

8.2.1 Material and Methods

The HYFLEX experimental sites of the August 2012 campaign are maintained by the Forschungszentrum Jülich/University of Bonn. They are located at Campus Klein-Altendorf (Rascher et al. 2013). To test if N-fertilization has an effect on sugar beet biophysical parameters and fluorescence signal, an experimental plot located at Campus Klein-Altendorf 1 (N50° 36' 55", E6° 59' 11") was chosen (Figure 8.5).

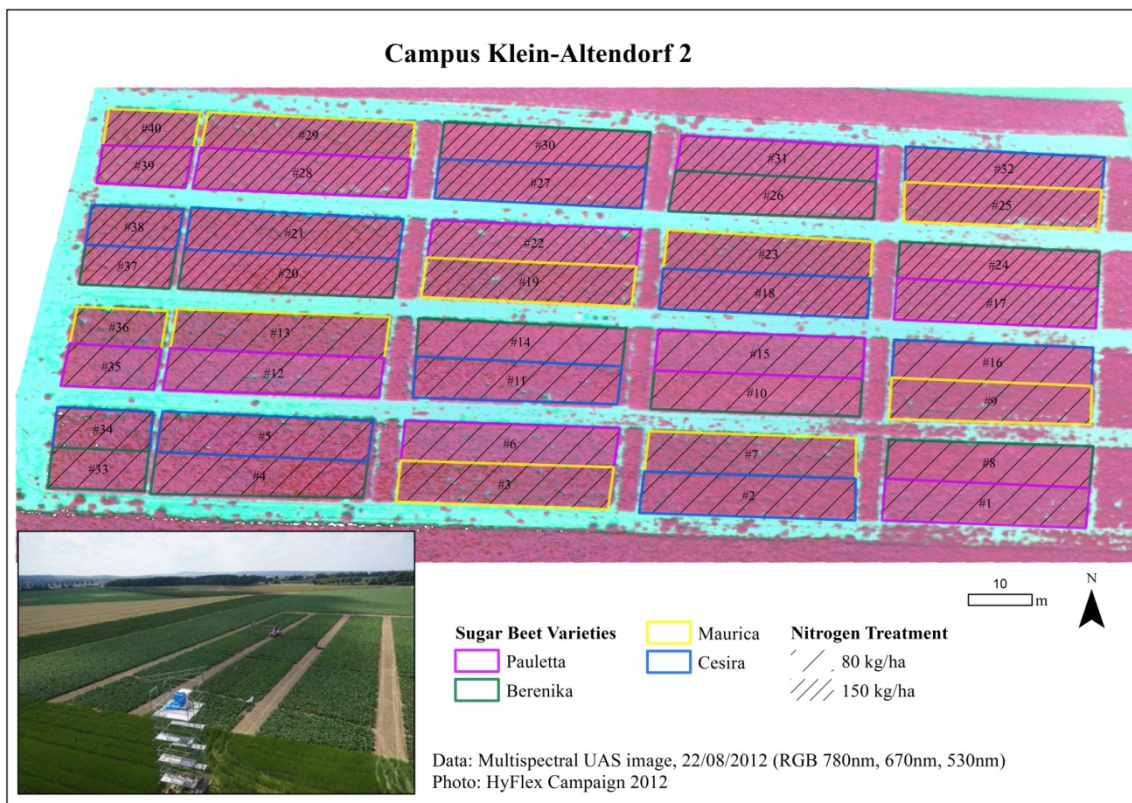


Figure 8.5 Study Site Campus Klein-Altendorf 1 (multispectral data)

8.2.1.1 Field Data Collection

Greylevel reference panels were laid out into the centre field tracks and their reflectance was measured during the ascent using a FieldSpec Handheld Pro spectrometer (ASD, USA). Using the fibre pistol, fifty measurements of the target, the dark current and the white reference (spectralon 25 cm x 25 cm) were averaged respectively. Three to five spectra for each reference panel were then averaged to one reflectance spectrum per panel. Furthermore, ground-control point markers were distributed along the plot boundary and on the inside tracks. For some of these, GPS coordinates were measured using a hand-held GARMIN GPS devices described in chapter 4.6.

8.2.1.2 Airborne Campaign and Data Processing

Two UAS flights, one with the multispectral miniMCA-6 and one with the thermal broadband camera UCM were carried out on 22/08/2012 around midday. Unfortunately, for that day, the weather was not ideal for fluorescence analysis as high cirrus and cumulus clouds moved through the area during the morning until midday. Yet, flights were carried out within cloud gaps when irradiance was high.

Multispectral Imagery

The multispectral flight took place between 12:24 h to 12:35 h UTC one hour after noon (11:35h UTC) with ~ 130 m flight altitude above ground. The MiniMCA-6' cameras were equipped with 25 mm-diameter FWHM +/-10 nm filters at the central wavelengths 531 nm, 570 nm, 670 nm, 750 nm, 780 nm and a FWHM +/- 1 nm at 760 nm. Exposure time was set to 4800 μ sec and other cameras were exposed according to their filter transmission: 670 nm: 130%; 750 nm: 20%; 760 nm: 200%, 780 nm: 30%). The six respective camera images were converted from RAW to 16-bit data format and corrected for vignetting effects followed by the alignment of slave camera images to the master band (570 nm) as described in chapter 5. As illumination was supposed to be homogeneous between image acquisition times, an orthophoto mosaic was to be averaged from of 8 selected multispectral images. The Agisoft PhotoScan Professional software was used for this process and included the following steps (chapter 5.3.4):

1. Camera calibration based on the master camera using the Brown distortion model
2. Photo alignment estimated from eight input UAS photos , UAS-derived GPS coordinates for photo centers (WGS84), GPS-altitude, and camera attitude angles during the flight (roll, pitch, yaw) as derived from UAS IMU. Camera locations and error estimates are given in Table 8.1 and Figure 8.6 on the next page.

Table 8.1 Photo attitude parameters and error estimates of multispectral UAS flight CKA1 (22/08/2012, 12:30 UTC)

Photo-Label	X/East	Y/North	Z/Altitude	Error (m)	X error	Y error	Z error
ka1_f159_ttc0769.tif	357599.922	5609918.810	362.600063	4.175	2.379	-3.427	-0.16
ka1_f159_ttc0772.tif	357565.203	5609922.718	361.400063	4.209	3.785	-1.838	0.10
ka1_f159_ttc0775.tif	357528.478	5609925.076	362.200063	6.007	4.889	3.489	0.07
ka1_f159_ttc0779.tif	357600.071	5609941.786	361.900063	5.092	-4.176	2.558	-1.39
(ka1_f159_ttc0781.tif	357621.115	5609942.829	360.100063	10.717	-10.473	-0.470	2.22)
ka1_f159_ttc0783.tif	357641.312	5609943.851	360.700063	2.462	-1.515	-0.090	-1.94
ka1_f159_ttc0785.tif	357660.756	5609944.909	360.500063	3.929	-3.610	-1.316	0.82
ka1_f159_ttc0787.tif	357671.344	5609945.603	362.000063	8.794	8.721	1.095	0.28
Total Error				5.291	4.671	2.292	0.96

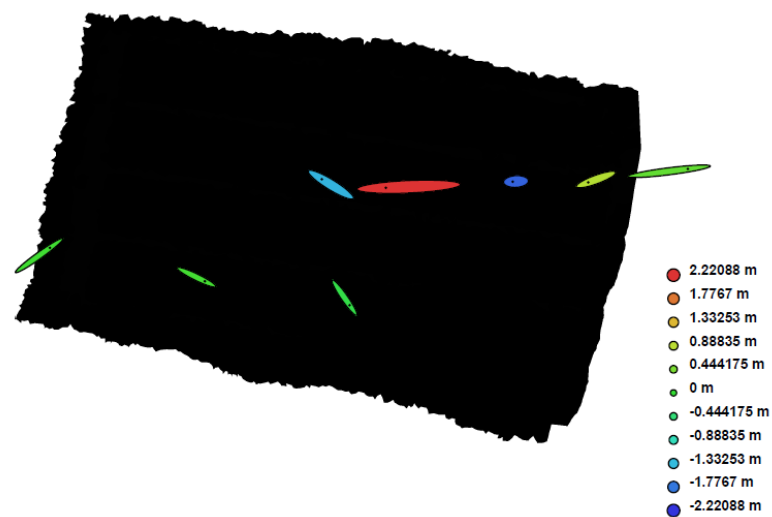


Figure 8.6 Camera locations and error estimates for multispectral UAS flight (Z error is represented by ellipse color, X,Y errors by ellipse shape)

3. A dense mesh model with ~ 180000 polygons was the generated.
4. Finally, an orthophoto was exported, textured with averaging function to a spatial resolution of 75 mm x 75 mm.

Radiometric correction consisted of an ELC (Smith and Milton 1999) using the greylevel reference panels to obtain reflectances. As exposure was optimized for dark vegetation targets, the white reference panel was saturated for the first three bands and, thus, excluded from correction process. Table 8.2 shows that reflectances could be accurately derived to up to 0.7 reflectance differences for reference panels.

Table 8.2 Empirical line and coefficient of determination (R^2) for radiometric correction of UAS image

22/08/2012		~ 11:35 UTC				
Band [nm]	Empirical line	R^2	$\Delta\rho$ white rp	$\Delta\rho$ light-grey rp	$\Delta\rho$ dark-grey rp	$\Delta\rho$ black rp
530	$\rho = 0.0003x - 0.0397$	0.9999	-	0.003	0.000	0.002
570	$\rho = 0.0003x - 0.0390$	0.9999	-	-0.010	-0.006	-0.003
670	$\rho = 0.0002x - 0.0259$	0.9930	-	-0.005	0.004	-0.006
750	$\rho = 0.0018x - 0.1187$	0.9998	-0.002	-0.005	-0.005	0.007
760	$\rho = 0.0054x - 0.5194$	1	-0.001	0.002	-0.004	0.001
780	$\rho = 0.0017x - 0.1604$	0.9999	-0.006	-0.008	-0.001	0.003

Several vegetation indices were computed which are listed in (Table 8.3). The NDVI was further employed to ensure image statistics derivation for only densely vegetated sugar beet areas within the plots: all pixels with a NDVI of less than 0.6 were masked to background value.

Table 8.3: Vegetation and fluorescence indices used in this study (R: reflectance, nIR: near infrared)

Vegetation index	Formulation	Author	Application
Normalized Difference Vegetation Index	$NDVI = (R_{nIR} - R_{red}) / (R_{nIR} + R_{red})$	Rouse <i>et al.</i> 1974	Structural index, plant vitality
Photochemical Reflectance Index	$PRI = (R_{531} - R_{570}) / (R_{531} + R_{570})$	Gamon <i>et al.</i> 1992	Carotenoids/Chl index, Chl fluorescence, radiation use efficiency, water stress
In-filling reflectance index I	$IFR I = R_{760} - R_{750}$	Modified from Pérez-Priego <i>et al.</i> 2005	Fluorescence
In-filling reflectance index II	$IFR II = R_{760} - (0.5 * (R_{750} + R_{780}))$	Modified from Pérez-Priego <i>et al.</i> 2005	Fluorescence
Fluorescence Ratio (FR I)	$FR I = R_{760} / R_{750}$	Modified from Zarco-Tejada <i>et al.</i> 2009	Fluorescence
Fluorescence Ratio (FR II)	$FR II = R_{760} / R_{530}$	<i>do.</i>	Fluorescence

Plots were digitized and used to derive zonal statistics for band reflectances and VI values versus nitrogen treatment and sugar beet variety (see plots in Figure 8.5).

Thermal Imagery

Thermal data were acquired using the ZEISS UCM at 13:27 h UTC and 95 m above ground (for information on camera characteristics, please refer to chapter 4.2.3). No further in-situ temperature measurements were made. As each thermal image employs the entire 8-bit data space at < 90mK at 30°C, three images covering the plots were selected and histogram-matching applied using dark to bright greylevel targets within the overlapping image zones. Agisoft Photoscan Professional was again applied to align photos, build a point cloud and to create an orthophoto mosaic (Figure 8.7).

Photo attitude parameters and error estimates for camera location are given in are listed in Table 8.4 and illustrated in Figure 8.8 and residuals for used ground control point markers are given in Table 8.5.

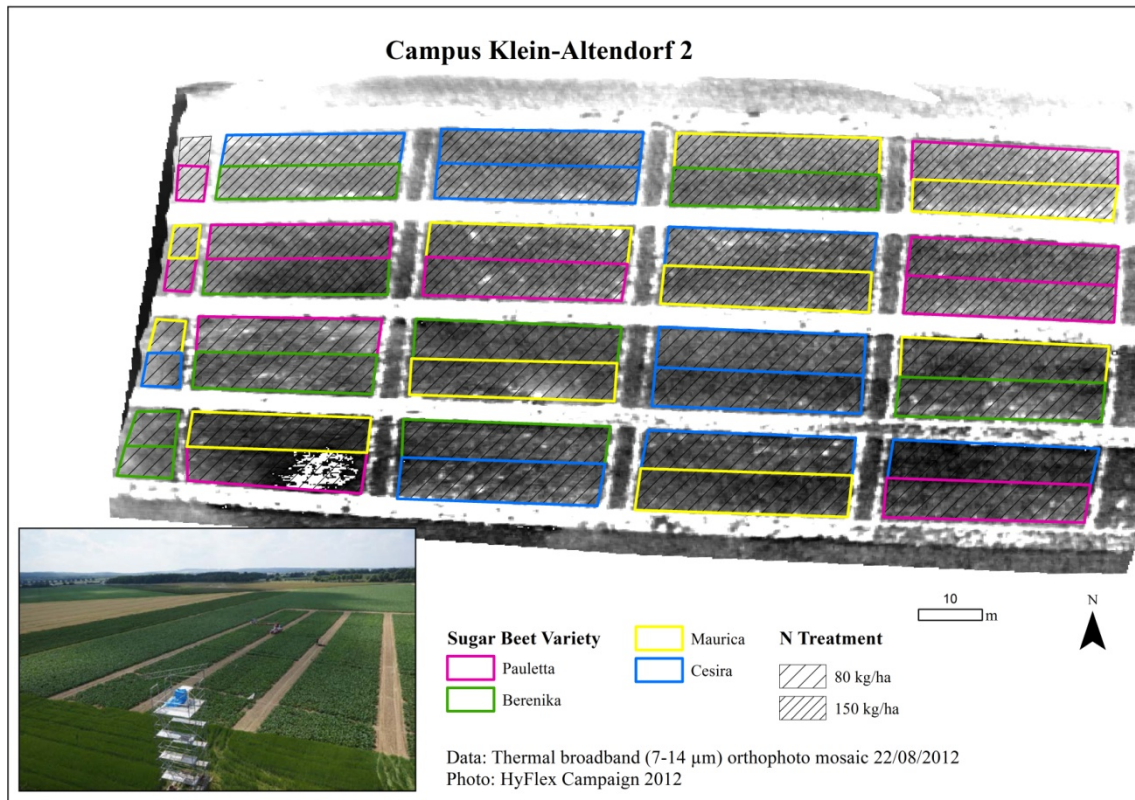


Figure 8.7 Study Site Campus Klein-Altendorf 1 (thermal data)

Table 8.4 Photo attitude parameters and error estimates of UAS flight CKA1 (22/08/2012, 13:27 UTC) with thermal camera

Photo-Label	GPS- X_{cam}	GPS- Y_{cam}	GPS- Z_{cam}	Yaw	Pitch	Roll	Error (m)	X error	Y error	Z error
SS0283.BMP	6.986786	50.623869	324.9	-84.7	-5.2	1	48.164	-15.057	-11.043	44.397
ka1_ss0281_hm2ss0283bmp.tif	6.986764	50.623784	322.4	-85.1	-5.8	-4.5	46.084	-17.626	-16.226	39.367
ka1_ss0285_hm2ss0283bmp.tif	6.987218	50.623853	320.7	-86.6	-0.5	1	46.797	27.878	-11.348	35.832
Total error							17.082	7.404	4.59165	14.693

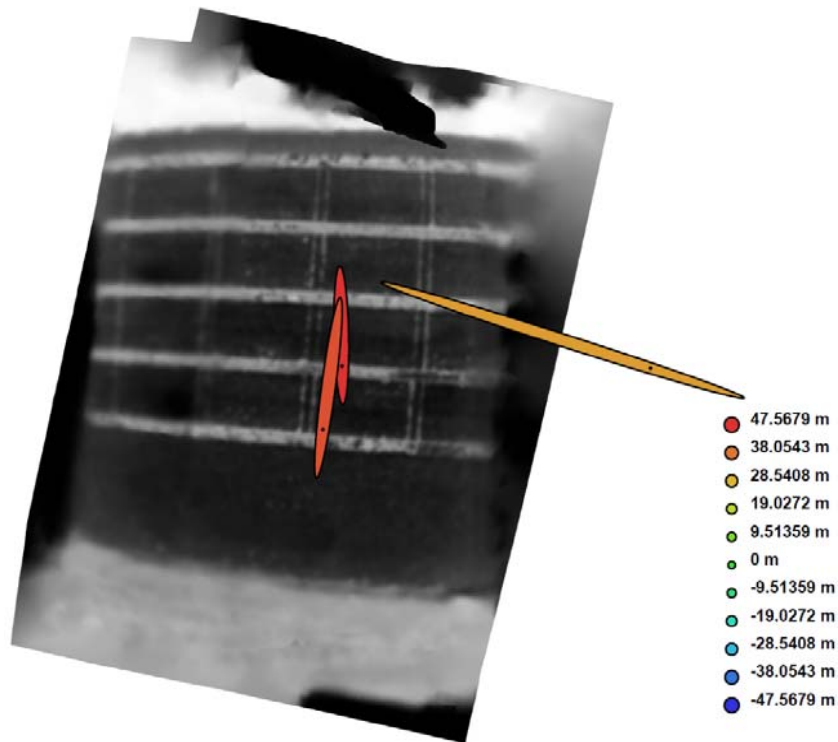


Figure 8.8 Camera locations and error estimates for thermal UAS flight (Z error is represented by ellipse color, X,Y errors by ellipse shape)

Table 8.5 Ground control marker position residuals for georeferencing multispectral data

Label	Xerror [m]	Yerror [m]	Zerror [m]	Error [m]	Projections	Error [pixels]
point 1	-1.014674	-0.139051	0.453303	1.119992	3	0.406496
point 3	-0.811614	-0.336366	3.975596	4.071514	3	0.516307
point 4	-0.920692	-0.068297	2.819942	2.967223	3	0.53594
point 5	3.435126	1.725167	3.463046	5.173875	2	0.281019
point 6	7.626207	-2.581539	3.988946	8.985269	2	0.26395
point 7	0.444271	0.200279	-0.212578	0.531674	3	0.194242
point 8	0.284905	1.043034	-1.643836	1.967558	3	0.157528
point 9	-0.689972	-0.375752	-3.598653	3.683416	3	0.427283
point 10	1.398811	-1.887947	3.522468	4.234241	2	0.006873
point 11	2.126856	-0.183164	3.378401	3.99633	2	0.159138
point 12	0.819137	-3.235283	2.305448	4.056246	2	0.614789
point 13	1.170009	0.44354	-6.828114	6.941815	2	0.275259
point 14	3.142091	-1.497698	0.675051	3.545636	1	0
point 15	3.158592	-1.021466	1.840858	3.7959	1	0
point 16	2.391164	-0.189872	1.793041	2.994781	1	0
point 17	0.496467	1.589735	-0.29391	1.691188	1	0
point 18	-0.088029	-0.23407	-1.617861	1.637075	3	0.442276
point 19	0.439934	0.709121	-0.655524	1.061181	3	0.417906
point 20	-0.747937	-0.183201	2.68954	2.797606	3	0.380311
point 21	-0.62459	-0.014259	3.575517	3.629688	3	0.592068
point 22	-0.016457	0.846361	2.616638	2.750163	3	0.161056
point 23	-0.355667	-0.754082	5.513943	5.576621	3	0.238979
point 24	-0.46155	-1.933659	5.187111	5.555014	3	0.503204
Total	2.177693	1.264461	3.214722	4.083582		0.375453

According to multispectral data, the thermal data were masked to include only densely vegetated sugar beet pixels using $NDVI \geq 0.6$ as threshold.

8.2.1.3 Statistical Analyses

For the analysis of separation of N-treatment on sugar beet varieties, a principal component analysis was calculated to infer the first principal component as another information input beside the multispectral bands, VI and fluorescence indices (Table 8.6). Visual inspection in form of boxplots was carried out with N treatment and variety as grouping factors, and thermal and multispectral bands and Vis (Table 8.3) as explanatory variables as a first impression on the bands/index suitability.

Two-factorial ANOVAs were computed between respective spectral bands, Vis, fluorescence indices versus variety and N treatment to evaluate the best distinction variables

to differentiate between groups. Finally, a linear discriminance analysis helped to find the best band/index combinations.

Statistics were retrieved using R 3.2.1 packages.

8.2.2 Results

There is an overall higher reflectance in the VIS/nIR and thermal radiation emission for higher rates of N fertilization as Table 8.6 shows. Regarding fluorescence, the IFR I and II also indicate a higher rate of fluorescence: 2.5% higher reflectance for 150 kg N compared to 80 kg N.

Table 8.6 Mean values and standard deviation for bands and fluorescence index for N treatments at CKA1

Wavelengths/Index	Mean N 80 kg/ha	Standard deviation	Mean N 150 kg/ha	Standard deviation
7-14 μ m	27.5	7.2	44.8	8.3
530 nm	0.03	0.007	0.04	0.006
570 nm	0.04	0.007	0.05	0.006
670 nm	0.01	0.003	0.01	0.003
750 nm	0.45	0.037	0.49	0.028
760 nm	0.52	0.061	0.59	0.044
780 μ m	0.50	0.041	0.55	0.030
IFR I	0.071	0.026	0.096	0.020
IFR II	1.09	0.045	1.13	0.036

Visual inspection between boxplots confirm that N treatment may well be discriminated across the varieties with the thermal mean, multispectral bands and more so with selected VIs such as the NDVI and fluorescence indices (Figure 8.9)

Distinction among sugar beet varieties was best achieved by NDVI with the bands 780 nm and 570 nm or with 670 nm and 570 nm, the traditional NDVI (here: 780 nm and 670 nm), PC1 and the spectral bands at 570 nm, 670 nm and 780 nm (Figure 8.10). The fluorescence band at 760 nm showed higher variations from means. Regarding variety, variety 2 (Berenika) consistently showed highest DN variations from mean.

The two-factorial ANOVAs additionally showed (Table 8.7):

- N treatment was best separated by all spectral bands (thermal, multispectral bands) and the VIs: $NDVI_{570,670}$, PC1, NDVI, IFR I and to a lesser extent by FR I (significance level <0.05).
- Variety was best separated by $NDVI_{780,570}$, all spectral bands, 570 nm respectively and NDVI, PC1 and also by IFRI.

This also indicates differing fluorescence patterns for sugar beet varieties.

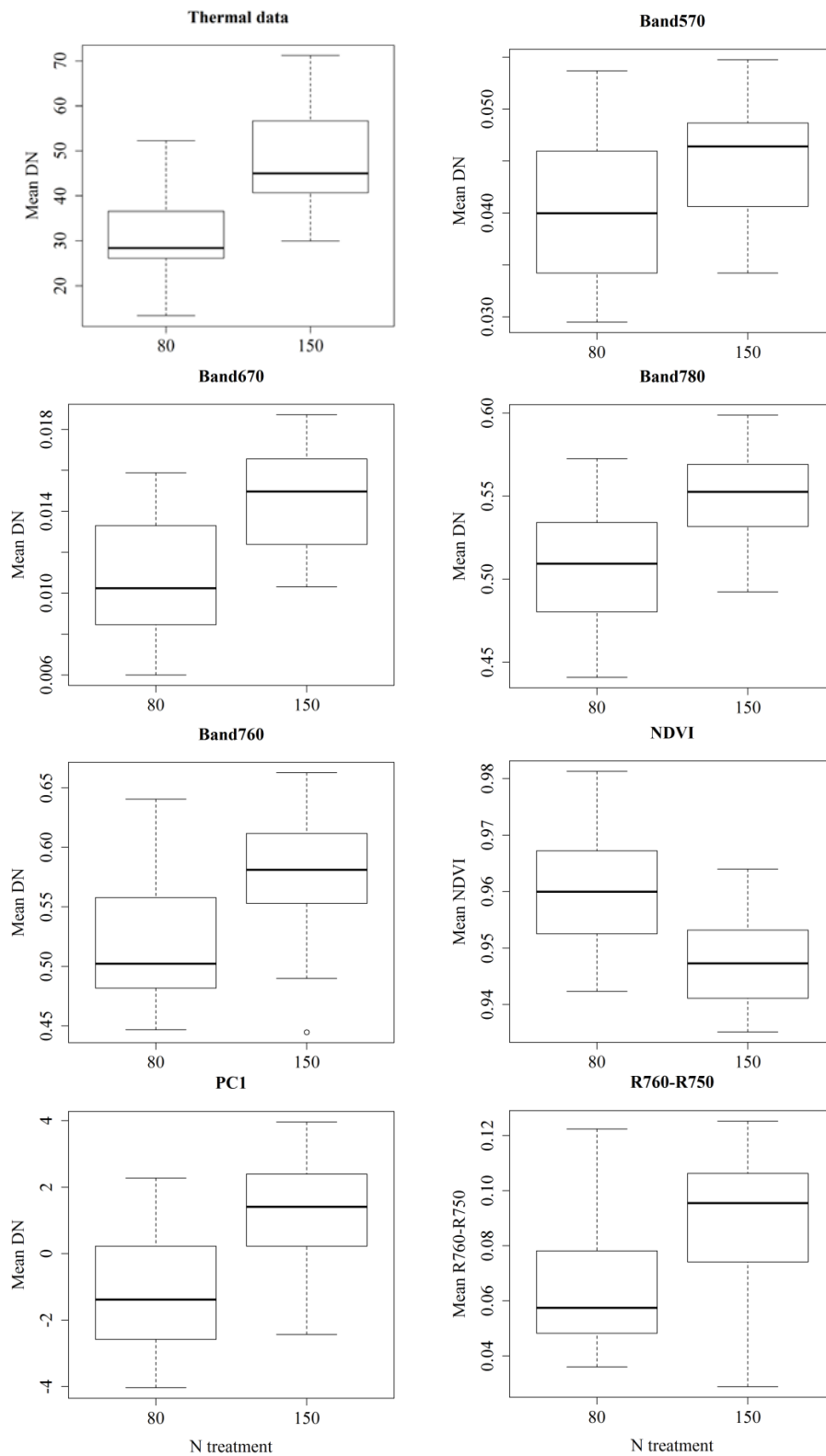


Figure 8.9 Box-plots of band means or VIs versus N treatment [kg/ha] (x-axis) for the CKA1 (black line: median, boxes: minimum and maximum values, tails: non-outlier range, circles: outliers)

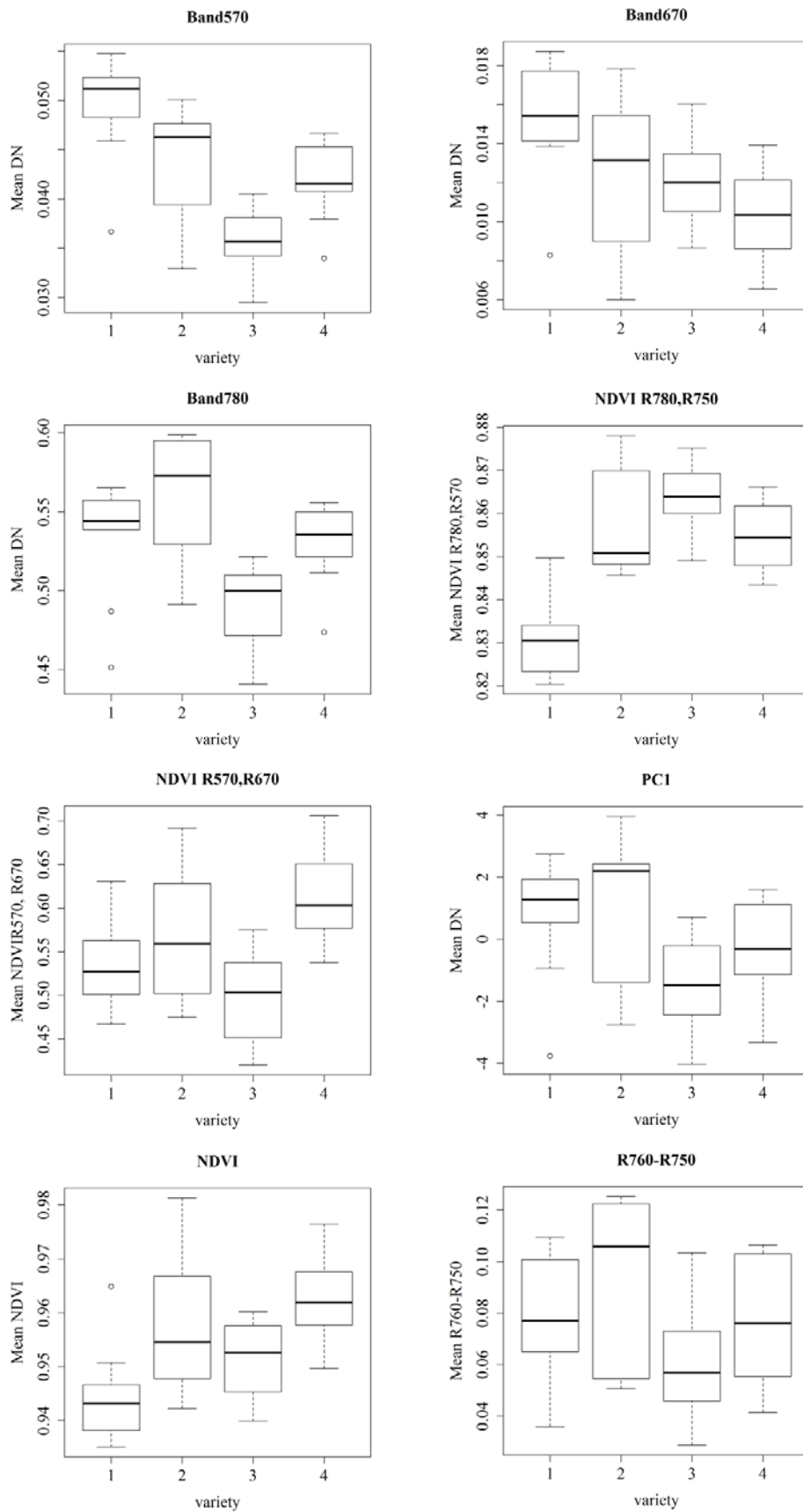


Figure 8.10 Box-plots of band means or VIs versus sugar beet variety (x-axis) for the CKA1 (black line: median, boxes: min. and max. values, tails: non-outlier range, circles: outliers)

Table 8.7 Results of two-factorial ANOVA between spectral band/VI versus N treatment/sugar beet variety (Sign. codes: 0 '***' 0.001 '**' 0.01 '*' 0.05 '.' 0.1 ' ' 1)

Variables	Factors	Df	Sum	RMS	F_value	Pr(>F)	
NDVI_{780,570}	as.factor(variety)	3	0.006265	0.0020885	25.35	6.77E-09	***
	as.factor(N)	1	0.00006	0.0000603	0.732	0.398	
	Residuals	35	0.002884	0.0000824			
NDVI_{570,670}	as.factor(variety)	3	0.06587	0.02196	16.15	9.32E-07	***
	as.factor(N)	1	0.07244	0.07244	53.28	1.57E-08	***
	Residuals	35	0.04759	0.00136			
Thermal	as.factor(variety)	3	48.63	16.21	7.819	0.000401	***
	as.factor(N)	1	61.75	61.75	29.784	4.01E-06	***
	Residuals	35	72.56	2.07			
NDVI	as.factor(variety)	3	0.001822	0.0006072	10.68	3.93E-05	***
	as.factor(N)	1	0.001324	0.0013236	23.29	2.71E-05	***
	Residuals	35	0.001989	0.0000568			
PC1	as.factor(variety)	3	48.63	16.21	7.819	0.000401	***
	as.factor(N)	1	61.75	61.75	29.784	4.01E-06	***
	Residuals	35	72.56	2.07			
R570	as.factor(variety)	3	0.0009416	3.14E-04	16.646	6.88E-07	***
	as.factor(N)	1	0.0001695	1.70E-04	8.988	0.00497	**
	Residuals	35	0.0006599	1.89E-05			
R670	as.factor(variety)	3	0.0001252	4.17E-05	8.198	0.00029	***
	as.factor(N)	1	0.0001663	1.66E-04	32.653	1.84E-06	***
	Residuals	35	0.0001782	5.09E-06			
R780	as.factor(variety)	3	0.0265	0.008833	15.26	1.63E-06	***
	as.factor(N)	1	0.01853	0.01853	32	2.19E-06	***
	Residuals	35	0.02027	0.000579			
R750	as.factor(variety)	3	0.02102	0.007006	12.59	9.75E-06	***
	as.factor(N)	1	0.01308	0.013082	23.5	2.54E-05	***
	Residuals	35	0.01948	0.000557			
R530	as.factor(variety)	3	0.0008109	2.70E-04	12.158	1.32E-05	***
	as.factor(N)	1	0.0002203	2.20E-04	9.909	0.00335	**
	Residuals	35	0.0007781	2.22E-05			
R760	as.factor(variety)	3	0.04525	0.01508	7.258	0.000655	***
	as.factor(N)	1	0.0329	0.0329	15.83	0.000332	***
	Residuals	35	0.07274	0.00208			
IFR_I	as.factor(variety)	3	0.004865	0.001622	2.804	0.05399	.
	as.factor(N)	1	0.00449	0.00449	7.764	0.00855	**
	Residuals	35	0.020241	0.000578			
IFR_II	as.factor(variety)	3	0.00161	0.0005366	0.914	0.444	
	as.factor(N)	1	0.001625	0.0016248	2.766	1.05E-01	
	Residuals	35	0.020557	0.0005873			
FR I	as.factor(variety)	3	0.00932	0.003108	1.540	0.2213	
	as.factor(N)	1	0.01081	0.010809	5.357	0.0266	*
	Residuals	35	0.07062	0.0020189			

Linear discriminance analysis of N treatment or variety as grouping factor and standardized input band means as explanatory variables showed that both grouping factors could be differentiated (Table 8.8). For variety, the first two LD accounted for 97% of the explained variance. Here, the reflective bands 780 nm, 530 nm at LD1 and 570 nm and 780 nm scored the highest loads on the discriminant functions.

Table 8.8 Standardized linear discriminant coefficients for LDA models separating N treatment and sugar beet varieties with thermal and Vis/nIR bands (n=40)

	N treatment	Variety		
	LD1	LD1	LD2	LD3
Mean_thermal	1.32652325	-0.9068415	0.08226368	-2.218759
Mean_530nm	-0.0448856	2.8138949	-0.6326936	4.104628
Mean_570nm	-1.7606547	-0.9740505	3.74350113	-4.0363345
Mean_670nm	0.87681572	-2.0599449	-0.3883455	2.8981613
Mean_750nm	2.32610242	-0.7964128	1.55295756	-8.4999073
Mean_760nm	-0.2255469	-1.598749	-0.840383	-0.5571513
Mean_780nm	-0.3037208	4.0379599	-2.8374513	7.8675644
Proportion of trace	1	0.5451	0.3144	0.1406

When only Vis/nIR filter bands are considered (Table 8.9), filters located at 570 nm and 670 nm perform best in separating N. Sugar beet varieties are best differentiated with filters at 530 nm, 670 nm (LD1) and 570 nm and 780 nm (LD2).

Table 8.9 Standardized linear discriminant coefficients for LDA models separating N treatment and sugar beet varieties with VIS/nIR bands (n=40)

	N treatment	Variety		
	LD1	LD1	LD2	LD3
Mean_530nm	0.437499	1.5724315	0.538167	-4.2362185
Mean_570nm	-2.516591	0.3556094	-3.6149465	2.935714
Mean_670nm	2.046494	-3.0007735	0.2479098	-0.2627325
Mean_750nm	1.628201	1.3946366	-1.3059914	9.1569044
Mean_760nm	-1.837667	-0.9443518	0.8762137	-2.8740098
Mean_780nm	1.537649	1.4317332	2.615851	-5.8770948
Proportion of trace	1	0.5929	0.3767	0.0304

8.2.3 Discussion

Results of ANOVA and LDA clearly showed that higher rates of N-fertilization produced higher rates of reflectance in the O2-A absorption band at 760 nm. From the fluorescence indices, however, only IFR_I and to a lesser extent the ratio of R760/R750 were able to significantly discriminate plot means. This is in accordance with FLD analysis of corn fields and fluorescence ratio R688/R760 ratio applied by Corp et al. (2006). Thermal and reflective bands in the remaining Vis/nIR do also increase with magnitude of N treatment. Plots treated with 150 kg N clearly showed higher values in all cases. Other traditional VIs such as the NDVI of nIR to red and red to 570 nm and also the first PC were well able to differentiate plot means in relation to N treatment.

Results suggest that N-induced fluorescence differences are generally detectable which is in agreement with findings of the Middleton et al. (2008) and Corp et al. (2006), even when weather conditions were not ideal for that day. The fluorescence band 760 nm and the IFR II showed relatively large value ranges which may be attributed to fluorescence. However, results might be sharper, if the spectral position of the fluorescence filter were shifted to 760.5 nm oder 761 nm (Pérez-Priego et al. 2005; Zarco-Tejada et al. 2009; Damm et al. 2014). Inherent noise and radiometric processing inefficiencies of the empirical line calibration compared to atmospheric processing are another factor contributing to the strong variations in that spectral range and fluorescence detection (Damm et al. 2014). Finally, as the irradiation on that day was not stable, overall smaller amount of F_s should be expected.

Concluding, under the given sensor configuration N-fertilization is best mapped with thermal and Vis/nIR bands rather than the fluorescence bands as Figure 8.9 - Figure 8.10 illustrated and the ANOVAs showed (Table 8.7).

Ultimately, when solar irradiance is at maximum, a precise atmospheric correction of the aerial images may yield absolute, quantitative F_s values. As is the situation, the filter combinations allow for comparative rather than an absolute analysis of F_s values.

8.3 Experiment Campus Klein-Altendorf 2 (CKA2): Diurnal Solar-Induced Fluorescence Measurements of Sugar Beet

8.3.1 Material and Methods

8.3.1.1 Site Description

On 23/08/2012, a sugar beet field located at Campus Klein-Altendorf 2 (N50° 36' 55'', E 6° 50' 30'') was selected for diurnal F_s measurements.

8.3.1.2 Field Data Collection

During the whole day, reference field irradiance and canopy radiance measurements were made using a Multiplexer-based Radiometer Irradiometer (MRI) by the University of Milan. The instrument is based on a OceanOptics optical multiplexer and measures incident radiance, upwelling radiance with a FOV of 25° and has a blind channel for dark current quantification. In addition, the setup enclosed two HR4000 spectrometers (OceanOptics, USA) measuring the spectral range between 400 to 1000 nm with a FWHM of 1 nm and a FWHM of 0.1 nm within the 700-800 nm range. The devices were mounted on a stair within the sugar beet field (N50° 36' 54.5'', E6° 59' 31'') from 8:17 UTC until nearly 16 UTC. The spectrometer fibre was mounted to a height of 2.24 m above the sugar beet canopy with an average height of 46 cm (Figure 8.11) and measured a footprint of roughly 1 m in diameter. Three to five scans were averaged to one measurement per time (Rascher et al. 2013, p. 32f and 65).



Figure 8.11 Field measurement setup at CKA2: field spectrometer and grey-level reference panels (Photo: M. Perez)

8.3.1.3 Airborne Campaign and Data Processing

Starting from 8:00 UTC until $\sim 14:00$ UTC, two to three quadrocopter flights per hour were carried out at about 70 m above ground at an altitude of approximately 180 m a.s.l.. The MiniMCA-6 multispectral camera was mounted with the same filter setup as in the previous experiment. Measurements were supposed to extend until late afternoon, however, the base station failed to work from 14:00 UTC onwards and it was therefore not possible to assure target focus and image acquisition was terminated then. Image nadir was pointed towards the location of the in-situ irradiance and F_s measurements. Images were selected where the fluorescence and reference panels were mostly in nadir position and angles deviations from nadir viewing of $< 3^\circ$ were selected.

Reference panels were laid out near the fluorescence tower of partners and were measured simultaneously to flights using the ASD spectrometer while ascending. The reference panels were then used for radiometric correction of the selected diurnal images by means of empirical line correction (Smith and Milton 1999).

Parallel to thus the HyFlex sensor was flown at various altitudes, please refer to Rascher et al. (2013) for more detailed information.

8.3.1.4 Diurnal Sun-Induced Fluorescence Retrieval

To compare fluorescence trends with the Italian partners, areas of interests (AOIs) were digitized on the respective images for each time and used for comparison with field spectrometer data. The footprint of ~ 1 m in diameter was chosen to match the sensor footprint by Italian partners. F_s for each selected image/times was computed using the 3FLD method (equation (8.1)) and c3FLD method (equation (8.4)), using the linearly averaged neighbouring filter bands of 750 nm and 780 nm as reference to the fluorescence band at 1 nm wide filter at 760 nm (Zarco-Tejada et al. 2013c). According to partners, the white and light grey reference panels were chosen as non-fluorescent target.

For diurnal F_s illustrations maps were finally visualized for CKA2.

8.3.2 Results

Table 8.10 lists the ELC for converting DN into radiance values using the greylevel reference panels's radiance measurements.

Table 8.10 ELC parameters for diurnal F_s retrieval at CKA2, 23/08/2012 (Δrad : difference of resulting radiance values [$Wm^{-2}sr^{-1}nm^{-1}$] to the input reference panels' radiances rp: reference panel).

Band [nm]/ UTC	Empirical line	R ²	Δrad white rp	Δrad light-grey rp	Δrad dark-grey rp	Δrad black rp
08:06						
530	$\rho = 0.00002 x - 0.00004$	0.9993	-	0.0016	-0.0005	-0.0004
570	$\rho = 0.00002 x - 0.0012$	0.9996	-	0.0003	-0.0001	0.0001
670	$\rho = 0.00001 x - 0.0004$	0.9992	-	0.0036	0.0016	0.0010
750	$\rho = 0.00009 x + 0.0001$	0.9998	-0.0001	0.0007	0.0002	0.0002
760	$\rho = 0.00006 x - 0.0021$	0.9998	0.0003	0.0002	0.0001	0.0001
780	$\rho = 0.00008 x - 0.0025$	0.9999	-0.0005	0.0001	-0.0002	0.0001
08:29						
530	$\rho = 0.00003 x - 0.0003$	1	-	-0.0021	-0.0009	-0.0004
570	$\rho = 0.00002 x - 0.0012$	0.9999	-	0.0032	0.0015	0.0009
670	$\rho = 0.00002 x + 0.0003$	1	-	-0.0035	-0.0015	-0.0006
750	$\rho = 0.0001 x + 0.0009$	1	-0.0004	0.0001	0.0000	0.0001
760	$\rho = 0.00007 x - 0.0014$	0.9997	0.0001	0.0001	0.0000	0.0003
780	$\rho = 0.00009 x - 0.0012$	1	-0.0006	-0.0001	0.0001	0.0000
08:51						
530	$\rho = 0.00003 x + 0.0008$	1	-	-0.0010	0.0004	-0.0002
570	$\rho = 0.00003 x - 0.0007$	1	-	-0.0023	-0.0011	-0.0006
670	$\rho = 0.00002 x + 0.0007$	1	-	-0.0021	-0.0008	-0.0004
750	$\rho = 0.0001 x + 0.0015$	0.9998	0.0109	0.0012	0.0009	0.0003
760	$\rho = 0.00008 x - 0.0015$	0.9996	-0.0009	-0.0002	0.0002	0.0002
780	$\rho = 0.0001 x - 0.0013$	0.9997	-0.0028	-0.0003	0.0006	0.0004
09:02						
530	$\rho = 0.00003 x - 0.0007$	1	-	-0.0020	-0.0009	-0.0005
570	$\rho = 0.00003 x - 0.0006$	0.9999	-	-0.0031	-0.0015	-0.0007
670	$\rho = 0.00002 x - 0.0003$	1	-	-0.0027	-0.0012	-0.0006
750	$\rho = 0.0001 x - 0.0043$	0.9999	0.0086	0.0014	0.0011	0.0012
760	$\rho = 0.0009 x - 0.005$	0.9992	-0.0009	-0.0007	0.0001	0.0002
780	$\rho = 0.00009 x - 0.0061$	0.9998	0.0000	-0.0006	0.0000	0.0005
09:19						
530	$\rho = 0.00003 x - 0.0022$	0.9987	-	0.0029	0.0009	0.0010
570	$\rho = 0.00003 x - 0.0021$	0.9994	-	0.0005	-0.0001	0.0004
670	$\rho = 0.00005 x - 0.0014$	0.9989	-	-0.0004	-0.0005	0.0001
750	$\rho = 0.0001 x - 0.0083$	1	0.0166	0.0039	0.0018	0.0019
760	$\rho = 0.00009 x - 0.0081$	0.9997	-0.0016	-0.0004	-0.0005	-0.0001
780	$\rho = 0.0001 x - 0.0094$	0.9999	0.0039	0.0009	0.0002	0.0008
09:42						
530	$\rho = 0.00003 x - 0.0018$	0.9986	-	0.0000	-0.0001	0.0001
570	$\rho = 0.00003 x - 0.0015$	0.9998	-	-0.0013	-0.0007	-0.0002
670	$\rho = 0.00002 x - 0.0009$	0.9998	-	-0.0018	-0.0010	-0.0003
750	$\rho = 0.0001 x - 0.0061$	0.9999	0.0115	0.0024	0.0016	0.0015
760	$\rho = 0.0001 x - 0.007$	0.9989	-0.0008	-0.0008	-0.0003	0.0002
780	$\rho = 0.0001 x - 0.007$	0.9988	0.0038	0.0005	0.0006	0.0009

Band [nm]/ UTC	Empirical line	R ²	Δ rad white rp	Δ rad light-grey rp	Δ rad dark-grey rp	Δ rad black rp
10:13						
530	$\rho = 0.00003 x - 0.0027$	0.9999	-	0.0033	0.0017	0.0009
570	$\rho = 0.00003 x - 0.0020$	1	-	0.0012	0.0005	0.0003
670	$\rho = 0.00002 x - 0.0015$	0.9998	-	0.0012	0.0004	0.0004
750	$\rho = 0.0001 x - 0.0087$	0.9999	0.0233	0.0053	0.0032	0.0019
760	$\rho = 0.00009 x - 0.0082$	1	0.0000	-0.0004	0.0003	0.0003
780	$\rho = 0.0001 x - 0.0099$	1	0.0129	0.0027	0.0017	0.0011
10:45						
530	$\rho = 0.00003 x - 0.0016$	0.9955	-	-0.0012	-0.0012	0.0001
570	$\rho = 0.00003 x - 0.0018$	0.9959	-	-0.0024	-0.0017	-0.0003
670	$\rho = 0.00002 x - 0.0014$	0.9942	-	-0.0032	-0.0020	-0.0005
750	$\rho = 0.0001 x - 0.0033$	0.9999	0.0031	0.0010	-0.0001	0.0004
760	$\rho = 0.00007 x - 0.0004$	0.9999	0.0002	0.0002	0.0001	0.0000
780	$\rho = 0.00009 x - 0.0053$	0.9999	0.0005	0.0004	-0.0003	0.0003
10:57						
530	$\rho = 0.00004 x - 0.0019$	0.9999	-	-0.0017	-0.0009	-0.0004
570	$\rho = 0.00003 x - 0.0013$	1	-	0.0031	0.0014	0.0007
670	$\rho = 0.00002 x - 0.0007$	0.9999	-	0.0021	0.0008	0.0005
750	$\rho = 0.0001 x - 0.001$	1	0.0270	0.0041	0.0018	0.0010
760	$\rho = 0.0001 x - 0.0023$	1	-0.0006	0.0001	-0.0001	0.0000
780	$\rho = 0.0001 x - 0.0019$	1	0.0205	0.0037	0.0018	0.0014
11:07						
530	$\rho = 0.00004 x - 0.0021$	1	-	-0.0010	-0.0004	-0.0003
570	$\rho = 0.00004 x - 0.0016$	0.9999	-	-0.0029	-0.0013	-0.0008
670	$\rho = 0.00002 x - 0.0011$	1	-	0.0027	0.0012	0.0007
750	$\rho = 0.0001 x - 0.0076$	1	0.0338	0.0070	0.0043	0.0037
760	$\rho = 0.0001 x - 0.0079$	0.9997	0.0038	0.0009	0.0006	0.0001
780	$\rho = 0.0001 x - 0.0091$	1	0.0269	0.0056	0.0040	0.0031
11:32						
530	$\rho = 0.00004 x - 0.0027$	0.9998	-	0.0016	0.0009	0.0003
570	$\rho = 0.00004 x - 0.0026$	0.9999	-	-0.0001	0.0001	-0.0001
670	$\rho = 0.00003 x - 0.0016$	0.9999	-	-0.0036	-0.0015	-0.0010
750	$\rho = 0.0002 x - 0.0084$	1	-0.0173	-0.0054	-0.0033	-0.0031
760	$\rho = 0.0001 x - 0.0086$	0.9998	0.0076	0.0018	0.0016	0.0010
780	$\rho = 0.0001 x - 0.0103$	1	0.0356	0.0082	0.0054	0.0042
11:49						
530	$\rho = 0.00004 x - 0.0024$	0.9999	-	0.0007	0.0005	0.0001
570	$\rho = 0.00004 x - 0.0018$	1	-	-0.0016	-0.0007	-0.0004
670	$\rho = 0.00002 x - 0.0017$	1	-	0.0039	0.0017	0.0010
750	$\rho = 0.0002 x - 0.0073$	1	-0.0232	-0.0060	-0.0039	-0.0034
760	$\rho = 0.0001 x - 0.0087$	0.9999	0.0060	0.0016	0.0015	0.0012
780	$\rho = 0.0001 x - 0.0093$	0.9999	0.0293	0.0068	0.0044	0.0032
12:06						
530	$\rho = 0.00004 x - 0.0023$	1	-	0.0005	0.0002	-0.0002
570	$\rho = 0.00004 x - 0.0025$	1	-	-0.0011	-0.0005	-0.0011
670	$\rho = 0.00002 x - 0.0013$	1	-	0.0036	0.0016	0.0005
750	$\rho = 0.0002 x - 0.0064$	1	-0.0208	-0.0056	-0.0032	-0.0055
760	$\rho = 0.0001 x - 0.008$	0.9998	0.0065	0.0020	0.0014	0.0001
780	$\rho = 0.0001 x - 0.009$	1	0.0291	0.0066	0.0041	0.0024

Band [nm]/UTC	Empirical line	R ²	Δ rad white rp	Δ rad light-grey rp	Δ rad dark-grey rp	Δ rad black rp
12:34						
530	$\rho = 0.00004 x + 0.0007$	0.9997	-	0.0007	0.0001	0.0002
570	$\rho = 0.00004 x - 0.0016$	0.9996	-	-0.0008	-0.0006	-0.0001
670	$\rho = 0.00002 x - 0.001$	0.9998	-	0.0032	0.0011	0.0006
750	$\rho = 0.0002 x - 0.0082$	0.9999	-0.0138	-0.0053	-0.0022	-0.0022
760	$\rho = 0.0001 x - 0.0008$	0.9998	0.0060	0.0010	0.0006	0.0001
780	$\rho = 0.0002 x - 0.00008$	1	-0.0236	-0.0047	-0.0019	-0.0010
13:13						
530	$\rho = 0.00004 x - 0.002$	0.9999	-	0.0008	0.0004	0.0001
570	$\rho = 0.00004 x - 0.0022$	1	-	-0.0006	-0.0003	-0.0003
670	$\rho = 0.00003 x - 0.0015$	1	-	0.0039	0.0018	0.0009
750	$\rho = 0.0002 x - 0.0064$	0.9999	-0.0155	-0.0046	-0.0028	-0.0022
760	$\rho = 0.0001 x - 0.0072$	0.9998	0.0066	0.0013	0.0008	0.0006
780	$\rho = 0.0001 x - 0.0084$	1	0.0273	0.0064	0.0037	0.0028
13:56						
530	$\rho = 0.0003 x - 0.0017$	1	-	0.0011	-	0.0004
570	$\rho = 0.00003 x - 0.0014$	1	-	-0.0003	-	-0.0001
670	$\rho = 0.00001 x - 0.0002$	1	-	-0.0016	-	-0.0009
750	$\rho = 0.0001 x - 0.0057$	1	0.0178	0.0045	0.0000	0.0026
760	$\rho = 0.00009 x - 0.0058$	0.9997	0.0007	0.0002	0.0000	0.0003
780	$\rho = 0.0001 x - 0.0071$	1	0.0114	0.0028	0.0000	0.0018

Figure 8.12 shows the incoming solar radiance measured at the field spectrometer by partners.

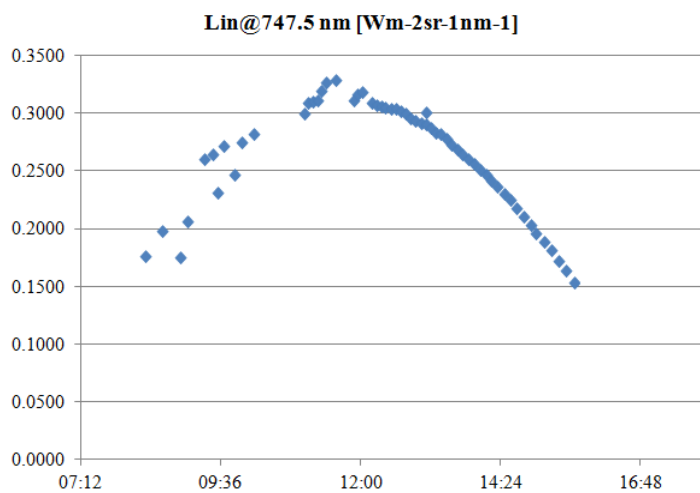


Figure 8.12 Incoming radiance measured with field spectrometer at 747.5 nm [$\text{Wm}^{-2}\text{sr}^{-1}\text{nm}^{-1}$] [mod. from Rascher et al. 2013]

Figure 8.13 shows the diurnal F_s values retrieved from field spectrometers (blue diamonds) and UAS data (red triangles) for the 3FLD method (left) and the c3FLD method (right). F_s values were retrieved until 14:00h UTC as the ground station failed to function at this point, thus it was not possible to map a full diurnal course. UAS-based F_s

values are a factor of 10 higher than the spectrometer measurements, values rised until noon (~11:30 UTC), then reclined. Data gaps in the morning are due to unstable atmospheric conditions, and the respective images were removed from analysis.

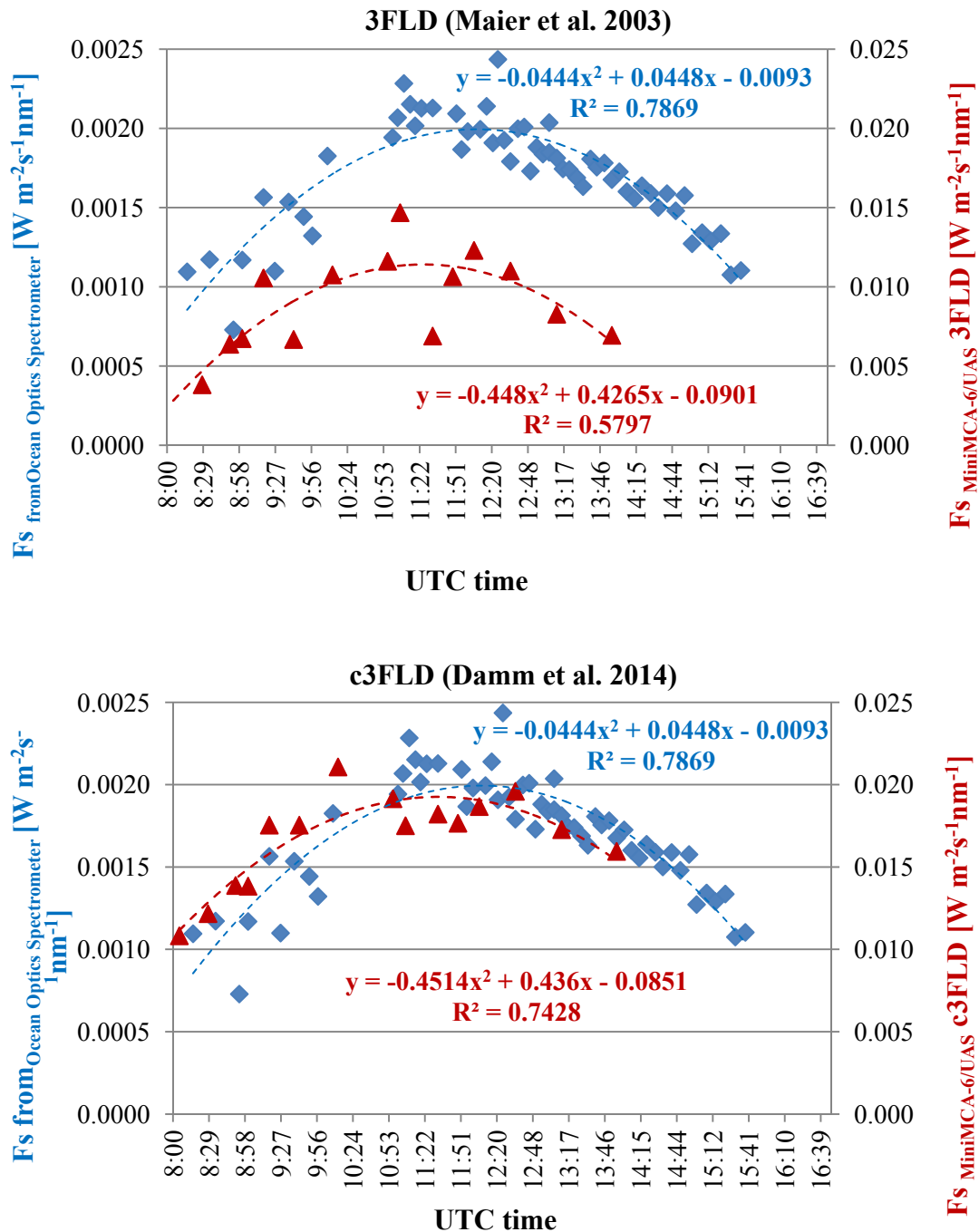


Figure 8.13 Diurnal sun-induced fluorescence for CKA2 derived from multispectral UAS data (right axis, red triangles) and Ocean Optics Spectrometer (left axis, blue diamonds) retrieved by Meroni (2015, personal communication), 23/08/2012.

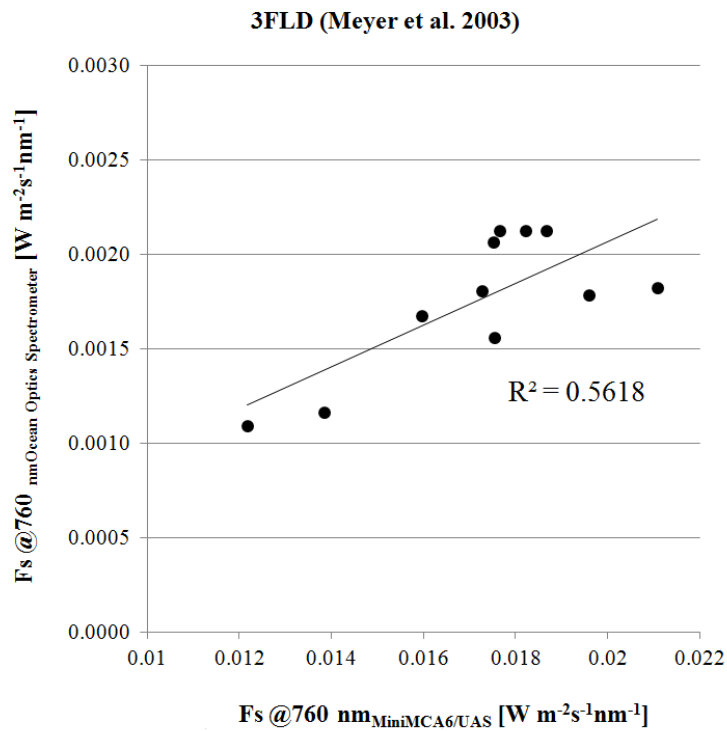


Figure 8.14 Correlation between field- and UAS-derived sun-induced fluorescence at 760 nm at CKA2, 23/08/2012

Measurements of F_s at 760 nm derived from the field-spectrometers and drone image acquisition did not always temporarily coincide (Figure 8.14), and show a relatively weak correlation between the two data sets (linear regression R^2 0.5618).

A comparison of F_s in relation to non-fluorescing reference target for 3FLD methods based on Maier et al. (2003) and Damm et al. (2014) in Figure 8.15 shows, values are following a related course but are scaled differently: highest F_s values are obtained using the white reference panel.

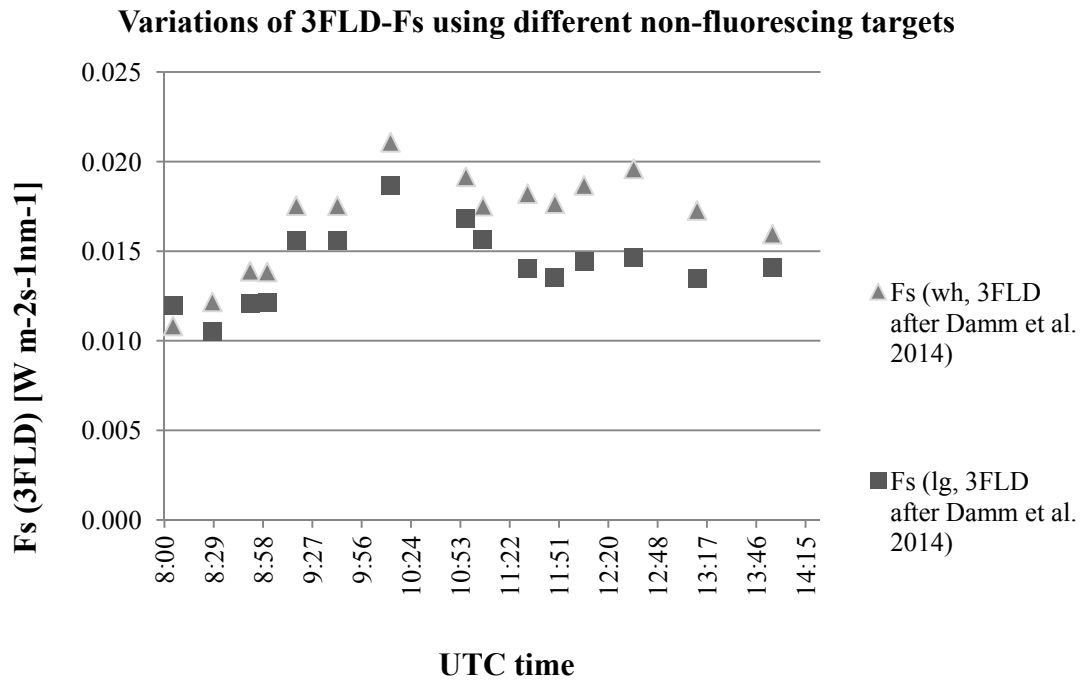


Figure 8.15 Diurnal course of $F_{s,UAS}$ (3FLD) values retrieved using different reference non-fluorescent target (wh: white reference panel, lg: light-grey reference panel)

$NDVI_{UAS}$ do decline until midday which is in accordance with wilting processes visibly detectable in the field on that day. The high $NDVI$ values together with the high fluorescence values (Figure 8.16) generally show that the bi-annual crop is still dense and green and photosynthetically active.

The daily progression of $NDVI$ and PRI values also point out the differences between measurement devices and height above sugar beet (Figure 8.16). $NDVI_{UAS}$ do decline until midday which is in accordance with wilting processes visibly detectable in the field on that day. The diurnal PRI_{UAS} is showing no diurnal trend compared to PRI_{field} spectrometer.

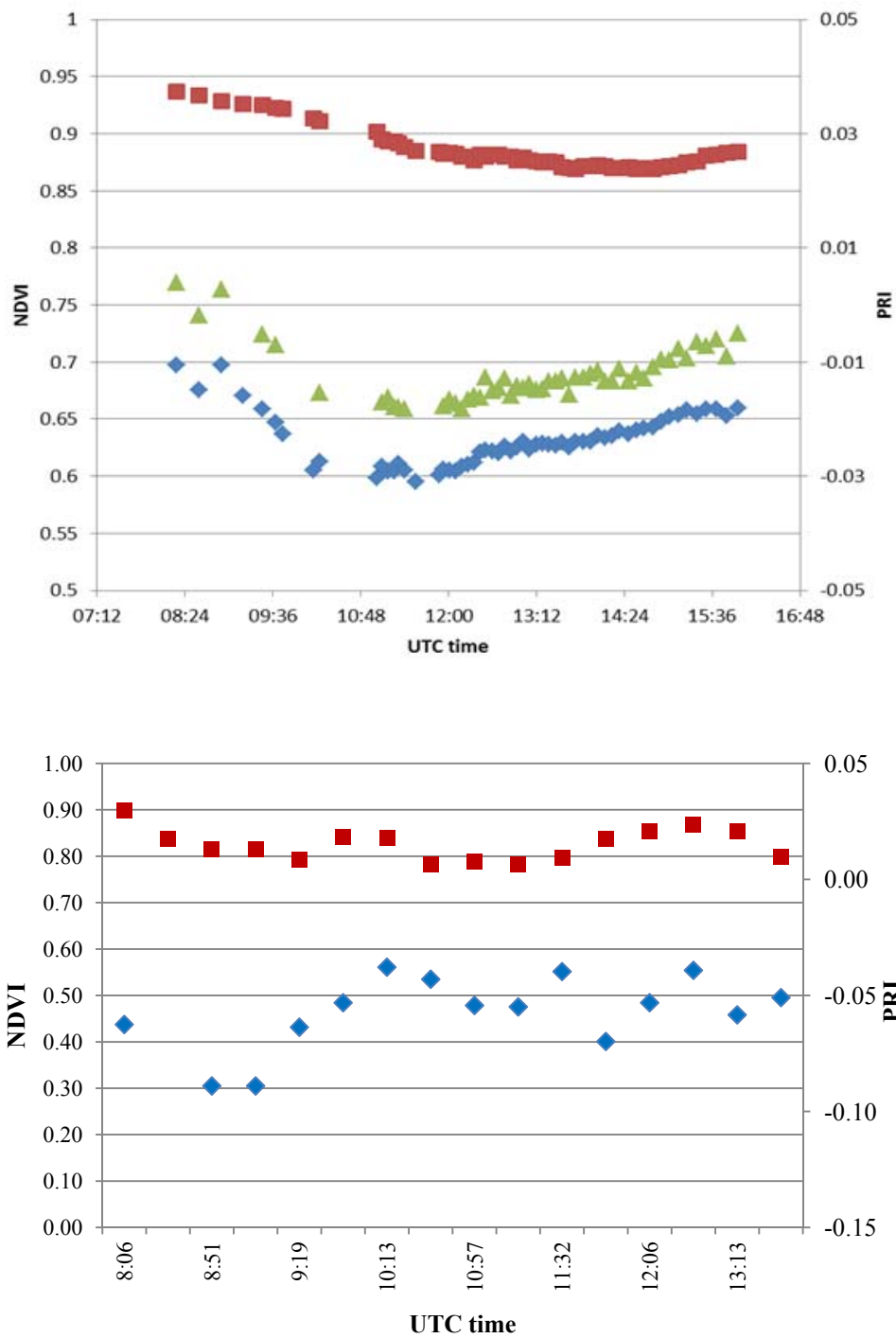


Figure 8.16 Diurnal course of NDVI and PRI at CKA2, 23/08/2012 for spectrometer data (top) and MiniMCA-6/UAS data (bottom). Red square: NDVI, green triangles: PRI_{1nm-bandwidth}, blue diamonds: PRI_{10nm-bandwidth}

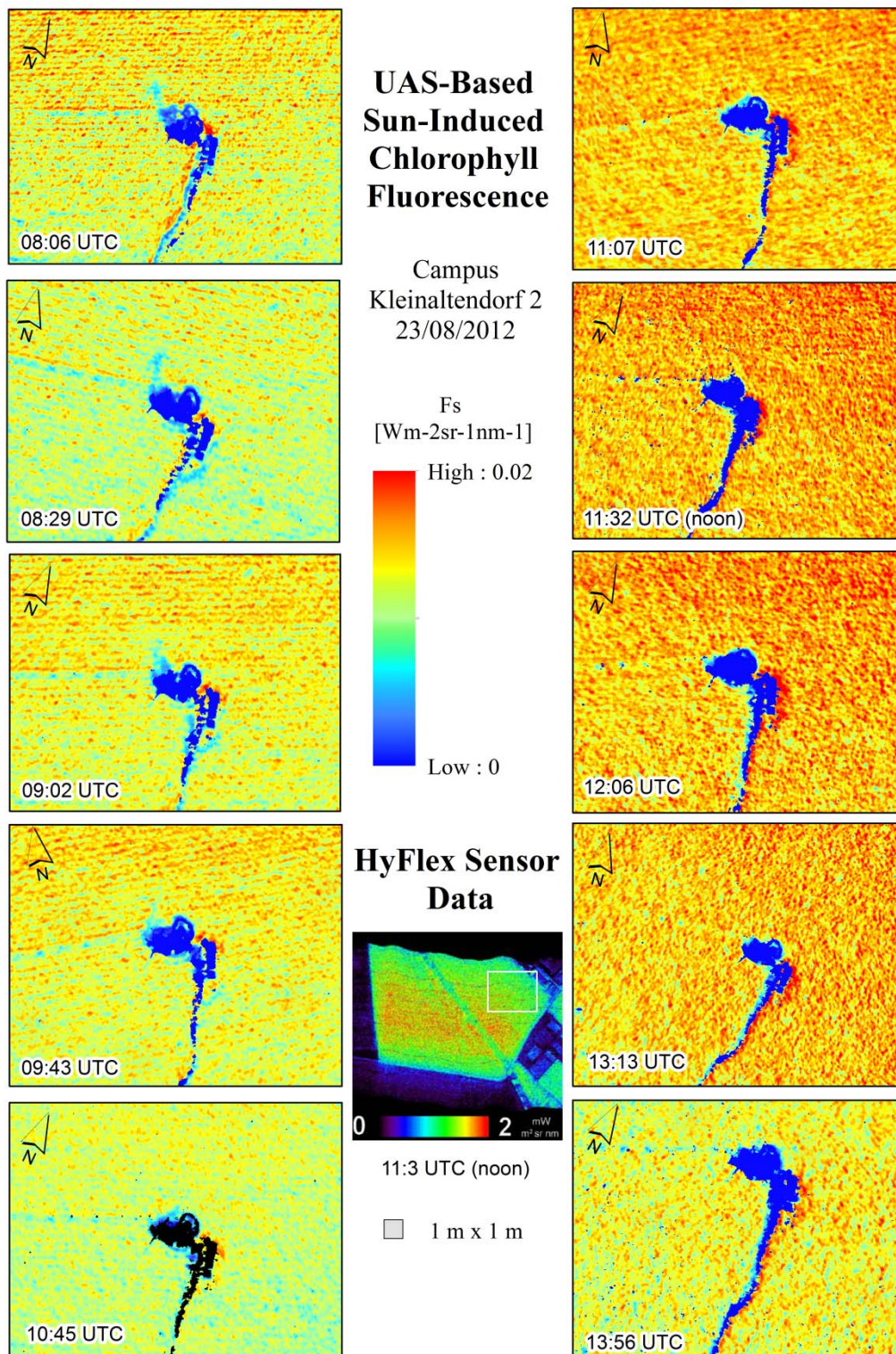


Figure 8.17 Diurnal sun-induced chlorophyll $F_{s,UAS}$ (c3FLD) for a sugar beet field at CKA2 (23/08/2012). Centre image HyFlex $F_{s,HyFlex}$ data derived at noon at 600 m a.s.g. (white square shows field). HyFlex data from Rascher et al. (2013).

From the individual images in Figure 8.17 the rise in F_s values until midday (11:32 UTC image) may be detected as well as a slight descent in F_s values towards the afternoon. However, the images also show higher F_s values at the NE rim and lower F_s values at the SW corner of the image.

8.3.3 Discussion

The UAS-derived F_s values were able to depict the expected diurnal process of sun-induced chlorophyll fluorescence (Figure 8.13) with increasing fluorescence until midday and decreasing values towards the afternoon following a 2nd order polynomial trend function. However, the $F_{s,UAS}$ overestimated the actual (i.e. field) F_s values by a factor of 10 for the c3FLD and by a factor of ~ 8 for the FLD, as was reported by other airborne campaigns (Zarco-Tejada et al. 2009). Yet, the amount of F_s retrieved is well inside the ranges reported in a review published by Meroni et al. (2009) who found F_s values for the O2-A band vary from 0 to $17 \text{ Wm}^{-2}\text{sr}^{-1}\text{nm}^{-1}$ for different illumination intensities and crops. The drone-derived F_s (c3FLD) values better match the diurnal process ($R^2 = 0.74$) than the 3FLD ($R^2 = 0.58$) values. Alonso et al. (2008) furthermore proved that the sFLD-derived F_s values ranges may well deviate by an order of one magnitude regardless of measurement device due to the uncertainty of the reflectance curve shape in that wavelength range which is assumed to remain constant. The 3FLD method assumes linear relationships between the shoulders of absorption bands wavelengths. This assumption is only valid when close shoulder wavelengths are selected for F_s retrieval. A violation yields a relative positive F_s bias of up to 50% at the O2-B band even for the well-established field spectrometers and airborne sensors (Meroni et al. 2010). Compared to the field spectrometer data (753 \pm 3 nm and 777 \pm 3nm, respectively), shoulder wavelengths were less close for the UAS data.

Recent publications within the FLEX programme, have found a precise radiometric and atmospheric correction mandatory for accurate F_s retrieval (Guanter et al. 2010; Damm et al. 2014). The $F_{s,UAS}$ variations for the CKA2 site and field data may well be attributed to radiometric correction errors resulting from the ELC where deviation of radiance values of reflectance panels in some cases exceeds the amount of F_s (Table 8.10). The reference panels had been based on top of the canopy within the sugar beet field, hence their radiance/reflectance may include adjacency effects of radiation/reflectance environmental components in their signal. Furthermore, measurements of solar irradiance values did not always coincide exactly with solar irradiance values measured by partners.

Up until noon, solar irradiance (Figure 8.12) was not stable and additionally obscured a potential maximum F_s course. Bi-directional reflectance effects within the image data may add to that effect.

It was further found that the absolute height of F_s ($c3FLD$) or F_s ($3FLD$) also depends on the use of reference non-fluorescing reference target as Figure 8.15 illustrated.

In some cases, negative F_s values occurred during the calculation, especially for the 3FLD formulation. Negative values occur when fluorescence approximates 0 and gets close to the multispectral camera's intrinsic noise level of 8 to 16 DNs (Kelcey and Lucieer 2012). Other authors have found similar difficulties (Zarco-Tejada et al. 2009). Damm et al. 2011 pointed out that the more sophisticated the F_s retrieval method the more sensitive it behaves to retrieval accuracies. Differences in atmospheric scattering introducing varying path lengths, illumination/observation geometry variations and transmission differences have been shown to be contribute considerably to estimation errors:

- F_s bias of 15% for reference non-fluorescing targets being situated at larger distances from vegetation target,
- F_s bias of 17% for flight altitude of 200 m (Damm et al. 2014), and d
- Due to structural components, i.e. shaded versus sunny canopies also influence the F_s retrieval (Rascher et al. 2009).

A transmittance correction was applied by these authors utilizing bare soils which should be free of any F_s signal.

Both, the individual F_s images derived for the sugar beet field (Figure 8.13) and the PRI values (Figure 8.16) may still be influenced by the altogether low deviations from nadir viewing and potentially sun azimuth directions obtained during image acquisition (Figure 8.18), although these have been moderately low. The individual images show high F_s values in the NE and drop-off to the SE may suggest that there still are inherent illumination differences for the UAS images not corrected by the ELC approach. Airborne F_s imagery obtained from the FLEX Campaign in CKA2 at 600 m above ground level (a.g.l.) illustrated in Figure 8.19, though, did retrieve similar variations for the sugar beet field: enerally, the sugar beet field showed highest F_s values when compared with other crops and for that field respectively, rising F_s values from the shed visible at the image corner towards the left to the hedge in the field (Rascher et al. 2013). In the UAS images, the shed is situated at the lower left corner.

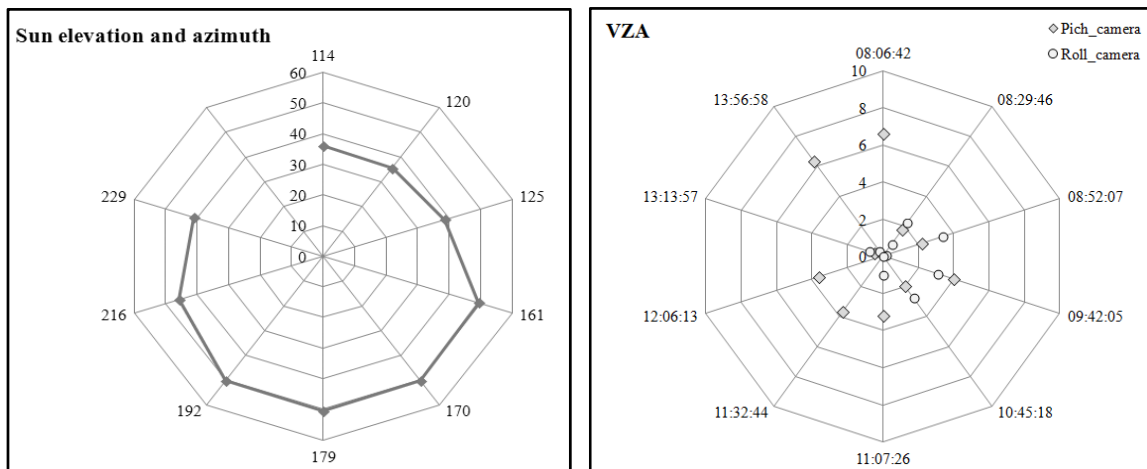


Figure 8.18 Illumination (left) and viewing zenith angle (VZA) deviation from nadir (right) for UAS image acquisitions

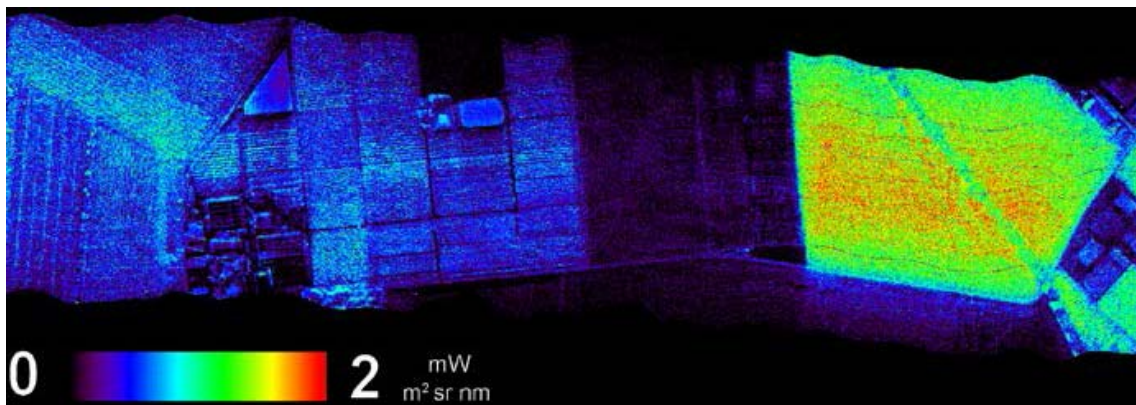


Figure 8.19 F_s for CKA2 sugar beet field derived from airborne data obtained at 600 m a.g.l. (top right field corner). Image source has been subsetting from final HyFlex report (Rascher et al. 2013, p. 78).

Concerning the oscillating PRI values (Figure 8.16), the index has shown to be quite sensitive to BRD which may explain the failure of obtaining a similar diurnal patterns (Filella et al. 2004, Hilker et al. 2008; Rascher and Pieruschka 2008; Damm et al. 2010b). Sensitivity analysis in chapter 6 (figure 6.18) yet found stable PRI values for VZA close to nadir. But azimuth variations in relation to sun position do contribute to index differences, which may not have been totally corrected by the ELC approach. PRI has also been demonstrated to be more correlated with NPQ than with PSII (Evain et al. 2004). Another argument for the poor correspondence of PRI field and UAS-values, may be the early stop at 14 UTC which omitted the documented afternoon rise of PRI values obtained by partners.

Diurnal measurements of F_s may be retrieved with means of multispectral UAS imagery. Values varied within the order of a magnitude compared to canopy-based field measurements but showed an overall agreement of $R^2 = 0.56$. This could be related to less than ideal filter centre locations and widths (760 nm compared to 760.5 nm as was suggested by Damm et al. 2011). Thus, UAS campaigns may aid in diurnal F_s and stress detection and although absolute physical fluorescence values may be overestimated, they do indeed allow the detection of diurnal variations and may aid in fast overviews across agricultural sites and different species.

8.4 Conclusion

Principally, the fluorescence of different crop species may be analyzed by UAS-based fluorescence behavior as the experiment of CKA1 has illustrated. In this case, F_s was due to less than ideal weather conditions not at its maximum. However, different N treatment levels could well be distinguished and as could the sugar beet varieties with multispectral bands, indices and fluorescence indices. Again, the standard NDVI reliably succeeded in differentiation among N treatment levels and varieties. Further tests could include more treatment levels and crops to test if these also can be distinguished by means of multispectral UAS-based remote sensing.

Concluding, retrieval of physical fluorescence values requires synchronous ancillary data of irradiance and aerosol optical depths following a strict protocol to quantify atmospheric transmission and influence on the fine fluorescence signal. Yet, comparative diurnal F_s analysis across sites may well be retrieved by means of UAS multispectral measurements using close reference targets to approximate atmospheric disturbances (Zarco-Tejada et al. 2012; Damm et al. 2014).

More precise, absolute physical F_s values may be obtained by currently being developed micro-hyperspectral sensors with narrow band widths or finer filter FWHM bandwidths. This would also yield the potential to include other fluorescence bands, too. Prerequisite of physically absolute F_s retrieval is an accurate radiometric pre-processing including camera calibration, noise correction and atmospheric correction with synchronous aerosol optical measurements which was out of scope for this work. Parallel comparative F_s measurements of (non-)fluorescing targets do support F_s retrieval help to calibrate the UAS data.

Recently, spectral fitting methods (SFM) for hyperspectral narrow-band data have been shown to be more accurate in retrieving F_s at various noise settings: the respective spectral regions around the absorption lines may be described by polynomial functions or other appropriate mathematical functions (Meroni et al. 2010). Other authors fluorescence spectrum reconstruction over various absorption bands (Zhao et al. 2014, Zhao et al. 2014). Thus, once hyperspectral micro-sensors are operationally available, more accurate F_s estimation may be achieved for precision agriculture.

9 UAS-Based Archaeological Reconnaissance at the Roman Settlement of Los Bañales de Uncastillo, Spain

9.1 Introduction

9.1.1 Overview of Geomatic Prospection Sensors

Archaeological sites nowadays are generally studied embracing different geomatic prospection methods (Bitelli et al. 2004, p. 116-117) from large to small scales. Figure 9.1 illustrates the relative prominence of the individual methods at different scales from point-based measurements to 2D- and 3D mapping.

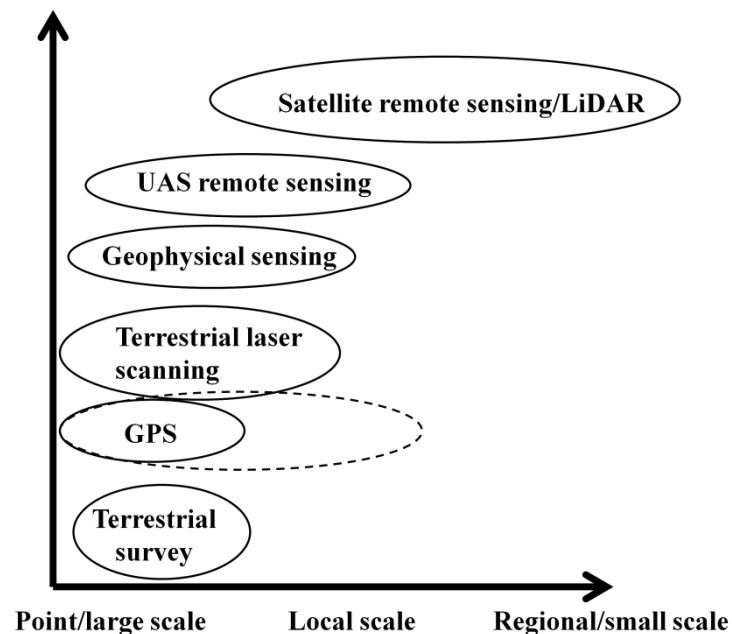


Figure 9.1 Geomatic methods and their application scales in archaeological prospection (modified from Bitelli 2012)

1D measurements use tachymeter or total stations to map archaeological finds and structures often in local reference systems. Data acquisition is time consuming yet provides maps of high precision accuracy within the mm- to cm-range. 2D- to 3D measurements then use global satellite positioning systems based on the American Navstar Global Po-

sitioning System (GPS) or Russian Glonass data amongst others. Again, depending, on the measurement setup used, within mm-accuracy of point data in 2D and within cm-range for height data are feasible. GPS-data may also be obtained for surveying and ground control point reference measurements for aerial surveys. Terrestrial laser scanning, finally, is yet another method obtaining a 3D representation of objects at a large scale within mm-accuracy from which areal information may be derived by combining several point clouds. The need to detect buried materials brought forward proximal sensing with geoelectric, geomagnetic or radar sensors, retrieve point data that are then interpolated to grids (Masini et al. 2012). Local to small-scale 2D to 3D areal mapping is then achieved by remote sensing applications on aerial and satellite platforms. Their advantage lies in synoptic views that may be obtained using various sensor systems measuring in the VIS/nIR, SWIR, TIR, microwave (radar) spectral regions. From these orthophotos and DEMs may be derived as well as further spectrally-derived data such as land cover classifications, feature maps, thermal maps, etc. Space-borne LiDAR is another information source and more recently, geoelectric and geomagnetic sensors find growing attention operate in close-range remote sensing. Another benefit from remote sensing data is the possibility to monitor site by revisiting sensors or flight campaigns thus facilitating exploration progress. Lasaponara and Masini (2012b) summarize archaeological applications of satellite remote sensing, visual inspection and data processing methods.

9.1.2 Remote Sensing of Cultural Heritage Patterns

Former settlement structures show geometric patterns of various kinds like rectangular or circular wall remains, linear elements like walls, and transport routes or ditches (Aber et al. 2010). These may occur on the surface or hidden underneath the surface. Where they are close to the surface they tend to show specific surface traces. That is why, among the most frequent analysis technique in archaeological remote sensing is visual interpretation of aerial photographs to obtain overviews and mapping products which often supersedes automatic detection (De Laet et al. 2009). The trained eye quickly derives sites of interest which may then be tackled by the digital image processing suite available in the remote sensing domain. The extension of the spectral domain to wavelengths beyond the visual system, may reveal more patterns indiscernible to the human eye and multi- and hyperspectral remote sensing and standard digital image processing find growing applications (Verhoeven 2009; Lasaponara and Masini 2012b; Verhoeven 2012).

Archaeological prospection with UAS data then encompasses various approaches of traditional digital image processing (Parcak 2009; Aber et al. 2010; Lasaponara and Masini 2012c; Masini et al. 2012):

1. Data fusion techniques for incorporation high spectral resolution to high spatial resolution data when data of different sensors are to be merged (Masini et al. 2012; Oltean and Abell 2012; Richards 2013),
2. Data reduction or image enhancement by way of digital feature space processing,
3. Computation of various vegetation indices unveil otherwise hidden patterns,
4. Cultural heritage feature tracing by edge detection, texture or pattern analyses,
5. structural mapping of building fragments (*i.e.* through incorporating DEM-derived data as height, slope, aspect),
6. land cover classification, and
7. change detection/monitoring of excavation sites (Lasaponara and Masini 2012a).

The presentation of all existing DIP methods is out of scope here and more information is provided in respective references, *e.g.* Jensen (2005), de Jong (2006) Jensen (2007), Lillesand et al. (2008), Richards (2013). Here, only the techniques applied in this work are shortly explained.

9.1.2.1 Crop and Soil Mark Analyses

It is not only the direct mapping of ancient masonry, but also the indirect mapping of sub-surface building remnants that is of interest to archaeologists. Verhoeven (2012) points out the neglectance of spectral ranges outside the VIS in aerial remote sensing within the field of archaeology. The reflectance characteristics of vegetation canopies have been presented in details in chapter 3, and may be used to indirectly map cultural heritage features by studying growth differences caused by soil substrate or moisture differences (Figure 9.2). Moisture and substrate alterations may induce stress and senescence in plant development, thus altering leaf pigment (Chl, carotenoids, brown pigments), moisture content, fluorescence differences as well as structural differences within the leaves. These changes trace back to the canopy signal altering spectral reflectance intensity: the vegetation signal flattens with increasing reflectance in the green spectral ranges, loss of the red absorption minimum and flattening nIR reflectances with shifts of the red edge (figure 3.10). Furthermore, stress causes variations in plant height leading to structural differences and micro-shading within a vegetation canopy. Depending on climate, crop and soil type, the sample crop-marks may lead to reverse findings

in relation to DN values. Resulting spectral signals further depend on the sensor used, and patterns may in fact be contrary depending on environmental condition and acquisition times: thermal sensors reveal inverse patterns during the day compared to nightly images.

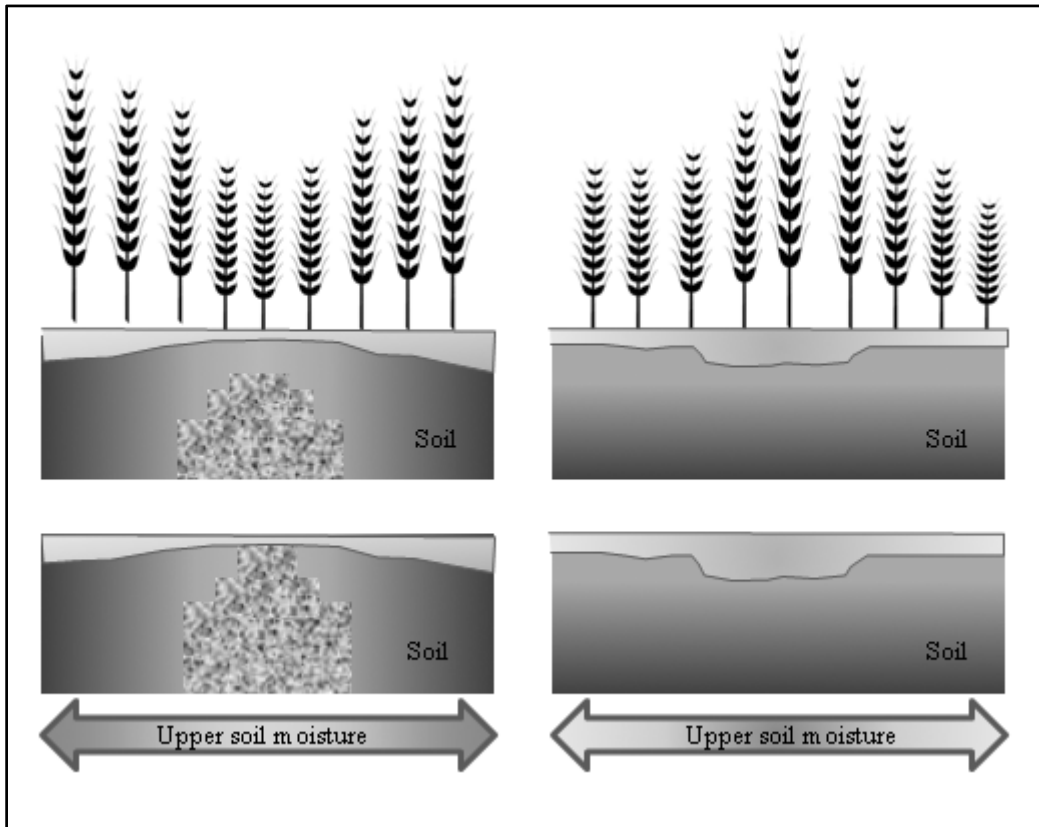


Figure 9.2 Crop-marks based on sub-surface cultural heritage features and their effects on upper soil moisture and crop growth: darker greyscale shades illustrate higher soil moisture and vice versa (modified from Lasaponara and Masini 2012c, p. 5)

9.1.2.2 Feature Enhancements Used in Archaeological Remote Sensing

Similar to crop mark/soil mark detection, surface archaeological structures need to be extracted from the multispectral signal of the environment. Wall and building remnants introduce relieved surfaces that include a portion of shadows and are thus highly spectrally structured. These features are enhanced by principal component analyses and (vegetation) indices, followed by edge and texture detection through filter operation (Masini et al. 2012; Richards 2013).

9.1.2.3 Land Cover Classification of Archaeological Sites

Once, cultural heritage patterns have been enhanced, the surface cover materials within the vicinity may be derived by classification:

- Unsupervised clustering (UC) techniques (Garrison 2010),
- Supervised classification using training sites/clusters (Lasaponara and Masini 2012a), spectral angle mapping (SAM) or support vector machines (SVM),
- Spectral methods, *i.e.* spectral mixture analysis to obtain sub-pixel land-cover components, spectral angle mapping (SAM) or support vector machines (SVM) (Mountrakis et al. 2011; Lasaponara and Masini 2012a),
- Object-oriented classification (OOC) incorporating spectral and spatial information measures, resulting in vector-based classification output (De Laet et al. 2009),

or a combination of the above (Lasaponara and Masini 2012a). There are many classification algorithms available which are described in detail by standard textbooks mentioned before.

9.1.3 Using Small UAS for Archaeology

Among the first UAS applications in archaeological remote sensing was aerial photography from balloons: Whittlesey (1970) mounted several camera types (Linhof, Graflex, Hasselblad) onto a tethered balloon to obtain stereographic images at various altitudes from ~ 10 m to 700 m a.g.l. of sites at Turkey, Greece, Italy and Cyprus. Within the past 10 years, use of UAS in the field of archaeology has increased manifold, as they provide fast and customized data collection to obtain (orthographic) photographs of sites of specific interest. Myers (1977) describes the aerial photographic mapping of Greek and Italian sites with a kite-balloon more appropriate for stronger breezes. Late Iron-age structures in South Africa were mapped using a remote-controlled camera mounted on a weather balloon within a tethered parachute (Noli 1985). Later, kites were rediscovered for aerial photography, allowing to be used with higher winds and had the advantage of being independent of gas and its handling (Anderson 2001). Colour and black and white films were used then. Within the past decade, the growing UAS market introduced many lightweight UAS with mostly off-the-shelf digital cameras for (photogrammetric) mapping applications (Colomina and Molina 2014). Plus, rotary and fixed-wing systems have found widening application in archaeological mapping. Verhoeven et al. (2014) presented a tethered multi-copter, and praised the independency of wind conditions and

GNSS signals. Williams (2012) used a fixed-wing light-weight UAS (swinglet CAM) to map the Medieval city of Merv along the Silk in Turkmenistan. And recently, Yan et al. (2014) compared low-altitude photogrammetry with LiDAR data and found the latter more performant for penetrating vegetation close to ancient walls, yet a more expensive system and lacking sub-decimetre mapping resolution. A UAV-LiDAR system introduced by Wallace et al. (2012) uses a Sigma Point Kalman Smoother to combine IMU, GPS receiver and video observations to point cloud densities of 62 points/m² with horizontal decimetre accuracy of around 34 cm and vertical of 14 cm at a 50 m flight altitude.

9.1.4 The Roman Settlement of Los Bañales

Los Bañales is located along the old Roman route joining *Caesar Augusta* (now Saragossa) to *Pompelo* to *Aquitania* and the Pyrenees. Starting as a Celtiberan, Flavian settlement within an agricultural environment in the 4th -3rd century B.C., it became a Roman economic and administrative centre within the first century B.C. consisting of an elite of indigenous yet romanised folk, war veterans and also Italians (Lasuén Alegre and Nasarre Otín 2008, Andreu Pintado et al. 2014). The urban structure became more complex including administrative, religious functions as well as a centre for agricultural production and trade/service centre (Lasuén Alegre and Nasarre Otín 2008). At the end of the 1st century AD, thermal baths and an aqueduct had been built, although monument-building is thought to have begun at Augustan times already (Andreu et al. 2011). The city extended to about 20 hectares in size (Andreu Pintado et al. 2014). In 2009 excavations revealed that around the late 2nd century, private spaces with arcades were added to the city, and streets suppressed upon to the west of the thermal baths, which led to the assumption – in the absence of any destruction signs - that the city was diminishing either through weakened significance of local authority or due to economic causes. From 4th -5th century AD, the settlement was supposed to have become residential but was still significant (Lasuén Alegre and Nasarre Otín 2008; Andreu et al. 2011). Coin finds dating to the Arabian Epoque (8th -9th century A.D.) suggest that depopulation happened gradually and peacefully (Andreu Pintado et al. 2014). Andreu lists other settlements facing similar desertions within the time period of 230 to 270 AD (2011, p. 122).

First known descriptions of buildings and sketch maps of the settlement have been given by the Portuguese cosmographer Laban of 1610 (Lasuén Alegre and Nasarre Otín 2008). As local place names have for long been referred to as “Bañales“, derived from

the Latin *Balneum*, the existence of the Roman baths was well known (Lasuén Alegre and Nasarre Otín 2008). The authors list further Spanish place names linked to Roman origins (Lasuén Alegre and Nasarre Otín 2008, p. 214).

In 1930 the area was referred to Eremita de los Bañales on the topographic map. The first systematic examination of the area was conducted from 1942-49 by Galiay and 1973-1979 by Beltrán. Recently, the Fundación Uncastillo together with the Universidad Nacional de Educación a Distancia (UNED) set up an investigation plan in 2008 with a first excavation beginning in 2009 (Lasuén Alegre and Nasarre Otín 2008; Andreu Pintado and Garcia Lopez 2012).

9.1.5 Objectives

The main aims of this study were to retrieve the extent and municipal area of the Roman city Los Bañales, *i.e.* (i) to retrieve a 3D representation of the settlement area on the hill El Pueyo as a basis for further archaeological mapping and surveying, (ii) retrieving appropriate classification procedures to evaluate signs of archaeological settlement structures from vegetation type composition, and (iii) to explore the surrounding fields in the E and S of El Pueyo for any subsurface remains of Roman city or road structures.

In the following, the work carried out begins with a description of the study site. The data used for this study are then presented followed by relevant pre-processing steps and description of the respective point-cloud modelling for the UAS data. Finally, the actual archaeological digital image processing focusing on the objectives are presented one by one.

9.2 Study Site

9.2.1 Historical Outline

Los Bañales is situated in the South of the Pyrenees within the Comarco Cinco Villas to the southeast of the town Layana in the municipal of Uncastillo within the Spanish province Zaragoza at 1.23° W and 42.29° N (Figure 9.3). Geologically, the settlement lies at the NE-SW tilting sloping area of the Pyrenees in the valley of the river Rigel, contributory to the Ebro at mean altitudes of 450 m a.s.l. (Figure 9.1). Locally, the Bañales Valley consists of Miocene substrates of sandstones, clays, marls, limestones and gypsum (Lasuén Alegre and Nasarre Otín 2008, p. 208). Soils are Cambisols Calcico-Rendzinae. The climate generally is temperate with a dry season and temperature

summers (Köppen-Geiger Cfb). At Saragossa Airport ($41^{\circ} 39' 38''\text{N}$, $1^{\circ} 0' 15''\text{E}$, 263 m a.s.l.) for the 1981-2010 period the mean temperature was 15.5°C and about 322 mm of annual precipitation, most of it falling generally in autumn/winter and late spring (Instituto Aragonés del Medio Ambiente 1993; AEMet 2015c). The region had been facing an extremely dry winter season 2011/2012, and received only half of mean March rainfall compared to the 1971-2000 mean (AEMet 2015b; AEMet 2015a).

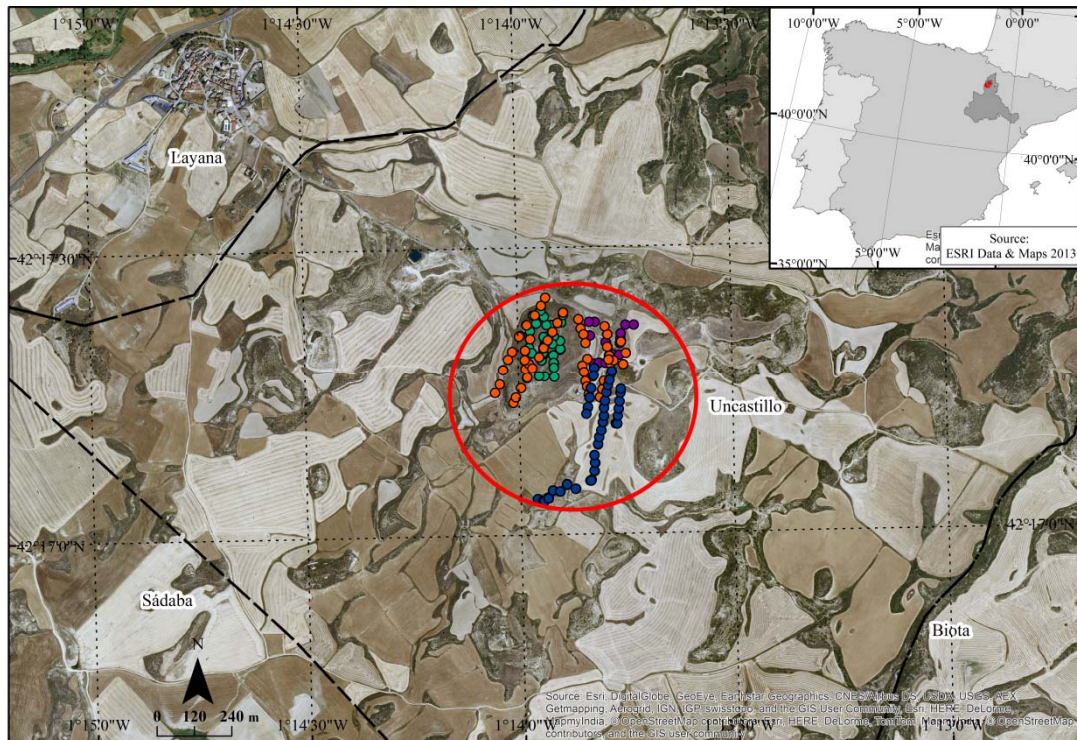


Figure 9.3 The study site of Los Bañales in Arragon, Spain. Dots indicate camera positions for individual flights.

The Roman city reached a size of about 20 hectares and was mainly located to the S of the hill El Pueyo de los Bañales (567 m a.s.l). Figure 9.4 illustrates the location of the Roman settlement parts on the site.



Figure 9.4 Roman buildings excavated at Los Bañales (1: centro de El Pueyo, 2: domestic/craft centre, 3: Forum, 4: domestic centre, 5: Roman Baths)

On its plateau, a housing area is assumed by remaining rock wall foundations and pole hollows and pits with excavated stones originally developed by indigenous folk. Towards the Eastern slopes and the first terrace follow village houses with a radial set up with probably poorer inhabitants (Lasuén Alegre and Nasarre Otín 2008). Along the second terrace to the E in the direction of the Hermitage, Roman buildings intersecting at right angles are situated. At the southwestern slopes, the necropolis of the city was established. On these Eastern plains of El Pueyo de los Bañales, the E-W-oriented Forum (Figure 9.3) was located and joining along in western direction, the domestic/craft centre is supposed to be situated as recent excavation have shown (Andreu Pintado et al. 2014). In 2012 excavations revealed a monumental building on top of El Pueyo, yet stratigraphically not confirmed, a temple (Lasuén Alegre and Nasarre Otín 2008; Andreu Pintado et al. 2014). Later finds suggest the hill to be used as a domestic area.

Water was assumingly supplied to the city through a hydraulic system including a natural water reservoir with dam wall situated about 300 m to the SE (Figure 9.5) and an aqueduct with more than 32 remnant pillars of 3-9 m in height following into the *villae* (Figure 9.5) running along a curvi-linear rocky crest (Viartola et al. 2013) and a cistern to the East of the Hermitage. A detailed description may be found in Viartola et al. (2013).



Figure 9.5 Assumed natural water reservoir (front) and dam of Los Bañales

From 22 March-5 April 2012, a field trip of members of the Archaeology and Regional and Environmental Sciences faculty including the Department of Physical Geography, Geobotany and Environmental Remote Sensing and Environmental Sciences visited the site. A team of the Universität Hamburg joined the team to carry out geomagnetic/electric field surveys.

9.2.2 Vegetation Patterns on El Pueyo

From visual inspection on the site surrounding El Pueyo, ruins and wall fragments are still reasonably preserved (Figure 9.12) and permit conclusions about the use of the different settlement areas. First analyses of soil chemistry and vegetation composition conducted by the Geobotany Department in spring 2012 showed distinct differences between the area surrounding the former Roman baths compared to agricultural, non-built-up areas. In the direct environment of the Roman baths, higher concentrations of Potassium (K) and plant-available phosphorus (P) were found in dried soils as well as higher electrical conductivity of diluted soils. Higher phosphate contents in dry soils may indicate long-term immission of human faecal matter during Roman settlement times as has been found for other ancient settlements to be the case (Ottaway 1984). The vegetation cover also clearly reveals compositional patterns of dominating areas of the perennial sub-shrub *Artemisia herba-alba* Asso (white wormwood) and the sweet grass *Brachypodium retusum* (Pers.). Within Spain, white wormwood is associated with nutrient- and salt-rich soils along agricultural fields whereas *Brachypodium retusum* dominates dry, nutrient-poor pastures (Peralta de Andrés 2000). The 2012 field trip revealed higher stony components and more sandy soil constituents within the *Brachypo-*

dium sites, and more open soils with higher clay- and silt-fractions within the *Artemisia* sites which may be attributed to the ancient land use (Figure 9.6).



Figure 9.6 Typical vegetation type pattern along wall remains with *Artemisia herba-alba* Asso (A) and *Brachypodium retusu* (B).

9.3 Data Sources

9.3.1 UAS Image Acquisition and Pre-Processing

On 22/03/2015, skies were clear and several flights were carried out with the md4-1000 from morning till midday as winds were less strong then. Table 9.1 list the UAS flights and camera payloads.

Table 9.1 UAS flights and camera payload used for the Los Bañales site

Flight No.	UTC	Sensor	Flight Altitude a.g.l.
#106	07:20h - 07:31h	Nikon DC3100	~ 100 m
#107	07:52h - 08:01h	Nikon DC3100	~ 80 m
#108	08:43h - 08:51h	MiniMCA-6	~ 130 m
#109	09:48h - 09:58h	MiniMCA-6	~ 115 m
#111	12:55h – 13:06h	MiniMCA-6	~ 130 m

For the derivations of an orthophoto mosaic and digital elevation model of El Puyeo and the necropolis, a 14 Mpixel Nikon DC3100 digital single lens reflex camera (DLSR)

was mounted with a digital 10 mm wide angle lens. Sensitivity was set to 800 ISO, image quality to fine JPEG as no spectral analysis was planned. Resulting images were corrected for vignetting effects.

For multispectral imagery to be used for vegetation classification and crop/soil mark studies, the MiniMCA-6 was equipped with spectral 10nm FWHM filters at 530 nm, 550 nm, 570 nm, 700 nm and 900 nm. Except for the first two flights, images were exposed automatically as smaller clouds appeared later that morning. Pre-processing included all steps described in chapter 5 including vignetting correction, image alignment to multispectral images, and where necessary histogram matching was applied for multispectral data using either grey-level reference panels described in chapter 6.2.4 or image-to-image matching.

9.3.2 GPS Data

For the georeferencing of aerial images, CDs were laid out within the study site as ground control points. Their location was defined using a differential GPS (Trimble GPS GeoXT) and 200 points per location were averaged to one measurement. Further characteristic wall remains and rocky feature locations were measured with a Garmin 60CSx device. See chapter 5 for a more detailed description of measurement devices. Data were acquired as geographic (WGS84) coordinates.

9.3.3 Ancillary Data

SITAR Plan Nacional Orthophotos were used as georeferencing base (Instituto Geográfico de Aragón 2009). The orthophoto mosaics have a spatial resolution of 0.5 m. Where no other data were available, height data was extracted from Google Earth data.

From point cloud modelling derived DEM, illumination, slopes and aspect were further computed and used as input to classifications.

Partners from the Archaeology department and the *Rheinisches Landesmuseum* surveyed building remains with a tachymeter using a locally set up orthogonal coordinate systems. Data were later transferred to UTM30N (ETRS89) coordinate system using ArcGIS 10.



The Universität Hamburg group conducted several geomagnetic point measurements from 2012 until 2015. They used a SENSYS® 5 Channel Magnetometer on the fields of specific interest. Surveyed areas are illustrated in Figure 9.7.

The Geobotany department undertook a first vegetation type classification along the SE slopes of the hill El Pueyo in 2012, where the distribution of different herbs and grasses were supposed to mirror settlement structures.

Analyses techniques applied for answering the objectives are described in the respective sections.

9.4 Methods

9.4.1 Pre-Processing: Point Cloud Modelling and Image Mosaicing

9.4.1.1 Derivation of Orthophoto Mosaic and DEM for the Roman City of Los Bañales as a Mapping Base (flight #106 and #107)

All point cloud modelling, meshing and image mosaicking was performed using Agisoft software 1.1 (AgiSoft LLC 2014) according to procedures described in chapter 5.3. To cover the whole extent of the hill and its surroundings, flights #106 and #107 were combined in point cloud modelling. UAS flights were performed by visual control of mapped areas with the help of the ground station only. This led to underestimation of some areas in the NE of the hill and to the S, W of the former Roman baths during flight #106 and #107 (Figure 9.8).

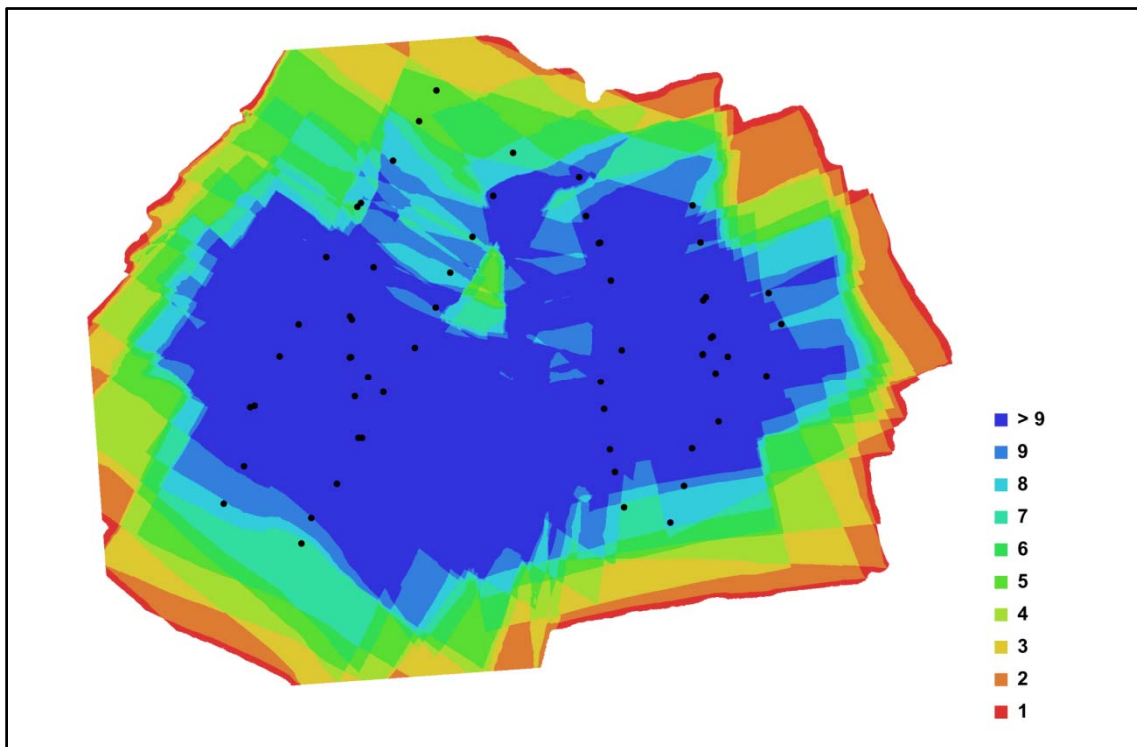


Figure 9.8 Camera locations and image overlap for UAS-DLSR flight. Numbers and colours illustrate amount of image overlap for the given location (*i.e.* projections)

The two UAS flights with the Nikon DLSR camera resulted in a total of 59 images at an average flight altitude of 88 m a.g.l to be used for image processing. For image alignment with ground markers ~ 730000 tie-points were used. The resulting point cloud was edited and meshed with a medium density and textured with image data by averaging DN. The resulting spatial resolution of the orthophoto mosaic (Figure 9.12) amounted to ~ 5 cm with a locational error in relation to GPS measurements of 3.56 pixels. Where image overlap was less dense, the digital elevation model retrieved erroneous height differences in surrounding areas and elevation values should only be analyzed at specified areas (bluish parts of Figure 9.8). The Z error therefore ranges from 0.05 to 10.69 m at maximum (Table 9.2).

Table 9.2: GCPs and their locational projection errors for flight #106 and #107

GCP#	X error [m]	Y error [m]	Z error [m]	Error [pixel]	Projections
point1	-1.21	0.93	-4.49	3.80	4
point2	0.11	-0.40	0.28	4.88	8
point3	0.72	0.13	3.14	2.31	7
point4	0.13	0.69	-0.72	1.99	4
point5	-0.78	0.41	0.05	8.27	9
point6	0.69	-1.64	3.23	1.99	10
point7	-1.06	0.93	-3.63	2.02	10
point8	-0.14	0.26	-4.16	6.04	10
point9	-0.55	0.24	-1.56	4.74	15
point10	0.60	1.52	10.69	10.93	7
point11	1.01	-0.74	2.39	7.46	6
point12	-0.07	0.32	-3.00	5.71	11
point13	0.03	-0.63	-3.22	3.19	13
Total	0.67	0.82	4.05	5.43	114

9.4.1.2 Derivation of Multispectral Orthophoto Mosaics for El Pueyo

Analogous to flight #109, photos collected with the MiniMCA-6 were modelled to a point cloud and georeferenced with the GCPs laid out in the field. About 44500 tie points were used and the overall RMSE was 0.51 pixel/0.21 m, the Z error amounted to 0.20 m, however, the respective DEM was not further used. Spatial resolution was set to 7 cm. As the orthophoto mosaic of flight #106_107 was the largest and had been selected as reference, the orthophoto mosaic #109 was further rubbersheeted onto this reference to increase accuracy where image overlap was scarce for that flight. Figure 9.9 shows image projections for flight #109.

Table 9.3 GCPs and their locational projection errors for flight #109 (Projections: indicates number of images where GCP could be located)

GCP#109	X error [m]	Y error [m]	Z error [m]	Error [m]	Error [pixel]	Projections
1	-0.030	0.010	-0.001	0.032	0	1
8	0.027	0.002	-0.056	0.062	0.467	5
10	-0.032	-0.003	0.098	0.103	0.579	5
11	0.149	0.082	-0.469	0.499	0.237	2
12	0.001	0.003	-0.021	0.021	0.761	4
13	0.001	-0.006	0.023	0.024	0.140	3
Total	0.064	0.034	0.198	0.512	0.512	20

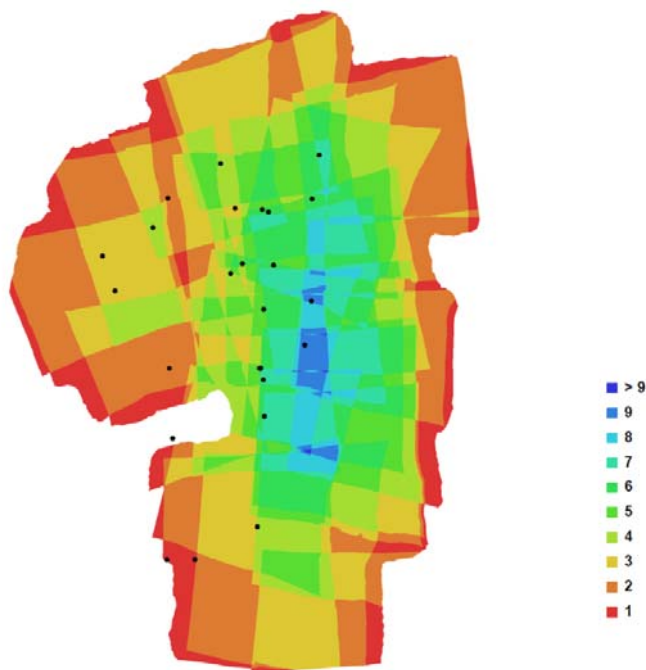


Figure 9.9 Camera locations and image overlap for orthophoto of flight #109

9.4.1.3 Derivation of Multispectral Orthophoto Mosaics for Cultural Pattern Reconnaissance in Agricultural Fields (#108 and #111)

Similarly, image alignment, point cloud modelling, meshing to medium resolution and texturing to orthophoto mosaics was carried out for the agricultural fields to the E (#108) and South of El Pueyo (#111) (Figure 9.10). As already mentioned, here, histogram matching was applied to imagery. For the eastern field due to image caption geometry, not one single model was able to cover the respective field. Two separate models were therefore processed which were later combined to one orthophoto mosaic by image rectification using a 1st order polynomial transformation and bilinear interpolation, reference points being retrieved from the Nikon mosaic and SITAR web server (<http://sitar.aragon.es/geoinformacion.jsp>, access date: 22/06/2012). Prior to that histogram matching was applied to obtain comparable radiometric data.

Table 9.4 Point cloud modelling and resolution parameters for multispectral data for the agricultural fields in the E (#108) and S (#111)

	#108 S	#108 N	#111
No. of images	16	4	11
tie-points	31968	1399	2611
Ground resolution	0.06	0.07	0.03
Error [pixel]	0.96	1.66	1.33

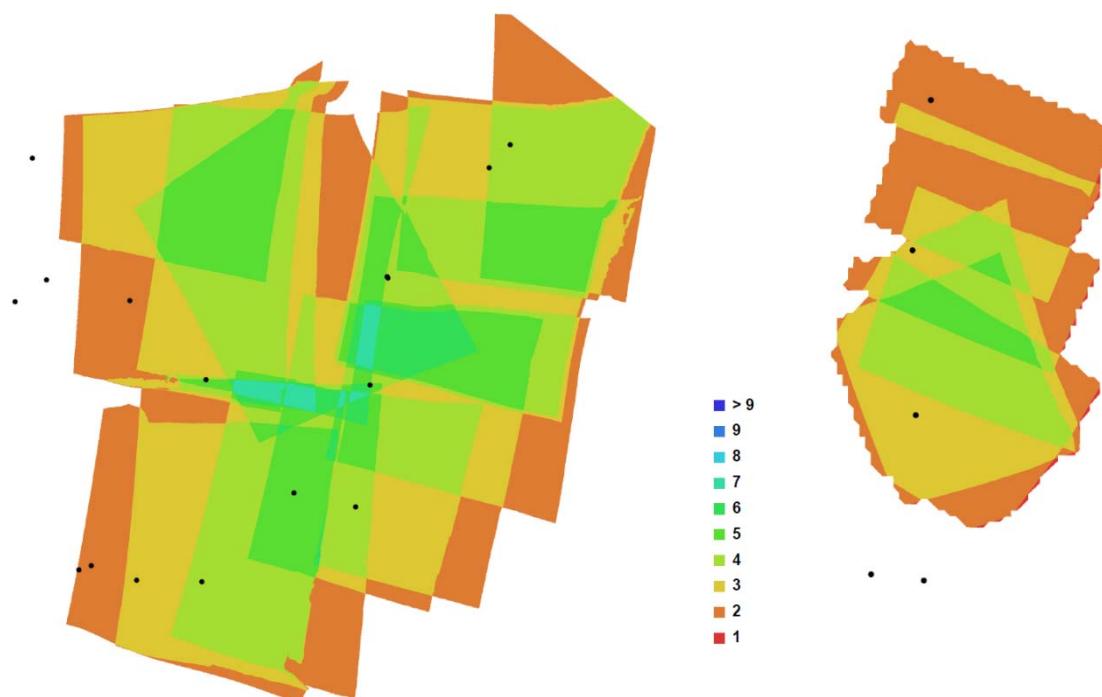


Figure 9.10: Camera locations and image overlap for orthophoto of flight #108 (left) and flight #111 (right)

For the southern field, only parts explored by the Universität Hamburg team using geomagnetic prospection were further analysed. The mesh model was textured by using the mosaic option and a rough georeferencing was carried out within Agisoft (Table 9.4) then the data was rubbersheeted to match the Hamburg prospection data using the SITAR orthophotos and the Nikon orthophoto mosaic reference.

Table 9.5 GCPs and their locational projection errors for flight #111

GCP#111	X error [m]	Y error [m]	Z error [m]	Error in pixels	Error [m]	Projections
point 24	10.844	-35.465	76.231	1.052	84.773	2
point 25	29.462	3.951	78.203	8.841	83.662	2
point 26	9.144	18.187	-6.793	0.000	21.459	1
Total	18.879	23.124	63.174	5.631	69.872	5

9.4.2 Feature Enhancement

Prior to land use classification, several feature enhancements were carried out. As the flight acquisition time at the end of March 2012 was less than ideal due to the dry preceding winter, the herbal vegetation was just starting to get active, and herbs still appeared quite dry. Several vegetation indices were computed to enhance the weak differences in vegetation types: NDVI, NDVI_{700nm, 530nm}, and TCARI (see chapter 7.4 for index definition).

Although very similar in DN, *Artemisia* sites (Figure 9.6, Figure 9.15) showed quite a different texture than other vegetated sites due to substrate/vegetation/shade components, thus inclusion of texture measures promised further separation capability. Several texture measures and filter sizes, provided by digital image processing (DIP) software and by Hass (2015), were tested. As it is out of scope to present all of them here, only the optimal texture measures are presented here: Texture was analysed by means of a 9x9 pixel filter operation calculated from the grey-level co-occurrence matrices (GLCM) of the 2nd principal component (PC) of the multispectral data, as it showed the highest variance in relation to vegetation features:

$$\begin{array}{l} \text{Cluster shade (CLS)} \\ \text{(Haralick et al. 1973;} \\ \text{Conners et al. 1982)} \end{array} \quad CLS = \sum_{i=1}^{N_g} \sum_{j=1}^{N_g} ((i - \mu) + (j - \mu))^3 P(i, j) \quad 10.1$$

$$\begin{array}{l} \text{Cluster prominence (CLP)} \\ \text{(Conners et al. 1982)} \end{array} \quad CLP = \sum_{i=1}^{N_g} \sum_{j=1}^{N_g} ((i - \mu) + (j - \mu))^4 P(i, j) \quad 10.2$$

$$\begin{array}{l} \text{Cluster coherence (COH)} \\ \text{(Haralick et al. 1973)} \end{array} \quad COH = \sum_{i=1}^{N_g} \sum_{j=1}^{N_g} \frac{(i, j) P(i, j) - \mu_x \mu_y}{\sigma_x \sigma_y} \quad 10.3$$

With:

- N_g : Number of quantization levels
- $P(i,j)$: entry (i,j) in the normalized and symmetrical GLCM
- μ : GLCM mean
- σ : GLCM standard deviation
- μ_x, μ_y : marginal column and row means
- σ_x, σ_y : marginal column and row standard deviation.

For a detailed discussion please refer to Haralick et al. (1973), Haralick (1979), Connors and Harlow (1980), Connors et al. (1982), and Hass (2015). The filter size was chosen smaller than the extent of an *Artemesia* cluster size of roughly 15 pixels. As image input the second principal component was chosen as it showed maximum difference in vegetation DN from soil substrate.

To decorrelate bands and to remove noise from the input data, a principal component analysis (Richards 2013) based on the correlation coefficient between bands was carried out in ENVI for the following input bands:

- A) lb109-orthophoto mosaic bands, NDVI_{700nm,670nm}, TCARI, texture measures (CLS, CLP, COH), and
- B) lb109-orthophoto mosaic bands, NDVI_{700nm,670nm}.

9.4.3 Land Cover Classification Using Support Vector Machines

The land use classification was then performed using SVM as they have been found to often outperform alternative (supervised) classification algorithms and are able to handle feature spaces of higher dimensionality. Its advantages are, that the SVM classifier is independent on the data distribution, and performs well in heterogeneous land covers with limited training data samples: only few training pixels are required to determine the support hyperplane (Melgani and Bruzzone 2004; Mountrakis et al. 2011).

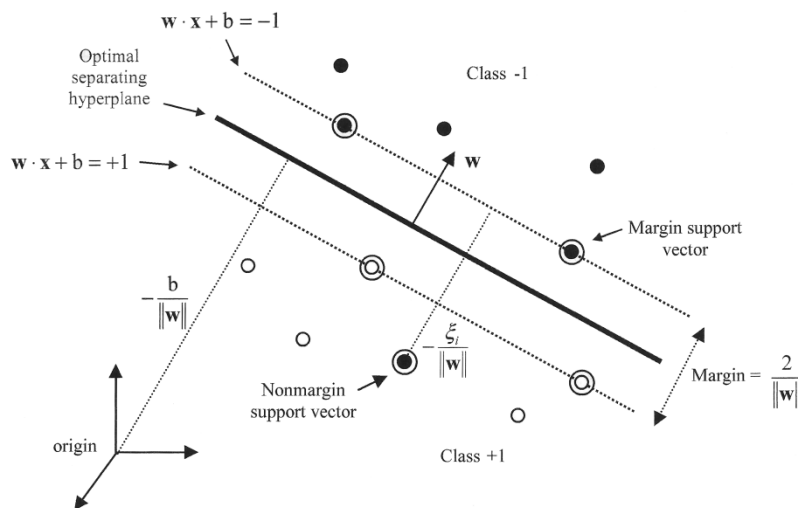


Figure 9.11 Support Vector (Melgani and Bruzzone 2004, p. 1781)

For each land cover class, a vector (Figure 9.11) is defined in the d -dimensional feature space. SVM searches for maximizing the distance between training samples (linear sur-

face). Two marginal hyperplanes maximizes the margin around a separating hyperplane between the training samples by the use of a subset of special training samples, the so-called support vectors (Richards 2013, p. 226f).

The decision-rule is then a discriminant function dependent on the hyperplane:

$$f(x) = w \cdot x + b \quad (10.1)$$

With:

w: vector

b: bias

A pixel is then a member of class 1 if $w \cdot x + b \geq 1$. w and b are estimated to obtain

$$y_i(w \cdot x_i + b) \geq 1 \quad (10.1)$$

Here, a non-linear SVM with a radial kernel method was selected for defining the hyperplanes of higher order PC space (see Melgani and Bruzzone 2004; Richards 2013, p. 230f for a detailed description).

$$\kappa(x_i, x) = \exp(-\gamma \|x_i - x\|^2) \quad (10.1)$$

For the estimation of the optimal kernel parameters, the penalty cost parameter C and γ , a parameter which is inversely proportional to the broadness of the Gaussian kernel, a grid search was guided by the cross-validation accuracy. An exhaustive searching was carried out using the hyperparameter optimization technique of a grid search:

- Cost parameter C [2, 4, 8, 16, 32, 64, 128]
- γ [0.312, 0.0625, 0.125, 0.25, 0.5, 1]

Training pixels for input were digitized with the help of the original multispectral bands and the Nikon orthophoto mosaic and resulted in a training set of $n = 904$ pixels. Care was taken to digitize sample sizes about ~ 10 times larger than required number of LC classes. A 5-fold cross-validation was used to produce an unbiased estimate of classification accuracy and from the resulting five images' pixel values the most frequent land cover was selected for the respective location. Additionally, during the classification process, the variances of the 5-fold cross-validations were used to optimize training samples for misclassified areas. Classification accuracy was computed for one classifi-

cation output including overall accuracy, error of omission (Richards 2013) and area-weighted κ (Pontius and Millones 2011).

9.5 Results

9.5.1 Base Map for Analysis of Settlement Patterns at El Pueyo and Surroundings

One of the aims of this work, was to obtain a map base for excavation and settlement structure surveys (Figure 9.12).

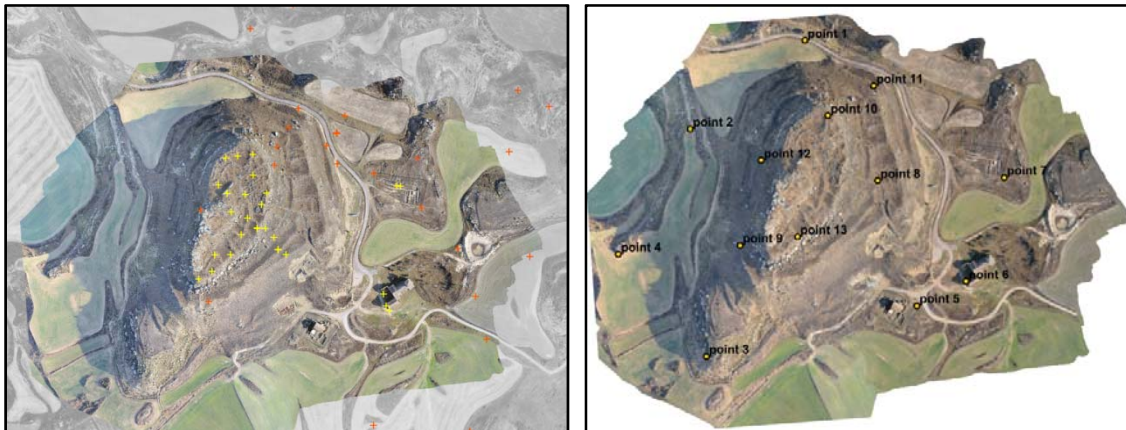


Figure 9.12 GPS measurements (red cross: Trimble GPS, yellow cross: Garmin GPS) and GCP for orthophoto-productions (RGB: bands 1,2,3)

As no other base map of a locational precision within centimetre range was available for further corrections, the resulting orthophoto was accepted as the base map for this area. The retrieved digital elevation model has a 20 cm spatial resolution (Figure 9.13).

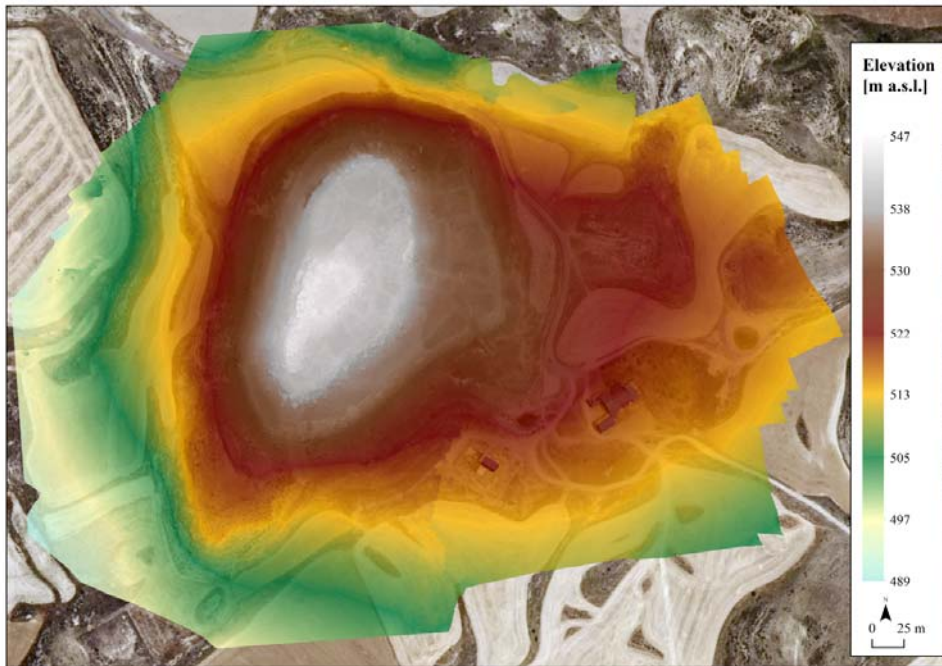


Figure 9.13 Digital elevation model of the study site as retrieved from DSLR UAS imagery (background data: SITAR orthophoto mosaic)

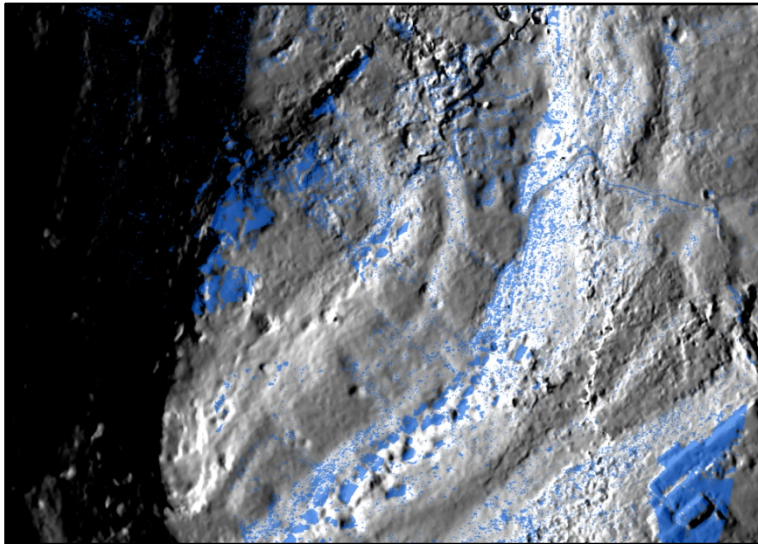


Figure 9.14 Hillshade of El Pueyo highlighting former settlement structures

Derived data, like hillshade (Figure 9.14), together with land cover data (here rocks) may help to map settlement structures.

9.5.2 Vegetation Type Classification as an Indicator for Former Land Use

The second aim was to obtain a vegetation composition/land cover map of the Pueyo and its surroundings as an indicator for potential former possibly Roman settlement structures in addition to wall structures and settlement remnants. The focus lies on the retrieval of the described *Artemisia* versus Non-*Artemisia* sites and settlement patterns.

The NDVI_{700nm,530nm} (Figure 9.15: top right) and TCARI (Figure 9.15: bottom right) best depicted DN differences between *Artemisia* sites and surrounding vegetation. This index was therefore stacked to the orthophoto for following analysis.

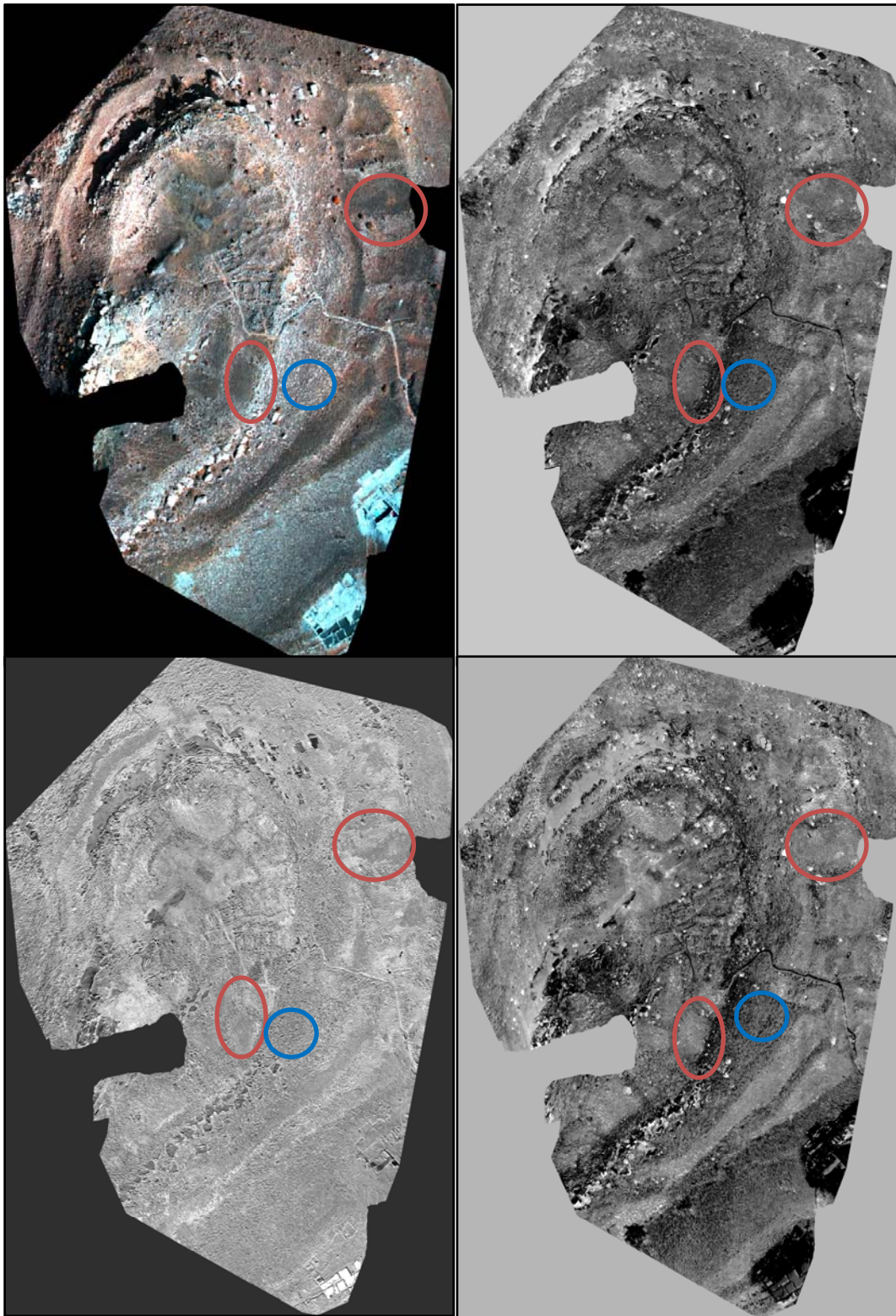


Figure 9.15 Multispectral orthophoto of flight 1b109 (RGB: 900, 700, 670 nm) top left, NDVI_{900nm,670nm} top right, NDVI_{700nm,530nm}: lower left, and TCARI (lower right. Red circles known *Artemisia* distribution sites; blue circles: other grassy/herb species)

Figure 9.16 shows the texture measure COH and illustrates the areas of lower texture for *Artemisia* sites.

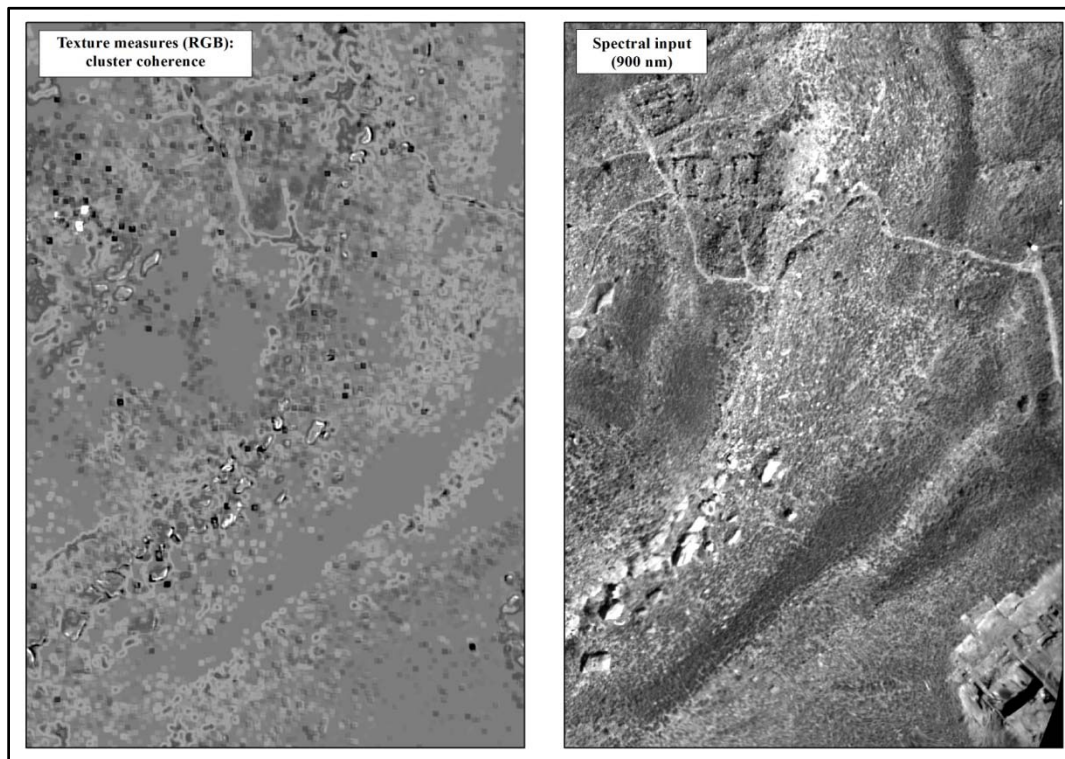


Figure 9.16 Differences in DN texture for *Artemisia* sites (homogeneous greyvalues in cluster correlation) and more grassy/stony environments in between (9x9 filter)

The PC transformation resulted in components (Figure 9.17) associated with different features and land cover classes for the A) input variant revealed that the PC6 is mostly characterized by periodic striping introduced by data acquisition and mosaicing errors and was therefore deleted from the image for further analysis.

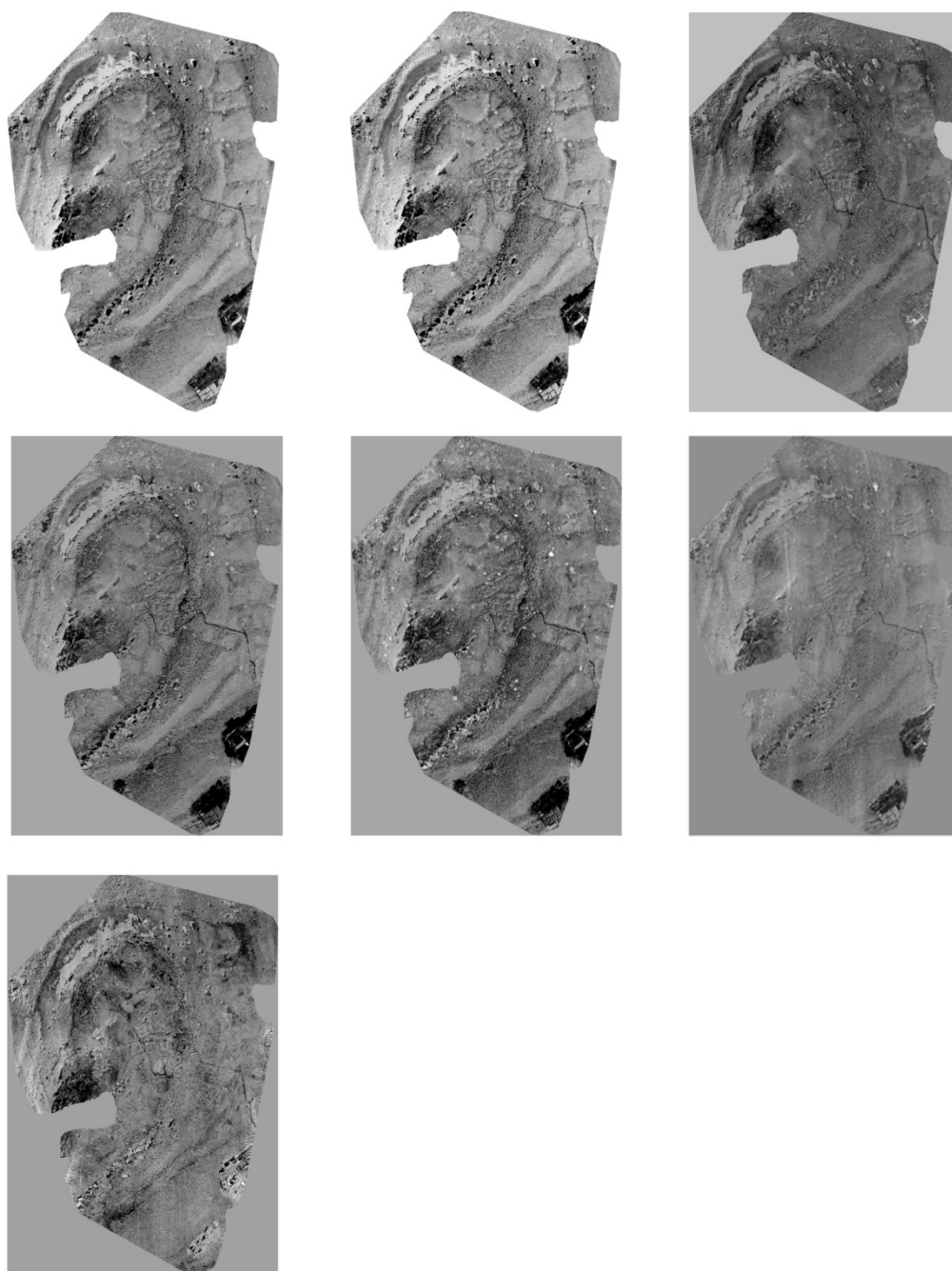


Figure 9.17 Principal components computed from correlation matrix of the multispectral input bands (1-6) and $NDVI_{700nm, 530nm}$ (PC1-7 from top left to bottom): PC 6 shows noise

Figure 9.18 shows the resulting land cover classification of variant A) the PC bands with NDVI, TCARI and texture measures and variant B) additionally including texture information. Selected kernel parameters are given in Table 9.6. The variant B), *i.e.* without texture measure, retrieved the best representation of the *Artemisia herba alba* site within the LCC (Table 9.7, Table 9.8) and was therefore chosen as the final land cover map.

Table 9.6 Selected radial kernel parameters for cross-validations in SVM LCC

Variant A	CV1	CV2	CV3	CV4	CV5
Γ	0.12500	64.00000	0.12500	8.00000	0.03125
C	128.00000	0.06250	16.00000	0.25000	16.00000
Variant B					
γ	0.25000	4.00000	0.25000	32.00000	0.50000
C	2.00000	0.03125	128.00000	0.12500	4.00000

Table 9.7 Area-weighted confusion matrix for land cover classification by SVM of multispectral orthophoto mosaic including texture for CV5 (variant A)

Training LC	Validation								Sum	User's accur.
	Rock	Soil	Excavation	Plastic foil	Pa veg.	Scarce veg	<i>Artemisia</i>	Shade		
Rock	0.108			0.002					0.110	98
soil bright		0.207							0.207	100
Excavation			0.009			0.000			0.009	100
Plastif foil				0.000		0.000			0.000	100
Pa veg.					0.008				0.008	100
Scarce veg		0.048			0.048	0.242	0.016		0.356	68
<i>Artemisia</i> .						0.012	0.242	0.012	0.265	91
Shade								0.040	0.040	100
Sum	0.108	0.255	0.009	0.002	0.057	0.254	0.258	0.051	1	
Producer's accuracy [%]	100	81	100	15	14	95	94	78		85

The overall accuracy retrieved for variant A) was 0.85, with an area-weighted κ of 0.82 for the best SVM land cover classification.

Table 9.8 Area-weighted confusion matrix for land cover classification by SVM of multispectral orthophoto mosaic without texture for CV5 (variant B)

	Validation									User's acc.
LCC	Rock	Soil	Excavation	Plastic foil	Pa vegetation	Scarce veg	Artemisia	Shade	Sum	
Rock	0.331			0.000					0.110	100
soil bright		0.238							0.207	100
Excavation			0.018			0.000			0.009	100
Plastif foil				0.003		0.000			0.000	100
Pa veg.					0.025				0.008	100
Scarce veg		0.018			0.009	0.117	0.000		0.356	81
Artemisia						0.006	0.061	0.003	0.265	88
Shade								0.124	0.040	100
Sum	0.331	0.256	0.018	0.003	0.034	0.122	0.061	0.127	1	
Producer's accuracy [%]	100	93	100	100	74	95	100	98		92

The overall accuracy for variant B) was 0.92 and the area-weighted κ 0.89.

Although less accurate for the sparsely vegetated environments (Table 9.8, the LCC depicts quite well the *Artemisia herba-alba* Asso sites using the noise-subtracted PC and NDVI_{700,530nm} data (see also the orthophoto compared to LCC in Figure 9.19). The species show a clumped occurrence in between sink areas within the wall fragments along the plateau and the terraces down to the road. The separation from *Brachypodium retusum* was not followed any further, as the phenology at image acquisition was not ideal and grasses not well separable from other shrubs and (reddish) soil substrates. However, once proven that the *Artemisia* distribution is not caused by alleopathy, the pattern may further be investigated by archaeologists with regard to former use. Classification accuracy surely be much smaller if field-data had been available at that detail.

The LCC including texture (Variant A)) shows overestimation of *Artemisia herba alba* sites, especially on the central plateau and to the SE. On the plateau, image overlap was small and the image therefore slightly unfocused. Texture measures therefore indicate low values for this area.

The texture measures do introduce spatial artefacts (Figure 9.16 left) for spectrally contrasting small objects such as rocks. Here, object-oriented LCC would yield better classification results for these types of highly structured land covers. Another potential LCC scheme could use a binary LC classification for *Artemisia* sites in relation to other LC, using the low texture values in the COH band to mask out only potential *Artemisia* sites.

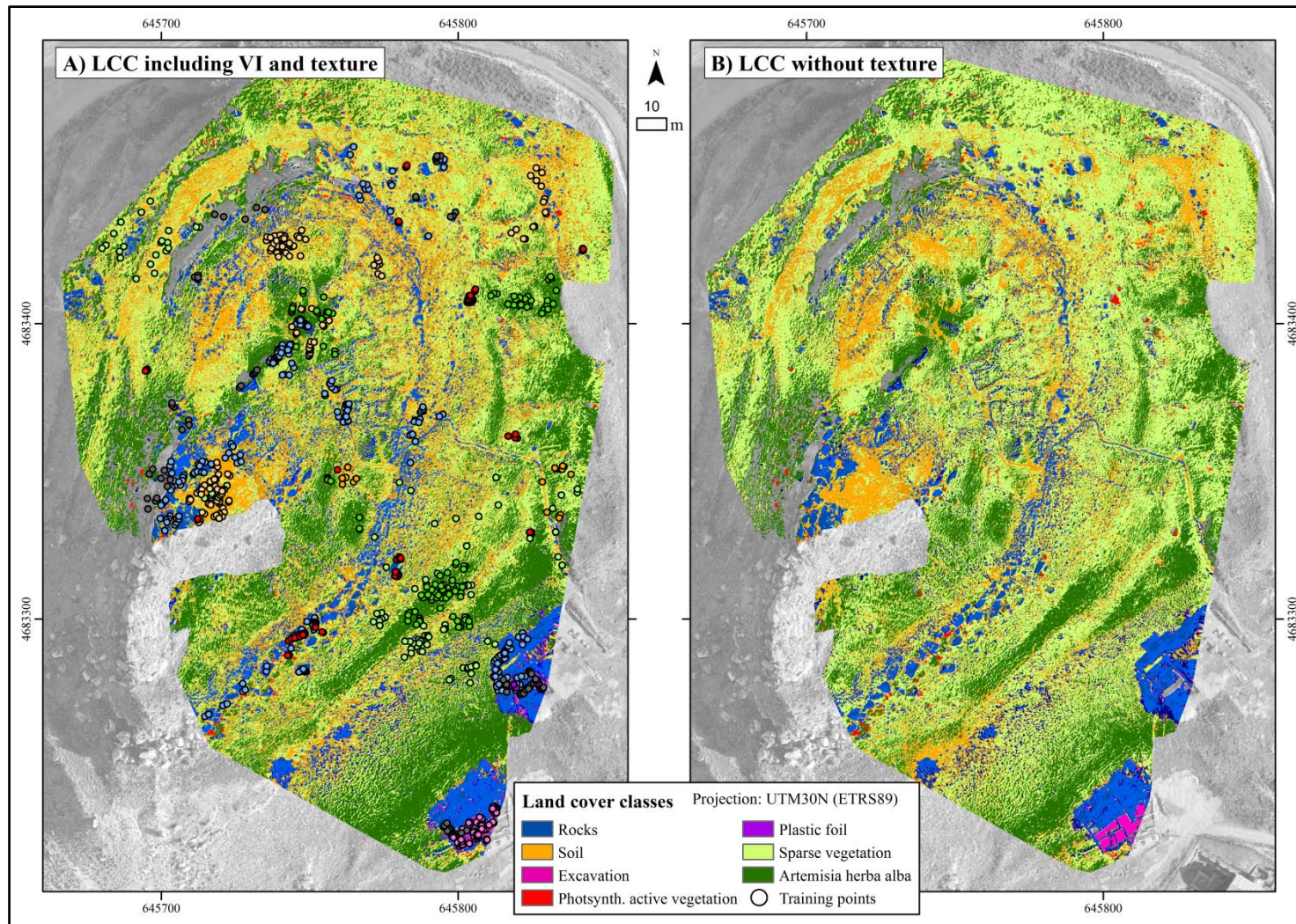


Figure 9.18: Land cover classification for vegetation types using multispectral image-derived PCs, VIs and texture

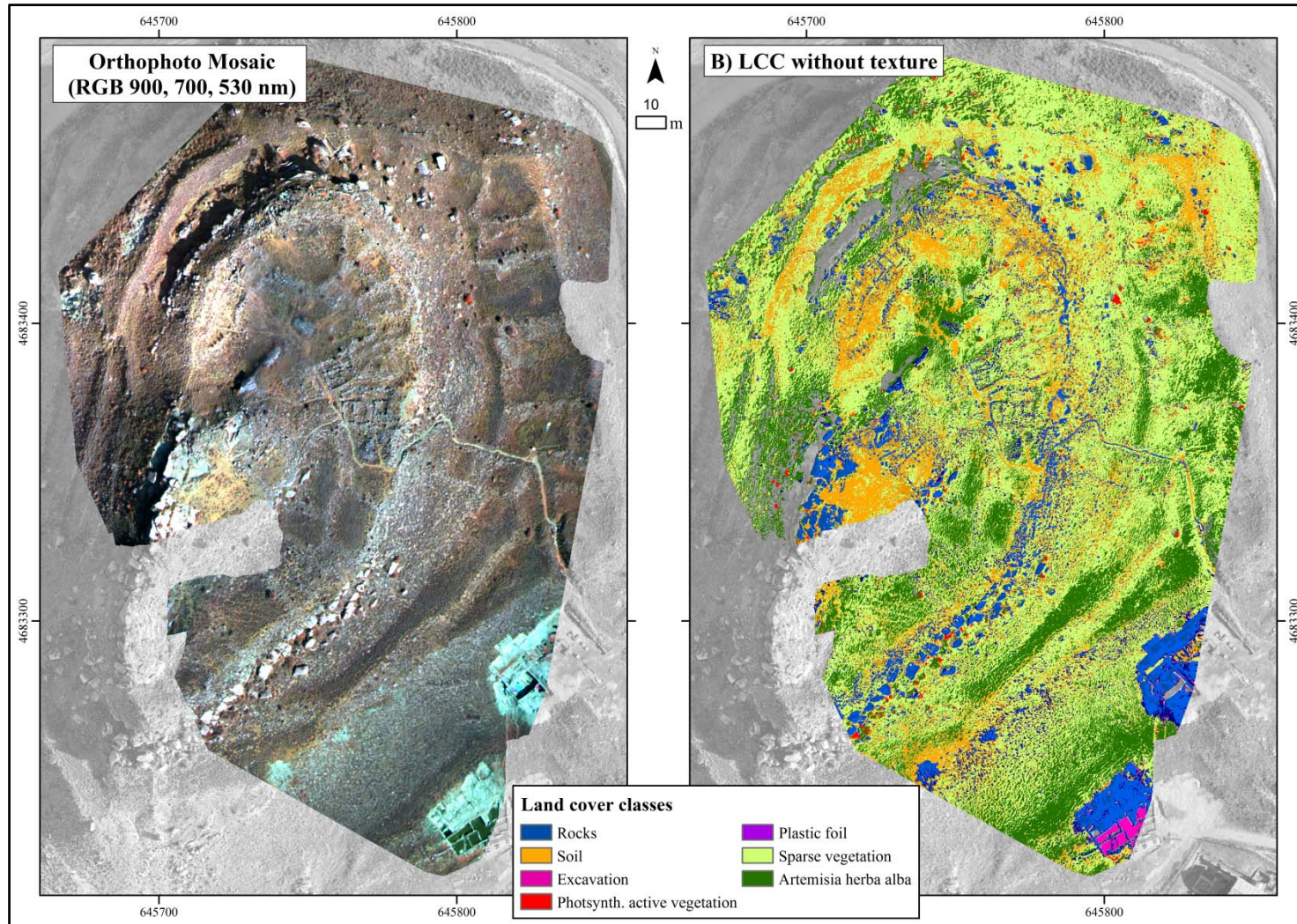


Figure 9.19 Orthophoto mosaic (left) and land cover classification result (right)

9.5.3 Detection of Cultural Heritage Patterns in the Eastern and Southern Vicinity of El Pueyo

Due to early season and crops not having developed to full canopy cover, reconnaissance of archaeological settlement features in the field E of El Pueyo (flight lb108) are difficult to obtain spectrally. The Universität Hamburg group kindly provided the interpolated geomagnetic data for comparison (Figure 9.7), and features may be derived visually on the UAS data, yet it had not been possible to retrieve them by DIP.

From the geomagnetic prospection data (Figure 9.20), several linear features were found at location A, B, and C. For the detected features at location A, a subsurface three-walled feature had been found. At the smaller plot B, vegetation just about emerged and therefore, no crop marks could be detected. In the multispectral data (Figure 9.20), these are hardly to be traced. For area C, however, a linear feature running NNE-SSW may be just detected in Figure 9.20 which was additionally visible in the NDVI image (Figure 9.21).

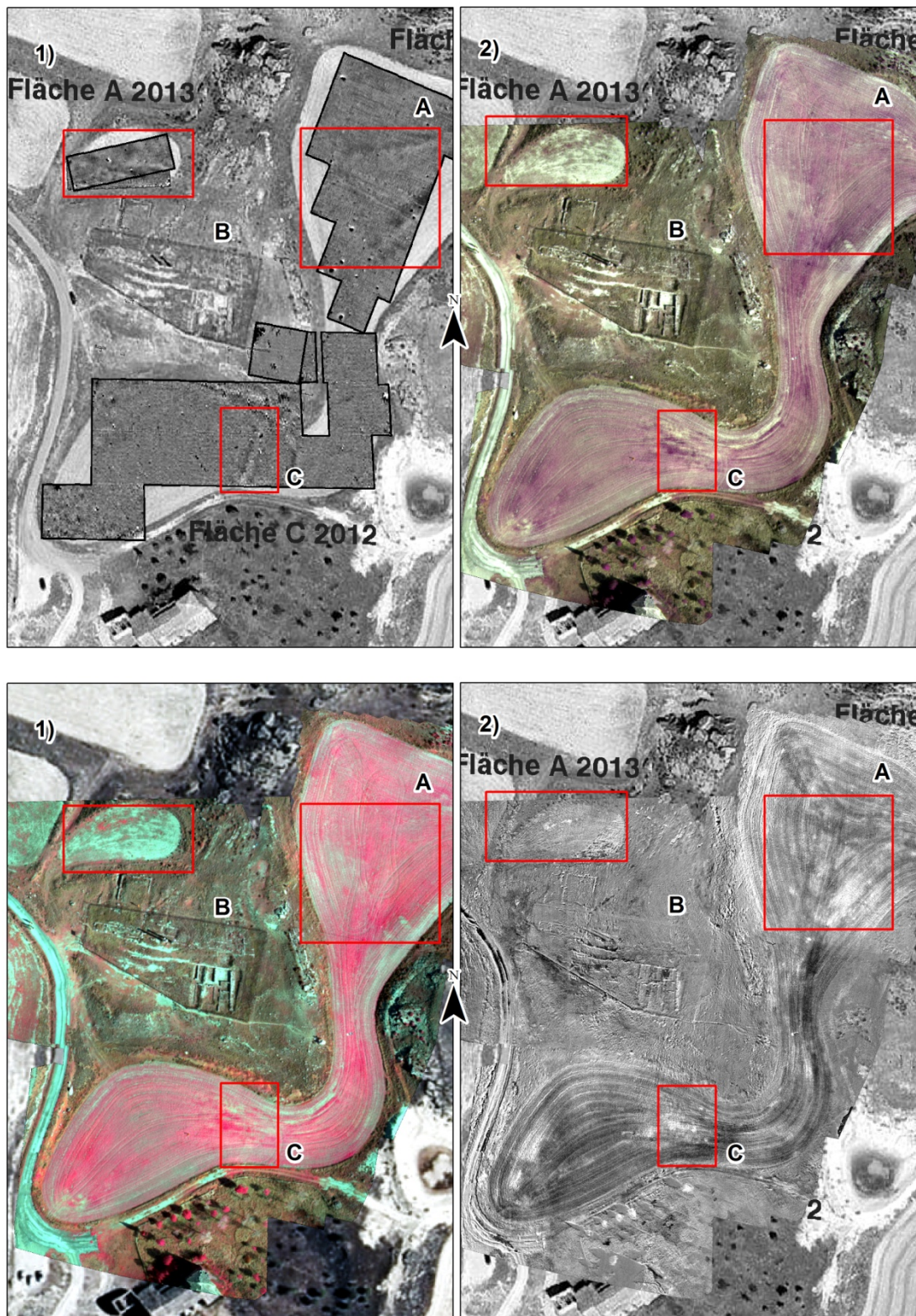


Figure 9.20 Reconnaissance for the agricultural field to the E of El Pueyo: Top left: results of geomagnetic survey (Prof. Dr. Seifert & team, Universität Hamburg) compared to spectral data (RGB 700, 670, 570 nm) on the right. Bottom row left shows the spectral data with (RGB 900, 700, 570 nm) and on the right the fifth principal component.

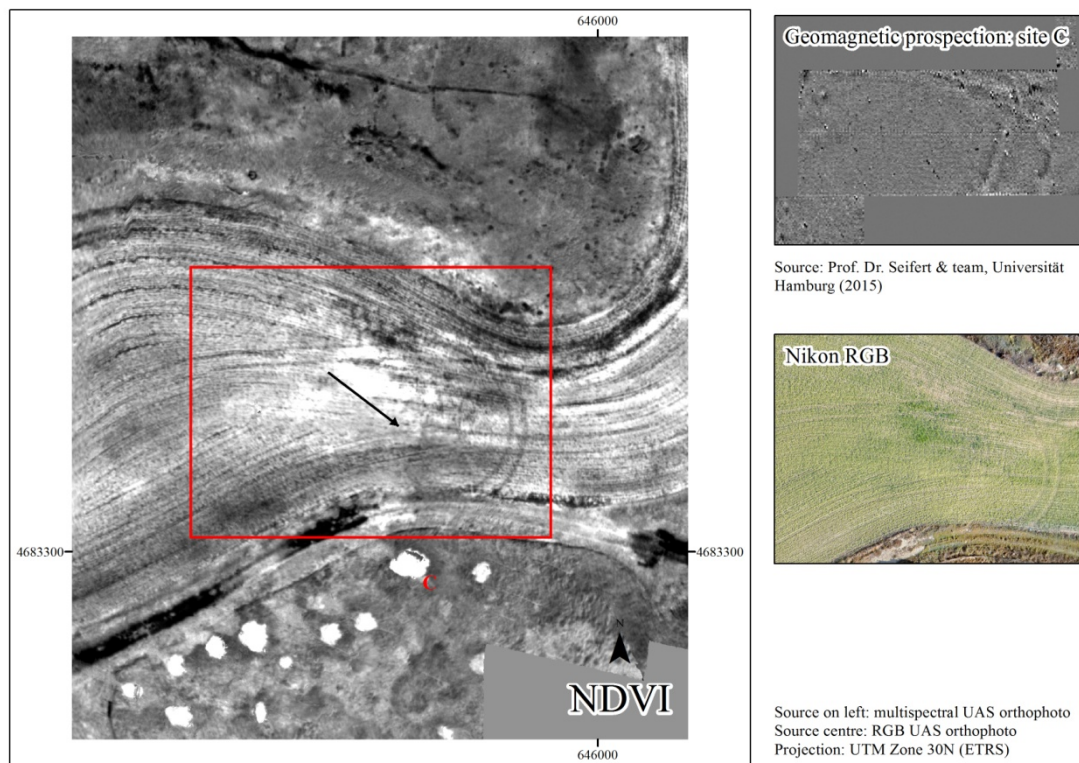


Figure 9.21 NDVI image of agricultural field E of El Pueyo.

The other field analyzed was situated to the SE of El Pueyo, and similar results were found. Despite the late and scarce crop development, some crop marks or other potential tracers of subsurface features are detectable by means of feature enhancement (PCA) and visual interpretation of multispectral data (Figure 9.22).

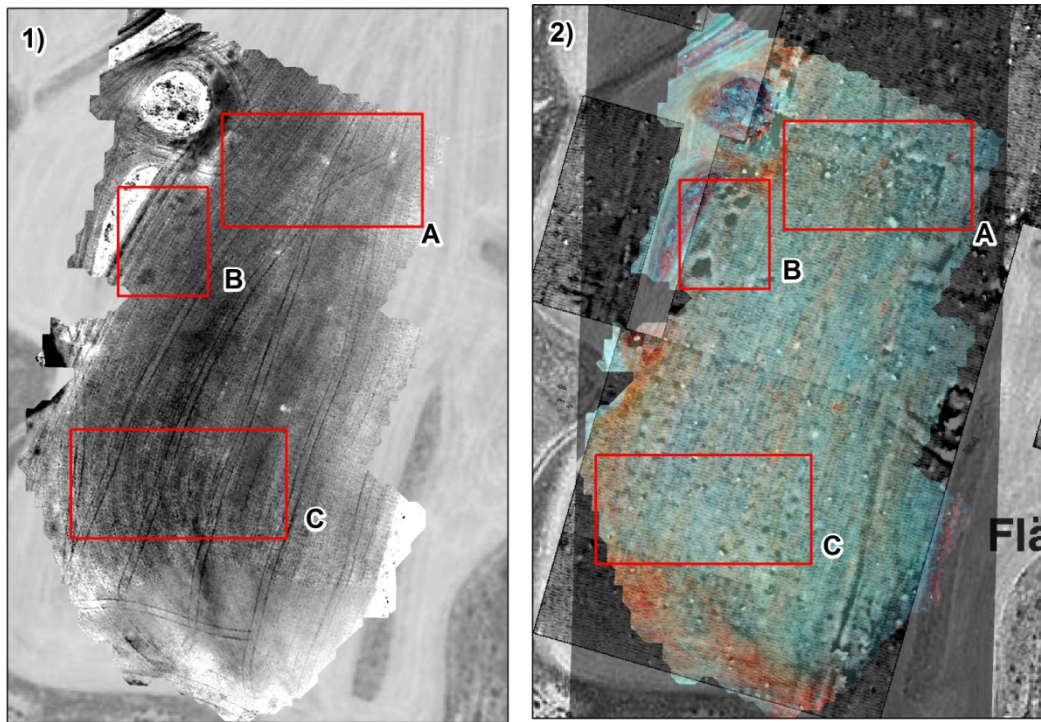


Figure 9.22 Crop marks found in agricultural field SE of El Pueyo. Left: PC2, right: geomagnetic data (Prof. Seifert and team) with overlaid transparent multispectral image (RGB 900,700,670 nm).

Again, the late crop development did not help to highlight potential archaeological features and signals are rather weak. Yet, the wall or road structure visible in rectangle A (Figure 9.22) is just traceable by PC2. The darker marks in rectangle B are also found in the 2015 magnetometer measurements reinforcing the assumption that the low magnetic values (dark areas) are a former ditch area or potential building fundamentals. The regular pattern of low magnetic values in rectangle C is not found for the aerial imagery.

9.6 Summary

As was shown by this study, by other publications (Verhoeven 2009; Verhoeven 2012, Williams 2012), and the manifold increasing flight requests for UAS pilots, Vis/nIR remote sensing imagery has been emerging as a cheap and ad-hoc information source for large-scale studies within the field of archaeology. Applications range from simple visual surveys to map excavation progress to photogrammetric surveys and retrieval of 3D objects to archaeological reconnaissance. In this study, visual data (Nikon camera),

were utilized to retrieve an orthophoto mosaic and DEM as a reference map for future work in that area and derived data (hillshade, slope, land cover material, etc.) support this kind of work. Due to high wind speeds, data was mostly acquired in the morning which resulted in a considerable amount of shadow in the image, impeding DIP within these areas. As image acquisition had to be prosecuted within a couple of days for a large area, flights were carried out manually, leading to scarce image overlap in some areas. These introduced artificial features within the imagery impeding automatic feature detection. Another noise source introduced in the imagery, are stripes introduced by the multispectral MiniMCA-6 and its progressive shutter and by platform vibrations during the flight. These could be eliminated to some extent by feature space transformations, in this case PCA, where often noise is mapped to one or two principal components which may then be eliminated for further processing.

A land cover map for the hill El Pueyo has shown the potential to provide further information about former land use if the assumption that *Artemisia herba-alba* is indeed an effect of ancient phosphorus input. The plant type areal dominances may, however, also be contributed to allelopathy used by the respective species (Escudero et al. 2000) or small-scale differences in soil constituents. This question can only finally be answered after more detailed field and plant pot comparative studies which up until now could not be performed but are planned for the future.

Aerial reconnaissance of cultural heritage patterns has also shown potential to indicate former land use features, although phenology of crops lacked behind the seasonal mean due the preceding very dry winter.

9.7 Conclusions

Today's spread of light-weight, easy-to-use small UAS provide archaeological explorations with almost immediately ready-to-use systems for low-cost image acquisition. As the work at Los Bañales has shown, for a successful archaeological data mining of UAS imagery, well-planned campaigns support reconnaissance. At the beginning, flight plans regarding sufficient image overlap should be established. Even if today's SfM-software takes advantage of slant-range imagery and uses self-calibration to builds reasonably accurate point cloud models (Rock 2010; Franjic and Bondeson 2014), total site coverage with high image overlap, and possibly differing viewing angles provide better quality orthophotos and DEMs to obtain centimeter-range pixel resolution for orthophoto mosaics (Nex and Remondino 2014). Furthermore, the acquisition of accurate ground

control points using advanced DGPS technology is essential to anchor retrieved 3D point models for decimetre/centimetre accuracy.

Image quality steers object recognition, demanding well-planned data acquisition in relation to

- choice of season, phenology, and time of the day,
- selection of appropriate sensors (spectral range, radiometric resolution),
- acquisition of mandatory ancillary data (GCPs, reference spectral measurements, field surveys)
- image pre-processing to correct for noise, radiometric and atmospheric effects, precise geopositioning, followed by
- adequate image-processing (Lasaponara and Masini 2012b).

Good practice guides for UAS surveys may be found online and support archaeological work (Gray 2009).

Minimal growth differences in height and vitality introduce – depending on sun-sensor-target geometry – different patterns in plant and crop signals, which may then be enhanced by DIP algorithms (*e.g.* texture measures, feature space transformations). Yet, visual interpretation still often beats DIP processing in pattern recognition.

In relation to sensors, multispectral, hyperspectral, thermal or even microwave sensors outperform human vision of spectral features. Yet, small RGB digital cameras will persist as they are cheaper and more ready to use with small UAS. They may be equipped with special filters to extend/limit the spectral signature to the nIR, or a set of configurable standard industry C-mount cameras may be equipped with spectral filters, thus extending pattern recognition likelihood of hidden archaeological features.

10 Summary and Discussion

The main aim of this work was to examine the potential use of small (quadrocopter) UAS for agricultural crop observations and archaeological applications. The discussion first describes the state-of-the-art pre-processing from image acquisition, radiometric calibration and correction to geometric processing to obtain orthophoto (mosaics) and DEMs. Finally, the findings of the agricultural and archaeological applications are discussed.

Drones have knocked in to the field of environmental remote sensing since the millennium like satellites have at the end of the last century. As chapter two has illustrated, UAS development is still increasing and new platforms and sensors continue to be developed. Applied at mostly larger scales (local to small regions), their utilization is still widening for nearly all environments. Their benefit first of all lies in the small costs compared to aircrafts and manned aircraft missions. Up until now, UAS pilots did not require licenses in Germany, and after a short training period are able to fly operationally. The other big advantage is the less strong importance of weather conditions. UAS are generally flown well underneath cloud level (*i.e.* < 100-300 m a.g.l.) and if precise radiometric correction of greylevels is of subordinate importance, they fastly deliver overviews over specific sites of interest, helping, for example, viticulturists to see areas of nutrient or water stress.

The limitations are first to be searched in allowed platform take-off weight. In Germany, general ascent permits are restricted to UAS with a take-off weight of < 5 kg, which is also limiting the weight of sensors. Camera miniaturization though, will surely help to provide advanced sensors at lower costs than are available now. For small UAS, and especially rotary-wing systems, batteries still restrict flight times hindering surveys of larger sites where fixed-wing UAS still are the platform of choice. Chapter 2.2 summarises today's UAS categories, and gives information about platform types in detail. Rotary-wing systems such as the md4-1000 quadrocopter, offer the advantage of vertical take-off and landing and thus are independent of runways and may hover over sites of interest, thus excluding forward-motion blur.

The sensor used for this study was a six-band multispectral camera (Tetracam MiniMCA-6) which, at the onset of this study, was the sensor with the best spectral resolution to be found within the <1 kg camera weight department and could be equipped with customized filters of variable FWHM. Furthermore, the study showed the

use of broadband thermal cameras in differentiating crop status, and the use of off-the-shelf digital slant range cameras the generation of orthophoto mosaics as map references. Other sensors find widening applications, too, but were out-of-scope in the context of this work and are solely listed in chapter 2.

Apart from these technical limitations, another restricting factor to the use of UAS may be the national airspace regulations. Some European countries, after a first open policy of the use of UAS are now backpedalling and requesting pilot training and health checks impeding application of technology as Pablo Zarco-Tejada asserted during the 9th EARSeL's SIG Imaging Spectroscopy Workshop in Luxembourg 2015. No-fly zones are being identified to protect sites of special security (*e.g.* government building) after UAS flying without permit into the park of the White House, within the city of Paris or London parks. Clearly, the expanding technology has overrun regulating bodies. In 2011, Europe's aviation bodies published a European strategy on civil UAS (EC 2012) and set up a road map and RPAS steering group for civil use of these systems, seeking secure integration into European airspace, developing an aviation regulation framework at national and EU level and their coordination. UAS will only be allowed into non-segregated airspace once they communicate their location to air traffic control either by constant broadcasting or by request. Mike Lissone, the RPAS ATM integration programme manager of Eurocontrol, spoke of over 1.2 million commercial RPAS worldwide. Equipping these with Automatic Dependent Surveillance-Broadcast (ADS-B) would soon bring the Universal Access Transceiver (UAT) down on their knees as they would not be able to handle that amount of requests and answers, said Lissone during the RPAS Workshop in the Netherlands, June 2015. Standards for integration of RPAS in European airspace are to be developed until 2022 (van Wagenen 2015).

However, general ascent permits are granted if flight altitude is below manned aircraft (different altitudes are used in different countries) and liability insurance has been procured. Then police/controlling authority on-site need to be informed beside the air traffic control. For the study presented here, a general ascent permit was granted for visual line of sight flights of up to 100 m a.g.l. outside restricted areas for Rhineland-Palatinate (chapter 2).

The general workflow from image acquisition to image analysis followed in this study is illustrated in Figure 10.1. Image acquisition as obviously the first step, requires careful flight planning to ensure sufficient data overlap and image quality (40-60%) if orthophoto mosaics are to be generated. Generally, 2-3 photos per location were taken to ensure the acquisition of focused images per location.

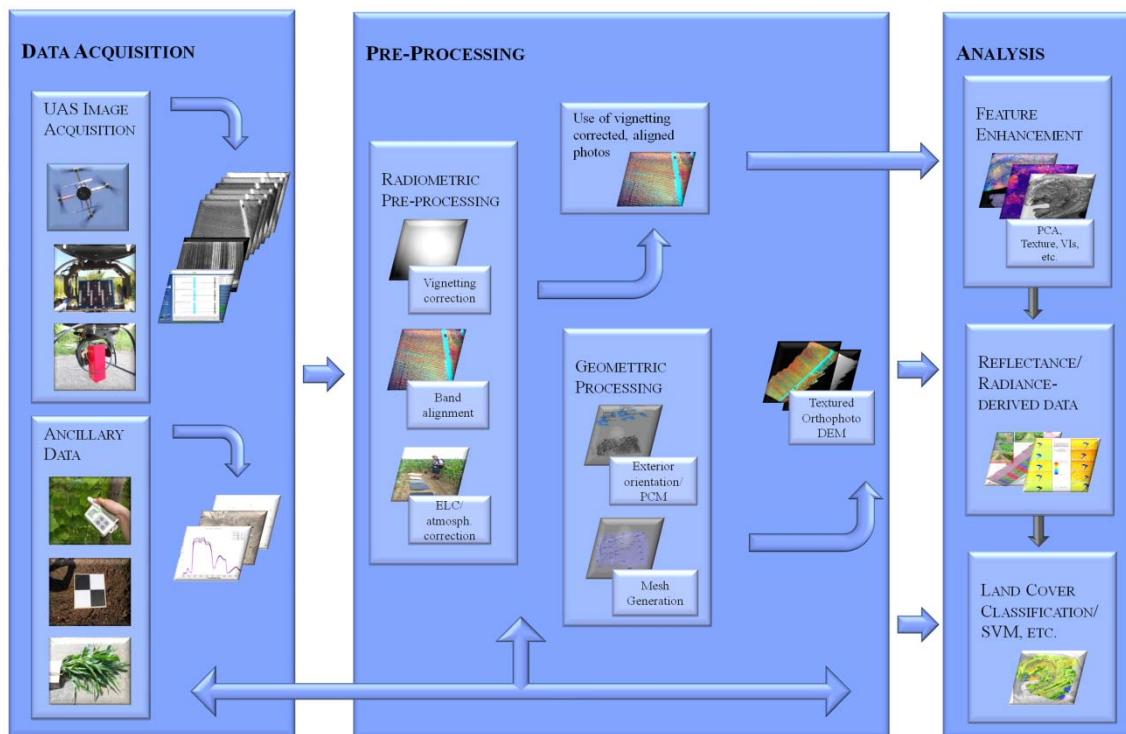


Figure 10.1 Summary of processing flowchart for UAS campaigns (ELC: empirical line calibration, PCA: principal component analysis, SVM: support vector machines)

The multispectral camera has shown to be affected by a) random and b) systematic noise (Kelcey and Lucieer 2012; Del Pozo et al. 2014). Random noise induced by the dark current may be eliminated by dark room image acquisition and averaging error effects in DN. The systematic bimodal noise is introduced by the progressive shutter and a chequerboard pattern by sensor induced differing DN levels. The band-dependent errors have shown to lie between ~ 0.5 to maximum 16 DN altogether, and may only partially be removed (Kelcey and Lucieer 2012; Del Pozo et al. 2014).

The progressive shutter mechanism used with the MiniMCA-6 does in cases show blurred areas when the UAS platform was affected by winds or flight-induced vibrations. Flight-planning is carried out with the respective ground station, offering either preloaded maps, in this case using Google Earth or any other maps as reference base. For spectral analysis of image data, it is then of further importance to ensure equal radiometric or illumination conditions for each image: flights should ideally be carried out when the sky is clear and the sun is at its peak to ascertain similar illumination conditions and to minimize shadows. This allows for fixed exposure times, thus, saving image-to-image radiometric corrections in case of automatic exposure. In practice, this is not always operationally possible, when several flights during one day are required, due

to battery-dependent flight times or when diurnal measurements are required. If absolute reflectances are required, reference reflectances need to be obtained during image acquisition.

The post-flight processing starts with data downloading of raw imagery and conversion to DIP image formats. Due to the rectangular sensor dimension in relation to optics (Verhoeven 2009), vignetting occurs and requires specific correction (chapter 5.1). The multispectral photos derived from the MiniMCA-6 for a respective location require band-to-band image alignment to obtain multispectral imagery. Alignment files with 1st order transformations (offset in x- and y-direction, scaling and rotation) are either provided by the producer, may be provided from the producer or by using images of infinite distance created by the user. In practice, camera handling, temperature differences and platform vibrations do cause modifications of camera parallaxes. Alignment files had thus to be generated for each flight campaign. Filter transmission and monochromatic camera response required further correction. Lens distortion is nowadays corrected within the Structure-from-motion software, and is not mandatory. As reference grey-level scales, panels of various colours or even just one Spectralon® panel are providing necessary calibrating targets to relate digital image numbers/values (DN) to reflectance values. In this work, grey-level panels (chapter 5) have been used, other groups used vinyl sheets or coloured boards (Del Pozo et al. 2014). Care needs to be taken to exclude environmental reflectances onto this panel, *e.g.* by placing a non-reflecting target underneath. The effect of tilted positioning and slant-range imaging on reference panels, *e.g.* in vineyards, requires further looking into.

Higher-order atmospheric effects like topographical influence are only removed by atmospheric and topographic correction (Tanré et al. 1990; Hill and Sturm 1991; Richter 2010; Hantson and Chuvieco 2011) with radiative transfer modeling. Here, with non-flat topography and the relative height differences of the 3D targets, ideally, 3D point cloud models should be derived prior to atmospheric correction, which is often not operational. However, to speed up data pre-processing, empirical line calibration by vicarious measurements of reference targets during the flight, approximate the actual radiation transfer quite well (Smith and Milton 1999; Karpouzli and Malthus 2003; Baugh and Groeneveld 2007).

Camera calibration and image-to-image alignments are extensively carried out with structure-from-motion software by multiple views and result in ground spatial resolution of about 3-8 cm for flight altitudes below a 100 m a.g.l.. Providing sufficient image overlap, the exterior orientation is estimated by utilizing GPS-measured photo centre

coordinates derived during the flight or by image matching. Image calibration may vary slightly for each run. An even distribution of GCPs within the field support point cloud referencing to accuracies of differential GPS measurements (Harwin and Lucieer 2012). There are also increasing number of companies that support users in point cloud modeling services, selling point clouds, orthophoto products from the user's UAS imagery.

Once images point cloud models are derived, they may be meshed and textured with image DNs, reflectance or radiance values for further analysis. DEMs may further be derived. The geometric correction may well be carried within a day or two depending on number of input images.

Part II of this work dealt with the agricultural and archaeological applications. At the beginning, the sensitivity analysis showed that the spectral filters chosen for the agricultural applications at 531, 550, 570, 670, 700 and 800 or 900 nm were appropriate to examine key crop and vegetation state parameters (chapter 7.2, Figure 7.5). Crop canopy simulations using PROSAIL (Feret et al. 2008; Jacquemoud et al. 2009) showed: for Chl_{a+b} , the wavelengths at 550 and 700-720 nm were negatively correlated, and 670-680 nm showed minor peak with lower negative correlation. Similarly, the N content highlighted the same wavelength regions, yet with positive correlation at lower absolute values. Dry matter content shows highest negative correlations with the spectral signal at spectral ranges beside the green peak, the red absorption minimum and alternating to positive correlation at the nIR. The selected filter wavelengths are therefore, well appropriate for studying crop-state. For LAI estimation, sensitive areas have been found for the green peak and red absorption minima, red edge and the nIR next to the red edge. For sun-induced Chl fluorescence measurements (chapter 8), though, the used filters around the $\text{O}_2\text{-B}$ absorption maximum, ideally should have been chosen at 761 nm instead of 760 nm (Damm et al. 2010) and shoulder wavelengths using FWHM widths less than 10 nm (Damm et al. 2011). The study of bidirectional reflectance effects of a maize field (chapter 7.3) revealed more structured differences in reflectance response in the UAS images than those simulated for a homogenous canopy. Azimuth angle differences between sensor and sun led to different patterns of bidirectional reflectances between simulated and measured reflectances: highest differences were found for 900 nm band (Figure 7.15) compared to simulated patterns where the 670 nm band would be expected to show highest variations and 900nm the lowest. For viewing zenith angles, the pattern varied as well. This may be attributed to several reasons: first of all, the underlying PROSAIL model was developed for homogenous canopies which may impede their use for a row crops like maize, even if in full developed canopies. Further work should be based on specific row models (e.g. Zhao et al. 2010) and should be re-

peated for denser viewing zenith angle differences and varying crops to be able to concisely summarize bidirectional reflectance effects on the MiniMCA-6 sensor. Commonly used vegetation indices (Table 7.4) like the SR, NDVI, PRI, RDVI and RE are quite strongly affected by azimuth angle changes, OSAVI and TCARI are less sensitive. Small deviation from nadir viewing show smaller effects on PRI and RE values, not, yet azimuth angles off the principal plane show stronger effects. This needs to be kept in mind when analyzing UAS imagery.

The sensitivity analysis also looked into the impact of radiometrical influence of the height of atmosphere between target and sensor and found the small air mass to indeed influence the DN signal from $\sim 0.5\text{-}3\%$ DN for 10-bit data for the black and to $\pm 5\%$ DN for the white reference panel (Figure 7.20 and Figure 7.21).

The agricultural applications (chapter 7 and 8) illustrated the advantage of small UAS for evaluating management strategies and crop state. Oblique images have proven to outperform nadir information when it comes to row-structured crops like vineyards where they well described crop state (Chl, N content, yield,) and its development within a growing season. Similarly, the multispectral data showed the potential to differentiate N-treatment within sugar beet varieties and their influence on sun-induced Chl fluorescence (chapter 8). Other authors have also shown the potential to use UAS data for early detection of disease detection (Calderón et al. 2013; Calderón et al. 2014).

Data pre-processing can be demanding, as precise image alignment to correct for the MiniMCA-6 individual cameras' parallaxes were found having to be set up for each flight campaign individually, as otherwise edge features were introduced into the image. For future applications, this could be automated through scale-invariant feature-matching algorithms (Lowe 2004). Empirical line calibration proved to be suitable for radiometrical calibration of UAS data of different acquisition times for a) one flight or b) different points in time.

Common vegetation indices may quickly be derived from multispectral UAS data, and NDVI, red-edge related indices, OSAVI and TCARI proved to be most successful for evaluating crop state and diseases (Calderón et al. 2013). The PRI only poorly described photosynthetic activity and moisture differences which may well be attributed to the fact that the 531 nm-band's 10 FWHM-width should be changed to 1 nm-FWHM.

Likewise, diurnal courses of crop state parameters may be derived as the diurnal measurements of sun-induced Chl fluorescence have illustrated in chapter 8 and by other authors (Zarco-Tejada et al. 2013b). Diurnal course of vegetation indices could be applied to monitor daily variations in plant water stress with filters at 900 and 970 nm for

the water index (Peñuelas et al. 1993) or a narrow-band PRI (Zarco-Tejada et al. 2013a) helping to identify stressed areas at water-intensive crops like vegetables.

Although not the main focus of application in this study, broadband uncorrected thermal data proved to help identifying crop varieties and soil management effects on grapevines. The automatic greyvalue stretching aggravates image processing. Momentarily, blackbodies of known temperatures are being fit to the camera allowing for capturing pixels with known temperature. The respective minimum and maximum temperatures are adapted to air temperature on-the-fly. Simultaneously, relative humidity and air pressure will be documented. This will facilitate image processing for future use. Broadband thermal data has been used in precision agriculture to map stomatal conductance on a daily and seasonal basis for cash crops like *e.g.* olive plantations and vineyards (Berni et al. 2009a, Berni et al. 2009b).

Other authors have shown how canopy properties of tree crops may be derived from the 3D structure of plants which is easily followed by UAS imagery (Mathews and Jensen 2013; Díaz-Varela et al. 2015). However, this also requires intensive field-work of ground- and crop-based temperature measurements, and if dense point clouds are required, higher image densities are required, which minimizes areal coverage.

With growing populations worldwide, precision agriculture is a growing application for UAS (Godfray et al. 2010, microdrones GmbH UAVweek 2015 workshop). UAS may also help bridging the gap between ground and satellite data and are more and more used for up-scaling ground-based information into EO satellite systems or updating of smaller scale data (Azmi et al. 2014). On the other hand, they are restricted to local and small regional scales at best. Explicitly for viticultural applications, Matese et al. (2015) compared NDVI surveys of vineyards and found an area threshold of five hectares to be the crossroads where airborne campaigns become cheaper than UAS applications.

UAS in archaeology have long been applied (see chapter 2) for site mapping, surveys, site monitoring, and archaeological reconnaissance. Near-infrared spectra, have been retrieved by filtering standard (digital) cameras and presents an acknowledged method for hidden cultural pattern recognition (Verhoeven 2009; Verhoeven 2012). Extending the spectral range to more wavelengths and spectral ranges beyond visible bands has been introduced by satellite and airborne remote sensing (Lasaponara and Masini 2012, Oltean and Abell 2012, Parcak 2009), and only recently has been used with UAS (Williams 2012). In this study, UAS has illustrated the potential for providing accurate maps at sub-decimetre accuracy for surveying and monitoring, and derivation of digital elevation models which may then be applied for further analysis. Archaeological recon-

naissance through pattern recognition takes advantage of the higher number of spectral bands and does find patterns similar to geomagnetic measurements (see previous chapter). Yet, within the experiment, reconnaissance on agricultural plots suffered from the early image acquisition date in Spain in March 2012 after a dry and cold winter, where vegetation had not yet developed much. Standard and evolved DIP methods allow for spectral feature enhancement to punctuate relevant information retrieval of archaeological features as, *e.g.*, land cover, vegetation patterns or settlement fragments.

11 Conclusion and Recommendations

This work has illustrated the potential and limitations of a multispectral small UAS for applications in agricultural and archaeological problems. UAS present a valuable, flexible and mostly easy-to-use remote sensing system for agricultural and archaeological multispectral remote sensing. They are mainly operated at large scales with sub-meter accuracy and study of short-term variations of sites of interest. The accuracy of derived orthophotos and DEMS is directly dependent on onboard or camera GPS accuracy to describe the exterior orientation but also to the accuracy of GCP measurements which equally require locational positioning in the decimetre/centimetre range. UAS are a flexible platform as they may be flown at less perfect weather conditions as they generally stay underneath cloud level. Since the specific advantage of rotary-wing UAS is the ability to hover over sites of interest and thus provide higher image quality as mostly no forward-motion blur occurs. The hovering capability also allows surveying a specific site for video capture or regular imagery. Although not possible in Germany, and not performed in this study, flights beyond visual sight do allow flying UAS in areas of impeding access or protected zones.

Limitations are mostly set by size of application area where five hectares have shown to be the crossroads to manned aircraft applications. In this case battery power is limiting flight time to an average of 15 minutes to up to an hour, depending on sensor payload. Platforms often lack in flight stability, yet with the fast development within that sector, accurate on-board IMU and miniaturized DGPS sensors will help to define attitude parameters with growing accuracy.

Another limiting factor is the size of UAS for which ascent permits are provided. General ascent permits in Germany's federal states are so far restricted to UAS below 5 kg. Larger UAS may be flown, but require applications for single ascent permits. The size of UAS is important for possible payload which for the small quadcopter chosen for this study was less than 1 kg. Miniature multispectral, thermal or the nowadays more widely available hyperspectral sensors are still quite expensive, yet sensor miniaturisation is in constant development. Services of UAS data acquisition and orthophoto mosaicking are being offered for users who do not have the capacity to run such a system on their own.

The multispectral sensor used in this study, the Tetracam Mini-MCA has successfully been applied at agricultural and archaeological applications but requires time-

consuming pre-processing and calibration to obtain reflectances or radiance values. The progressive shutter often results in striped images, but Tetracam has been offering a version with global snap shutter, recently. Band-to-band calibration of imagery requires either to be carried out for each flight campaign or by SIFT algorithms. First results with a broadband thermal camera showed promising findings, too. Hyperspectral sensors are becoming more widely available within the required weight limitations and a full new range of applications is waiting here for precision agriculture and related fields (Calderón et al. 2013; Calderón et al. 2014; Zarco-Tejada et al. 2013b; Bareth et al. 2014).

Experienced difficulties identified in this study are summarized in the following recommendations for an operational use of small UAS multispectral flight campaigns and good quality products:

- Sensible flight planning with a high image overlap (80-90% as suggested by Rosnell and Honkavaara 2012) including tilted images has shown to supersede manual flight plans, not necessarily requiring regular flight paths;
- Where required, collection of simultaneous in-situ reference spectral measurements for radiometric calibrations and atmospheric correction is mandatory for radiometric correction; likewise leaf- or ground-level temperature measurements for calibration of thermal cameras should be obtained;
- Reference panels for radiometric calibration should be placed on absorbing material (black fabric) and well-away of reflecting environmental surfaces;
- For high geometric accuracies of derived topographic data, ground control points should be distributed within and outside the study area, measured with a differential GPS.

More research may then be focused on the following issues:

- Comparison of ELC in accuracy for various topographies (flat versus sloped terrain) and environmental effects for oblique imagery;
- 3D-evaluation of crop illumination issues and crop parameters;
- Archaeological reconnaissance of hidden pattern using (hyper-)spectral data.

The study showed the potential of UAS to retrieve relevant physiological parameters for precision agriculture. UAS are, thus, contributing to food security demands for large-scale spatial information to derive risk areas where action is required for local crop management. Last not least, they contribute to a variety of application areas where large-scale environmental remote sensing data is required.

12 References

- Aber, J.S., Marzloff, I., & Ries, J.B. (2010): *Small-format aerial photography. Principles, techniques and geoscience applications* (First edition). Amsterdam, The Netherlands: Elsevier B.V.
- AEMet (2015a): Informe mensual climatológico. Marzo de 2012. Madrid, Spain: Agencia Estatal de Meteorología, Ministerio de Agricultura, Alimentación y Medio Ambiente.
- AEMet (2015b): Resumen Estacional Climatológico. Invierno (2011/2012). Madrid, Spain: Agencia Estatal de Meteorología, Ministerio de agricultura, Alimentación y Medio Ambiente.
- AEMet (2015c): Valores climatológicos normales (1981-2010), Zaragoza Aeropuerto In: M.d.A. Agencia Estatal de Meteorología, alimentación y medio ambiente, Spain (Ed.). Madrid: AEMet, Spain
- AESA (2015): Preguntas frecuentes sobre la normativa de drones.: http://www.seguridadaerea.gob.es/lang_castellano/cias_empresas/trabajos/marco_drones/preguntas/default.aspx, Spain
- AgiSoft LLC (2014): Agisoft PhotoScan User Manual: Professional Edition, Version 1.1 St. Petersburg, Russia: Agisoft LLC
- Agüera, F., Carvajal, F., & Pérez, M. (2011): Measuring Sunflower Nitrogen Status from an Unmanned Aerial Vehicle-Based System and an on the Ground Device. In, *UAV-g 2011, Conference on Unmanned Aerial Vehicle in Geomatics*. (pp. 1-6). Zürich, Switzerland: International Archives of the Photogrammetry, Remote Sensing and Spatial Information Sciences
- Alonso, L., Gomez-Chova, L., Vila-Frances, J., Amoros-Lopez, J., Guanter, L., Calpe, J., & Moreno, J. (2008): Improved Fraunhofer Line Discrimination Method for Vegetation Fluorescence Quantification. *Geoscience and Remote Sensing Letters*, IEEE, **5**, 620-624
- Anderson, R.C. (2001): Kite Aerial Photography for Archaeology: An Assessment and Short Guide. *British School at Athens Studies*, **8**, 167-180
- Andreu Pintado, J., & Garcia Lopez, J.F. (2012): Los Banales de Uncastillo, una ciudad romana por descubrir. *TecnoAmbiente*, **226**
- Andreu Pintado, J., Bienes Calvo, J.J., & Jordán Lorenzo, À.A. (2014): Monumentalización y regresión urbana en un municipio flavio del norte del convento jurídico Cesaraugustano: Los Banales de Uncastillo. In: S.F. Ramallo Asensio, & Q. Sánchez (Eds.), *Las ciudades de la Tarraconense Oriental entre*

- los S. II-IV D.C. Evolución urbanística y contextos materiales*, (p. 244). Murcia, Spain: Universidad de Murcia, Servicio de Publicaciones
- Andreu, J., Pérez, M.J., & Bienes, J.J. (2011): New findings of late antiquity in a town of the Vacscones Area (Los Banales de Uncastillo, Zaragoza, Spain). In: D. Hernández de la Fuente (Ed.), *New Perspectives on Late Antiquity*, (pp. 119-123). Newcastle-upon-Tyne: Cambridge Scholars Publishing
- Arnó, J., Rosell, J.R., Blanco, R., Ramos, M.C., & Martínez-Casasnovas, J.A. (2012): Spatial variability in grape yield and quality influenced by soil and crop nutrition characteristics. *Precision Agriculture*, **13**, 393-410
- Asner, G.P. (1998): Biophysical and Biochemical Sources of Variability in Canopy Reflectance. *Remote Sensing of Environment*, **64**, 234-253
- Atzberger, C., & Richter, K. (2012): Spatially constrained inversion of radiative transfer models for improved LAI mapping from future Sentinel-2 imagery. *Remote Sensing of Environment*, **120**, 208-218
- Austin, R. (2010): *Unmanned Aircraft Systems: UAVS Design, Development and Deployment*. Chichester, U.K.: John Wiley & Sons, Ltd.
- Azmi, S. M., B. Ahmad, and A. Ahmad. 2014. Accuracy assessment of topographic mapping using UAV image integrated with satellite images. IOP Conference Series: Earth and Environmental Science **18(1)**, 012015
- Baluja, J., Diago, M., Balda, P., Zorer, R., Meggio, F., Morales, F., & Tardaguila, J. (2012a): Assessment of vineyard water status variability by thermal and multispectral imagery using an unmanned aerial vehicle (UAV). *Irrigation Science*, **30**, 511-522
- Baluja, J., Diago, M.P., Goovaerts, P., & Tardaguila, J. (2012b): Assessment of the spatial variability of anthocyanins in grapes using a fluorescence sensor: relationships with vine vigour and yield. *Precision Agriculture*, **13**, 457-472
- Bareth, G., Aasen, H., Bendig, J., Gnyp, M.L., Bolten, A., Jung, A., Michels, R., & Soukkamäki, J. (2014): Spectral comparison of low-weight and UAV-based hyperspectral frame cameras with portable spectroradiometer measurements. In: J.B. Bendig, G. (Ed.), *Workshop on UAV-based Remote Sensing Methods for Monitoring Vegetation*. (pp. 6). Köln: Universität Köln
- Barman, D., Sehgal, V.G., Sahoo, R.N., & Nagarajan, S. (2010): Relationship of Bidirectional Reflectance of Wheat with Biophysical Parameters and its Radiative Transfer Modeling using Prosail. *Journal of the Indian Society of Remote Sensing*, **38**, 35-44
- Baugh, W. M. and D. P. Groeneveld. 2007. Empirical proof of the empirical line. *International Journal of Remote Sensing* **29**:665-672.
- Beisl, U. (2001): Correction of Bidirectional Effects in Imaging Spectrometer Data. In, *Remote Sensing Laboratories*. (pp. 189). Zurich: University of Zurich

- Beisl, U., & Woodhouse, N. (2004): Correction of atmospheric and bidirectional effects in multispectral ADS40 images for mapping purposes. In, *20th ISPRS Congress*. (pp. 1682-1750). Istanbul, Turkey: IAPRS
- Berjón, A.J., Cachorro, V.E., Zarco-Tejada, P.J., & de Frutos, A. (2013): Retrieval of biophysical vegetation parameters using simultaneous inversion of high resolution remote sensing imagery constrained by a vegetation index. *Precision Agriculture*, **14**, 541-557
- Berni, J.A.J., Zarco-Tejada, P.J., Sepulcre-Cantó, G., Fereres, E., & Villalobos, F. (2009a): Mapping canopy conductance and CWSI in olive orchards using high resolution thermal remote sensing imagery. *Remote Sensing of Environment*, **113**, 2380-2388
- Berni, J.A.J., Zarco-Tejada, P.J., Suárez, L., & Fereres, E. (2009b): Thermal and narrowband multispectral remote sensing for vegetation monitoring from an Unmanned Aerial Vehicle. *IEEE Transactions on Geoscience & Remote Sensing*, **47**, 722-738
- Berni, J.A.J., Zarco-Tejada, P.J., Suárez, L., González-Dugo, V., & Fereres, E. (2009c): Remote sensing of vegetation from UAV platforms using lightweight multispectral and thermal imaging sensors. In: C. Heipke, J. K., M. S., & U. Sörgel (Eds.), *High-Resolution Earth Imaging for Geospatial Information* (pp. 6 pages). Hannover, Germany
- Bitelli, G. (2012): Remote sensing and integration with other geomatic techniques in Archaeology. In: R. Lasaponara, & N. Masini (Eds.), *Satellite remote sensing: a new tool for archaeology*, (pp. 113-127). Dordrecht, Heidelberg, London, New York: Springer
- Bitelli, G., Girelli, V.A., Tini, M.A., & Vittuari, L. (2004): Low-height aerial imagery and digital photogrammetrical processing for archaeological mapping. *International Archives of the Photogrammetry, Remote Sensing and Spatial Information Sciences*, **35 (B5)**, 498-504
- Blyenburgh & Co (2011): *2011-2012 UAS Yearbook - UAS: The Global Perspective*. (9th edition ed.). Paris
- Boochs, F., Kupfer, G., Dockter, K., & KÜHbauch, W. (1990): Shape of the red edge as vitality indicator for plants. *International Journal of Remote Sensing*, **11**, 1741-1753
- Bramley, R.G.V., Ouzman, J., & Boss, P.K. (2011a): Variation in vine vigour, grape yield and vineyard soils and topography as indicators of variation in the chemical composition of grapes, wine and wine sensory attributes. *Australian Journal of Grape and Wine Research*, **17**, 217-229
- Bramley, R.G.V., Trought, M.C.T., & Praat, J.P. (2011b): Vineyard variability in Marlborough, New Zealand: characterising variation in vineyard performance

- and options for the implementation of Precision Viticulture. *Australian Journal of Grape and Wine Research*, **17**, 83-89
- Brown, D.C. (1966): Decentering Distortion of Lenses. *Photogrammetric Engineering and Remote Sensing*, **32**, 444-462
- Brown, D.C. (1971): Close-range camera calibration. *Photogrammetric Engineering*, **37**, 854-866
- Cabello-Pasini, A., & Macias-Carranza, V. (2011): Optical properties of grapevine leaves: reflectance, transmittance, absorptance and chlorophyll concentration. *Agrociencia*, **45**, 943-957
- Calderón, R., Montes-Borrego, M., Landa, B.B., Navas-Cortés, J.A., & Zarco-Tejada, P.J. (2014): Detection of downy mildew of opium poppy using high-resolution multi-spectral and thermal imagery acquired with an unmanned aerial vehicle. *Precision Agriculture*, **15**, 639-661
- Calderón, R., Navas-Cortés, J.A., Lucena, C., & Zarco-Tejada, P.J. (2013): High-resolution airborne hyperspectral and thermal imagery for early detection of Verticillium wilt of olive using fluorescence, temperature and narrow-band spectral indices. *Remote Sensing of Environment*, **139**, 231-245
- Campbell, J.B., & Wynne, R.H. (2011): *Introduction to remote sensing* (5th edition ed.). London: The Guildford Press
- Carl Zeiss Optronics GmbH (2008): User Manual Thermal Imager UCM. (pp. 25). Oberkochen: Carl Zeiss Optronics GmbH
- Carl Zeiss Optronics GmbH (2011): UCM - Un-Cooled Module. Hochleistungs-Miniatur-Wärmebildgerät. Oberkochen: Carl Zeiss Optronics GmbH, 73446 Oberkochen
- Ceccato, P., Flasse, S., Tarantola, S., Jacquemoud, S., & Grégoire, J.-M. (2001): Detecting vegetation leaf water content using reflectance in the optical domain. *Remote Sensing of Environment*, **77**, 22-33
- Cerdeira, J.O., Duarte Silva, P., Cadima, J., & Minhoto, M. (2014): The 'subselect' R package Vers. 0.12.
- Clark, L. (1997): A short history of ballooning. In: NOVA (Ed.): PBS Online by WGBH, <http://www.pbs.org/wgbh/nova/space/short-history-of-ballooning.html>, 07/07/2015
- Clarke, S., Coombes, N., Holloway, J., Hutton, R., Lemerle, D., Loch, A., Meunier, M., Loothfar, R., Rouse, E., Smith, R., Stevens, M., Tesic, D., & Weckert, M. (2006): Floor management systems to reduce vineyard inputs and improve grape quality. Final report. In: N.W.G.I. Centre (Ed.), *Grape and Wine Research and Development Corporation*. (pp. 219) Wagga Wagga: National Wine & Grape Industry Centre

- Clot, A.J. (2012): European Unmanned System Centre. In: Blyenburgh & Co (Ed.), *2012 RPAS Yearbook - RPAS: The Global Perspective*, (p. 47). Paris: Blyenburgh & Co
- Colomina, I., & Molina, P. (2014): Unmanned aerial systems for photogrammetry and remote sensing: A review. *ISPRS Journal of Photogrammetry and Remote Sensing*, **92**, 79-97
- Connors, R.W., & Harlow, C.A. (1980): Toward a structural textural analyzer based on statistical methods. *Computer Graphics and Image Processing*, **12**, 224-256
- Connors, R.W., Trivedi, M.M., & Harlow, C.A. (1982): Segmentation of a high-resolution Urban Scene Using Texture Operators. *Computer vision, graphics and image processing*, **25**, 273-310
- Conrady (1919): Decentering lens systems. *Monthly notices of the Royal Astronomical Society*, **79**, 384-390
- Corbane, C., Jacob, F., Raclot, D., Albergel, J., & Andrieux, P. (2012): Multitemporal analysis of hydrological soil surface characteristics using aerial photos: A case study on a Mediterranean vineyard. *International Journal of Applied Earth Observation and Geoinformation*, **18**, 356-367
- Corp, L.A., Middleton, E.M., Daughtry, C.S.T., & Campbell, P.K.E. (2006): Solar induced fluorescence and reflectance sensing techniques for monitoring nitrogen utilization in corn. In, IEEE International Conference on Geoscience and Remote Sensing Symposium (IGARSS) 2006. (pp. 2267-2270). Denver, CO, USA: IEEE
- Curry, M. (2009): ERAST - Environmental Research Aircraft and Sensor Technology. In: M. Curry (Ed.): Fact Sheets, <http://www.nasa.gov/centers/dryden/news/FactSheets/FS-020-DFRC.html>, 13.09.2011: NASA, Dryden Flight Research Center
- DAC (2014): General conditions for unmanned aircraft system (UAS) operations within the Luxembourg airspace: <http://www.dac.public.lu/actualites/2014/2/General-conditions-for-unmanned-aircraft-system-UAS-operations-within-the-Luxembourg-airspace/index.html>, 25/04/2015, Luxembourg
- Damm, A., Elbers, J.A.N., Erler, A., Gioli, B., Hamdi, K., Hutjes, R., Kosvancova, M., Meroni, M., Miglietta, F., Moersch, A., Moreno, J., Schickling, A., Sonnenschein, R., Udelhoven, T., Van Der Linden, S., Hostert, P., & Rascher, U.W.E. (2010): Remote sensing of sun-induced fluorescence to improve modeling of diurnal courses of gross primary production (GPP). *Global Change Biology*, **16**, 171-186
- Damm, A., Erler, A., Hillen, W., Meroni, M., Schaepman, M.E., Verhoef, W., & Rascher, U. (2011): Modeling the impact of spectral sensor configurations on the FLD retrieval accuracy of sun-induced chlorophyll fluorescence. *Remote Sensing of Environment*, **115**, 1882-1892

- Damm, A., Guanter, L., Laurent, V.C.E., Schaepman, M.E., Schickling, A., & Rascher, U. (2014): FLD-based retrieval of sun-induced chlorophyll fluorescence from medium spectral resolution airborne spectroscopy data. *Remote Sensing of Environment*, **147**, 256-266
- Darvishzadeh, R., Atzberger, C., Skidmore, A., & Schlerf, M. (2011): Mapping grassland leaf area index with airborne hyperspectral imagery: A comparison study of statistical approaches and inversion of radiative transfer models. *ISPRS Journal of Photogrammetry and Remote Sensing*, **66**, 894-906
- Daughtry, C.S.T., Walthall, C.L., Kim, M.S., de Colstoun, E.B., & McMurtrey, J.E. (2000): Estimating Corn Leaf Chlorophyll Concentration from Leaf and Canopy Reflectance. *Remote Sensing of Environment*, **74**, 229-239
- de Jong, S.M. (2006): *Remote sensing image analysis. Including the spatial domain*. Dordrecht: Springer
- De Laet, V., Paulissen, E., Meuleman, K., & Waelkens, M. (2009): Effects of image characteristics on the identification and extraction of archaeological features from Ikonos-2 and Quickbird-2 imagery: case study Sagalassos (southwest Turkey). *International Journal of Remote Sensing*, **30**, 5655-5668
- Del Pozo, S., Rodríguez-González, P., Hernández-López, D., & Felipe-García, B. (2014): Vicarious Radiometric Calibration of a Multispectral Camera on Board an Unmanned Aerial System. *Remote Sensing*, **6**, 1918
- Demmig-Adams, B., & Adams, W.W. (1996): Xanthophyll cycle and light stress in nature: uniform response to excess direct sunlight among higher plant species. *Planta*, **198**, 460-470
- Díaz-Varela, R., R. de la Rosa, L. León, and P. J. Zarco-Tejada. 2015. High-resolution airborne UAV imagery to assess olive tree crown parameters using 3D photo reconstruction: application in breeding trials *Remote Sensing* **7**:4213-4232.
- Dobrowski, S.Z., Pushnik, J.C., Zarco-Tejada, P.J., & Ustin, S.L. (2005): Simple reflectance indices track heat and water stress-induced changes in steady-state chlorophyll fluorescence at the canopy scale. *Remote Sensing of Environment*, **97**, 403-414
- Dorigo, W., Richter, R., Baret, F., Bamler, R., & Wagner, W. (2009): Enhanced Automated Canopy Characterization from Hyperspectral Data by a Novel Two Step Radiative Transfer Model Inversion Approach. *Remote Sensing*, **1**, 1139-1170
- Dryden Flight Research Center (2007): Fact Sheet FS-097 Ikhana Unmanned Science and Research Aircraft System In: M. Curry (Ed.): NASA Dryden Fact Sheets, <http://www.nasa.gov/centers/dryden/news/FactSheets/FS-097-DFRC.html>, 13/02/2013: Brian Dunbar

- Duan, S.-B., Li, Z.-L., Wu, H., Tang, B.-H., Ma, L., Zhao, E., & Li, C. (2014): Inversion of the PROSAIL model to estimate leaf area index of maize, potato, and sunflower fields from unmanned aerial vehicle hyperspectral data. *International Journal of Applied Earth Observation and Geoinformation*, **26**, 12-20
- EC (2012): Towards a European strategy for the development of civil applications of Remotely Piloted Aircraft Systems (RPAS). Commission staff working document (pp. 26). Brussels: European Commission
- ECA Piloting Safety (2015): Airborne Threats of low level Remotely Piloted Aircraft System (RPAS). Brussels, Belgium: European Cockpit Association AISBL
- Eisenbeiß, H. (2009): *UAV Photogrammetry*. Zürich: Institute of Geodesy and Photogrammetry
- Epiphanio, J.N., & Huete, A.R. (1995): Dependence of NDVI and SAVI on sun/sensor geometry and its effect on fAPAR relationships in Alfalfa. *Remote Sensing of Environment*, **51**, 351-360
- ERDAS Inc. (2010): LPS Project Manager. User's Guide (pp. 421). Norcross, GA, USA: ERDAS Inc.
- ERSG (2013): Roadmap for the integration of civil Remotely-Piloted Aircraft Systems in to the European Aviation System.: European RPAS Steering Group
- Escudero, A., Albert, M., Pita, J., & Pérez-García, F. (2000): Inhibitory effects of Artemisia herba-alba on the germination of the gypsophyte Helianthemum squamatum. *Plant Ecology*, **148**, 71-80
- España, M.a.L., Baret, F., Aries, F., Chelle, M., Andrieu, B., & Prévot, L. (1999): Modeling maize canopy 3D architecture: Application to reflectance simulation. *Ecological Modelling*, **122**, 25-43
- Evain, S., Flexas, J., & Moya, I. (2004): A new instrument for passive remote sensing: 2. Measurement of leaf and canopy reflectance changes at 531 nm and their relationship with photosynthesis and chlorophyll fluorescence. *Remote Sensing of Environment*, **91**, 175-185
- Everaerts, J. (2008): The Use of Unmanned Aerial Vehilces (UAVS) for Remote Sensing and Mapping. In, *ISPRS Congress*. (pp. 1187-1192). Beijing, China: The International Archives of the Photogrammetry, Remote Sensing and Spatial Information Sciences
- Evers, D., Behr, M., Molitor, D., Juilleret, J., Hissler, C., Deußer, H., & Jonville, M.-C. (2012): Study of the impact of soil and grape disease management on plant health status and wine quality. In: C.d.R.P.G. Lippmann (Ed.), Final report of VITISOL project. (pp. 71) Belvaux, Luxembourg

- FAO (2011): The state of the world's land and water resources for food and agriculture (SOLAW) - Managing systems at risk. In: London: Food and Agriculture Organization of the United Nations, Rome
- Feilhauer, H., Asner, G.P., & Martin, R.E. (2015): Multi-method ensemble selection of spectral bands related to leaf biochemistry. *Remote Sensing of Environment*, **164**, 57-65
- Feret, J.-B., François, C., Asner, G.P., Gitelson, A.A., Martin, R.E., Bidel, L.P.R., Ustin, S.L., le Maire, G., & Jacquemoud, S. (2008): PROSPECT-4 and 5: Advances in the leaf optical properties model separating photosynthetic pigments. *Remote Sensing of Environment*, **112**, 3030-3043
- Filella, I., Peñuelas, J., Llorens, L., & Estiarte, M. (2004): Reflectance assessment of seasonal and annual changes in biomass and CO₂ uptake of a Mediterranean shrubland submitted to experimental warming and drought. *Remote Sensing of Environment*, **90**, 308-318
- Fladeland, M. (2009): The NASA SIERRA Unmanned Aircraft System (UAS) In: NASA (Ed.): NASA Blogs: NASA CASIE Mission, http://blogs.nasa.gov/cm/blog/CASIE/posts/post_1247597221711.html, 13/02/2013: NASA
- FLIR^R Systems Inc. (2011): TauTM 640. LWIR Thermal Imager. USA: FLIR^R Systems Inc.
- Forschungsanstalt für Waldökologie und Forstwirtschaft (2015): Klima und Witterung: <http://www.kwis-rlp.de/index.php?id=6867>, Trippstadt
- Fourie, J.C. (2011): Soil Management in the Breede River Valley Wine Grape Region, South Africa. 3. Grapevine Performance. *South African Journal of Enology and Viticulture*, **32**, 60-70
- Franjic, Z., & Bondeson, J. (2014): Quality Assessment of Self-Calibration with Distortion Estimation for Grid Point Images. *Int. Arch. Photogramm. Remote Sens. Spatial Inf. Sci.*, **XL-3**, 95-99
- Frankenberg, C. (2012): Retrieval of chlorophyll fluorescence from space. Pasadena, CA: Jet Propulsion Laboratory, California Institute of Technology
- Fraunhofer, J. (1817): Bestimmung des Brechungs- und des Farbenzerstreungs-Vermögens verschiedener Glasarten, in Bezug auf die Vervollkommnung achromatischer Fernröhre. *Annalen der Physik*, **56**, 264-313
- Gamaya SA (2015): A novel integrated solution for large-scale monitoring and diagnostics of farmland based on breakthrough hyperspectral imaging (HSI) and small unmanned aircraft system (sUAS) technologies. Lausanne, Switzerland: Gamaya SA

- Gamon, J.A., Field, C.B., Bilger, W., Björkman, O., Fredeen, A.L., & Peñuelas, J. (1990): Remote sensing of the xanthophyll cycle and chlorophyll fluorescence in sunflower leaves and canopies. *Oecologia*, **85**, 1-7
- Gamon, J.A., Peñuelas, J., & Field, C.B. (1992): A narrow-waveband spectral index that tracks diurnal changes in photosynthetic efficiency. *Remote Sensing of Environment*, **41**, 35-44
- Gamon, J.A., Serrano, L., & Surfus, J.S. (1997): The photochemical reflectance index: an optical indicator of photosynthetic radiation use efficiency across species, functional types, and nutrient levels. *Oecologia*, **112**, 492-501
- Gao, B.-c. (1996): NDWI—A normalized difference water index for remote sensing of vegetation liquid water from space. *Remote Sensing of Environment*, **58**, 257-266
- Garmin Ltd. (2007): GPSMAP 60CSx with sensors and maps. Owner's manual (pp. 105). Olathe, Kansas, USA: Garmin International Inc.
- Garrison, T.G. (2010): Remote sensing ancient Maya rural populations using QuickBird satellite imagery. *International Journal of Remote Sensing*, **31**, 213-231
- Gausman, H.W., & Allen, W.A. (1973): Optical Parameters of Leaves of 30 Plant Species. *Plant Physiology*, **52**, 57-62
- Gege, P., Fries, J., Haschberger, P., Schötz, P., Schwarzer, H., Strobl, P., Suhr, B., Ulbrich, G., & Jan Vreeling, W. (2009): Calibration facility for airborne imaging spectrometers. *ISPRS Journal of Photogrammetry and Remote Sensing*, **64**, 387-397
- Gil-Perez, B., Zarco-Tejada, P.J., Correa-Guimaraes, A., Relea-Gangas, E., Navas-Gracia, L.M., Hernandez-Navarro, S., Sanz-Requena, J.F., Berjon, A., & Martin-Gil, J. (2010): Remote sensing detection of nutrient uptake in vineyards using narrow-band hyperspectral imagery. *Vitis*, **49**, 167-173
- Godfray, H.C.J., Beddington, J.R., Crute, I.R., Haddad, L., Lawrence, D., Muir, J.F., Pretty, J., Robinson, S., Thomas, S.M., & Toulmin, C. (2010): Food Security: The challenge of feeding 9 billion people. *Science*, **327**, 812-818
- Goulas, Y., Cerovic, Z.G., Cartelat, A., & Moya, I. (2004): Dualex: a new instrument for field measurements of epidermal ultraviolet absorbance by chlorophyll fluorescence. *Applied Optics*, **43**, 4488-4496
- Gray, S. (2009): UAV Survey: A guide to good practice, http://guides.archaeologydataservice.ac.uk/g2gp/AerialPht_UAV, 01/07/2015. Bristol, GB: University of Bristol, Dep. of Archaeology
- Grenzdörffer, G.J., & Niemeyer, F. (2011): UAV based BRDF-measurements of agricultural surfaces with PFIFFIKUS. In: Z. ETH (Ed.), *UAV-g 2011, Conference on Unmanned Aerial Vehicle in Geomatics*. Zurich, Switzerland:

- International Archives of the Photogrammetry, Remote Sensing and Spatial Information Sciences.
- Guanter, L., Alonso, L., Gómez-Chova, L., Meroni, M., Preusker, R., Fischer, J., & Moreno, J. (2010): Developments for vegetation fluorescence retrieval from spaceborne high-resolution spectrometry in the O2-A and O2- B absorption bands. *Journal of Geophysical Research*, **115**, D19303
- Guanter, L., Del Carmen González-Sanpedro, M., & Moreno, J. (2007): A method for the atmospheric correction of ENVISAT/MERIS data over land targets. *International Journal of Remote Sensing*, **28**, 709-728
- Guanter, L., Rossini, M., Colombo, R., Meroni, M., Frankenberg, C., Lee, J.E., & Joiner, J. (2013): Using field spectroscopy to assess the potential of statistical approaches for the retrieval of sun-induced chlorophyll fluorescence from ground and space. *Remote Sensing of Environment*, **133**, 52-61
- Guanter, L., Zhang, Y., Jung, M., Joiner, J., Voigt, M., Berry, J.A., Frankenberg, C., Huete, A.R., Zarco-Tejada, P., Lee, J.-E., Moran, M.S., Ponce-Campos, G., Beer, C., Camps-Valls, G., Buchmann, N., Gianelle, D., Klumpp, K., Cescatti, A., Baker, J.M., & Griffis, T.J. (2014): Global and time-resolved monitoring of crop photosynthesis with chlorophyll fluorescence. *Proceedings of the National Academy of Sciences*, **111**, E1327-E1333
- Guillen-Climent, M.L., Zarco-Tejada, P., Berni, J.A.J., North, P.R.J., & Villalobos, F.J. (2012): Mapping radiation interception in row-structured orchards using 3D simulation and high-resolution airborne imagery acquired from a UAV. *Precision Agriculture*, **13**, 473-500
- Guoqan, D., & Zhengzhi, L. (1992): The apparent emissivity of vegetation canopies. *International Journal of Remote Sensing*, **14**, 183-188
- Guyot, G. (1990): Optical properties of vegetation canopies. In: M.D. Steven, & J.A. Clark (Eds.), *Applications of remote sensing in agriculture*, (pp. 19-43). London: Butterworths
- Haboudane, D., Miller, J.R., Tremblay, N., Zarco-Tejada, P.J., & Dextraze, L. (2002): Integrated narrow-band vegetation indices for prediction of crop chlorophyll content for application to precision agriculture. *Remote Sensing of Environment*, **81**, 416-426
- Hack, H., Bleiholder, H., Buhr, L., Meier, U., Schnock-Frickke, U., Weber, E., & Witzenberger, A. (1992): Erweiterte BBCH-Skala, allgemein. Braunschweig
- Hakala, T., Suomalainen, J., & Peltoniemi, J.I. (2010): Acquisition of Bidirectional Reflectance Factor Dataset Using a Micro Unmanned Aerial Vehicle and a Consumer Camera. *Remote Sensing*, **2**, 819-832

- Hall, A., Lamb, D.W., Holzapfel, B., & Louis, J. (2002): Optical remote sensing applications in viticulture - a review. *Australian Journal of Grape and Wine Research*, **8**, 36-47
- Hall, A., Lamb, D.W., Holzapfel, B.P., & Louis, J.P. (2011a): Within-season temporal variation in correlations between vineyard canopy and winegrape composition and yield. *Precision Agriculture*, **12**, 103-117
- Hall, F.G., Hilker, T., & Coops, N.C. (2011b): PHOTOSYNSAT, photosynthesis from space: Theoretical foundations of a satellite concept and validation from tower and spaceborne data. *Remote Sensing of Environment*, **115**, 1918-1925
- Hall, F.G., Hilker, T., Coops, N.C., Lyapustin, A., Huemmrich, K.F., Middleton, E., Margolis, H., Drolet, G., & Black, T.A. (2008): Multi-angle remote sensing of forest light use efficiency by observing PRI variation with canopy shadow fraction. *Remote Sensing of Environment*, **112**, 3201-3211
- Hansen, P.M., & Schjoerring, J.K. (2003): Reflectance measurement of canopy biomass and nitrogen status in wheat crops using normalized difference vegetation indices and partial least squares regression. *Remote Sensing of Environment*, **86**, 542-553
- Hantson, S., & Chuvieco, E. (2011): Evaluation of different topographic correction methods for Landsat imagery. *International Journal of Applied Earth Observation and Geoinformation*, **13**, 691-700
- Haralick, R.M. (1979): Statistical and Structural Approaches to Texture. *Proceedings of the IEEE*, **67**, 786-804
- Haralick, R.M., Shanmugam, K., & Dinstein, I. (1973): Textural features for image classification. *IEEE transactions on systems, man and cybernetics.*, **SMC-3**, 610-621
- Harwin, S. and A. Lucieer. 2012. Assessing the Accuracy of Georeferenced Point Clouds Produced via Multi-View Stereopsis from Unmanned Aerial Vehicle (UAV) Imagery. *Remote Sensing* **4**:1573.
- Hass, E. (2015): Texture-based classification of forest types using high resolution aerial photographs, Masterarbeit. Trier: Universität Trier, Umweltfernerkundung und Geoinformatik
- Headwall Photonics Inc. (2014a): Data Sheet: MICRO-HYPERSPEC® Airborne Hyperspectral Sensor Fitchburg, MA, USA: Headwall Photonics Inc.,
- Headwall Photonics Inc. (2014b): Data Sheet: Nano-Hyperspec. Small, light airborne hyperspectral sensor. Fitchburg, Massachusetts, USA: Headwall Photonics Inc.
- Hilker, T., Coops, N.C., Hall, F.G., Black, T.A., Wulder, M.A., Nesic, Z., & Krishnan, P. (2008): Separating physiologically and directionally induced changes in PRI using BRDF models. *Remote Sensing of Environment*, **112**, 2777-2788

- Hill, J., & Sturm, B. (1991): Radiometric correction of multitemporal Thematic Mapper data for use in agricultural land-cover classification and vegetation monitoring. *International Journal of Remote Sensing*, **12**, 1471-1491
- Hill, J., Mehl, W., & Radeloff, V.C. (1995): Improved forest mapping by combining corrections of atmospheric and topographic effects in Landsat TM Imagery. In, *EARSel Symposium on Sensors and Environmental Applications in Remote Sensing*. (pp. 143-151). Göteborg, Sweden
- Hodson, M.J., & Bryant, J.A. (2012): *Functional Biology of Plants*. Chichester: Wiley-Blackwell
- Honkavaara, E., Saari, H., Kaivosoja, J., Pölönen, I., Hakala, T., Litkey, P., Mäkynen, J., & Pesonen, L. (2013): Processing and Assessment of Spectrometric, Stereoscopic Imagery Collected Using a Lightweight UAV Spectral Camera for Precision Agriculture. *Remote Sensing*, **5**, 5006-5039
- Huete, A.R. (1988): A soil-adjusted vegetation index (SAVI). *Remote Sensing of Environment*, **25**, 295-309
- Huete, A.R., & Jackson, R.D. (1988): Soil and atmosphere influences on the spectra of partial canopies. *Remote Sensing of Environment*, **25**, 89-105
- Huete, A.R., Hua, G., Qi, J., Chehbouni, A., & van Leeuwen, W.J.D. (1992): Normalization of multidirectional red and NIR reflectances with the SAVI. *Remote Sensing of Environment*, **41**, 143-154
- Hunt, E.R.J., Hively, W.D., Fujikawa, S.J., Linden, D.S., Daughtry, C.S.T., & McCarty, G.W. (2010): Acquisition of NIR-Green-Blue Digital Photographs from Unmanned Aircraft for Crop Monitoring. *Remote Sensing*, **2010**, 290-305
- ICAO (2011): Cir 328, Unmanned Aircraft Systems (UAS) In, *Technical Report*. Montréal, Canada: International Civil Aviation Authority
- Instituto Aragonés del Medio Ambiente (1993): Sistema informacion medio ambiente de Aragón In: Diputación General de Aragón, Instituto Aragonés del Medio Ambiente, Zaragoza, Spain
- Instituto Geográfico de Aragón (2009): Plan Nacional de Ortofotografía Aérea - Ortofoto de Aragón 50 cms: 22/06, Zaragoza, Spain: Instituto Geográfico de Aragón. Gobierno de Aragón
- Intergraph Corporation (2013): ERDAS Field GuideTM. In. Huntsville, AL, USA: Intergraph Corporation
- Israel, M. (2011): A UAV-Based Roe Deer Fawn Detection System In, *UAV-g 2011, Conference on Unmanned Aerial Vehicle in Geomatics*. (pp. 1-6). Zürich, Switzerland: International Archives of the Photogrammetry, Remote Sensing and Spatial Information Sciences

- Jackson, D.I., & Lombard, P.B. (1993): Environmental and management practices affecting grape composition and wine quality - A review. *American Journal of Enology and Viticulture*, **44**, 409-430
- Jacquemoud, S. (1993): Inversion of the PROSPECT + SAIL canopy reflectance model from AVIRIS equivalent spectra: Theoretical study. *Remote Sensing of Environment*, **44**, 281-292
- Jacquemoud, S., Verhoef, W., Baret, F., Bacour, C., Zarco-Tejada, P.J., Asner, G.P., François, C., & Ustin, S.L. (2009): PROSPECT + SAIL models: A review of use for vegetation characterization. *Remote Sensing of Environment*, **113**, **Supplement 1**, S56-S66
- Jensen, J.R. (2005): *Introductory digital image processing*. (3rd ed.). Upper Saddle River, N.J., USA: Pearson Prentice Hall
- Jensen, J.R. (2007): *Remote sensing of the environment. An earth resource perspective.*: Prentice Hall series in Geographic Information Sciences, 592, Upper Saddle River, NJ: Pearson Prentice-Hall
- Jensen, T., Apan, A., Young, F., & Zeller, I. (2007): Detecting the attributes of a wheat crop using digital imagery acquired from a low-altitude platform. *Computers & Electronics in Agriculture*, **59**, 66-77
- Johnson, L.F., Roczen, D.E., Youkhana, S.K., Nemani, R.R., & Bosch, D.F. (2003): Mapping vineyard leaf area with multispectral satellite imagery. *Computers & Electronics in Agriculture*, **38**, 33
- Jones, H.G., & Vaughan, R.A. (2010): *Remote sensing of vegetation. Principles, techniques, and applications*. Oxford: Oxford University Press
- Jordan, C.F. (1969): Derivation of leaf-area index from quality of light on the forest floor. *Ecology*, **50**, 663-666
- Kallevig, T.B. (2012): Working Group 73 on Unmanned Aircraft Systems. In: B. Co (Ed.), *2012 RPAS Yearbook: The Global Perspective*, (pp. 32-33). Paris: Blyenburgh & Co
- Karpouzli, E. and T. J. Malthus. 2003. The empirical line method for the atmospheric correction of IKONOS imagery. *International Journal of Remote Sensing* **24**:1143-1150.
- Kelcey, J., & Lucieer, A. (2012): Sensor correction of a 6-band multispectral imaging sensor for UAV remote sensing. *Remote Sensing*, **4**, 1462-1493
- Kempeneers, P., Zarco-Tejada, P.J., North, P.R.J., de Backer, S., Delalieux, S., Sepulcre-Cantó, G., Morales, F., van Aardt, J.A.N., Sagardoy, R., Coppin, P., & Scheunders, P. (2008): Model inversion for chlorophyll estimation in open canopies from hyperspectral imagery. *International Journal of Remote Sensing*, **29**, 5093-5111

- Kimes, D.S. (1983): Remote sensing of row crop structure and component temperatures using directional radiometric temperatures and inversion techniques. *Remote Sensing of Environment*, **13**, 33-55
- Kirkpatrick, S., Gelatt, C.D., & Vecchi, M.P. (1983): Optimization by simulated annealing. *Science*, **220**, 671-680
- Konica Minolta Sensing Inc. (2009): Chlorophyll Meter SPAD-502Plus. Instruction Manual. In. Japan: Konica Minolta
- Kraus, K. (1996): *Photogrammetrie. Bd. 2. Verfeinerte Methoden und Anwendungen* (3., völlig neue und erw. Aufl. ed.). Bonn: Fer. Dümmlers Verlag
- Kraus, K. (2004): *Photogrammetrie. Band 1 Geometrische Informationen aus Photographien und Laserscanneraufnahmen.* (7., vollst. bearb. und erw. Aufl. ed.). Berlin: de Gruyter
- Krock, L. (2002): Time Line of UAVs: NOVA Science Programming on Air and Online, <http://www.pbs.org/wgbh/nova/spiesfly/uavs.html>, 08.09.2011: 2010 WGBH Educational Foundation
- Kurz, F. (2003): Schätzung von Vegetationsparametern aus multispektralen Fernerkundungsdaten. *Deutsche Geodätische Kommission, Reihe C Dissertationen*, **Heft Nr. 569**, 101
- Kuusk, A. (1995): A fast, invertible canopy reflectance model. *Remote Sensing of Environment*, **51**, 342-350
- Laliberte, A.S., Goforth, M.A., Steele, C.M., & Rango, A. (2011): Multispectral remote sensing from unmanned aircraft: Image processing workflows and applications for rangeland environments. *Remote Sensing*, **3**, 2529-2551
- Lancashire, P.D., Bleiholder, H., van den Boom, T., Langelüddeke, P., Stauss, R., Weber, E., & Witzemberger, A. (1991): A uniform decimal code for growth stages of crops and weeds. *Annals of Applied Biology*, **119**, 561-601
- Lasaponara, R., & Masini, N. (2012a): Pattern recognition and classification using VHR data for archaeological research. . In: R. Lasaponara, & N. Masini (Eds.), *Satellite remote sensing. A new tool for archaeology.*, (pp. 65-85). Dordrecht, Heidelberg, London, New York: Springer
- Lasaponara, R., & Masini, N. (2012b): Remote sensing in archaeology: from visual data interpretation to digital data manipulation. In: R. Lasaponara, & N. Masini (Eds.), *Satellite remote sensing.* , (pp. 3-17). Dordrecht, Heidelberg, London, New York.: Springer
- Lasaponara, R., & Masini, N. (2012c): *Satellite remote sensing. A new tool for archaeology.* Dordrecht, Heidelberg, London, New York: Springer

- Lasuén Alegre, M.D., & Nasarre Otín, E. (2008): El yacimiento arqueológico de Los Bañales (Uncastillo, Zaragoza): ensayo de actualización. *Espacio, Tiempo y Forma*, (pp. 207-234)
- Leijgraaf, R.v.d. (2012a): JARUS - Entering the Next Phase. In: B. Co (Ed.), *2012 RPAS Yearbook - RPAS: The Global Perspective*, (pp. 58-59). Paris: Blyenburgh & Co
- Leijgraaf, R.v.d. (2012b): Working Group 93 on Light RPAS. In: Blyenburgh & Co (Ed.), *RPAS Yearbook - RPAS: The Global Perspective*, (pp. 34-35). Paris: Blyenburgh & Co
- Lelong, C.C.D., Burger, P., Jubelin, G., Roux, B., Labbé, S., & Baret, F. (2008): Assessment of Unmanned Aerial Vehicles Imagery for Quantitative Monitoring of Wheat Crop in Small Plots. *Sensors*, **8**, 3557-3585
- Lichtenthaler, H.K., & Miehe, J.A. (1997): Fluorescence imaging as a diagnostic tool for plant stress. *Trends in Plant Science*, **2**, 316-320
- LI-COR Biosciences: FV2000. The LAI-2000 data file viewer. Lincoln, NE, USA: LI-COR, Inc.
- LI-COR Inc. (1992): LAI-2000 Plant Canopy Analyzer. *Instrument Manual*. Lincoln, Nebraska, USA: LI-COR, Inc.
- Lillesand, T.M., Kiefer, R.W., & Chipman, J.W. (2008): *Remote sensing and image interpretation*. (6th ed. ed.). John Wiley & Sons, Inc.
- Lin, Y., Hyypä, J., & Jaakkola, A. (2011): Mini-UAV-Borne LIDAR for Fine-Scale Mapping. *IEEE Transactions on Geoscience & Remote Sensing Letters*, **8**, 426-430
- Lorenz, D.H., Eichhorn, K.W., Bleiholder, H., Klose, R., Meier, U., & Weber, E. (1995): Phenological growth stages of the grapevine, *Vitis vinifera* L. ssp. *vinifera*. Codes and descriptions according to the extended BBCH scale. *Australian Journal of Grape and Wine Research*, **1**, 100-103
- Lowe, D. G. 2004. Distinctive Image Features from Scale-Invariant Keypoints. *International Journal of Computer Vision* **60**:91-110.
- Mabrouk, H., & Sinoquet, H. (1998): Indices of light microclimate and canopy structure of grapevines determined by 3D digitising and image analysis, and their relationship to grape quality. *Australian Journal of Grape and Wine Research*, **4**, 2-13
- Maier, S.W., Günther, K.P., & Stellmes, M. (2003): Sun-induced fluorescence: a new tool for precision farming. In: M. McDonald, J. Schepers, L. Tarty, T. van Toai, & D. Major (Eds.), *Digital imaging and spectral techniques: applications to precision agriculture and crop physiology*, (pp. 209-222): Madison, Wis.

- Malenowský, Z., Mishra, K.B., Zemek, F., Rascher, U., & Nedbal, L. (2009): Scientific and technical challenges in remote sensing of plant canopy reflectance and fluorescence. *Journal of Experimental Botany*, **60**, 2987-3004
- Markwell, J., Osterman, J.C., & Mitchell, J.L. (1995): Calibration of the Minolta SPAD-502 leaf chlorophyll meter. *Photosynthesis Research*, **46**, 467-472
- Martín, P., Zarco-Tejada, P.J., González, M.R., & Berjon, A. (2007): Using hyperspectral remote sensing to map grape quality in 'Tempranillo' vineyards affected by iron deficiency chlorosis. *Vitis*, **46**, 7-14
- Martinon, V., Fadailli, E.M., Becu, M., Duval, C., & Fumery, J. (2010): Innovative optical sensors for diagnosis, mapping and real-time management of row crops: the use of polyphenolics and fluorescence In, *ASA, CSSA, and SSSA 2010 International Annual Meetings, 31/10 - 03/11/2010*. (pp. 1). Long Beach, CA, USA
- Masini, N., Lasaponara, R., Rizzo, E., & Orefici, G. (2012): Integrated remote sensing approach in Cahuachi (per): studies and results of the ITACA mission (2007-2010). In: R. Lasaponara, & N. Masini (Eds.), *Satellite remote sensing. A new tool for Archaeology.*, (pp. 307-344). Dordrecht, Heidelberg, London, New York: Springer
- Matese, A., P. Toscano, S. Di Gennaro, L. Genesio, F. Vaccari, J. Primicerio, C. Belli, A. Zaldei, R. Bianconi, and B. Gioli. 2015. Intercomparison of UAV, Aircraft and Satellite Remote Sensing Platforms for Precision Viticulture. *Remote Sensing* **7**:2971.
- Mathews, A. and J. Jensen. 2013. Visualizing and quantifying vineyard canopy LAI using an Unmanned Aerial Vehicle (UAV) collected high density Structure from Motion point cloud. *Remote Sensing* **5**:2164-2183.
- MAVinci GmbH (2009-2011): MAVinci - Unmanned Aerial Systems.: <http://www.mavinci.de>, 13.09.2011, St. Leon-Rot, Germany: MAVinci GmbH
- MAVinci GmbH (2011): SIRIUS Aerial Image UAS & MAVinci Desktop Manual. Version 2.1.b9555 In. St. Leon-Rot, Germany: MAVinci GmbH
- MAVinci GmbH (2014): SIRUS-UAS. St. Leon-Rot: MAVinci GmbH
- Mayer, F., Noo, A., Sinnaeve, G., Dardenne, P., Gerin, P.A., & Delfosse, P. (2013): Prediction of the biochemical methane potential (BMP) of maize silages reduced to a powder using NIR spectra from wet and dried samples In, *NIR 2013 - 16th International Conference on Near Infrared Spectroscopy*. 34280 La Grande-Motte
- Meggio, F., Zarco-Tejada, P.J., Miller, J.R., Martin, P., Gonzalez, M.R., & Berjon, A. (2008): Row orientation and viewing geometry effects on row-structured vine crops for chlorophyll content estimation. *Canadian Journal of Remote Sensing*, **34**, 220-234

- Meggio, F., Zarco-Tejada, P.J., Núñez, L.C., Sepulcre-Cantó, G., González, M.R., & Martín, P. (2010): Grape quality assessment in vineyards affected by iron deficiency chlorosis using narrow-band physiological remote sensing indices. *Remote Sensing of Environment*, **114**, 1968-1986
- Meier, U. (2001): *Entwicklungsstadien mono- und dikotyle Pflanzen*. (2nd edition ed.). Braunschweig: Biologische Bundesanstalt für Land und Forstwirtschaft, Julius-Kühn-Institut
- Melgani, F., & Bruzzone, L. (2004): Classification of hyperspectral remote sensing images with support vector machines. *IEEE Transactions on Geoscience & Remote Sensing*, **42**, 1778-1789
- Memarsadeghi, N., Mount, D.M., Netanjahu, N.S., & LeMoigne, J. (2007): A Fast Implementation of the ISODATA Clustering Algorithm. *International Journal of Computational Geometry and Applications*, **17**, 71-103
- Meroni, M. (2015): Solar irradiance, fluorescence and reflectances derived by Ocean Optics spectrometer data for Campus Klein-Altendorf 2, 23/08/2015. Personal Communication
- Meroni, M., Busetto, L., Colombo, R., Guanter, L., Moreno, J., & Verhoef, W. (2010): Performance of Spectral Fitting Methods for vegetation fluorescence quantification. *Remote Sensing of Environment*, **114**, 363-374
- Meroni, M., Rossini, M., Guanter, L., Alonso, L., Rascher, U., Colombo, R., & Moreno, J. (2009): Remote sensing of solar-induced chlorophyll fluorescence: Review of methods and applications. *Remote Sensing of Environment*, **113**, 2037-2051
- Meyers, J.M., & Van den Heuvel, J.E. (2008): Enhancing the precision and spatial acuity of point quadrat analysis via calibrated exposure mapping. *American Journal of Enology and Viticulture*, **59**, 425-431
- microdrones GmbH (2004-2007): Bedienerhandbuch md4-200. Version 2.2. (pp. 114). Siegen: microdrones GmbH
- microdrones GmbH (2007): Description of MD_DownLink. Siegen: microdrones GmbH
- microdrones GmbH (2007-2013): mdCockpit3.2 - Benutzer-Handbuch. Siegen: microdrones GmbH
- microdrones GmbH (2008-2010): mdCockpit Standard Edition. Vorläufige Bedienungsanleitung. Siegen: microdrones GmbH
- microdrones GmbH (2009): md4-1000. Siegen: microdrones GmbH
- Middleton, E.M., Corp, L.A., & Campbell, P.K.E. (2008): Comparison of measurements and FluorMOD simulations for solar-induced chlorophyll fluorescence and reflectance of a corn crop under nitrogen treatments. *International Journal of Remote Sensing*, **29**, 5193-5213

- Mikhail, E.M., Bethel, J.S., & McGlone, J.C. (2001): *Introduction to Modern Photogrammetry*. New York, Chichester, Weinheim, Brisbane, Singapore, Toronto: John Wiley & Sons, Inc.
- Miller, J.R., Wu, J., Boyer, M.G., Belanger, M., & Hare, E.W. (1991): Seasonal patterns in leaf reflectance red-edge characteristics. *International Journal of Remote Sensing*, **12**, 1509-1523
- Mobasheri, M.R., & Fatemi, S.B. (2013): Leaf Equivalent Water Thickness assessment using reflectance at optimum wavelengths. *Theoretical and Experimental Plant Physiology*, **25**, 196-202
- Mountrakis, G., Im, J., & Ogole, C. (2011): Support vector machines in remote sensing: A review. *ISPRS Journal of Photogrammetry and Remote Sensing*, **66**, 247-259
- Murchie, E.H., & Lawson, T. (2013): Chlorophyll fluorescence analysis: a guide to good practice and understanding some new applications. *Journal of Experimental Botany*, **64**, 3983-3998
- Myers, J.W. (1978): Balloon Survey Field Season, 1977. *Journal of Field Archaeology*, **5**, 145-159
- Nagai, M., Chen, T., Shibasaki, R., Kumagai, H., & Ahmed, A. (2009): UAV-Borne 3-D Mapping System by Multisensor Integration. *IEEE Transactions on Geoscience & Remote Sensing*, **47**, 701-708
- Nex, F., & Remondino, F. (2014): UAV for 3D mapping applications: a review. *Applied Geomatics*, **6**, 1-15
- Nichol, C., Rascher, U., Matsubara, S., & Osmond, B. (2006): Assessing photosynthetic efficiency in an experimental mangrove canopy using remote sensing and chlorophyll fluorescence. *Trees*, **20**, 9-15
- Nicodemus, F.E., Richmond, J.C., Hsia, J.J., Ginserb, I.W., & Limperis, T. (1977): Geometrical considerations and nomenclature for reflectance In: U.S.D.o. Commerce (Ed.), *National Bureau of Standards Mono.* Washington D.C.: U.S. Government Printing Office
- Nikon Inc. (2011): D3100. In. Mississauga, Ontario, Canada, Melville, New York, USA: Nikon Corporation
- Noli, D. (1985): Low altitude aerial photography from a tethered balloon. *Journal of Field Archaeology*, **12**, 497-501
- Nonami, K. (2007): Prospect and Recent Research & Development for Civil Use Autonomous Unmanned Aircraft as UAV and MAV. *Journal of System Design and Dynamics*, **1**, 120-128
- Oberthür, T., Cock, J., Andersson, M.S., Naranjo, R.N., Cataneda, D., & Blair, M. (2007): Acquisition of low altitude digital imagery for local monitoring and

- management of genetic resources. *Computers and Electronics in Agriculture*, **58**, 60-77
- Ollat, N., Fermaud, M., Tandonnet, J.P., & Neveux, M. (1998): Evaluation of an indirect method for leaf area index determination in the vineyard: Combined effects of cultivar, year and training system. *Vitis*, **37**, 73-78
- Oltean, I. A. and L. L. Abell. 2012. High-resolution satellite imagery and the detection of buried archaeological features in ploughed landscapes. *in* R. Lasaponara and N. Masini, editors. *Satellite remote sensing. A new tool for archaeology*. Springer, Dordrecht, Heidelberg, London, New York.
- Oltean, I.A., & Abell, L.L. (2012): High-resolution satellite imagery and the detection of buried archaeological features in ploughed landscapes. In: R. Lasaponara, & N. Masini (Eds.), *Satellite remote sensing. A new tool for archaeology*. Dordrecht, Heidelberg, London, New York: Springer
- Oppenheim, A.V., & Schaffer, R.W. (1975): *Digital Signal Processing*. Englewood Cliffs, New Jersey, USA: Prentice-Hall Inc.
- Ordóñez, C., Martínez, J., de Cos, J.F., & Sánchez, F. (2011): Determining vine leaf water stress by functional data analysis. *International Journal of Computer Mathematics*, **88**, 1941-1948
- Ottaway, J.H. (1984): *Persistence of organic phosphates in buried soils*.
- Otterman, J., Susskind, J., Brakke, T., Kimes, D., Pielke, R., & Lee, T.J. (1995): Inferring the thermal-infrared hemispheric emission from a sparsely-vegetated surface by directional measurements. *Boundary-Layer Meteorology*, **74**, 163-180
- Ovod, D. (2015): Orthomosaic texturing: a vera and mosaic option. *Personal Communication by Email with R. Retzlaff*, St. Petersburg/Trier, 08/07/2015: AgiSoft LLC
- Panigada, C., Rossini, M., Meroni, M., Cilia, C., Busetto, L., Amaducci, S., Boschetti, M., Cogliati, S., Picchi, V., Pinto, F., Marchesi, A., & Colombo, R. (2014): Fluorescence, PRI and canopy temperature for water stress detection in cereal crops. *International Journal of Applied Earth Observation and Geoinformation*, **30**, 167-178
- Panigada, C., Rossini, M., Meroni, M., Cilia, C., Busetto, L., Amaducci, S., Boschetti, M., Cogliati, S., Picchi, V., Pinto, F., Marchesi, A., & Colombo, R. (2014): Fluorescence, PRI and canopy temperature for water stress detection in cereal crops. *International Journal of Applied Earth Observation and Geoinformation*, **30**, 167-178
- Parcak, S.H. (2009): *Satellite remote sensing for Archaeology*. New York: Routledge
- Peñuelas, J., I. Filella, C. Biel, L. Serrano, and R. Savé. 1993. The reflectance at the 950-970 nm region as an indicator of plant water status. *International Journal of Remote Sensing* **14**:1887-1905.

- Peralta de Andrés, J. (2000): *Series de vegetación y sectorización fitoclimática de la comarca agraria III*.
- Pérez-Priego, O., Zarco-Tejada, P.J., Miller, J.R., Sepulcre-Cantó, G., & Fereres, E. (2005): Detection of water stress in orchard trees with a high-resolution spectrometer through chlorophyll fluorescence in-filling of the O2-A band. *IEEE Transactions on Geoscience & Remote Sensing*, **43**, 2860-2869
- Plascyk, J.A. (1975): The MK II Fraunhofer Line Discriminator (FLD-II) for Airborne and Orbital Remote Sensing of Solar-Stimulated Luminescence. *Optical Engineering*, **14**, 330-339
- Poni, S., Intrieri, C., & Silvestroni, O. (1994): Interactions of Leaf Age, Fruiting, and Exogenous Cytokinins in Sangiovese Grapevines Under Non-Irrigated Conditions. II. Chlorophyll and Nitrogen Content. *American Journal of Enology and Viticulture*, **45**, 278-284
- Pontius, R.G., & Millones, M. (2011): Death to Kappa: birth of quantity disagreement and allocation disagreement for accuracy assessment. *International Journal of Remote Sensing*, **32**, 4407-4429
- Preu, C., Naschold, R., & Weerakkody, U. (1987): Der Einsatz einer Ballon-Fotoeinrichtung für küstenmorphologische Fragestellungen. In: B. Hofmeister, & F. Voss (Eds.): *Beiträge zur Geographie der Küste und Meere*. Berliner geographie Studien, 377-388, Berlin
- Primicerio, J., Di Gennaro, S., Fiorillo, E., Genesio, L., Lugato, E., Matese, A., & Vaccari, F. (2012): A flexible unmanned aerial vehicle for precision agriculture. *Precision Agriculture*, **13**, 517-523
- Qi, J., Cabot, F., Moran, M.S., & Dedieu, G. (1995): Biophysical parameter estimations using multidirectional spectral measurements. *Remote Sensing of Environment*, **54**, 71-83
- Qin, W., & Gerstl, S.A.W. (2000): 3-D Scene Modeling of Semidesert Vegetation Cover and its Radiation Regime. *Remote Sensing of Environment*, **74**, 145-162
- Rahman, H., Pinty, B., & Verstraete, M.M. (1993): Coupled surface-atmosphere reflectance (CSAR) model: 2. Semiempirical surface model usable with NOAA advanced very high resolution radiometer data. *Journal of Geophysical Research: Atmospheres*, **98**, 20791-20801
- Rascher et al., U. (2013): Final Report. Technical Assistance for the Deployment of an Advanced Hyperspectral Imaging Sensor during HYFLEX. In response to ESA Contract No. 4000107143/12/NL/FF/If. In: Jülich: Forschungszentrum Jülich
- Rascher, U., & Pieruschka, R. (2008): Spatio-temporal variations of photosynthesis: the potential of optical remote sensing to better understand and scale light use efficiency and stresses of plant ecosystems. *Precision Agriculture*, **9**, 355-366

- Rascher, U., Agati, G., Alonso, L., Cecchi, G., Champagne, S., Colombo, R., Damm, A., Daumard, F., de Miguel, E., Fernandez, G., Franch, B., Franke, J., Gerbig, C., Gioli, B., Gómez, J.A., Goulas, Y., Guanter, L., Gutiérrez-de-la-Cámara, Ó., Hamdi, K., Hostert, P., Jiménez, M., Kosvancova, M., Lognoli, D., Meroni, M., Miglietta, F., Moersch, A., Moreno, J., Moya, I., Neininger, B., Okujeni, A., Ounis, A., Palombi, L., Raimondi, V., Schickling, A., Sobrino, J.A., Stellmes, M., Toci, G., Toscano, P., Udelhoven, T., van der Linden, S., & Zaldei, A. (2009): CEFLES2: the remote sensing component to quantify photosynthetic efficiency from the leaf to the region by measuring sun-induced fluorescence in the oxygen absorption bands. *Biogeosciences*, **6**, 1181-1198
- Resonon (2015): Hyperspectral imaging cameras Bozeman, MT, USA: Resonon
- Retzlaff, R., Molitor, D., Behr, M., Bossung, C., Rock, G., Hoffmann, L., Evers, D., & Udelhoven, T. (2015): UAS-based multi-angular remote sensing of soil management strategy effects on grapevine. *Journales Internationales des Sciences de la Vigne et du Vin*, **46**, 2, 85-102
- Retzlaff, R., Molitor, D., Behr, M., Wantzenrieder, T., Hoffmann, L., Evers, D., & Udelhoven, T. (2013): Assessment of grapevine leaf and canopy vigour properties by quadcopter-carried VIS/NIR multispectral camera In: J. Bendig, & G. Bareth (Eds.), *Workshop on UAV-based Remote Sensing Methods for Monitoring Vegetation*. (pp. 75-82). Köln: Universität Köln
- Ribeiro da Luz, B., & Crowley, J.K. (2007): Spectral reflectance and emissivity features of broad leaf plants: Prospects for remote sensing in the thermal infrared (8.0–14.0 μm). *Remote Sensing of Environment*, **109**, 393-405
- Richards, J.A. (2013): *Remote Sensing Digital Image Analysis. An Introduction*. (5th edition ed.). Berlin, Heidelberg: Springer
- Richter, R. (2010): Atmospheric/Topographic Correction for Airborne Imagery., (*ATCOR-4 User Guide, Version 5.1, January 2010*). Wessling, Germany: DLR - German Aerospace Center
- Rikola Ltd. (2015): Snapshot hyperspectral camera is airborne. Oulu, Finland: Rikola Ltd.
- Ripoche, A., Metay, A., Celette, F., & Gary, C. (2011): Changing the soil surface management in vineyards: immediate and delayed effects on the growth and yield of grapevine. *Plant and Soil*, **339**, 259-271
- Roberts, D.A., Yamagushi, Y., & Lyon, R.J.P. (1985): Calibration of Airborne Imaging Spectrometer data to percent reflectance using field spectral measurements. In, *19th International Symposium on Remote Sensing of Environment*. (pp. 679-688). Ann Arbor, Michigan, USA
- Rock, G. (2010): Sensitivitätsanalyse zur UAV-Photogrammetrie. Dargestellt an einer Befliegung mit einer autonom fliegenden Modellflugzeug-Drohne.

- Diplomarbeit, Trier: Universität Trier, Umweltfernerkundung und Geoinformatik
- Rondeaux, G., Steven, M., & Baret, F. (1996): Optimization of soil-adjusted vegetation indices. *Remote Sensing of Environment*, **55**, 95-107
- Rosnell, T., & Honkavaara, E. (2012): Point Cloud Generation from Aerial Image Data Acquired by a Quadcopter Type Micro Unmanned Aerial Vehicle and A Digital Still Camera. *Sensors*, **12**, 453-480
- Roujean, J.-L., & Breon, F.-M. (1995): Estimating PAR absorbed by vegetation from bidirectional reflectance measurements. *Remote Sensing of Environment*, **51**, 375-384
- Rouse, J.W., Haas, R., Schell, J., & Deering, D. (1974): Monitoring vegetation systems in the Great Plains with ERTS In: S.e.a. Fredon (Ed.), Third Earth Resources Technical Satellite Symposium. (pp. 309-317). Washington, DC
- Roze, A., Zufferey, J.-C., Beyeler, A., & McClellan, A. (2009-2015): eBee RTK accuracy assessment. In: senseFly (Ed.), *White Paper* Cheseaux-Lausanne, Switzerland
- Rubio, E., Caselles, V., Coll, C., Valour, E., & Sospedra, F. (2003): Thermal-infrared emissivities of natural surfaces: improvements on the experimental set-up and new measurements. *International Journal of Remote Sensing*, **24**, 5379-5390
- Sandmeier, S.R. (2000): Acquisition of Bidirectional Reflectance Factor Data with Field Goniometers. *Remote Sensing of Environment*, **73**, 257-269
- Sandmeier, S.R., & Itten, K.I. (1999): A Field Goniometer System (FIGOS) for Acquisition of Hyperspectral BRDF Data. *IEEE Transactions on Geoscience & Remote Sensing*, **37**, 978-986
- Schiefer, S., Hostert, P., & Damm, A. (2006): Correcting brightness gradients in hyperspectral data from urban areas. *Remote Sensing of Environment*, **101**, 25-37
- Schlerf, M., Atzberger, C., & Hill, J. (2005): Remote sensing of forest biophysical variables using HyMap imaging spectrometer data. *Remote Sensing of Environment*, **95**, 177-194
- Schneider, T., & Manakos, I. (2003): BRDF Approximation of maize and canopy parameter retrieval by ProSail inversion. In, *3rd EARSeL Workshop on Imaging Spectroscopy*. (pp. 569-579). Herrsching
- Schneider, V. (2010): Primer on atypical aging. *Wines and Vines*, **4**, 45-51
- Schott, J.R., Salvaggio, C., & Volchok, W.J. (1988): Radiometric scene normalization using pseudoinvariant features. *Remote Sensing of Environment*, **26**, 1-16
- Schübeler, D., & Eickhoff, D. (2010): md4-1000 technical drawing. Siegen: microdrones GmbH

- Schultz, H.R. (1996): Leaf absorptance of visible radiation in *Vitis vinifera* L.: estimates of age and shade effects with a simple field method. *Scientia Horticulturae*, **66**, 93-102
- Schultz, H.R., & Löhnertz, O. (2002): Cover crop use in Germany and possible effects on wine quality. In: I.I.T.d. Vin (Ed.), *Mondiaviti*. (pp. 56-64). Bordeaux: ITV (FRA)
- Schultz, H.R., & Stoll, M. (2010): Some critical issues in environmental physiology of grapevines: future challenges and current limitations. *Australian Journal of Grape and Wine Research*, **16**, 4-24
- Scrucca, L. (2013): GA: A Package for Genetic Algorithms in R. *Journal of Statistical Software*, **53**, 1
- Sepulcre-Cantó, G., Zarco-Tejada, P.J., Jiménez-Muñoz, J.C., Sobrino, J.A., Miguel, E.d., & Villalobos, F.J. (2006): Detection of water stress in an olive orchard with thermal remote sensing imagery. *Agricultural and Forest Meteorology*, **136**, 31-44
- Serrano, L., González-Flor, C., & Gorchs, G. (2012): Assessment of grape yield and composition using the reflectance based Water Index in Mediterranean rainfed vineyards. *Remote Sensing of Environment*, **118**, 249-258
- Sinauer Associates, Inc.
- Smart, R., & Robinson, M. (1991): *Sunlight into wine. A handbook for winegrape canopy management*. . Adelaide, SA, Australia
- Smit, J.L., Sithole, G., & Strever, A.E. (2010): Vine signal extraction - an application of remote sensing in precision viticulture. *South African Journal of Enology and Viticulture*, **31**, 65-74
- Smith, G.M., & Milton, E.J. (1999): The use of the empirical line method to calibrate remotely sensed data to reflectance. *International Journal of Remote Sensing*, **20**, 2653-2662
- Sobrino, J.A., Franch, B., Jimenez-Muñoz, J.C., Hidalgo, V., Soria, G., Julien, Y., Oltra-Carrio, R., Mattar, C., Ruescas, A., Daumard, F., Champagne, S., Fournier, A., Goulas, Y., Ounis, A., & Moya, I. (2011): Fluorescence estimation in the framework of the CEFLES2 campaign. *International Journal of Remote Sensing*, **32**, 5875-5889
- Soliman, A., Heck, R., Brenning, A., Brown, R., & Miller, S. (2013): Remote Sensing of Soil Moisture in Vineyards Using Airborne and Ground-Based Thermal Inertia Data. *Remote Sensing*, **5**, 3729-3748
- Song, S., Gong, W., Zhu, B., & Huang, X. (2011): Wavelength selection and spectral discrimination for paddy rice, with laboratory measurements of hyperspectral leaf reflectance. *ISPRS Journal of Photogrammetry and Remote Sensing*, **66**, 672-682

- Steele, M., Gitelson, A.A., & Rundquist, D. (2008): Nondestructive Estimation of Leaf Chlorophyll Content in Grapes. *Papers in Natural Resources*, 1-8
- Suárez, L., Zarco-Tejada, P.J., Berni, J.A.J., González-Dugo, V., & Fereres, E. (2009): Modelling PRI for water stress detection using radiative transfer models. *Remote Sensing of Environment*, **113**, 730-744
- Suárez, L., Zarco-Tejada, P.J., González, M.R., Berni, J.A.J., Sagardoy, R., Morales, F., & Fereres, E. (2010): Detecting water stress on fruit quality in orchards with time-series PRI airborne imagery. *Remote Sensing of Environment*, **114**, 286-298
- Suits, G.H. (1983): Extension of a uniform canopy reflectance model to include row effects. *Remote Sensing of Environment*, **13**, 113-129
- Taiz, L., & Zeiger, E. (2010): *Plant Physiology*. (5th edition ed.). Sunderland, MA, USA
- Tanré, D., Deroo, C., Duhaut, P., Herman, M., Morcrette, J.J., Perbos, J., & Deschamps, P.Y. (1990): Description of a computer code to simulate the satellite signal in the solar spectrum: the 5S code. *International Journal of Remote Sensing*, **11**, 659-668
- Tardaguila, J., Baluja, J., Arpon, L., Balda, P., & Oliveira, M. (2011): Variations of soil properties affect the vegetative growth and yield components of “Tempranillo” grapevines. *Precision Agriculture*, **12**, 762-773
- Tesic, D., Keller, M., & Hutton, R. (2007): Influence of vineyards floor management practices on grapevine vegetative growth, yield, and fruit composition. *American Journal of Enology and Viticulture*, **58**, 1-11
- Tetracam Inc. (2010): Agricultural Camera User's Guide Chatsworth, CA 91311 USA: Tetracam Inc.
- Tetracam Inc. (2011): Multi-Camera Array User's Guide. Chatsworth, CA, USA: Tetracam Inc.
- Tetracam Inc. (2015): Tetracam introduces new Micro-MCA product line. Chatsworth, CA, USA: Tetracam Inc.
- The R Core Team (2014): R: A Language and Environment for Statistical Computing. Vienna, Austria: The R Foundation for Statistical Computing
- Thorp, K.R., Wang, G., West, A.L., Moran, M.S., Bronson, K.F., White, J.W., & Mon, J. (2012): Estimating crop biophysical properties from remote sensing data by inverting linked radiative transfer and ecophysiological models. *Remote Sensing of Environment*, **124**, 224-233
- Triggs, B., McLaughlan, P.F., Hartley, R.I., & Fitzgibbon, A.W. (1999): Bundle Adjustment - A Modern Synthesis In: B. Triggs, A. Zisserman, & R. Szeliski (Eds.), *Vision Algorithms: Theory and Practice, International Workshop on*

- Vision Algorithms, held during ICCV'99.* (pp. 298-372). Corfu, Greece: Springer-Verlag
- Trimble Navigation Limited (2008): Datasheet: GeoXT handheld. Westminster, CO, USA: Trimble Navigation Limited
- Tripathi, R., Sahoo, R., Sehgal, V., Tomar, R.K., Chakraborty, D., & Nagarajan, S. (2012): Inversion of PROSAIL Model for Retrieval of Plant Biophysical Parameters. *Journal of the Indian Society of Remote Sensing*, **40**, 19-28
- Tucker, C.J. (1979): Red and photographic infrared linear combinations for monitoring vegetation. *Remote Sensing of Environment*, **8**, 127-150
- Tytgat, L. (2012): The European UAS Integration Approach. In: B. Co (Ed.), *2012 RPAS Yearbook - RPAS: The Global Perspective*, (pp. 36-37). Paris: Blyenburgh & Co
- Udelhoven, T., Emmerling, C., & Jarmer, T. (2003): Quantitative analysis of soil chemical properties with diffuse reflectance spectrometry and partial least-square regression: A feasibility study. *Plant and Soil*, **251**, 319-329
- Udovic, A. (2012): RPAS Regulatory Situation in Germany. In: Blyenburgh & Co (Ed.), *2012 - RPAS Yearbook - RPAS: The Global Perspective*, (p. 132). Paris: Blyenburgh & Co
- Ullmann, H. (1971): Hochmoor-Luftbilder mit Hilfe eines Kunststoffballons. *Österreichische Botanische Zeitschrift*, **119**, 548-556
- Unmanned Aerial Vehicle System Association (2011): UAV or UAS? : 07/07,
- van Blyenburgh, P. (2012): RPAS: The Global Perspective. In: P. van Blyenburgh (Ed.), *RPAS Yearbook 2012/2013*. Paris: Blyenburgh & Co, UVS International
- van Blyenburgh, P. (2013): RPAS: The Global Perspective. In: P. van Blyenburgh (Ed.), *The International Remotely Piloted Aircraft Systems Yearbook* (p. 228). Paris: Blyenburgh & Co, UVS International
- van Blyenburgh, P. (2014a): 2014 Yearbook - RPAS: The Global Perspective 2014/2015. In: P. van Blyenburgh (Ed.), (p. 240). Paris, France: Blyenburgh & Co, UVS International
- van Blyenburgh, P. (2014b): Regulation Monitor: RPAS Regulation in Europe. Status: 17 March 2014. In: *RegMon_EU_RPAS-Regulation_140317-1.pdf* (Ed.), http://uvs-international.org/index.php?option=com_content&view=article&id=266&Itemid=818. Paris: UVS International
- van Blyenburgh, P. (2015): 2015 Yearbook - RPAS: The Global Perspective 2015/2016. In: P. van Blyenburgh (Ed.), (p. 252). Paris, France: Blyenburgh & Co.,
- van den Broek, W.H.A.M., Derks, E.P.P.A., van de Ven, E.W., Wienke, D., Geladi, P., & Buydens, L.M.C. (1996): Plastic identification by remote sensing

- spectroscopic NIR imaging using kernel partial least squares (KPLS). *Chemometrics and Intelligent Laboratory Systems*, **35**, 187-197
- van der Meer, F.D., van der Werff, H.M.A., van Ruitenbeek, F.J.A., Hecker, C.A., Bakker, W.H., Noomen, M.F., van der Meijde, M., Carranza, E.J.M., Smeth, J.B.d., & Woldai, T. (2012): Multi- and hyperspectral geologic remote sensing: A review. *International Journal of Applied Earth Observation and Geoinformation*, **14**, 112-128
- van Wagenen, J. (2015): European RPAS Workshop looks to tackle technical, regulatory issues. *Avionics Today* (June 4, 2015)
- Verhoef, W. (1984): Light scattering by leaf layers with application to canopy reflectance modeling: The SAIL model. *Remote Sensing of Environment*, **16**, 125-141
- Verhoeven, G. (2009): Beyond conventional boundaries. New technologies, methodologies, and procedures for the benefit of aerial archaeological data acquisition and analysis. Docotorate, p. 347). Faculty of Arts and Philosophy, Dep. of Archaeology and Ancient History of Europe, Ghent University, Ghent, the Netherlands
- Verhoeven, G. (2012): Near-Infrared Aerial Crop Mark Archaeology: From its Historical Use to Current Digital Implementations. *Journal of Archaeological Method and Theory*, **19**, 132-160
- Verhoeven, G., Lupashin, S., Briese, C., & Doneus, M. (2014): Airborne imaging for heritage documentation using the Fotokite tethered flying camera. In: D.o. Archaeology (Ed.), *EGU General Assembly 2014: History and Archaeology*. (pp. 1). Vienna, Austria: European Geosciences Union
- Viertola, L.M., Andreu, J., & Peréx, M.J. (2013): The Roman Aqueductbridge of Los Banales (Uncastillo, Spain). Structural Analysis In: G. Wiplinger (Ed.), *Historische Wasserleitungen. Gestern - Heute - Morgen*. Wien: Babesch Foundation, Beschaving
- Vierling, L.A., Fersdahl, M., Chen, X., Zhenpeng, L., & Zimmermann, P. (2006): The Short Wave Aerostat-Mounted Imager (SWAMI): A novel platform for acquiring remote sensed data from a tethered balloon. *Remote Sensing of Environment*, **103**, 255-264
- Wallace, L., Lucieer, A., Watson, C., & Turner, D. (2012): Development of a UAV-LiDAR system with application to forest inventory. *Remote Sensing*, **4**, 1519-1543
- Walter-Shea, E.A., & Norman, J.M. (1991): Leaf Optical Properties. In: R.B. Myneni, & J. Ross (Eds.), *Photon-Vegetation Interactions: Applications in Optical Remote Sensing and Plant Ecology*, (pp. 229-251). Berlin: Springer-Verlag

- Wantzenrieder, T.N. (2011): Fernerkundliche Erfassung von Pflanzenzustandsgrößen mittels Strahlungstransfermodellierung und einer Drohne, Masterarbeit. Trier: Universität Trier, Umweltfernerkundung und Geoinformatik
- Watts, A.C., Ambrosia, V.G., & Hinkley, E.A. (2012): Unmanned Aircraft Systems in Remote Sensing and Scientific Research: Classification and Considerations of Use. *Remote Sensing*, **4**, 1671-1692
- Whittlesey, J.H. (1970): Tethered Balloon for Archaeological Photos. *Photogrammetric Engineering and Remote Sensing*, **36** 181-186
- Williams, T.E. (2012): Unmanned Aerial Vehicle Photography: Exploring the Medieval City of Merv, on the Silk Roads of Central Asia. *Archaeology International*, **15**, 54-68
- Wu, C., Niu, Z., Tang, Q., & Huang, W. (2008): Estimating chlorophyll content from hyperspectral vegetation indices: Modeling and validation. *Agricultural and Forest Meteorology*, **148**, 1230-1241
- Wundram, D., & Löffler, J. (2008): High-resolution spatial analysis of mountain landscapes using a low-altitude remote sensing approach. *International Journal of Remote Sensing*, **29**, 961-974
- Xue, L., & Yang, L. (2009): Deriving leaf chlorophyll content of green-leafy vegetables from hyperspectral reflectance. *ISPRS Journal of Photogrammetry and Remote Sensing*, **64**, 97-106
- Yan, B., Xu, X., & Fan, W. (2012): A unified canopy bidirectional reflectance (BRDF) model for row ceops. *Science China Earth Sciences*, **55**, 824-836
- Yan, Y., Li, Z., & Shao, H. (2014): Research of low-altitude photogrammetry implementation strategy of China's ancient circumvallation. *Studies in Surveying and Mapping Science*, **20-25**
- Yao, Y., Liu, Q., Liu, Q., & Li, X. (2008): LAI retrieval and uncertainty evaluations for typical row-planted crops at different growth stages. *Remote Sensing of Environment*, **112**, 94-106
- Yu, K., Lenz-Wiedemann, V., Chen, X., & Bareth, G. (2014): Estimating leaf chlorophyll of barley at different growth stages using spectral indices to reduce soil background and canopy structure effects. *ISPRS Journal of Photogrammetry and Remote Sensing*, **97**, 58-77
- Zarco-Tejada, P.J., Berjón, A., & Miller, J.R. (2004): Stress Detection in Crops with Hyperspectral Remote Sensing and Physical Simulation Models In, *Airborne Imaging Spectroscopy Workshop*. Bruges, Belgium
- Zarco-Tejada, P.J., Berjon, A., Lopez-Lozano, R., Miller, J.R., Martin, P., Cachorro, V., Gonzalez, M.R., & de Frutos, A. (2005): Assessing vineyard condition with hyperspectral indices: Leaf and canopy reflectance simulation in a row-structured discontinuous canopy. *Remote Sensing of Environment*, **99**, 271-287

- Zarco-Tejada, P.J., Berni, J.A.J., Suárez, L., Sepulcre-Cantó, G., Morales, F., & Miller, J.R. (2009): Imaging chlorophyll fluorescence with an airborne narrow-band multispectral camera for vegetation stress detection. *Remote Sensing of Environment*, **113**, 1262-1275
- Zarco-Tejada, P.J., Catalina, A., González, M.R., & Martín, P. (2013a): Relationships between net photosynthesis and steady-state chlorophyll fluorescence retrieved from airborne hyperspectral imagery. *Remote Sensing of Environment*, **136**, 247-258
- Zarco-Tejada, P.J., González-Dugo, V., & Berni, J.A.J. (2012): Fluorescence, temperature and narrow-band indices acquired from a UAV platform for water stress detection using a micro-hyperspectral imager and a thermal camera. *Remote Sensing of Environment*, **117**, 322-337
- Zarco-Tejada, P.J., González-Dugo, V., Williams, L.E., Suárez, L., Berni, J.A.J., Goldhamer, D., & Fereres, E. (2013b): A PRI-based water stress index combining structural and chlorophyll effects: Assessment using diurnal narrow-band airborne imagery and the CWSI thermal index. *Remote Sensing of Environment*, **138**, 38-50
- Zarco-Tejada, P.J., Miller, J.R., Mohammed, G.H., Noland, T.L., & Sampson, P.H. (2000): Chlorophyll Fluorescence Effects on Vegetation Apparent Reflectance: II. Laboratory and Airborne Canopy-Level Measurements with Hyperspectral Data. *Remote Sensing of Environment*, **74**, 596-608
- Zarco-Tejada, P.J., Miller, J.R., Morales, A., Berjón, A., & Agüera, J. (2004): Hyperspectral indices and model simulation for chlorophyll estimation in open-canopy tree crops. *Remote Sensing of Environment*, **90**, 463-476
- Zarco-Tejada, P.J., Morales, A., Testi, L., & Villalobos, F. (2013c): Spatio-temporal patterns of chlorophyll fluorescence and physiological and structural indices acquired from hyperspectral imageray as compared with carbon fluxes measured with eddy covariance. *Remote Sensing of Environment*, **133**, 102-115
- Zarco-Tejada, P.J., Pushnik, J.C., Dobrowski, S.Z., & Ustin, S. (2003): Steady-state chlorophyll a fluorescence detection from canopy derivative reflectance and double-peak red-edge effects. *Remote Sensing of Environment*, **84**, 283-294
- Zhang, C., & Kovacs, J. (2012): The application of small unmanned aerial systems for precision agriculture: a review. *Precision Agriculture*, **13**, 693-712
- Zhang, Y. (1999): MODIS UCSB emissivity library: <http://www.ices.ucsb.edu/modis/EMIS/html/em.html>, 08/07/2015, Santa Barbara, CA, USA: University of California, Institute for Computational Earth System Science
- Zhao, F., Gu, X., Verhoef, W., Wang, Q., Yu, T., Liu, Q., Huang, H., Qin, W., Chen, L., & Zhao, H. (2010): A spectral directional reflectance model of row crops. *Remote Sensing of Environment*, **114**, 265-285

- Zhao, F., Guo, Y., Verhoef, W., Gu, X., Liu, L., & Yang, G. (2014): A Method to Reconstruct the Solar-Induced Canopy Fluorescence Spectrum from Hyperspectral Measurements. *Remote Sensing*, **6**, 10171-10192
- Zufferey, V., Murisier, F., & Schultz, H.R. (2000): A model analysis of the photosynthetic response of *Vitis vinifera* L. cvs Riesling and Chasselas leaves in the field: I. Interaction of age, light and temperature. *Vitis*, **39**, 19-26

Summary

The work examined the potential use of small unmanned aerial systems (UAS) for agricultural crop observations and archaeological applications. The term UAS encompasses the aerial vehicle and its propulsion mechanism, the sensor payload, a ground control station, the communication means between ground station and the vehicle and any other support equipment like, for example, transport means. Due to their flexibility UAS have found a booming development since the turn of the millennium.

For the world's growing population, agricultural production requires a sensible intensification to ensure food security to all people and to avoid further soil and land degradation. Precision agriculture subsumes the technical improvements aiming at more efficient yet less harmful agricultural practices. In this context, one prerequisite for food production is the fast and easy access to geospatial data required to local farmers. UAS have bridged the gap on cost-intensive manned aircraft and satellite imagery.

Potential benefits lie in the ad-hoc acquisition of large-scale environmental remote sensing data, the lower costs of data acquisition compared to manned aircraft, relative independency of cloud coverage as they are generally flown below cloud level. Most UAS being developed are Mini-UAS (< 5kg take-off weight), and thereof vertical take-off and landing (VTOL) systems. They offer the potential to hover over sites, yet are slower than fixed wing systems, and appropriate for sites ≤ 5 ha during one flight, flight times range from 15-60 min. Flight regulations and integration into manned airspace are currently being worked on at the European and national levels. To date, general ascent permits in Rhineland-Palatinate are granted for limited flight altitudes (< 100 m above ground) in unrestricted areas, liability insurance and the responsibility to inform regulating bodies and police authorities 24 hours prior to ascent.

The main aims of this study were to evaluate how key physiological crop parameters (chlorophyll content, nitrogen content, LAI, yield, sun-induced chlorophyll fluorescence: F_s) may best be retrieved with a UAS, and how multispectral data may be used for archaeological reconnaissance. A quadrocopter UAS (md4-1000, microdrones GmbH, payload of < 1 kg) was equipped with a digital single-lens reflex, a six-band multispectral (MiniMCA-6, Tetracam Inc.) and a broadband thermal camera (UCM, Zeiss).

A sensitivity analysis selected suitable wavelengths and assessed bidirectional and altitudinal effects on the multispectral signal. The study then describes the required workflow from image acquisition to preprocessing for the respective cameras with special focus on the multispectral camera (equipped with 10 nm-FWHM spectral filters in the

range of 530 nm – 900 nm). Pre-processing included sensor radiometric corrections (lens distortion, vignetting correction, band-to band image alignment), radiometric calibration to reference spectra by means of empirical line calibration or atmospheric correction, and geometric corrections by Structure from Motion (SfM) software (point cloud modelling by bundle block adjustment, meshing and texturing) to retrieve digital elevation models and orthophoto mosaics of centimeter-range spatial resolution.

For a vineyard, the best viewing geometry to detect soil management effects on the spectral signal were evaluated. Oblique viewing geometries of illuminated canopies 45° off nadir were found to be most suitable for estimating physiological parameters for row crops, and soil management strategies could well be differentiated. Thus, plant parameters could be predicted throughout the season by regression analysis, i.e. chlorophyll R^2_{cv} of 0.65, nitrogen balance index by 0.76 (2012), and yield with 0.84 for 2011, and R^2_{cv} for early season and mid-season of 0.87 and 0.73 respectively.

Effects of nitrogen fertilizer experiments on the F_s of sugar beet were analyzed by visual inspections and two-factorial ANOVAs of the multispectral and thermal signal during the HyFlex campaign in 2012. Varieties could well be discriminated by spectral and broadband thermal signal, less though for respective fluorescence vegetation indices within the O_2 absorption band. Diurnal fluorescence signals were obtained by multiple UAS flights (23/08/2012, 8:00 – 14:00 UTC). Despite less stable atmospheric conditions in the morning, a diurnal course of F_s could be retrieved, yet F_s signals showed to be higher than comparative field measurements.

Archaeological reconnaissance has been applied since the 1970ies when tethered balloons were used. Pattern recognition is improved through the extension of the human vision to multispectral, thermal, or recent hyperspectral ranges, a.o.. Studies in Los Bañales, Spain illustrated the general information gain UAS data, pattern recognition of possible land-use related vegetation distribution by means of land cover classification of multispectral data and texture measures by support vector machines. Furthermore, crop mark detection was analyzed.

Concluding, high quality multispectral/thermal UAS data may be derived by high image overlap (80-90%) including oblique imagery, where required, simultaneous reference spectral or thermal measurements for radiometric calibration should be carried out, and geometric referencing with ground control points derived at cm to dm accuracy. Thus UAS imagery provides the missing gap for large-scale quantitative environmental monitoring.

Curriculum Vitae

Name, Surname Retzlaff, Rebecca
Address Louis-Pasteur-Str. 6, 54296 Trier, Germany
Birth date, location 25.01.1967, Tübingen, Germany

Education

1973 – 1977 Grundschule Innenstadt, Tübingen, Germany
1977 – 1986 Wildermuth-Gymnasium, Tübingen, Germany

University Education

10/1987 – 06/1995 Studies of Applied Physical Geography, Universität Trier, Minor subjects. Remote sensing, climatology (Dipl. Geographin)
10/1995 – 09/1996 Postgraduate Studies in GIS, University of Edinburgh, Scotland, Great Britain (Master of Science in GIS), DAAD postgraduate scholarship)

Professional Experience

10/1996 – 02/1997 GIS Officer, Scottish Natural Heritage, Edinburgh, Great Britain
04/1997 – 01/2000 Scientific staff, EC-project „Land Use Change Interactions with Fire in Mediterranean Landscapes“, Remote Sensing Department, Universität Trier, Germany
02/2000 – 12/2002 Scientific staff, GIS and Data Management, Sonderforschungsbereich 522 „Umwelt und Region“, Universität Trier, Germany
05/2003 – 03/2005 Scientific staff, Wildtierinformationssystem des Deutschen Jagdschutz-Verbandes. e.V., Biogeography Dep., Universität Trier, Germany
02/2009 – 06/2010 Support specialist, alta4 Geoinformatik AG, Trier, Germany
07/2010 – 09/2014 Scientific staff, Environmental Remote Sensing and Geoinformatics Dep., Universität Trier, Germany